Experiments and Theory of Induced Optical Magnetization

by

Alexander A. Fisher

A dissertation submitted in partial fulfillment
of the requirements for the degree of
Doctor of Philosophy
(Applied Physics)
in the University of Michigan
2016

Doctoral Committee:

Professor Stephen C. Rand, Co-chair
Research Scientist John F. Whitaker, Co-chair
Professor Jinsang Kim
Professor Çagliyan Kurdak
Professor Herbert Graves Winful

To Mom and Dad.

Acknowledgements

It is imperative that I thank my adviser Dr. Stephen Rand for his help, guidance, and support on this thesis as well as his availability throughout the past four years. Without him, this project surely would not have been possible.

I would also like to thank my co-adviser Dr. John Whitaker for his patience and for our long discussions on instrumentation, experimentation, and everything else in life. I could always rely on John to provide clarity and direction on projects, even when things seemed impossible.

I also need to thank my other committee members, Dr. Jinsang Kim for his help on selecting and preparing samples, Dr. Herbert Winful for his useful criticisms along the way, and Dr. Çagliyan Kurdak for his support and interest in this project from the beginning.

I am very grateful to the Applied Physics Program at the University of Michigan for their support and help throughout the years and for providing me the opportunity to conduct graduate research.

I am also indebted to the past and current members of our research group, Ayan, Liz, Brad, Will, Mike, and Manish, as well as friends in the program, Bob, Skyler, and Justin, who were always available to bounce ideas off of and help solve problems along the way.

I would especially like to thank my mother, father, family, and friends for their support, love, and patience throughout the years. I surely would not have made it this far had it not been for them.

Preface

If I had listened to the naysayers, I would still be in the Austrian Alps yodeling. – Arnold Schwarzenegger

TABLE OF CONTENTS

LIST OF FIGURES

LIST OF TABLES

LIST OF APPENDICES

LIST OF ABBREVIATIONS

APD avalanche photodiode

CEP carrier-envelope phase

CLOM complete Lorentz oscillator model

COM center-of-mass

CPA chirp-pulse amplified

cw continuous-wave

DFG difference frequency generation

ED electric dipole

EMI electro-magnetic interference

FWHM full-width at half-max

IPA isopropyl alcohol

ITO indium tin oxide

LHS left-hand side

LOM Lorentz oscillator model

MD magnetic dipole

ME magneto-electric

MIIPS multiphoton intrapulse interference phase scan

ND neutral density

OR optical rectification

PMT photomultiplier tube

RHS right-hand side

RWA rotating wave approximation

SH second-harmonic

SHG second-harmonic generation

SLM spatial light modulator

SRR split ring resonator

TE transverse electric

TIR total internal reflection

THz terahertz

TM transverse magnetic

XPW cross-polarized wave

ABSTRACT

This thesis reports the results of light scattering experiments at moderate optical intensities ($\sim 10^8$ W/cm^2) in which the magnetic component of light induces magnetic dipolar response of unprecedented intensity by a novel nonlinear mechanism. Both experimentally and theoretically the amplitude of induced magnetization is found to be as large as electric polarization ($M = cP$) at intensities above $\sim 10^8$ W/cm^2 in different materials, greatly exceeding the conventional bounds of the multipole expansion. The transverse nature of the magnetization, its frequency, and its quadratic dependence on incident light intensity are in agreement with an exact theory which identifies the importance of magnetically-induced torque in achieving 2-photon resonance of this ultrafast process.

In this work we report and compare the intensity dependence of cross-polarized scattering in the transparent molecular liquids CCl_4, $SiCl_4$, $SiBr_4$, $SnCl_4$, C_6H_6, C_6D_6, $C_6H_5NH_2$, and C_6H_5CN and the crystalline solid $Gd_3Ga_5O_{12}$. Complete radiation patterns of co-polarized and cross-polarized light scattering were recorded as a function of intensity in these homogeneous media and subsequently decomposed into polarized and unpolarized components to provide a more complete picture of scattering dynamics than has been possible in past experiments.

The cross-polarized scattering observed from spherical-top molecules CCl_4, $SiCl_4$, $SiBr_4$, and $SnCl_4$ and crystalline GGG is argued to originate from magnetic dipoles induced by a second-order optical nonlinearity driven jointly by the E and B fields of light. Among the spherical top molecular liquids, $SnCl_4$ developed more intense magnetic scattering at a fixed intensity than CCl_4, in agreement with the predicted dependence on rotational frequency and damping. Cross-polarized scattering in anisotropic molecules C_6H_6, C_6D_6, $C_6H_5NH_2$, and C_6H_5CN, on the other hand, is known to originate from optical orientation of permanent electric dipole moments in first-order or differential polarizability in third-order. The importance of rotational dynamics to depolarization in all the liquids studied is outlined and confirmed through observation of an isotopic effect in the scattering from C_6H_6 vs. C_6D_6. Finally, the new nonlinear optical process investigated here provides a method for generating oriented rotations of molecules.

CHAPTER 1

Introduction

This thesis expands on the conventional model of light-matter interactions dominated by electrically-driven phenomena to include high-frequency magnetism proportional to the electric polarization of dielectric media. The work reported herein is a continuation of the seminal work done by Oliviera which reported evidence of strong, nonlinear magnetic dipole scattering in liquid dielectric samples at non-relativistic intensities [1]. Surprisingly, this phenomenon had not previously been observed, although it required relatively low input intensities (of the order 10^8 W/cm^2) and the 90° detection geometry that is commonplace for light scattering experiments [4]. Subsequent work by Fisher and Rand developed classical [5] and quantum [6] models intended to explain optically-induced magnetization and make detailed comparisons between theoretical and experimental results [2]. Their models provided a physical mechanism that could qualitatively explain the magnetic response, and they predicted two more novel nonlinear processes: sum- and difference-frequency magneto-electric harmonic generation. These three processes constituted a new family of nonlinearities driven by the joint action of the electric and magnetic components of the optical field, referred to here as magneto-electric (ME) nonlinearities. A unique aspect of these nonlinearities driven by the field combination EB, is that unlike all-electric quadratic nonlinearities, they are predicted to occur in centrosymmetric as well as non-centrosymmetric media.

Earlier work raised questions as to how magnetically-driven nonlinearities can be enhanced and how to determine whether they can be observed in all dielectric media. Prior to the present research, only three liquid samples had been studied, all of which had distinctively different molecular and electronic structure: H_2O with an internal dipole moment, C_6H_6 with π-delocalized, anisotropic charge distributions, and CCl_4 with an optically isotropic, tetrahedral geometry [2]. Because these samples presented no systematic variation of properties, comparisons between them provided no compelling clues regarding which properties were important for inducing large cross-polarized scattering that was truly magnetic in origin. The experiments also offered no insight as to whether this effect

would be present in other phases of matter, such as solids. The classical model provided perturbative solutions for quadratic magneto-electric dynamics as well as a useful physical picture of charge deflection due to the magnetic field [5], but no exact analytic solution to the problem has been published. Similarly, the initial quantum picture relied on rare electronic properties and handled the magnetic interaction as a weak perturbation [6]. While these early theoretical models predicted the same trio of nonlinear ME effects, they did not provide proof that the effects could take place universally in all dielectric media or account quantitatively for their magnitudes. The aim of this thesis is to clarify these issues both through experimental observations and theoretical analysis.

This thesis is organized as follows. Chapter 1 first discusses high-frequency magnetism as well as traditional light scattering phenomena. We then provide an overview of initial magnetic scattering experiments and the classical treatment of ME nonlinear processes. In Chapter 2 we develop a new quantum model using a dressed state approach which treats the magnetic field in an *exact* way and describes the sequential action of electric and magnetic fields as interaction terms responsible for mixing the states of an initially symmetric system. This theory is developed in two stages, first by considering an atomic system and then a molecular system. This treatment again confirms the existence of a trio of nonlinear ME effects but for the first time provides correct qualitative and quantitative agreement with experimental findings. The main result of the "molecular model" is the finding that magnetic torque can mediate a nearly-resonant 2-photon transition to rotationally-excited states and account for the large magnetic response measured experimentally. Chapter 3 outlines the experimental approach and methods for measuring the induced magnetization, which is central to this discussion. Special care is taken to discuss the experimental components, procedure for processing the data, and sample selection and preparation.

In Chapter 4 we discuss the main results of this work. We show for the first time that magnetic dipole scattering can be induced in crystalline gadolinium gallium garnet (GGG) and that it is as intense as electric dipole scattering. Following this, comparisons are made of the two series of molecular liquids whose chemical structure systematically varies the electron density or the moment of inertia. First we compare systems with π-delocalized electronic orbitals and then we show a comparison of molecules with tetrahedral symmetry. An important conclusion of these comparisons is that the moment of inertia and molecular damping affect enhanced magnetic response. This comparative study also provides a basis by which to distinguish molecular rotations initiated via a second-order ME process from conventional electrically-induced rotations which have cubic dependence on the field [7]. It is shown that in spherical top molecules that lack anisotropy or internal dipole moments, the cross polarized scattering is magnetic in origin, while in molecules with large anisotropy

it is dominated by an all-electric process. In the second half of Chapter 4, results from the quantum theoretical model are presented. Plots of the induced nonlinear effects versus intensity and detuning are provided. The detuning plots confirm that the calculated moments depend on electric and magnetic detunings as expected. A comparison is made between the classical and quantum models to show that the quantum model not only introduces a mechanism to explain magnetic enhancement, but also includes important corrections to the perturbative solutions from the classical theory, namely that the normalization of quantum states provides a physical limit for how big the predicted moments may be.

In the final chapter, Chapter 5, we summarize the main results from both the experimental findings and the theoretical models. A comparison between the two shows that theory can both qualitatively and quantitatively explain magnetic scattering as intense as Rayleigh scattering ($M = cP$). The outlook that these results provide on the field of high-frequency magnetism is then discussed and some commentary on other experimental platforms which could be used to investigate this trio of nonlinear effects is offered. We conclude with a brief overview of experimental improvements to the magnetic scattering system that are needed to improve dynamic range and to better understand these nonlinearities.

1.1 High-frequency magnetism

High-frequency magnetism has attracted increasing attention in the last few years due to its relevance to metamaterials, spintronics, quantum information, high-speed optical magnetic storage, and other topics. This topic has benefited from decades of advances in techniques to produce novel material properties reliant on magnetic response, such as negative permeability in structured materials [8], coherent optical spin control of semiconductor charge carriers [9] or luminescent centers [10], and ultrafast switching of magnetic domains [11]. In sharp contrast to this, the possibility of harnessing magnetic response in natural, unstructured, "non-magnetic" materials has received virtually no attention. This is understandable in light of traditional arguments suggesting that high frequency magnetism can be neglected in homogeneous media [12]. A dimensional argument from Landau and Lifshitz is provided in their book, *Electrodynamics of Continuous Media*:

> For a given frequency, the most favourable conditions for measuring the susceptibility are those where the body is as small as possible (to increase the spatial derivatives in **curl** $\mathbf{M}$) and where the electric field is weak as possible (to reduce $\mathbf{P}$). The field of an electromagnetic wave does not satisfy the latter condition, because $E \sim H$. Let us therefore consider a variable magnetic

field, say in a solenoid, with the body under investigation placed on the axis. The electric field is due only to induction by the variable magnetic field, and the order of magnitude of E inside the body can be obtained by estimating the terms in the equation **curl** $\mathbf{E} = -(1/c)\partial\mathbf{B}/\partial t$, whence $E/l \sim \omega H/c$ or $E \sim (\omega l/c)H$, where l is the dimension of the body. Putting $\epsilon - 1 \sim 1$, we have $\partial P/\partial t \sim \omega E \sim \omega^2 l H/c$. For the space derivatives of the magnetic moment $\mathbf{M} = \chi\mathbf{H}$ we have c **curl** $\mathbf{M} \sim c\chi\mathbf{H}/l$. If $|\partial\mathbf{P}/\partial t|$ is small compared with $|c$ **curl** $\mathbf{M}|$, we must have

$$l^2 \ll \chi c^2/\omega^2 \, .$$

It is evident that the concept of magnetic susceptibility can be meaningful only if this inequality allows dimensions of the body which are (at least) just macroscopic, i.e. if it is compatible with the inequality $l \gg a$, where a is the atomic dimension. This condition is certainly not fulfilled for the optical frequency range; for such frequencies, the magnetic susceptibility is always $\sim v^2/c^2$, where v is the electron velocity in the atom; but the optical frequencies themselves are $\sim v/a$, and therefore the right hand side of the inequality [above] is $\sim a^2$.

Thus there is no meaning in using the magnetic susceptibility from optical frequencies onward, and in discussing such phenomena we must put $\mu = 1$. To distinguish between $\mathbf{B}$ and $\mathbf{H}$ in this frequency range would be an overrefinement. Actually, the same is true for many phenomena even at frequencies well below the optical range.

This argument has long since discouraged research into magnetic effects at optical frequencies.

Another reason to expect the effects of optical B fields to be small is simply that $B \ll E$. Recall the Maxwell equation for the curl of the electric field,

$$\nabla \times \mathbf{E} = -\frac{\partial \mathbf{B}}{\partial t} \, , \tag{1.1}$$

and assume we have a harmonic plane wave oscillating at frequency ω traveling along $\hat{z}$,

$$\mathbf{E} = E_0 e^{-i(\omega t - kz)}\hat{x} \quad \text{and} \quad \mathbf{B} = B_0 e^{-i(\omega t - kz)}\hat{y} \, . \tag{1.2}$$

Substituting $\mathbf{E}$ and $\mathbf{B}$ into the curl equation yields

$$kE_0 e^{-i(\omega t - kz)}\hat{y} = \omega B_0 e^{-i(\omega t - kz)}\hat{y}\ . \tag{1.3}$$

This can be rearranged to yield

$$E_0 = \frac{\omega}{k} B_0\ . \tag{1.4}$$

Thus we see that $|B_0| = |E_0|/c$ since $c = \omega/k$, so the amplitude of the magnetic field is smaller than the electric field by a factor of the speed of light. This argument, or the one presented above by Landau, suggest that effects arising from the magnetic component of light should be much smaller than their electric counterparts.

There are two known situations which reverse this conclusion: (1) in the regime of relativistic optics where $v^2/c^2 \sim 1$ [13] (the Lorentz force is large), and (2) in specially designed structures which enable large magnetic response such as metamaterials [14] (E can mimic the effects of B). The results presented in this thesis, however, provide compelling evidence of strong, induced magnetic dipole scattering in transparent dielectric media at non-relativistic intensities [1, 2, 15]. If high-frequency magnetic response could be induced with moderate light intensities in optical materials regardless of their symmetry, it goes without saying that new horizons would emerge for materials and photonic technologies. Among the intriguing possibilities that have been discussed are the conversion of electromagnetic energy directly to electricity in "optical capacitors," solar power generation without semiconductors, the achievement of negative permeability in natural materials, and the generation of large (oscillatory) magnetic fields without current-carrying coils [5, 6, 16].

Traditional nonlinear optical theory, which assumes dissipation-free parametric interactions [17], dictates that magnetic dipole (MD) moments of atoms are at most small fractions of their ED counterparts (unless the ED moment vanishes altogether), so large magnetic response is difficult to understand in a conventional context. The traditional upper limit of the MD/ED intensity ratio is the square of the fine-structure constant, $\alpha^2 \doteq (1/137)^2$, and transverse magnetization would normally be ruled out altogether in transparent liquids where inversion symmetry is a property of the medium. This maximum ratio can be easily estimated by calculating the induced ED and MD moments in an atomic picture. Take for example atomic hydrogen and assume there are three relevant states of the system by which the optical field may drive transitions. Between states $|1,0,0\rangle$ and $|2,1,0\rangle$ the electric field may establish an electric dipole transition moment and between states $|2,1,0\rangle$ and $|2,1,\pm1\rangle$ the magnetic field may establish a magnetic dipole transition moment. These moments exist if we assume $|1,0,0\rangle$ is the ground $1s$ state, $|2,1,0\rangle$ is the first excited $2p$ state,

and $|2,1,\pm1\rangle$ is just an orthogonal projection of the $2p$ state. Evaluating the magnitudes of $\hat{p}$ and $\hat{m}$ follows the standard procedure to give

$$\hat{p} = \langle 1,0,0|\, e\hat{r}\, |2,1,0\rangle = \cdots = \frac{128\sqrt{2}}{243} a_0 e \tag{1.5}$$

and

$$\hat{m} = \langle 2,1,0|\, \frac{e}{2m_e}\hat{L}\, |2,1,\pm1\rangle = \cdots = \frac{e\hbar}{2m_e}\,, \tag{1.6}$$

where we have assumed hydrogenic wavefunctions and the details of the integration are shown in Appendix B. The ratio m/cp can then be easily computed,

$$\frac{m}{cp} = \frac{e\hbar}{2m_e}\frac{243}{128\sqrt{2}}\frac{1}{a_0 ec} \approx \alpha\,, \tag{1.7}$$

where the approximation $243/256\sqrt{2} \approx 1$ has been used and the fine structure constant is taken to be $\alpha = \hbar/a_0 m_e c$. Since α is the ratio of the induced moments, the intensity here would be the square, giving us α^2, as stated above. Regardless of traditional estimates such as these, a very large ME susceptibility driven by the bilinear product of the optical and magnetic fields was inferred from even the earliest magnetic scattering data of Ref. [2]. The obvious question then arises as to how such a large effect may arise.

A straightforward classical derivation of magnetization in a dielectric driven by an electromagnetic field is as follows. Ampére's law in the presence of free charges states that [18],

$$\nabla \times \mathbf{B} = \mu_0 \left(\mathbf{J}_c + \frac{\partial \mathbf{D}}{\partial t} + \nabla \times \mathbf{M} \right)\,. \tag{1.8}$$

Here $\mathbf{B}$ is the magnetic flux, $\mathbf{J}_c$ is the conduction current, $\mathbf{D}$ is the electric displacement vector, $\mathbf{M}$ is the magnetization, and μ_0 is the magnetic permeability of free space. We are concerned with dielectric media, so $\mathbf{J}_c = 0$. In the presence of an electric field of amplitude E_0, the displacement current may be replaced with the time-varying electric field and dielectric polarization, $\mathbf{P}$, using the relation

$$\mathbf{D} = \varepsilon \mathbf{E} = \varepsilon_0 \left(1 + \chi_e\right) \mathbf{E} = \varepsilon_0 \mathbf{E}_0 + \mathbf{P}\,, \tag{1.9}$$

where ε is the electric permittivity of the dielectric, ε_0 is the permittivity of free space, and χ_e is the electric susceptibility of the dielectric. Upon this substitution, the curl equation for $\mathbf{B}$ becomes,

$$\nabla \times \mathbf{B} = \mu_0 \left(\varepsilon_0 \frac{\partial \mathbf{E}_0}{\partial t} + \frac{\partial \mathbf{P}}{\partial t} + \nabla \times \mathbf{M} \right) , \tag{1.10}$$

which we may rewrite in terms of the magnetic field vector $\mathbf{H}$ according to

$$\mathbf{B} = \mu \mathbf{H} = \mu_0 \left(1 + \chi_m\right) \mathbf{H} , \tag{1.11}$$

where μ is the magnetic permeability of the dielectric and χ_m is the magnetic susceptibility of the dielectric. From Eq. (1.10) we then have

$$\nabla \times \mathbf{H} = \frac{\mu_0}{\mu_0 \left(1 + \chi_m\right)} \left(\varepsilon_0 \frac{\partial \mathbf{E}_0}{\partial t} + \frac{\partial \mathbf{P}}{\partial t} + \nabla \times \mathbf{M} \right) . \tag{1.12}$$

If we now assume the induced magnetic dipoles are far off resonance, we can consider the limit in which $\chi_m \ll 1$. This restricts the result for induced magnetization to transparent media with small polarization and magnetization far from resonance [4], which is in fact precisely the conditions under which our experiments were performed. With the assumption that $\chi_m \ll 1$, the curl equation reduces to

$$\nabla \times \mathbf{H} \doteq \varepsilon_0 \frac{\partial \mathbf{E}_0}{\partial t} + \frac{\partial \mathbf{P}}{\partial t} + \nabla \times \mathbf{M} . \tag{1.13}$$

However, from Faraday's law we also have the result

$$\begin{aligned} \nabla \times \mathbf{E} &= -\frac{\partial \mathbf{B}}{\partial t} \\ &= i\omega\mu_0 \left(1 + \chi_m\right) \mathbf{H} \\ &\doteq i\omega\mu_0 \mathbf{H} , \end{aligned} \tag{1.14}$$

where we have assumed $\mathbf{B} \propto e^{-i(\omega t - kz)}$ (i.e. $\mathbf{B}$ is a plane wave oscillating at frequency ω) and we again consider the limit $\chi_m \ll 1$. Rearranging Eq. (1.14) we find

$$\mathbf{H} = \frac{\nabla \times \mathbf{E}}{i\omega\mu_0} . \tag{1.15}$$

Note that upon taking the curl of Eq. (1.15) we have

$$\begin{aligned}\nabla \times \mathbf{H} = \nabla \times \left(\frac{\nabla \times \mathbf{E}}{i\omega\mu_0}\right) &= \frac{(ik)\,(ik)\,\mathbf{E}}{i\omega\mu_0} \\ &= -i\frac{k^2\mathbf{E}}{\omega\mu_0} = -i\omega\mathbf{E}\left(\frac{k^2}{\omega^2\mu_0}\right) \\ &= \frac{\partial\mathbf{E}_0}{\partial t}\left(\frac{1}{c^2\mu_0}\right) = \frac{\partial\mathbf{E}_0}{\partial t}\left(\frac{\mu\varepsilon}{\mu_0}\right) \ . \end{aligned} \tag{1.16}$$

Far from any electronic resonance, in the limit of transparent media, we again note that $\chi_m \ll 1$, $\chi_e \ll 1$. Thus Eq. (1.16) reduces to

$$\nabla \times \mathbf{H} \doteq \varepsilon_0 \frac{\partial \mathbf{E}_0}{\partial t} \ . \tag{1.17}$$

By direct substitution of Eq. (1.17) into Eq. (1.13) we find that the induced magnetization and polarization are therefore related by

$$\nabla \times \mathbf{M} \doteq -\frac{\partial \mathbf{P}}{\partial t} \ , \tag{1.18}$$

or equivalently,

$$|M| = c|P| \ . \tag{1.19}$$

The implication of Eqs. (1.18) and (1.19) is that if the driving field is linearly polarized along the $\hat{x}$ direction and light propagates along the z-axis so that $\mathbf{k} = k\hat{z}$, then the magnetization should have a nonzero component along the direction of the inducing B-field, which lies along $\hat{y}$ and is proportional to the electric polarization $\mathbf{P}$. If $\mathbf{M}$ has a component along $\hat{y}$ only, then the curl term in the left-hand side (LHS) of Eq. (1.18) will have the form

$$\begin{aligned}\nabla \times \mathbf{M} \ &= \begin{vmatrix} \hat{x} & \hat{y} & \hat{z} \\ \partial/\partial x & \partial/\partial y & \partial/\partial z \\ 0 & M_y & 0 \end{vmatrix} \\ &= \hat{z}\frac{\partial M_y}{\partial x} - \hat{x}\frac{\partial M_y}{\partial z} \ . \end{aligned} \tag{1.20}$$

Equating this to the right-hand side (RHS) of Eq. (1.18), we see

$$\hat{z}\frac{\partial M_y}{\partial x} - \hat{x}\frac{\partial M_y}{\partial z} = -\frac{\partial \mathbf{P}}{\partial t} \ . \tag{1.21}$$

To be self-consistent, the polarization components associated with this magnetization are limited to

$$\frac{\partial M_y}{\partial z} = \frac{\partial P_x}{\partial t}\,, \tag{1.22}$$

$$\frac{\partial M_y}{\partial x} = -\frac{\partial P_z}{\partial t}\,. \tag{1.23}$$

The magnetization in Eq. (1.22) arises from the first-order polarization component $p_x(\omega) = \varepsilon_0 \chi^{(1)}_{xx} E_x$, induced along $\hat{x}$. This equation tells us that M_y oscillates at the optical frequency and has a gradient along $\hat{z}$. The second equation (Eq. (1.23)) arises from the second-order nonlinear polarization, $p(2\omega) = \varepsilon_0 \chi^{(2)}_{zyx} H_y E_x$, which is non-zero in centrosymmetric media and which depends on the second-order susceptibility. Thus the polarization along $\hat{z}$ causes a nonzero gradient in M_y along $\hat{x}$. Together, the magnetization components in Eqs. (1.22) and (1.23) predict a magnetization which is nonzero and transverse.

When analyzed in terms of *static* symmetry, the indices i, j, and k of the magneto-electric susceptibility $\chi^{(2)}_{ijk}$ in a medium with inversion symmetry must all be different. Consequently, static symmetry prohibits transverse magnetization because the susceptibility $\chi^{(2)}_{yxy}$ in $M_y \propto \chi^{(2)}_{yxy} E_x H_y$ is zero. However, it is shown later in this thesis that dynamic symmetry-breaking takes place in systems undergoing a second-order interaction driven by E and H. As a result, the symmetry of the driven medium excludes inversion. In this way, the joint action of E and H enables transverse magnetization to take place. Furthermore, a dressed state analysis shows that optically-induced magnetization can be *as intense as* the linear electric polarization in agreement with the classical result $M = cP$ given by Eq. (1.22). The quantum theory displays a quadratic dependence on the input optical field at low intensities and a linear dependence when saturated.

In the next section we consider basic aspects of light scattering in dielectric media to relate the scattered field amplitudes and orientations to induced electric and magnetic moments. The mechanism responsible for the formation of nonlinear moments is described later in Section 1.5.

1.2 Light scattering in dielectric media

The interaction of light with matter was studied long before the advent of lasers since scattering is responsible for what makes an object visible to the human eye. The appearance of an object is determined by the fact that light scatters from it and the human eye subsequently detects the scattered light [19]. The observations in this thesis are due to the interaction of

light with fluctuations in material properties which similarly lead to light scattering. For the purpose of comparing the fields scattered by electric and magnetic dipoles, it is sufficient to consider standard expressions for scattering from a particle of diameter a. There are essentially three cases for scattering from particles, including atoms or molecules: (i) $a \ll \lambda$, (ii) $a \sim \lambda$, and (iii) $a \gg \lambda$. Cases (i) and (ii) can be analyzed using a multipole approach [20], while case (iii) can be treated macroscopically in a semi-geometric approach. This third case is the condition for what is collectively referred to as diffraction. Case (ii) is known as Mie scattering and is typically observed in suspensions of large nanoparticles in liquid. Case (i) is most relevant to this thesis.

For the case of small ($a \ll \lambda$) dielectric scatterers with bound charges, we can describe how the distribution of electrical charge in the material responds to an incoming electromagnetic field by simply specifying the scattered fields in terms of the induced electric and magnetic dipole moments. These dipole moments are the dynamic analogue to the standard definitions of electrically- or magnetically-displaced currents in electrostatics [20]. Specifically, the electric dipole moment is defined in integral form as

$$\mathbf{p} = \int \mathbf{x}' \rho(\mathbf{x}') d^3\mathbf{x}' \,, \tag{1.24}$$

where $\rho(\mathbf{x})$ represents a spatially-dependent charge distribution, $\mathbf{x}$ is the position vector relative to a reference origin, and the integration is taken over the primed variable to determine the net dipole moment. Likewise, the magnetic dipole moment is defined as the integral over the magnetic moment density or magnetization,

$$\mathcal{M}(\mathbf{x}) = \frac{1}{2}\mathbf{x} \times \mathbf{J}(\mathbf{x}) \,, \tag{1.25}$$

as

$$\mathbf{m} = \frac{1}{2} \int \mathbf{x}' \times \mathbf{J}(\mathbf{x}') d^3\mathbf{x}' \,, \tag{1.26}$$

where $\mathbf{J}(\mathbf{x})$ is a localized current density. When the charge density ρ or current density $\mathbf{J}$ are induced by a high-frequency optical wave, the definitions of the electro- and magnetostatic moments remain the same but include time-dependence. Higher-order moments can in principle contribute to the vector potential $\mathbf{A}(\mathbf{x}, t)$ [20],

$$\mathbf{A}(\mathbf{x}, t) = \frac{\mu_0}{4\pi} \frac{e^{ikr}}{r} \sum_n \left(\frac{1}{i\lambda}\right)^n \frac{1}{n!} \int \mathbf{J}(\mathbf{x}', t) \left(\mathbf{n} \cdot \mathbf{x}'\right)^n d^3\mathbf{x}' \,, \tag{1.27}$$

from which the scattered fields are determined using the relations

$$\mathbf{E} = -\frac{\partial \mathbf{A}}{\partial t} \quad \text{and} \quad \mathbf{B} = \nabla \times \mathbf{A} \,. \tag{1.28}$$

However, Eq. (1.27), which is known as the multipole expansion is dominated by effects of the electric dipole $\mathbf{p}$, followed by the magnetic dipole and electric quadrupole, and then higher-order terms. This is consistent with the estimate showing $|\mathbf{p}| \gg |\mathbf{m}|$ in the previous section.

The solution for the scattered field at point $\mathbf{x}$ due to an electric dipole moment at point $\mathbf{x}_0$ is

$$\mathbf{E}(\mathbf{x}, t) = \frac{3\mathbf{n}\left[\mathbf{p}(\mathbf{x}, t) \cdot \mathbf{n}\right] - \mathbf{p}(\mathbf{x}, t)}{4\pi\epsilon_0 \left|\mathbf{x} - \mathbf{x}_0\right|^3} \,, \tag{1.29}$$

as derived in Chapter 4 of Ref. [20]. Here $\mathbf{n}$ is a unit normal vector directed from $\mathbf{x}$ to $\mathbf{x}_0$. The scattered field is linearly proportional to the induced dipole moment, which in the case of linear response is proportional to the input field. The same is true for the magnetic induction field produced by a magnetic dipole moment, which yields the expression

$$\mathbf{B}(\mathbf{x}, t) = \frac{\mu_0}{4\pi} \left\{ \frac{3\mathbf{n}\left[\mathbf{n} \cdot \mathbf{m}(\mathbf{x}, t)\right] - \mathbf{m}(\mathbf{x}, t)}{\left|\mathbf{x}\right|^3} \right\} \,. \tag{1.30}$$

This too is proportional to the induced dipole (see Chapter 5 of Ref. [20]). However, in the present work, the induced magnetization is *nonlinear*, with the result that the scattered or radiated $\mathbf{B}$ field is expected to grow nonlinearly with respect to incident intensity. The angle made between $\mathbf{p}$ and $\mathbf{m}$ is also of relevance to our current discussion because electric and magnetic scattering intensities are measured separately and compared later in this dissertation. Therefore we note that the scattered fields are parallel to their respective moments: $\mathbf{E} \parallel \mathbf{p}$ and $\mathbf{B} \parallel \mathbf{m}$. But the incident fields $\mathbf{E}_i$ and $\mathbf{B}_i$ are mutually perpendicular. So $\mathbf{p} \perp \mathbf{m}$ and the scattered fields are orthogonal ($\mathbf{E} \perp \mathbf{B}$) in a 90° detection geometry. In the following section we consider some early light scattering experiments in which cross-polarized signals were observed using a 90° detection geometry to contrast them with the observations of induced magnetization presented later in this thesis.

1.3 Overview of related work on light scattering

The topics of nonlinear optics and light scattering are well-developed and there exist several useful review papers [21, 22] that describe in great detail the nonlinear effects expected under particular experimental conditions. To describe each of these effects in detail here is beyond the scope of this thesis. However, since the primary novelty of this thesis is

the observation of magnetization at optical frequencies with a quadratic dependence on the incident laser field, it is imperative to compare and contrast the results with other known nonlinear phenomena. In this section we discuss several known optical effects that might be thought to offer alternative explanations to the results presented in this thesis. However, these alternatives are ruled out one by one by considering important factors such as frequency, polarization, geometry, intensity, and so on.

In Chapter 4 (see Fig. 4.2) polarization analysis data is presented that shows no rotation or alteration of the polarization of the laser beam transmitted through the sample under the conditions of our experiments. Hence induced linear birefringence, ellipse rotation, and cross-polarized wave (XPW) generation are all absent. The results of previous experiments on XPW generation in cubic crystals [23, 24] did measure polarization rotation in the forward direction, but found that ellipse rotation efficiency varied harmonically versus intensity and required input intensity above 10^{12} W/cm^2, at least 4 orders of magnitude larger than in our experiments. These observations are therefore inconsistent with the experimental findings of this thesis for spherical-top molecules. No consistent explanation of cross-polarized scattering can be based on these particular phenomena. Other past experiments that used a 90° scattering geometry reported harmonics that were interpreted as being induced by correlated scattering [25], but the signals were at a frequency twice that of the laser. Moreover, there is no evidence of correlated scattering in our experiments since the samples were completely transparent to incident and scattered light. Multiple scattering was visibly absent. Finally, numerous earlier studies reported depolarization ratios in molecular liquids [26], but not one of these experiments reported quadratic growth of cross-polarized scattering at the optical frequency ω or measured the radiation pattern of scattered light as we show in this current body of work.

Numerous precautions were taken to eliminate other mechanisms that potentially generate cross-polarized scattering in the 90° geometry. These precautions fell into the categories of sample selection, sample preparation, control of the input polarization state, and spectral filtering. The choice of non-birefringent, non-chiral, centrosymmetric samples eliminated effects due to linear birefringence (which requires anisotropy), circular birefringence (which requires chirality), and second-order all-electric interactions (which require non-centrosymmetry and take place at frequencies other than ω). Spherical-top molecules CCl_4, $SiCl_4$, $SiBr_4$, and $SnCl_4$ were chosen for the main study because they have no internal dipoles or anisotropy, no optical resonances near the laser frequency, and exhibit isotropic optical response. The samples were double-filtered through 0.2 μm millipore mesh filters to remove any contaminates that could cause multiple or correlated scattering. Input polarization was chosen to be linear, thereby eliminating effects such as the inverse Faraday

effect, which requires circular polarization to induce a longitudinal static magnetization.

Spectral filtering was used to restrict scattered light detection to the fundamental laser frequency. This eliminated nonlinear effects such as hyper-Rayleigh scattering which generates photons at 2ω and other nonlinear light scattering phenomena that generate light at second [27] or third [28] harmonics of the input frequency. In our experiments, it was only possible to detect light scattered quasi-elastically from electric and magnetic dipole moments. Therefore, the effects measured in this thesis cannot be explained by the results of Terhune [25] or Maker [29] in which second-harmonic light scattering was observed in liquids. Nevertheless, it is still the case that rotational modes of the sample can be excited and detected in our experiments, leading to Raman scattering with small frequency shifts. Rotational Raman processes generate scattered light very close to the fundamental frequency of the laser. Spectral filtering in our apparatus was narrow enough to prevent vibrationally-excited Raman scattering from reaching the detector, but rotationally-excited Raman scattering was transmitted.

The intensities used in the experiments described in this thesis are much lower than those necessary to generate self-phase modulation or self-focusing. These effects require input intensities approaching 10^{13} W/cm^2 while the experiments reported here were performed at 10^8 W/cm^2 or lower. Induced refractive index changes can also be caused by electrostriction [30, 31] or electrocaloric effects [32], but these cannot alter the polarization of light scattered at 90°. Nonlinear index changes affect only the speed at which components of the waves travel because these linearly-polarized components are exactly parallel or perpendicular to the fields that induce the nonlinear index anisotropy.

The choices of 90° detection geometry, linear optical polarization, centrosymmetric samples with spherical-top geometry, narrowband filtering, and the use of low input intensity allow us to rule out known, all-electric nonlinear mechanisms which might explain the results reported in Chapter 4. We emphasize in particular that no cross-polarized scattering or scattering ellipticity can be generated by nonlinear index changes parallel or perpendicular to the input fields. The measurements recorded in this thesis also showed purely dipolar nature of both the induced electric and magnetic moments, so no quadrupole or higher-order multipole effects need be considered. Furthermore, the novel measurements reported in this thesis are consistent with both classical and quantum theoretical models which predict a quadratic optical magnetization proportional to the electric polarization as being responsible for this induced response. We therefore draw the conclusion that our experimental results in CCl_4, $SiCl_4$, $SiBr_4$, and $SnCl_4$ reflect high-frequency magnetization. In the final two sections of this chapter we review some prior experimental results together with a classical picture of induced nonlinear magnetization which will assist the reader in

later discussions of quantum dynamics.

1.4 Prior experiments on strong, induced magnetic scattering

Light scattering experiments which sought to measure the relative amplitudes of induced ED and MD moments in transparent, dielectric media began in 2007 [1]. These, and subsequent experiments, revealed for the first time that intense, nonlinear magnetic response that was comparable in amplitude to the measured electric response was possible [2, 15, 16]. Here liquid samples of CCl_4 (carbon tetrachloride), H_2O (water), and C_6H_6 (benzene) were specifically chosen because they included no atomic resonances near the input laser wavelength and their liquid nature permitted them from having symmetric properties that would normally support second-order optical response (such as structured crystalline samples which lack inversion symmetry). These experiments relied on a unique 90° detection geometry which allowed for the separation of the induced ED and MD moments, as the two moments are indistinguishable in the forward direction.

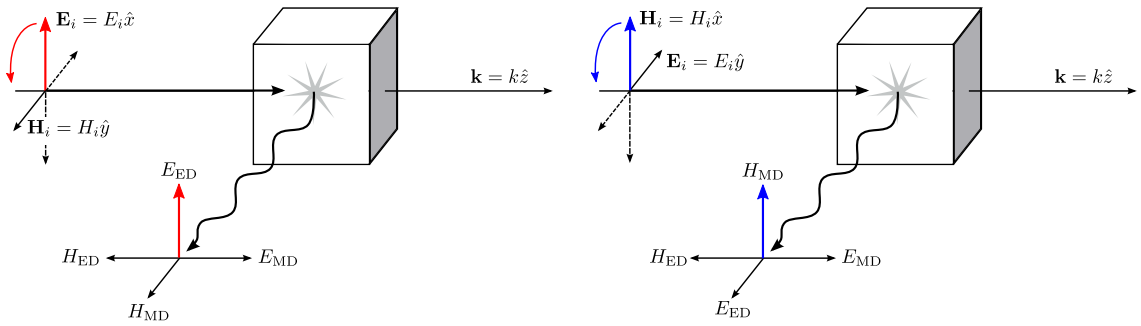

Figure 1.1: Depiction of the 90° scattering geometry which is required for distinguishing between induced (a) electric and (b) magnetic dipole moments.

Figure 1.1 is a depiction of why this 90° geometry is required. If the incident field has its electric component oriented along the vertical axis (along $\hat{x}$), then the induced electric dipole moment will also be oriented along $\hat{x}$. If a detector is placed at a right-angle to the input field direction, $\hat{z}$, then light scattered from the induced dipole moment will have its electric component polarized along $\hat{x}$. If an analyzer is then placed in the beam path along this detection arm, we will see a maximum electric signal when its orientation is vertical (i.e. along $\hat{x}$). On the other hand, if the incident field has its magnetic component oriented along the vertical axis, then the induced magnetic dipole in the sample will also

be oriented along $\hat{x}$ and magnetically-scattered light will have its magnetic component along $\hat{x}$ (see Fig. 1.1(b)). The analyzer is of course only able to select for the electric polarization state[1], so it must be oriented horizontally (i.e. along $\hat{y}$) in order to measure the maximum magnetic signal. The selection between electric and magnetic dipole moments is then purely dependent on the orientation of the analyzer: vertical to measure electric and horizontal to measure magnetic.

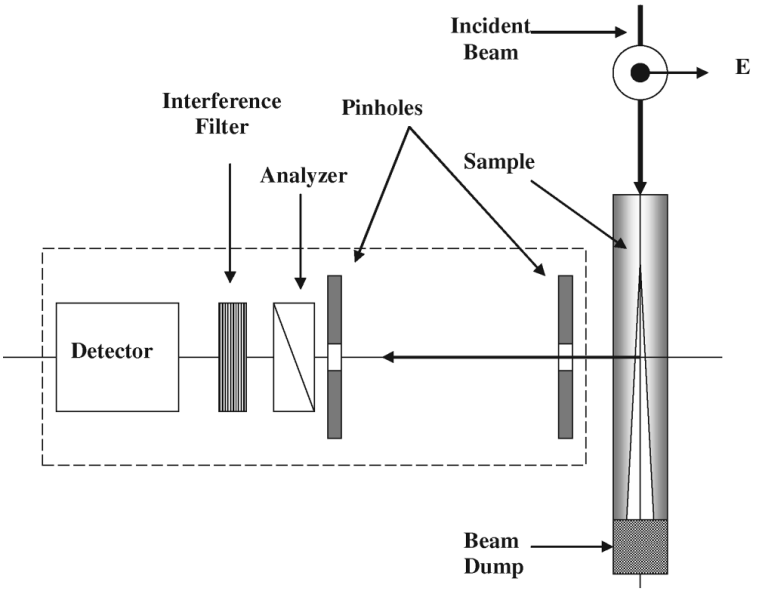

Figure 1.2: Schematic diagram for initial scattering experiments showing the 90° detection geometry.

The first experiments of this type were performed using ultrafast optical pulses from the mode-locked, amplified Clark-MXR CPA-2001 laser system consisting of 150 fs pulses at 775 nm. To avoid damaging optical components or generating third-order optical effects, the 1 kHz, μJ pulses were attenuated to intensities below $I = 10^{13}$ W/cm^2. The linearly polarized pulses were directed into a liquid sample of pure CCl_4 that was prefiltered twice through a 0.2 μm millipore mesh filter and held in a cylindrical glass holder. A liquid-cooled photomultiplier tube with a 10 nm passband filter centered on the laser wavelength was used as a detector and was placed 90° relative to the input beam. An f8 focusing optic was used so that the axial field component (i.e. the out-of-plane component of the detected light) was completely negligible ($E_z/E_0 \ll 10^{-3}$). The geometry for this detection scheme is shown in Fig. 1.2. The detected light was passed through the analyzer before the detector which was set to vertical for measuring electric signals or horizontal for magnetic signals.

[1]This is why the two signals are indistinguishable in the forward direction: there is no way to separate light scattered from the induced electric and magnetic signals since the analyzer is sensitive only to the electric component of light.

The input field was then rotated through 360° using a $\lambda/2$ plate in order to map out the patterns shown in Fig. 1.3(a). As one would expect, the intensity of the measured signals could be fit to a cosine-squared function as

$$I = a\cos^2(\theta + \phi)\,, \tag{1.31}$$

where a is some amplitude, θ is the angle of the field, and ϕ is some phase term.

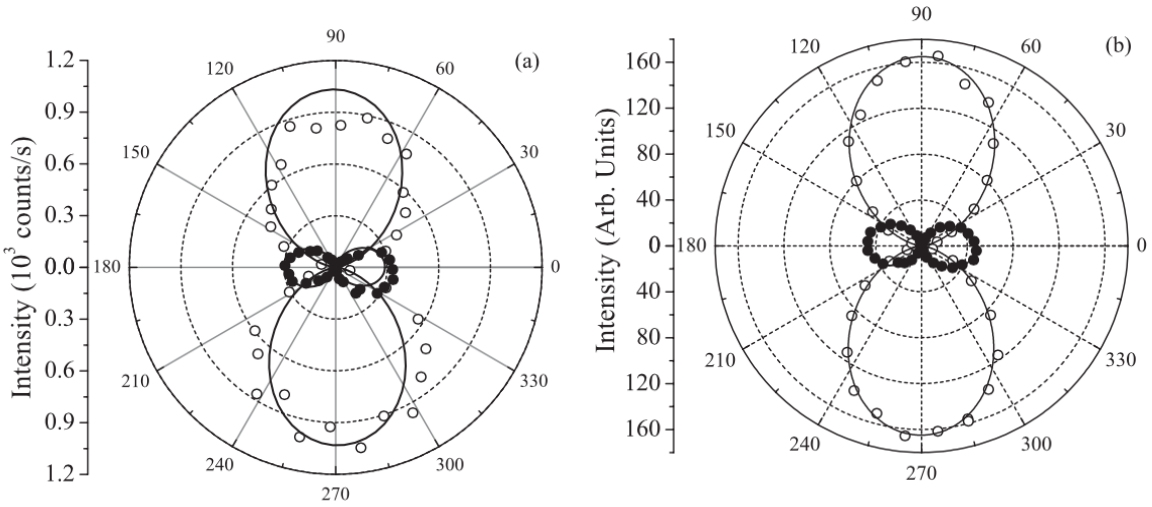

Figure 1.3: Measured dipole response for magnetic (closed circles) and electric (open circles) scattering in liquid sample CCl_4 for (a) amplified laser (b) and oscillator. Plots taken from Ref. [1].

In the same study, similar measurements were made using a rectangular sample cuvette instead of the cylindrical glass holder and a mode-locked Ti:Al_2O_3 oscillator of 80 MHz repetition rate was used. Here the peak intensities were limited to $I \sim 10^{10}$ W/cm^2 and the photomultiplier tube was switched out for an EG&G FND-100 photodiode. The induced magnetic and electric dipole moments were again measured in CCl_4 and it was found that the magnetic response was again comparable to the electric response (see Fig. 1.3(b)). The response for the intensity of the magnetic dipole was then measured as a function of input laser intensity and found to have a quadratic dependence (see Fig. 1.4). Similar experiments on the aforementioned liquids H_2O and C_6H_6 were also conducted and large induced magnetic dipole response was recorded. A continuous-wave (cw) argon gas laser was also used to do this experiment, with input intensities which never exceeded 10^5 W/cm^2. These experiments however showed that no observable magnetic dipole emission took place at these low intensities. This suggested that a transition between the regime of no magnetic signal and large magnetic signal must take place [2].

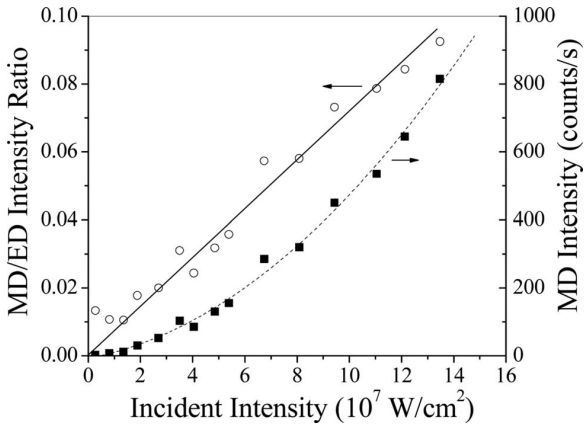

Figure 1.4: Experimental measurement of induced magnetic dipole scattering as a function of laser intensity (lower curve). The ratio of induced magnetic to electric signal (ED/MD) as a function of laser intensity (upper curve). Plot taken from Ref. [2].

These profound results showed for the first time that high-frequency magnetic response at low intensities in natural materials is not only present, but is remarkably large when compared to the induced electric response. Perhaps more unique to these experimental findings is the frequency and intensity dependence of the measured magnetic response. Careful review of existing nonlinear optical phenomena determined that an explanation for this nonlinear effect was apparently overlooked in the past. This prompted the development of several theoretical models which sought to explain this nonlinear effect as the result of the joint action of electric and magnetic components of light acting together to create a nonlinearity of the type EB [5, 6]. A straight-forward extension to the Lorentz oscillator model for electrons in a dielectric medium is perhaps the most intuitive model for understanding this new nonlinear process.

1.5 Complete Lorentz oscillator model

Before moving forward, it is useful to review the classical model of ME processes [5] that was developed to explain the results described in the previous section. A widely accepted model of the electron dynamics in a dielectric medium is the Lorentz oscillator model (LOM). This model assumes that the motion of an electron bound to a nucleus may be approximated by that of a harmonic oscillator. When the material has centrosymmetry, the restoring force of the electron is simply

$$\mathbf{F} = -k\mathbf{x}\,, \tag{1.32}$$

where k is the effective spring constant and $\mathbf{x}$ is the displacement vector of the charge from

its initial rest position. Once perturbed the electron loses energy due to damping, which can be taken into account by including an additional term which is proportional to the velocity of the charge, $\dot{\mathbf{x}}$. The force equation then becomes

$$\mathbf{F} = -k\mathbf{x} - A\dot{\mathbf{x}} \,, \tag{1.33}$$

where A is just a proportionality constant and the overhead dot notation denotes a time derivative. From Newton's second law, the vector sum of the forces on an object is equal to the mass of that object times its acceleration. We can then write

$$m_e\ddot{\mathbf{x}} + A\dot{\mathbf{x}} + k\mathbf{x} = 0 \,, \tag{1.34}$$

where m_e is the mass of an electron and $\ddot{\mathbf{x}}$ is its acceleration. This is the homogeneous second-order differential equation for motion of a damped oscillator and has the familiar solutions which are exponential.

In the presence of an optical field, the electron-spring system will experience a driving force. This is given by the Lorentz force,

$$\mathbf{F} = e\left(\mathbf{E} + \dot{\mathbf{x}} \times \mathbf{B}\right) \,, \tag{1.35}$$

for electric field $\mathbf{E}$ and magnetic field $\mathbf{B}$. The general equation of motion to solve is then

$$m_e\ddot{\mathbf{x}} + A\dot{\mathbf{x}} + k\mathbf{x} = e\left(\mathbf{E} + \dot{\mathbf{x}} \times \mathbf{B}\right) \,, \tag{1.36}$$

which is known as the complete Lorentz oscillator model (CLOM) [5]. However, since $|\mathbf{B}| = |\mathbf{E}|/c$ and $|\mathbf{v}| \ll c$ (where c is the speed of light) for non-relativistic intensities, the magnetic field is typically ignored and the equation reduces to

$$m_e\ddot{\mathbf{x}} + A\dot{\mathbf{x}} + k\mathbf{x} = e\mathbf{E} \,. \tag{1.37}$$

Dividing through by m_e yields

$$\ddot{\mathbf{x}} + \gamma\dot{\mathbf{x}} + \omega_0^2\mathbf{x} = \frac{e}{m_e}\mathbf{E} \,, \tag{1.38}$$

where $\gamma = A/m_e$ and $\omega_0^2 = k/m_e$. This simplified version is referred to as just the LOM. So long as the electric field is only moderately intense ($I < 10^{13}$ W/cm^2), this equation can be used to accurately describe the resulting dynamics associated with the electron motion. Given an input field of the form

$$\mathbf{E} = E_0 e^{i(kz-\omega t)}\hat{x} \ , \tag{1.39}$$

where E_0 is the electric field amplitude, k is the wave vector, and ω is the oscillation frequency, the vector equation above reduces to an equation for motion of the electron about only the x-axis. Solutions for this problem are of the form

$$x(t,\omega) = \frac{eE_0}{m_e\sqrt{\left(\omega_0^2-\omega^2\right)^2+\gamma_x^2\omega^2}}\cos\left(\omega t+\phi_0\right) \ , \tag{1.40}$$

where $\phi_0 = \tan^{-1}\left[-\gamma\omega/\left(\omega_0^2-\omega^2\right)\right]$. The solution for x is typically recast in a slightly more familiar form by multiplying by a factor of e. Given that x is a time-varying displacement and e is a charge, their product yields an oscillating dipole moment, defined by the usual relationship, $\mathbf{p} = e\mathbf{x}$. This solution is then

$$p(t,\omega) = ex(t,\omega) \ , \tag{1.41}$$

which is the single-atom form for the electric polarization of a dielectric material[2].

When the curl term in the Lorentz force is retained in the oscillator model, the vector equation can be broken down into a set of two coupled differential equations which are a generalization of the Hill's equations [33]. We arrive at these equations by first specifying the incident optical field. Without loss of generality, we take the optical field to have its electric component along $\hat{x}$, magnetic component along $\hat{y}$, and propagation direction along $\hat{z}$,

$$\mathbf{E}(t) = E_0 e^{i(kz-\omega t)}\hat{x} \ , \tag{1.42}$$

$$\mathbf{B}(t) = B_0 e^{i(kz-\omega t)}\hat{y} \ , \tag{1.43}$$

where $B_0 = E_0/c$. The cross-product from the Lorentz force reduces to

$$\begin{aligned}\dot{\mathbf{x}}\times\mathbf{B} &= \begin{vmatrix}\hat{x} & \hat{y} & \hat{z}\\ \dot{x} & \dot{y} & \dot{z}\\ 0 & B_0 & 0\end{vmatrix}\\ &= -B_0\dot{z}\hat{x}+B_0\dot{x}\hat{z} \ ,\end{aligned} \tag{1.44}$$

[2]To obtain the macroscopic polarization, a sum must be taken over all participating atoms in the medium and their coherences must be taken into account.

where we have temporarily suppressed the spatial and temporal dependence. From here it is obvious that the resulting electron motion will be a superposition of motions along both the electric field polarization axis *and* the direction of propagation. If the assumption is made that the damping and restoring coefficients can have different values along the orthogonal directions $\hat{x}$ and $\hat{z}$ (see Ref. [2]), then the coupled equations to solve are[3]

$$\ddot{x} + \gamma_x \dot{x} + \omega_x^2 x = \frac{e}{m_e} \left(E_0 - B_0 \dot{z}\right) e^{i(kz - \omega t)} \,, \tag{1.45a}$$

$$\ddot{z} + \gamma_z \dot{z} + \omega_z^2 z = \frac{eB_0}{m_e} \dot{x} e^{i(kz - \omega t)} \,, \tag{1.45b}$$

where γ_x and γ_z are dampings along $\hat{x}$ and $\hat{z}$, respectively, and $\omega_x = \sqrt{k_x/m_e}$ and $\omega_z = \sqrt{k_z/m_e}$ are natural frequencies of the system along these same directions. Equations of this type have no analytic solution, so a perturbative approach must be used in order to write down explicit forms for x and z. This is done following the standard perturbation chain,

$$x(t) = x_0(t) + \lambda x_1(t) + \lambda^2 x_2(t) + \cdots \,, \tag{1.46}$$

$$z(t) = z_0(t) + \lambda z_1(t) + \lambda^2 z_2(t) + \cdots \,, \tag{1.47}$$

where λ is an order parameter. Using this approach [5], we can determine the lowest-order, nonzero solutions to the electron excursions along the orthogonal directions $\hat{x}$ and $\hat{z}$. The lowest-order solution for x is the same as given above,

$$\begin{aligned} x(t) &= \frac{eE_0}{m_e \sqrt{\left(\omega_x^2 - \omega^2\right)^2 + \gamma_x^2 \omega^2}} \cos\left(\omega t + \phi_0\right) \\ &= x(t, \omega) \,, \end{aligned} \tag{1.48}$$

while there are two terms present in the lowest-order solution for motion along z,

[3] Note that a different extension to the oscillator equation is to include a nonlinear restoring potential, which leads to the anharmonic oscillator, $\ddot{\mathbf{r}} + \gamma \dot{\mathbf{r}} + \omega_0^2 \mathbf{r} + \eta \mathbf{r}^2 = e\mathbf{E}/m_e$ (where η is a small nonlinearity). This can be solved perturbatively to produce second-order expressions that are driven by EE and EE^* processes. The main distinction between this model and the one being discussed here is where the nonlinearity comes from. The anharmonic oscillator includes the nonlinearity as a material property while the CLOM allows for it by including the Lorentz term.

$$
\begin{aligned}
z(t) = & \frac{-\omega e^2 E_0 B_0}{2m_e^2 \omega_z^2 \sqrt{\left(\omega_x^2 - \omega^2\right)^2 + \gamma_x^2 \omega^2}} \sin\phi_0 \\
& + \frac{1}{\sqrt{\left(\omega_z^2 - (2\omega)^2\right)^2 + \gamma_z^2 (2\omega)^2}} \\
& \times \frac{\omega e^2 E_0 B_0}{2m_e^2 \sqrt{\left(\omega_x^2 - \omega^2\right)^2 + \gamma_x^2 \omega^2}} \sin\left(2\omega t + \phi_0 - \phi_1\right) , \\
= & \, z(t,0) + z(t,2\omega) \, .
\end{aligned} \tag{1.49}
$$

The phase terms are defined as

$$
\phi_0 = \tan^{-1}\left[\frac{-\gamma_x \omega}{\omega_x^2 - \omega^2}\right] \tag{1.50}
$$

and

$$
\phi_1 = \tan^{-1}\left[\frac{-\gamma_z 2\omega}{\omega_z^2 - (2\omega)^2}\right] . \tag{1.51}
$$

Inspection of Eqs. (1.48) and (1.49) reveal three distinct features: (1) the dependence of field amplitude, (2) the resonant detunings, and (3) the oscillation frequency. Not surprisingly, the solution for motion along the direction of the electric field polarization, $x(t,\omega)$, is linearly-dependent on the electric field, has a 1-photon detuning when $\omega_x = \omega$, and is oscillating at the frequency of the incident light. The solutions for motion along z have a quadratic field dependence that is proportional to $E_0 B_0$ and oscillate at frequencies that go as 0 and 2ω. These effects are analogous to the sum and difference frequency solutions that come from solving the anharmonic oscillator for second-order EE and EE^* solutions. The term at 0-frequency is a "static" charge separation effect while the term at 2ω is related to a second-harmonic generation. Furthermore, the nonlinear solutions for z have both 1- and 2-photon detunings in their denominators, which reflects the fact that the electric field has to initiate the charge motion before the magnetic field may act on it.

Once again these solutions may be related to an electric dipole moment by using the same relationship as above, $\mathbf{p} = e\mathbf{x}$. We thus have a set of three electric polarizations which arise due to the inclusion of $\mathbf{B}$ in the oscillator model,

$$\mathbf{p}^{(1)}(\omega) = ex(t,\omega)\hat{x}\,, \tag{1.52}$$

$$\mathbf{p}^{(2)}(0) = ez(t,0)\hat{z}\,, \tag{1.53}$$

$$\mathbf{p}^{(2)}(2\omega) = ez(t,2\omega)\hat{z}\,, \tag{1.54}$$

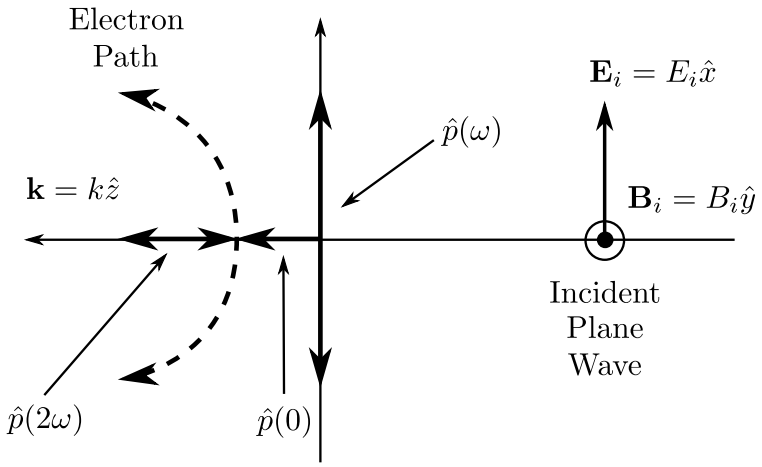

Figure 1.5: Representation of the three dielectric polarizations within the Cartesian plane. The arc represents the resulting electron path due to the inclusion of the magnetic term in the Lorentz force. This curved path is responsible for a third nonlinear effect, $\mathbf{m}^{(2)}(\omega)$.

where the superscript notation denotes the order in the optical field and the argument denotes the frequency at which the polarization oscillates at. The net polarization within the dielectric is then a sum of these three moments, which leads to a curved electron path. This arced electron trajectory in turn produces an oscillating magnetization along $\hat{y}$. These effects are represented diagrammatically in Fig. 1.5 which is a useful diagram for understanding the dynamics of the system. This oscillating magnetization is a third nonlinear effect which is quadratic in the optical fields but is oscillating at the fundamental frequency of the input field. The orientation, field dependence, and frequency dependence of this magnetization match the results of the experimental scattering results described in the previous section.

The three nonlinear moments,

$$\mathbf{p}^{(2)}(0)\,, \qquad \mathbf{p}^{(2)}(2\omega)\,, \qquad \mathbf{m}^{(2)}(\omega) \tag{1.55}$$

constitute the aforementioned trio of nonlinear ME effects. This fact is unique only to this set of processes since conventional quadratic effects typically rely on an asymmetric property of the sample in order to produce a nonlinear polarization. Here the symmetry is

broken purely by choice of retaining the magnetic field in the Lorentz force and allowing for the sequential action of the electric and then magnetic fields to act on the electron distribution; it is purely the action of the magnetic field by which symmetry is no longer preserved. The fact that symmetry is broken and no assumptions have been made about the atomic or molecular structure suggest that these ME nonlinearities should be present in *any* dielectric media.

CHAPTER 2

Quantum Theory of Optical Magnetization

The classical theory presented in Chapter 1 correctly predicts the existence and qualitative behavior of a new family of magneto-electric nonlinearities, but it is limited to being perturbative in nature and a general solution to the coupled Hill's equations [33] is beyond the scope of this thesis. The classical approach also fails to explicitly address issues associated with the character of the available quantum states of the atomic or molecular system under consideration and the prohibition against transverse magnetization that emerges from static symmetry analysis. An exact theory and one which is formalized using quantum mechanics is therefore needed in order to confirm that these effects may in fact take place in *all* optical media, regardless of symmetry. In our theoretical model we use a quantized optical field. This is done for two reasons: (1) so we can solve the problem exactly with both E and B fields, and (2) to make clear the constraints on which levels are coupled to via electric and magnetic interactions, therefore identifying between which states electric and magnetic polarizations may arise.

In our model we adopt a dressed atom approach for establishing a quantum mechanical picture of this new family of magneto-electric nonlinear processes. We show via a simple extension of the typical case of a 2-level atom dressed by the electric field that inclusion of the optical magnetic field predicts new "doubly-dressed" states between which second-order polarizations and magnetizations may arise. Our doubly-dressed model is developed in two stages: in the first stage a simple atomic picture is used which predicts the correct qualitative behavior of the induced nonlinear moments, and in the second stage a molecular model is considered which (through coupling to rotational angular momentum states) accounts quantitatively for the behavior seen in experiments, specifically the result that $M = cP$. In both stages the interaction Hamiltonian is modified to account for both electric and magnetic interactions. This work is in accord with standard treatments of dressed atoms [34]. The following subsections lay the framework of both stages of our new doubly-dressed models, but first we review the main results of the "singly-dressed" atom.

2.1 Atoms dressed by a single field, E

We consider the interaction of an optical electric field with a stationary 2-level atom consisting of an $\ell = 0$ ground state and an $\ell = 1$ excited state (see Fig. 2.1). The atomic nucleus is fixed in position at the origin (Born-Oppenheimer approximation) and the fields are assumed to be uniform over the region occupied by the atom (dipole approximation). The two levels are separated by atomic frequency ω_0 and light of frequency ω is turned on adiabatically. We assume angular momentum is a good quantum number and take the atomic states to consist of $|1,0,0\rangle$ and $|2,1,0\rangle$, where the ket notation $|\alpha,\ell,m_\ell\rangle$ is used. Here α is the principal quantum number, ℓ is the angular momentum, and m_ℓ is the spin quantum number. The quantization axis is taken to lie along the electric field polarization $\mathbf{e}_3$, perpendicular to the direction of light propagation $\mathbf{e}_1$[1]. This reference frame is used in accordance with typical quantum systems having a z-axis (or rather $\mathbf{e}_3$-axis) quantization, and an arbitrary rotation of reference frame can always be made between atomic and laboratory frames. Within a quantized field formalism, a photon must be exchanged between the atomic system and the field in order for a transition to occur between the ground and excited state. Hence we must take into consideration the mode of the optical field. This is done by taking the basis states of this system to consist of atom-field product states, where the field state is specified by the Fock state $|n\rangle$ and n denotes the photon occupation number.

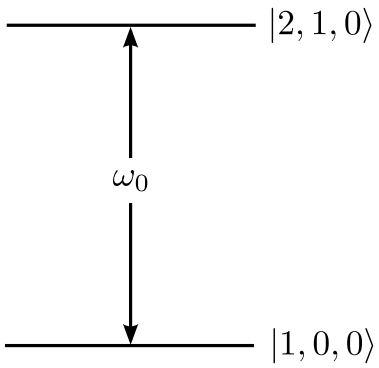

Figure 2.1: A 2-level atom with ground and excited states denoted by $|g\rangle$ and $|e\rangle$, respectively. ω_0 denotes the atomic frequency between these two levels.

[1]To avoid confusion when writing quantum operators in terms of their Cartesian components, the set $(\mathbf{e}_1,\mathbf{e}_2,\mathbf{e}_3)$ is used as the basis for Cartesian unit vectors (where $1,2,3$ correspond to x,y,z).

We construct a simplified notation for the uncoupled $|\text{atom}\rangle\,|\text{field}\rangle$ product states,

$$|1\rangle \equiv |1,0,0\rangle\,|n\rangle\ , \tag{2.1a}$$

$$|2\rangle \equiv |2,1,0\rangle\,|n-1\rangle\ . \tag{2.1b}$$

These states are eigenstates of the atom-field Hamiltonian given by

$$\hat{H}_{af} = \hat{H}_{atom} + \hat{H}_{field} = \frac{\hbar\omega_0}{2}\hat{\sigma}_z + \hbar\omega\hat{a}^+\hat{a}_-\ , \tag{2.2}$$

with eigenenergies E_i (for $i = 1, 2$) defined by $\hat{H}_{af}\,|i\rangle = E_i\,|i\rangle$. Application of the atom-field Hamiltonian to the bare states in Eqs. (2.1) yield the explicit eigenenergies

$$E_1 = -\frac{\hbar\omega_0}{2} + n\hbar\omega\ , \tag{2.3a}$$

$$E_2 = \frac{\hbar\omega_0}{2} + (n-1)\hbar\omega = E_1 + \hbar\Delta_{21}\ , \tag{2.3b}$$

where $\Delta_{21} \equiv (E_2 - E_1)/\hbar = \omega_0 - \omega$ is the 1-photon detuning on the allowed electric dipole transition between levels $|1\rangle$ and $|2\rangle$. In Eq. (2.2), $\hat{\sigma}_z$ is a Pauli spin operator which returns the value of the atomic energy level and $\hat{a}^+$ ($\hat{a}^-$) is the raising (lowering) operator of the single-mode field and follows the usual definition,

$$\hat{a}^+\,|n\rangle = \sqrt{n+1}\,|n+1\rangle \qquad \text{and} \qquad \hat{a}^-\,|n\rangle = \sqrt{n}\,|n-1\rangle\ . \tag{2.4}$$

2.1.1 Derivation of interaction terms

Next we derive the interaction Hamiltonian. The form for the electric interaction of interest is the customary $-\boldsymbol{\mu}_\ell^{(e)} \cdot \mathbf{E}$. Here $\boldsymbol{\mu}_\ell^{(e)}$ is the atomic electric dipole moment operator and is defined as $\boldsymbol{\mu}_\ell^{(e)} = e\hat{r}$, where e is the charge of an electron. The subscript ℓ is used here to distinguish this moment as arising between *atomic* states and not molecular states, as will be important later on. It will be useful to first calculate the magnitude of the electric moment, as its value is critical in predicting the magnitude of the induced moments. For

this calculation we will use atomic hydrogenic wavefunctions for the $1s$ and $2p$ states,

$$|1,0,0\rangle = \frac{1}{\sqrt{\pi a_0^3}} e^{-r/a_0} \,, \tag{2.5a}$$

$$|2,1,0\rangle = \frac{1}{4\sqrt{2\pi a_0^3}} \frac{r}{a_0} e^{-r/2a_0} \cos\theta \,, \tag{2.5b}$$

where a_0 is the Bohr radius. The magnitude of the electric dipole operator is found by computing the inner product using integration (see Appendix B for explicit integration),

$$\mu_\ell^{(e)} = \left|\boldsymbol{\mu}_\ell^{(e)}\right| = \left|\langle 2,1,0| \, e\hat{r} \, |1,0,0\rangle\right| = \cdots = \left|\frac{128\sqrt{2}}{243} a_0 e \mathbf{e}_3\right| = \frac{128\sqrt{2}}{243} a_0 e \,. \tag{2.6}$$

so then

$$\mu_\ell^{(e)} = \frac{128\sqrt{2}}{243} a_0 e \,. \tag{2.7}$$

The electric interaction Hamiltonian is now

$$\begin{aligned}
\hat{H}_{int}^{(e)} &= -\boldsymbol{\mu}_\ell^{(e)} \cdot \mathbf{E}_\perp(\mathbf{r}) \\
&= \left[\boldsymbol{\mu}_\ell^{(e)} \left(\hat{\sigma}^+ + \hat{\sigma}^-\right)\right] \cdot \left[\sqrt{\frac{\hbar\omega}{2\epsilon_0 \mathcal{V}}} \boldsymbol{\varepsilon} \left(\hat{a}^- + \hat{a}^+\right)\right] \\
&= \mu_\ell^{(e)} \sqrt{\frac{\hbar\omega}{2\epsilon_0 \mathcal{V}}} \left(\hat{\sigma}^+ + \hat{\sigma}^-\right)\left(\hat{a}^- + \hat{a}^+\right) \\
&= \hbar g \left(\hat{\sigma}^+ + \hat{\sigma}^-\right)\left(\hat{a}^- + \hat{a}^+\right) \,,
\end{aligned} \tag{2.8}$$

where we have defined[2]

$$g = \frac{\mu_\ell^{(e)}}{\hbar} \sqrt{\frac{\hbar\omega}{2\varepsilon_0 \mathcal{V}}} = \frac{\mu_\ell^{(e)} \xi}{\hbar} \,. \tag{2.9}$$

as the quantized electric field amplitude for mode volume $\mathcal{V}$. Here ε_0 is the permittivity of free space and $\xi = (\hbar\omega/2\epsilon_0\mathcal{V})^{1/2}$. In writing $\mu_\ell^{(e)}$ as opposed to $\boldsymbol{\mu}_\ell^{(e)}$, we have taken

[2]Note that in general, g can be complex and so the interaction Hamiltonian would have the form $\hat{H}_{int}^{(e)} = \hbar\left(g\hat{\sigma}^+\hat{a}^- + g^*\hat{\sigma}^-\hat{a}^+\right)$ where $g = (\mu_\ell^{(e)}/\hbar)\sqrt{\hbar\omega/2\epsilon_0\mathcal{V}}$ as before, but where $\mu_\ell^{(e)}$ can be in general complex. Here we would define the moment by $\mu_{12}^{(e)} = \langle 1| \, e\hat{r} \, |2\rangle$ and $\mu_{21}^{(e)} = \langle 2| \, e\hat{r} \, |1\rangle$ so that $\mu_{12}^{(e)} = (\mu_{21}^{(e)})^*$. In this derivation, the moment is taken to be real.

the dot product with the electric field polarization axis $\boldsymbol{\varepsilon}$; the electric field polarization axis is what establishes the quantization axis, so these two vectors are parallel. Within the rotating wave approximation (RWA), which retains only the energy-conserving terms, the interaction Hamiltonian may be written as

$$\hat{H}_{int}^{(e)} = \hbar g \left(\hat{\sigma}^{+} \hat{a}^{-} + \hat{\sigma}^{-} \hat{a}^{+} \right) \ . \tag{2.10}$$

The RWA is valid when the optical frequency is slightly detuned from the atomic frequency. For the present case, the detuning that corresponds to the secular terms in the electric dipole transition goes as $\omega_0 - \omega$ while the detuning from the non-secular terms goes as $\omega_0 + \omega$. Since the 1-photon detuning is typically chosen to be relatively small (i.e. near resonance), the secular terms dominate the interaction and the RWA may be made.

2.1.2 Rediagonalizing the Hamiltonian

The complete Hamiltonian is now

$$\hat{H} = \hat{H}_{atom} + \hat{H}_{field} + \hat{H}_{int}^{(e)} \ . \tag{2.11}$$

We are interested in determining the new eigenenergies and eigenstates of this 2-level system after interaction with the electric field. This is done by solving the eigenvalue equation

$$\hat{H} \left| D_{\pm}(n) \right\rangle = E_{D\pm} \left| D_{\pm}(n) \right\rangle \ , \tag{2.12}$$

for dressed eigenenergies and eigenstates, $E_{D\pm}$ and $|D_{\pm}(n)\rangle$, respectively. The subscript notation $\pm$ is adopted here since there are only two states in the system and so we may reserve numbered notation for the following sections. Application of the full Hamiltonian to states $|1\rangle$ and $|2\rangle$ yields

$$\hat{H} \left| 1 \right\rangle = E_1 \left| 1 \right\rangle + \hbar g \sqrt{n} \left| 2 \right\rangle \ , \tag{2.13a}$$

$$\hat{H} \left| 2 \right\rangle = E_2 \left| 2 \right\rangle + \hbar g \sqrt{n} \left| 1 \right\rangle \ . \tag{2.13b}$$

Next we construct the matrix $\hat{H}$, whose components are specified by $\hat{H}_{ij} = \langle i | \hat{H} | j \rangle$ for all combinations of $i = 1, 2$ and $j = 1, 2$. Upon computing these inner products, we may rewrite Eq. (2.12) in matrix form,

$$\begin{pmatrix} E_2 & \hbar g\sqrt{n} \\ \hbar g\sqrt{n} & E_1 \end{pmatrix} \begin{pmatrix} b_\pm \\ a_\pm \end{pmatrix} = E_{D\pm} \begin{pmatrix} b_\pm \\ a_\pm \end{pmatrix} , \tag{2.14}$$

and look for solutions of the form

$$|D_\pm(n)\rangle = a_\pm |1,0,0\rangle |n\rangle + b_\pm |2,1,0\rangle |n-1\rangle \ , \tag{2.15}$$

where the expansion coefficients must obey the standard normalization condition $|a_\pm|^2 + |b_\pm|^2 = 1$.

An analytic solution to Eq. (2.14) exists and is easy to derive [35]. This is done by solving the secular equation, $\det(\hat{H} - \hat{I}E_{Di}) = 0$, and determining the new dressed eigenenergies. The energies are

$$E_{D\pm} = \left(n - \frac{1}{2}\right)\hbar\omega \pm \frac{1}{2}\hbar\sqrt{\Delta_{21}^2 + 4|g|^2 n} \, , \tag{2.16}$$

and the singly-dressed eigenstates can be written as admixed components of the initial basis states as

$$|D_+(n)\rangle = \sin\theta \, |1,0,0\rangle |n\rangle + \cos\theta \, |2,1,0\rangle |n-1\rangle \ , \tag{2.17}$$

$$|D_-(n)\rangle = \cos\theta \, |1,0,0\rangle |n\rangle - \sin\theta \, |2,1,0\rangle |n-1\rangle \ . \tag{2.18}$$

In the above equation,

$$\sin 2\theta = \frac{2|g|\sqrt{n}}{\Omega_g} \equiv \frac{\Omega}{\Omega_g} \, , \tag{2.19}$$

$$\cos 2\theta \equiv \frac{\Delta_{21}}{\Omega_g} \, , \tag{2.20}$$

where $\Omega_g = (\Delta_{21}^2 + 4|g|^2 n)^{1/2}$ is the generalized Rabi frequency [35]. We note that coefficients $a_\pm$ and $b_\pm$ are defined explicitly as

$$a_+ = \sin\theta \qquad \text{and} \qquad b_+ = \cos\theta \, , \tag{2.21}$$

$$a_- = \cos\theta \qquad \text{and} \qquad b_- = -\sin\theta \, . \tag{2.22}$$

It is useful to consider the interpretation of these new eigenenergies and how they com-

pare to the initial "undressed" (or bare) atom-field energies. This is most easily done by taking the limit of Eq. (2.16) when $g \longrightarrow 0$, which effectively turns off the interaction. In this limit, $E_{D\pm}$ reduces to,

$$\lim_{g\to 0} E_{D\pm} = \left(n - \frac{1}{2}\right)\hbar\omega \pm \frac{1}{2}\hbar\Delta_{21} \ , \tag{2.23}$$

or rather

$$\lim_{g\to 0} E_{D-} = -\frac{\hbar\omega_0}{2} + n\hbar\omega = E_1 \ , \tag{2.24}$$

$$\lim_{g\to 0} E_{D+} = \frac{\hbar\omega_0}{2} + (n-1)\,\hbar\omega = E_2 \ . \tag{2.25}$$

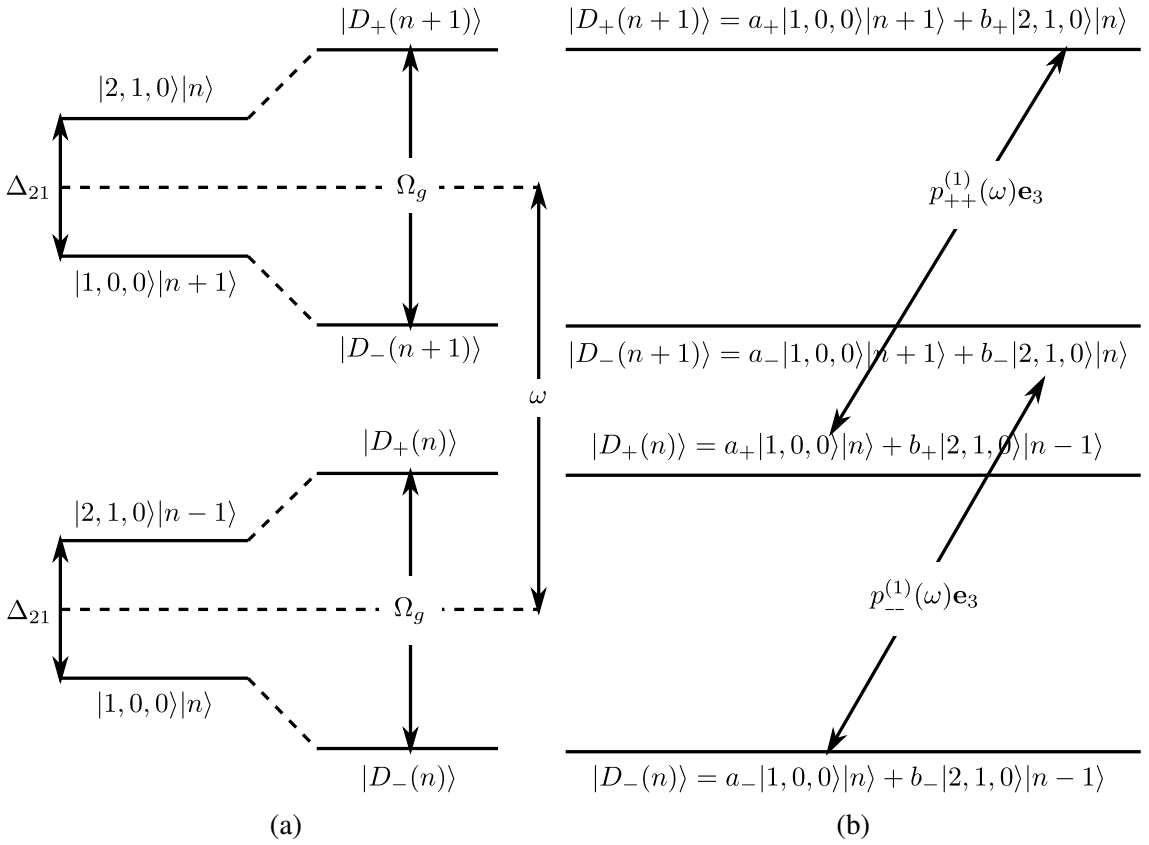

Figure 2.2: (a) Energy level representation of atom-field product states before interaction (left) and once the interaction has been turned on (right). The separation between levels is the generalized Rabi frequency with the interaction on. (b) Nonzero electric moments at ω between adjacent states of the driven system.

So apparently, E_{D-} reduces to E_1 and E_{D+} reduces to E_2 when the interaction is turned off. This is illustrated in Fig. 2.2(a) which shows the atom-field energy levels and how

they effectively shift when the interaction is turned on. Note that since n is not a "good" quantum number, any energy level diagram which includes representations of the quantized field will have an infinite set of energy levels. As will be obvious below, we care only about adjacent energy bands which differ from the initial set of basis states by 1 unit of the photon occupation state (and in our subsequent sections on doubly-dressed systems, we care about states differing by up to 2 units of photon occupation state).

2.1.3 Determining induced dipole moments

Using the solutions for the singly-dressed atom we can calculate the nonzero electric dipole moments which arise between adjacent states of the driven system. The electric dipole moment is calculated using the customary formula, $\hat{p} = e\hat{r}$, which is evaluated between adjacent $|D_{\pm}(n)\rangle$ states of varying photon occupation number. Of relevance to us are the moments oscillating at the fundamental frequency[3], which are illustrated in Fig. 2.2(b). Computing the inner product shows that there are two contributions to the linear electric moment which oscillate at the fundamental frequency and are given by

$$\begin{aligned}
\left\langle \hat{p}^{(1)}_{\pm\pm}(\omega) \right\rangle &= \langle D_{\pm}(n+1)| \, e\hat{r} \, |D_{\pm}(n)\rangle + h.c. \\
&= a_{\pm} b^{*}_{\pm} \, \langle n| \, \langle 2,1,0| \, e\hat{r} \, |1,0,0\rangle \, |n\rangle + h.c. \\
&= \mu^{(e)}_{\ell} \left(a_{\pm} b^{*}_{\pm} + c.c. \right) \mathbf{e}_3 \\
&= 2\mu^{(e)}_{\ell} a_{\pm} b_{\pm} \mathbf{e}_3 \, ,
\end{aligned} \tag{2.26}$$

where in the final step we have used the fact that both $a_{\pm}$ and $b_{\pm}$ are real quantities. The superscript (1) is used in Eq. (2.26) to denote the order of dependence on the electric field. As anticipated, these moments oscillate along the electric field polarization axis. A "net" polarization may be written down by taking the incoherent sum of the two contributions $\hat{p}^{(1)}_{++}$ and $\hat{p}^{(1)}_{--}$ and substituting in the analytic forms for the coefficients $a_{\pm}$ and $b_{\pm}$. It is required that we compute the incoherent sum since the individual moments are not coherent with one another and a simple addition of the two effects would cancel out to give a net polarization of zero (this is obvious if the sum $a_{+}b_{+} + a_{-}b_{-}$ is computed). The incoherent sum giving the net induced electric dipole moment per atom is thus,

[3]This approach may also be used to determine the electric dipole moments at $\omega \pm \Omega_g$, which correspond to Stokes and anti-Stokes scattering events but are not of interest to our current discussion.

$$\left|\hat{p}^{(1)}_{net}(\omega)\right| = \left(\sum_{i=+,-}\left|2\mu^{(e)}_{\ell}a_i b_i \mathbf{e}_3\right|^2\right)^{1/2}$$
$$= 2\mu^{(e)}_{\ell}\left(\left|\sin\theta\cos\theta\right|^2 + \left|\cos\theta\,(-\sin\theta)\right|^2\right)^{1/2}$$
$$= 2\sqrt{2}\mu^{(e)}_{\ell}\sin\theta\cos\theta\,. \tag{2.27}$$

Plots of this moment as a function of intensity and detuning are presented later in Chapter 4. In the next section this theoretical approach is extended to include both the electric and magnetic fields of light.

2.2 Atoms dressed by two fields (E and B)

The first stage of our extended theoretical model allows us to account for coupling between atom-field product states by *both* electric and magnetic interactions while still considering the 2-level atom as the system of interest. All of the same assumptions which were made about the 2-level system considered in the previous section are again made here. The dynamics are assumed to begin in the atomic ground state and light of frequency ω is turned on adiabatically. Orbital angular momentum ℓ is again assumed to be a good quantum number in the absence of light, and the ground (excited) state is taken to be $\ell = 0$ ($\ell = 1$). Hence, the undriven system has inversion symmetry (i.e. is centrosymmetric); this point is worth making because non-centrosymmetry is a requirement for standard second-order EE^* effects to arise. As we will show, a main result of this theory is that second-order effects of the type EB^* and EB may arise due to dynamic symmetry breaking caused by the magnetic interaction. The Born-Oppenheimer and dipole approximations are both made, and the quantization axis again lies along $\mathbf{e}_3$, perpendicular to the direction of light propagation $\mathbf{e}_1$. In the excited state, the projections of angular momentum yield magnetic sub-states denoted by $m_\ell = \{-1, 0, 1\}$. The ket notation $|\alpha, \ell, m_\ell\rangle$ is again used and therefore the atomic basis consists of the set $\{|1,0,0\rangle, |2,1,0\rangle, |2,1,1\rangle, |2,1,-1\rangle\}$ (see Fig. 2.3). The Fock state $|n\rangle$ again denotes the single-mode optical field and the electric and magnetic field components correspond to one and the same mode. Several atom-field product states are chosen for the uncoupled basis and the problem is again solved in the context of dressed state theory.

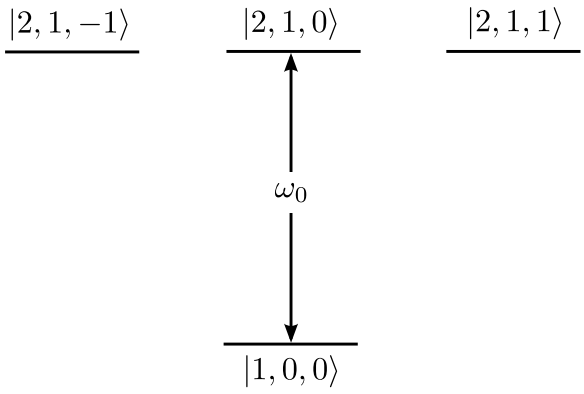

Figure 2.3: Ground ($\ell = 0$) and excited ($\ell = 1$) states of a 2-level atom where the excited state has magnetic quantum numbers $m_\ell = \{-1, 0, 1\}$. The allowed electric dipole transition is at the atomic frequency ω_0.

The set

$$|1\rangle \equiv |1,0,0\rangle\,|n\rangle \ , \tag{2.28a}$$

$$|2\rangle \equiv |2,1,0\rangle\,|n-1\rangle \ , \tag{2.28b}$$

$$|3\rangle \equiv |2,1,1\rangle\,|n-2\rangle \ , \tag{2.28c}$$

$$|4\rangle \equiv |2,1,-1\rangle\,|n\rangle \ , \tag{2.28d}$$

is chosen as the basis atom-field product states of the initially uncoupled system. These states are eigenenergies of the atom-field Hamiltonian given by Eq. (2.2), with eigenenergies E_i (for $i = 1, 2, 3, 4$) and defined by $H_{af}\,|i\rangle = E_i\,|i\rangle$. The states specified by Eqs. (2.28) are the correct choice for the present problem because they are coupled by an absorptive electric interaction followed by a magnetic interaction which may be either absorptive or emissive. Application of the atom-field Hamiltonian on these bare states give the explicit eigenenergies

$$E_1 = -\frac{\hbar\omega_0}{2} + n\hbar\omega \ , \tag{2.29a}$$

$$E_2 = \frac{\hbar\omega_0}{2} + (n-1)\hbar\omega \ , \tag{2.29b}$$

$$E_3 = E_2 - \hbar\omega = \frac{\hbar\omega_0}{2} + (n-2)\hbar\omega \ , \tag{2.29c}$$

$$E_4 = E_2 + \hbar\omega = \frac{\hbar\omega_0}{2} + n\hbar\omega \ . \tag{2.29d}$$

The detunings between the ground state energy, E_1, and each of the excited state energies are important in predicting the resonance behavior of the nonlinear effects to be discussed later on. These detunings are defined as

$$\Delta_{21} \equiv (E_2 - E_1)/\hbar = \omega_0 - \omega \,, \tag{2.30}$$

$$\Delta_{31} \equiv (E_3 - E_1)/\hbar = \omega_0 - 2\omega \,, \tag{2.31}$$

$$\Delta_{41} \equiv (E_4 - E_1)/\hbar = \omega_0 \,. \tag{2.32}$$

Here Δ_{21} is again the 1-photon detuning on the allowed electric dipole transition, while Δ_{31} and Δ_{41} are 2-photon detunings on allowed magnetic dipole transitions.

2.2.1 Derivation of magnetic interaction Hamiltonian

Next we derive the magneto-electric interaction Hamiltonian consisting of both electric and magnetic terms. The electric interaction is the same as was derived above, but the magnetic interaction must be derived by beginning with the customary magnetic dipole potential, $-\boldsymbol{\mu}_\ell^{(m)} \cdot \mathbf{B}$. This new term will allow for coupling between states $|2,1,0\rangle$ and $|2,1,\pm 1\rangle$ via the magnetic field changing the projection of the angular momentum on the quantization axis. Again it will be useful to first compute the magnitude of the magnetic moment,

$$\boldsymbol{\mu}_\ell^{(m)} = \frac{e}{2m_e}\hat{L} \,, \tag{2.33}$$

where m_e is the mass of an electron. This can again be done by considering atomic hydrogenic wavefunctions for the $m_\ell = \pm 1$ states,

$$|2,1,1\rangle = \frac{1}{8\sqrt{\pi a_0^3}}\frac{r}{a_0}e^{-r/2a_0}\sin\theta e^{i\varphi} \,, \tag{2.34a}$$

$$|2,1,-1\rangle = \frac{1}{8\sqrt{\pi a_0^3}}\frac{r}{a_0}e^{-r/2a_0}\sin\theta e^{-i\varphi} \,. \tag{2.34b}$$

We note first a simplification for evaluating the operator $\hat{L}$ between states $\langle 2,1,\pm 1|$ and $|2,1,0\rangle$. We note that of $\hat{L} = \hat{L}_x\mathbf{e}_1 + \hat{L}_y\mathbf{e}_2 + \hat{L}_z\mathbf{e}_3$, only the $\hat{L}_x$ and $\hat{L}_y$ components will contribute to the inner product (since $\hat{L}_z|\alpha,\ell,m_\ell\rangle = \hbar m_\ell|\alpha,\ell,m_\ell\rangle$ does not change the state). Recall the relations between raising and lowering operators $\hat{L}_\pm$ and the Cartesian operators $\hat{L}_x$ and $\hat{L}_y$,

$$\hat{L}_x = \frac{1}{2}\left(\hat{L}_+ + \hat{L}_-\right) \quad \text{and} \quad \hat{L}_y = -\frac{i}{2}\left(\hat{L}_+ - \hat{L}_-\right) . \tag{2.35}$$

Using these relations, we evaluate the inner products,

$$\begin{aligned}
\langle 2,1,1|\,\hat{L}\,|2,1,0\rangle &= \langle 2,1,1|\left[\frac{1}{2}\left(\hat{L}_+ + \hat{L}_-\right)\mathbf{e}_1 + -\frac{i}{2}\left(\hat{L}_+ - \hat{L}_-\right)\mathbf{e}_2\right]|2,1,0\rangle \\
&= \langle 2,1,1|\left[\frac{1}{2}\hbar\sqrt{2}\,(\mathbf{e}_1 - i\mathbf{e}_2)\right]|2,1,1\rangle \\
&= \frac{\hbar\sqrt{2}}{2}\,(\mathbf{e}_1 - i\mathbf{e}_2)
\end{aligned} \tag{2.36}$$

and similarly

$$\begin{aligned}
\langle 2,1,-1|\,\hat{L}\,|2,1,0\rangle &= \langle 2,1,1|\left[\frac{1}{2}\left(\hat{L}_+ + \hat{L}_-\right)\mathbf{e}_1 + -\frac{i}{2}\left(\hat{L}_+ - \hat{L}_-\right)\mathbf{e}_2\right]|2,1,0\rangle \\
&= \langle 2,1,-1|\left[\frac{1}{2}\hbar\sqrt{2}\,(\mathbf{e}_1 - i\mathbf{e}_2)\right]|2,1,-1\rangle \\
&= \frac{\hbar\sqrt{2}}{2}\,(\mathbf{e}_1 + i\mathbf{e}_2)
\end{aligned} \tag{2.37}$$

where we have used the usual definition of the raising/lowering operator,

$$\hat{L}_\pm\,|\alpha,\ell,m_\ell\rangle = \hbar\sqrt{\ell(\ell+1) - m_\ell(m_\ell \pm 1)}\,|\alpha,\ell,m_\ell \pm 1\rangle \ . \tag{2.38}$$

We summarize the results of this inner product in the equation below,

$$\langle 2,1,\pm 1|\,\hat{L}\,|2,1,0\rangle = \frac{\hbar\sqrt{2}}{2}\,(\mathbf{e}_1 \mp i\mathbf{e}_2) \ . \tag{2.39}$$

So then we have

$$\mu_\ell^{(m)} = \left|\boldsymbol{\mu}_\ell^{(m)}\right| = \left|\langle 2,1,\pm 1|\,\frac{e}{2m_e}\hat{L}\,|2,1,0\rangle\right| = \left|\frac{e}{2m_e}\frac{\hbar\sqrt{2}}{2}\,(\mathbf{e}_1 \mp i\mathbf{e}_2)\right| = \frac{e\hbar}{2m_e} , \tag{2.40}$$

where in the last step above we have used that

$$|\mathbf{e}_1 \mp i\mathbf{e}_2| = \left[(1\cdot 1) + (\mp i \cdot \pm i)\right]^{1/2} = \sqrt{2}\,. \tag{2.41}$$

This magnitude has been determined using that the magnitude of a vector with arbitrary

complex coefficients a, b, and c of the form

$$\mathbf{r} = a\mathbf{e}_1 + b\mathbf{e}_2 + c\mathbf{e}_3 \tag{2.42}$$

has magnitude

$$|\mathbf{r}| = (aa^* + bb^* + cc^*)^{1/2} \ . \tag{2.43}$$

Apparently the magnetic dipole moment has magnitude

$$\mu_\ell^{(m)} = \frac{e\hbar}{2m_e} \ , \tag{2.44}$$

which allows us to write the magnetic dipole moment operator in the form

$$\boldsymbol{\mu}_\ell^{(m)} = \mu_\ell^{(m)} \hat{L}' \ , \tag{2.45}$$

where $\hat{L}' \equiv \hat{L}/\hbar$ is defined for notational convenience.

The magnetic interaction Hamiltonian is then

$$\begin{aligned}
\hat{H}_{int}^{(m)} &= -\boldsymbol{\mu}_\ell^{(m)} \cdot \mathbf{B} \\
&= -\left[\mu_\ell^{(m)} \hat{L}'\right] \cdot \left[\sqrt{\frac{\hbar k^2}{2\varepsilon_0 \omega \mathcal{V}}} \left(\boldsymbol{\kappa} \times \boldsymbol{\varepsilon}\right) \left(\hat{a}^- + \hat{a}^+\right)\right] \\
&= -\frac{e\hbar}{2m_e}\sqrt{\frac{\hbar k^2}{2\varepsilon_0 \omega \mathcal{V}}} \left(-\hat{L}'_y\right) \left(\hat{a}^- + \hat{a}^+\right) \\
&= -\frac{e\hbar}{2m_e}\sqrt{\frac{\hbar k^2}{2\varepsilon_0 \omega \mathcal{V}}} \frac{i}{2} \left(\hat{L}'_+ - \hat{L}'_-\right) \left(\hat{a}^- + \hat{a}^+\right) \\
&= \hbar \left(f \hat{L}'_+ + f^* \hat{L}'_-\right) \left(\hat{a}^- + \hat{a}^+\right) \ ,
\end{aligned} \tag{2.46}$$

where we have defined

$$f = -i\frac{e}{4m_e}\sqrt{\frac{\hbar k^2}{2\varepsilon \omega \mathcal{V}}} = -i\frac{\mu_\ell^{(m)}}{2\hbar}\sqrt{\frac{\hbar k^2}{2\varepsilon \omega \mathcal{V}}} = \frac{\mu_\ell^{(m)} \xi'}{\hbar} \tag{2.47}$$

as the quantized magnetic field amplitude for mode volume $\mathcal{V}$. Here

$$\xi' = -\frac{i}{2}\sqrt{\frac{\hbar k^2}{2\varepsilon_0 \omega \mathcal{V}}} \tag{2.48}$$

is related to the constant ξ from the electric derivation by a difference factor of $(-i/2)\,(k/\omega)$,

so

$$\xi' = -\frac{i}{2}\frac{k}{\omega}\xi \,. \tag{2.49}$$

Since the quantization axis is along $\mathbf{e}_3$ and the propagation axis is along $\mathbf{e}_1$, the magnetic field vector lies along $-\mathbf{e}_2$, according to the cross product $\boldsymbol{\kappa} \times \boldsymbol{\varepsilon} = \mathbf{e}_1 \times \mathbf{e}_3 = -\mathbf{e}_2$. This is how we simplified the dot product in the above derivation, as

$$\hat{L}' \cdot (\boldsymbol{\kappa} \times \boldsymbol{\varepsilon}) = -\hat{L}'_y = \frac{i}{2}\left(\hat{L}'_+ - \hat{L}_-\right) \,. \tag{2.50}$$

This explains where the factor of $-i/2$ comes from in the relation between ξ' and ξ: the substitution of raising and lowering operators for the Cartesian operator $\hat{L}'_y$ has this factor built in. This is a result of the fact that a measurement of $\hat{L}'$ along an axis which is not the quantization axis will change the quantum state of the system; in other words, we can know L_z but we cannot simultaneously know L_x and L_y as well.

Before moving on, it is worthwhile to investigate the magnetic field amplitude f a bit more closely. First, we note that we can write f in terms of only ω instead of the wavenumber k by using that $k/\omega = 1/v$ and $v = c/n_\omega$, where n_ω is the real refractive index. It is worth noting that the refractive index only exists for a dense collection of polarizable scatterers, and so in the dilute limit (i.e. single atomic system) there is no effective refractive index and we may set $n_\omega = 1$. Then $k/\omega = 1/c$ and the magnetic coupling strength can be written in terms of the constant ξ as

$$f = -\frac{i}{2}\frac{\mu_\ell^{(m)}\xi}{\hbar c} \,. \tag{2.51}$$

With this explicit expression for f we can compare it to the electric field coupling strength, g, in order to gain a sense for the relative coupling of the electric and magnetic interactions. Computation of this ratio gives

$$\left|\frac{f}{g}\right| = \left(\frac{1}{2}\frac{\mu_\ell^{(m)}\xi}{\hbar c}\right) \cdot \left(\frac{\hbar}{\mu_\ell^{(e)}\xi}\right) = \left(\frac{1}{2c}\frac{e\hbar}{2m_e}\right)\left(\frac{243}{128\sqrt{2}}\frac{1}{a_0 e}\right) = \frac{243}{512\sqrt{2}}\alpha \,, \tag{2.52}$$

where we have used the definitions of $\mu_\ell^{(e)}$ and $\mu_\ell^{(m)}$ from before and have made the substitution

$$\alpha = \frac{\hbar}{a_0 m_e c} \,, \tag{2.53}$$

where $\alpha \approx 7.3 \times 10^{-3}$ is the fine structure constant. Numerical evaluation of this ratio gives $f/g \approx 0.0025$ (or about 1 in 400), which says that the coupling strength due to the electric interaction is about 400 times larger than the coupling due to the magnetic interaction. From Eq. (2.52) it is also apparent that the ratio of the two coupling strengths is approximately $|f/g| \approx (\mu_\ell^{(m)}/c\mu_\ell^{(e)})$, where the factor of c normalizes the units between electric and magnetic coupling. As we will show later on, this large difference in relative coupling strengths between the two interactions results in relatively weak magneto-electric nonlinearities. The second stage of our theoretical model (described in the next section) uses an enhancement mechanism which arises due to molecular rotations as a means to increase the overall induced effects.

2.2.2 Diagonalizing the total Hamiltonian

We now return to the magnetic interaction Hamiltonian that was derived in Eq. (2.46). When the RWA is made, this equation reduces to

$$\hat{H}_{int}^{(m)} = \hbar \left(f \hat{L}'_+ \hat{a}^- + f^* \hat{L}'_- \hat{a}^+ \right) , \tag{2.54}$$

and the atom-field basis states we specified earlier in Eq. (2.28) form a closed set. This means that subsequent applications of the magnetic interaction Hamiltonian on the basis states do not produce couplings to states outside the initial basis. In contrast to this, when the counter rotating terms (i.e. $\hat{L}'_+ \hat{a}^+$ and $\hat{L}'_- \hat{a}^-$) are kept in the Hamiltonian, coupling to new states outside the initial basis is possible and the set of states used to describe the interaction grows indefinitely. Whether or not these terms contribute to the overall dynamics of the system is an important question because the coupling to magnetic substates from state $|2,1,0\rangle$ is very far from resonance and so both co- and counter-rotating terms ought to contribute equally. The implications of including these non-RWA terms in the Hamiltonian is discussed in Appendix A, but the end result is that inclusion of these terms simply doubles the induced second-order magneto-electric moments (while changing little else). It is therefore appropriate to proceed with this problem having made the RWA for the magnetic interaction.

Starting from the ground state, the interaction of light with the atom can be described by a 2-photon excitation process. First, the electric field establishes a coherence between the ground state and the $m_\ell = 0$ excited state. Following this, the magnetic field may act between the $m_\ell = 0$ and $m_\ell = \pm 1$ excited states. This is to say, the first step is an allowed electric dipole interaction from $|1\rangle \rightarrow |2\rangle$ and the second step is an allowed magnetic dipole interaction from either $|2\rangle \rightarrow |3\rangle$ or $|2\rangle \rightarrow |4\rangle$. The resulting application of both the electric

and magnetic fields causes all four basis product states to be mixed into new quasi-states of this driven system. Following our previous discussion, the full magneto-electric interaction Hamiltonian is taken as

$$\hat{H}_{int} = \hat{H}^{(e)}_{int} + \hat{H}^{(m)}_{int} = \hbar g \left(\hat{\sigma}^{+}\hat{a}^{-} + h.c.\right) + \hbar \left(f\hat{L}'_{+}f^{*}\hat{a}^{-} + h.c.\right) \ . \tag{2.55}$$

The prefactors $\hbar g$ and $\hbar f$ both have units of energy, and we note that in general both g and f can be complex quantities. The complete Hamiltonian is then

$$\hat{H} = \hat{H}_{atom} + \hat{H}_{field} + \hat{H}_{int} \ , \tag{2.56}$$

and just as in the singly-dressed case, we must solve the eigenvalue equation

$$\hat{H}\left|D_i(n)\right\rangle = E_{Di}\left|D_i(n)\right\rangle \ , \tag{2.57}$$

for quasi-eigenenergies E_{Di} and quasi-eigenstates $|D_i(n)\rangle$, distinguished by index i (for $i = 1, 2, 3, 4$). Application of the full Hamiltonian to each of the four bare states yields

$$\hat{H}\left|1\right\rangle = E_1\left|1\right\rangle + \hbar g\sqrt{n}\left|2\right\rangle \ , \tag{2.58a}$$

$$\hat{H}\left|2\right\rangle = E_2\left|2\right\rangle + \hbar g\sqrt{n}\left|1\right\rangle + \hbar f\sqrt{2(n-1)}\left|3\right\rangle + \hbar f\sqrt{2n}\left|4\right\rangle \ , \tag{2.58b}$$

$$\hat{H}\left|3\right\rangle = E_3\left|3\right\rangle + \hbar f\sqrt{2(n-1)}\left|2\right\rangle \ , \tag{2.58c}$$

$$\hat{H}\left|4\right\rangle = E_4\left|4\right\rangle + \hbar f\sqrt{2n}\left|2\right\rangle \ , \tag{2.58d}$$

where the application of the raising and lowering angular momentum operators have followed the usual prescription

$$\hat{L}_{\pm}\left|\alpha, \ell, m_\ell\right\rangle = \hbar\sqrt{\ell(\ell+1) - m_\ell(m_\ell \pm 1)}\left|\alpha, \ell, m_\ell \pm 1\right\rangle \ . \tag{2.59}$$

The results of Eqs. (2.58) allow us to construct the matrix representation of the Hamiltonian, which is

$$\hat{H} = \begin{pmatrix} E_4 & 0 & \hbar f\sqrt{2n} & 0 \\ 0 & E_3 & \hbar f\sqrt{2(n-1)} & 0 \\ \hbar f\sqrt{2n} & \hbar f\sqrt{2(n-1)} & E_2 & \hbar g\sqrt{n} \\ 0 & 0 & \hbar g\sqrt{n} & E_1 \end{pmatrix} \ , \tag{2.60}$$

and then solve the secular equation $\det(\hat{H} - \hat{I}E_{Di}) = 0$ for the new doubly-dressed eigenvalues E_{Di} and eigenstates $|D_i(n)\rangle$. The new states are written as a linear combination of the original basis states in accordance with

$$\begin{aligned} |D_i(n)\rangle = a_i\,|1,0,0\rangle\,|n\rangle + b_i\,|2,1,0\rangle\,|n-1\rangle \\ + c_i\,|2,1,1\rangle\,|n-2\rangle + d_i\,|2,1,-1\rangle\,|n\rangle \ , \end{aligned} \tag{2.61}$$

where the expansion coefficients must obey the standard normalization condition $|a_i|^2 + |b_i|^2 + |c_i|^2 + |d_i|^2 = 1$.

2.2.3 Energy level anti-crossings

An analytic solution to this eigenvalue problem in the restricted 4-state basis requires finding the roots of a quartic equation and then determining analytic forms for the new eigenvectors. This approach is impractical, whereas the problem can be solved by numerical diagonalization and the resulting eigenenergies and eigenstates can be graphed to display their behavior. It is of critical importance that the ordering of the new eigensystem is known; in other words, we must keep track of which dressed states $|D_i(n)\rangle$ and dressed energies E_{Di} correspond to the initial uncoupled bare states $|i\rangle$ and bare energies E_i, respectively, in the limit that the interaction is turned off. This can be determined by sorting the eigenvalue/eigenvector pairs from the solved matrix equation in descending order of energy and then pairing the sorted eigenvalue to its corresponding eigenstate. The simplest way to do this is to construct plots of the bare state energies E_i and the dressed state energies E_{Di} versus the optical frequency, ω, for some set of input physical parameters and then track all possible energy level crossings which may occur.

Plots of E_i and E_{Di} versus ω are shown in Figs. 2.4 where the optical field $n\hbar\omega$ has been subtracted from the vertical axis. Figure 2.4(a) shows two energy level crossings, the first of levels $|1\rangle$ and $|3\rangle$ and the second of levels $|1\rangle$ and $|2\rangle$. The first of these crossings occurs at the 2-photon resonance condition $\Delta_{31} = 0$ while the second occurs at the 1-photon resonance condition $\Delta_{21} = 0$. Without rediagonalization these crossings are both real, but once the interaction has taken place any two levels that cross but which are also coupled to via electric or magnetic terms of the interaction Hamiltonian will become an anti-crossing. This fact has been used to produce Fig. 2.4(b) where the crossing of levels $|1\rangle$ and $|2\rangle$ becomes an anti-crossing because $\langle 1|\,\hat{H}_{int}\,|2\rangle \neq 0$, while the crossing of levels $|1\rangle$ and $|3\rangle$ is still a true crossing since $\langle 1|\,\hat{H}_{int}\,|3\rangle = 0$. This result is consistent with the singly-dressed theory, as levels E_- and E_+ do not cross after rediagonalization. The

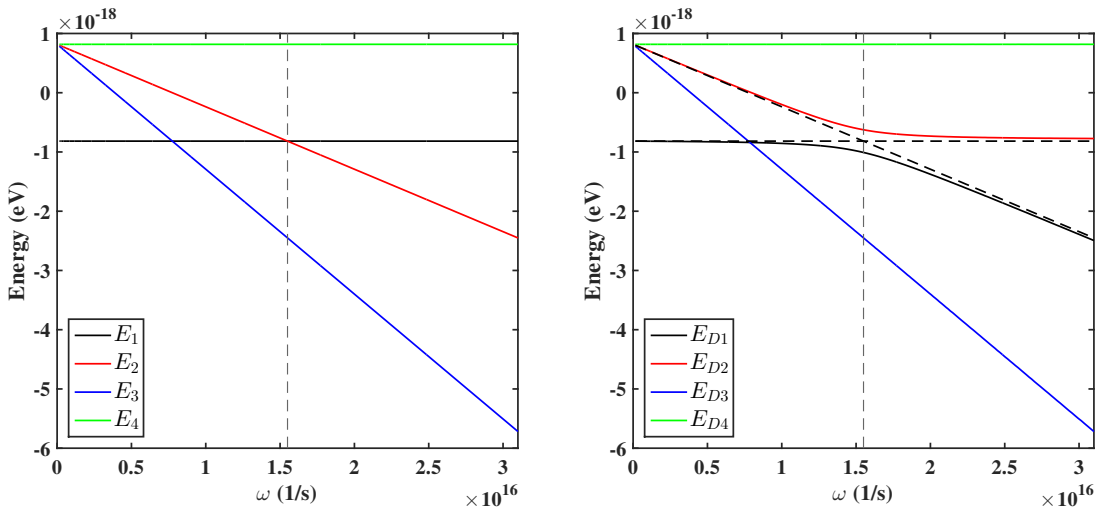

(a) Bare state energies

(b) Dressed state energies

Figure 2.4: (a) Bare state energies E_i and (b) dressed state energies E_{Di} as a function of detunings for $n = 10^{12}$ and $i = 1, 2, 3, 4$. For the plot in (b) the field amplitudes were taken to be $g = 10^9$ s$^{-1/2}$ and $f = (\mu_\ell^{(m)}/c\mu_\ell^{(e)})g$. Here the optical field $n\hbar\omega$ has been subtracted from the vertical axis.

energies from the singly-dressed theory actually track the energy levels of the doubly-dressed model very well (since $g \gg f$). Given these perspectives regarding crossings versus anti-crossings along with comparisons between the E_i and the analytic solutions to the dressed state energies ($E_\pm$) it is possible to sort and track the eigenstates numerically.

It is also of interest to understand how the new quasi-energies evolve as the intensity of the optical field is increased. A plot of the dressed energies as a function of photon number is shown in Fig. 2.5, where $\omega = 0.9\omega_0$, $\omega_0 = 15.5 \times 10^{15}$ 1/s, $g = 10^9$ s$^{-1/2}$, and $f = (\mu_\ell^{(m)}/c\mu_\ell^{(e)})g$. These are the relevant variables for atomic hydrogen. This plot shows dressed eigenenergies E_{Di} which correspond to the dressed levels $|D_i(n)\rangle$ as well as sets of dressed energy levels from adjacent manifolds which are obtained by adding or subtracting an integer multiple of $n\hbar\omega$ from the expressions for the dressed energies. Levels E_{D1} and E_{D2} are shown to depend on $n^{1/2}$ while E_{D3} and E_{D4} have no noticeable dependence on n. The dependence on $n^{1/2}$ of the first two eigenenergies is due to the strong electric field interaction between levels $|1\rangle$ and $|2\rangle$ and is reflected in Eq. (2.16), which gives an analytic expression for $E_\pm$ from the singly-dressed theory. Doubly-dressed energies E_{D1} and E_{D2} are approximated well by the singly-dressed energies E_- and E_+, respectively, so long as we are away from any 2-photon resonances. Energies E_{D3} and E_{D4} are not seen to have a strong dependence on n since the magnetic coupling is much weaker than the electric ($g \gg f$).

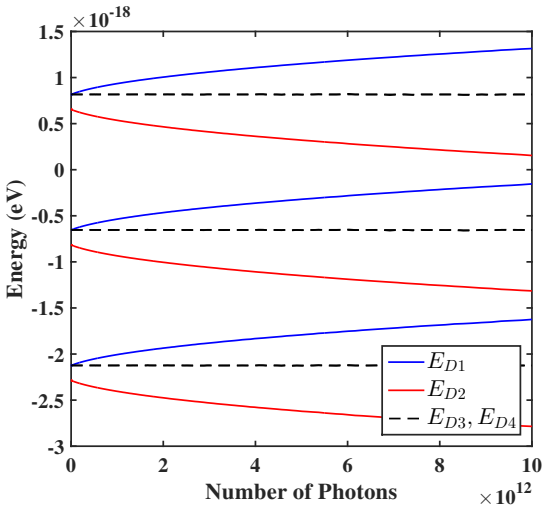

Figure 2.5: Dependence of dressed eigenenergies E_{Di} on photon number. Shown are dressed eigenenergies as labeled by the legend for three adjacent manifolds. The effect of the electric field is shown in the $n^{1/2}$ dependence of levels E_{D1} and E_{D2}. Levels E_{D3} and E_{D4} have no noticeable dependence on n due to the weak coupling via the magnetic interaction.

For practical purposes, it is more useful to use a diagrammatic representation of the energy level splitting such as the one shown in Fig. 2.6. In this diagram, the left-hand side shows the initial atom-field product states separated by the 1-photon detuning and the right-hand side shows the splitting of the energy levels due to the interaction Hamiltonian. We have divided all energies by $\hbar$. Here the degeneracy of the $m_\ell = 0$ excited state is lifted from the other $\ell = 1$ atomic levels with $m_\ell = \pm 1$. Because product states of the uncoupled basis have different photon occupation numbers, when the states are mixed by the incident fields, it is not surprising that n ceases to be a good quantum number. In other words, the energy level diagram repeats infinitely for all values of n, and the subsequent manifolds are separated by ω just as in standard dressed state theory. For low values of n (and because $g \gg f$) levels $|D_3(n)\rangle$ and $|D_4(n)\rangle$ shift very little with respect to their energies in the uncoupled basis. The splitting of states $|D_1(n)\rangle$ and $|D_2(n)\rangle$ is approximated by the electric Rabi frequency since $E_{D1} \approx E_-$ and $E_{D2} \approx E_+$, as $E_+ - E_- = \hbar\Omega_g$.

2.2.4 Determining induced dipole moments

With the quasi-eigenstates in hand, the various electric and magnetic dipole moments that exist between the driven (dynamic) states of the system can be readily determined. These moments are calculated using the customary expressions

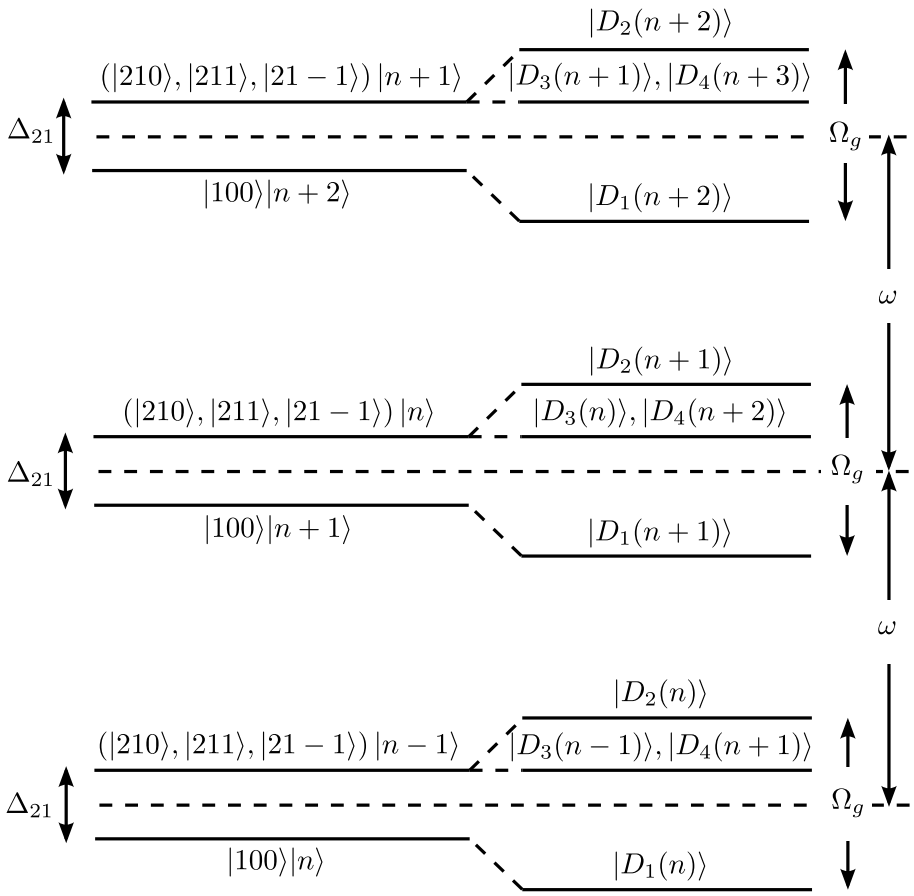

Figure 2.6: Dressed state picture of the energy levels driven by light of frequency ω at a detuning from resonance of Δ_{21}. The left-hand side of the figure represents the un-mixed atom-field product states and the right-hand side shows the resulting dressed states after the interaction Hamiltonian has been considered. Shown are only three energy-level manifolds; the diagram repeats infinitely for all values of n since it is not a good quantum number.

$$\hat{p} = e\hat{r} \quad \text{and} \quad \hat{m} = \frac{e}{2m_e}\hat{L}\,, \tag{2.62}$$

and we are interested in looking only for nonzero moments oscillating at 0, ω, or 2ω. Therefore we evaluate the expectation values of the above dipole moment operators between dressed states of the same index i. We need only to consider transitions occurring between adjacent states of a 3-manifold segment of the infinite energy level diagram like that shown in Fig. 2.6, so only the set of dressed states $|D_i(n)\rangle$, $|D_i(n+1)\rangle$, and $|D_i(n+2)\rangle$ are of use for this calculation. The dipole operators change only the atomic portion of the admixed atom-field states, so orthogonality of the photon states cause most of the cross terms to reduce to zero.

It is well known [36] that a static electric dipole moment cannot exist in the initial ground state of a system which has inversion symmetry, as it is energetically indistinguishable in inverted and non-inverted states. However, in the driven centrosymmetric model considered here, finite dipole moments are found to appear at three frequencies. These include a static moment at zero-frequency, along with an electric moment at the second-harmonic, and two magnetic moments at the fundamental frequency which constitute a new set of magneto-electric nonlinearities, and are shown in Fig. 2.7. Here the solid arrows represent allowed electric dipole transitions and the dashed arrows represent allowed magnetic dipole transitions. Calculations for these moments follow.

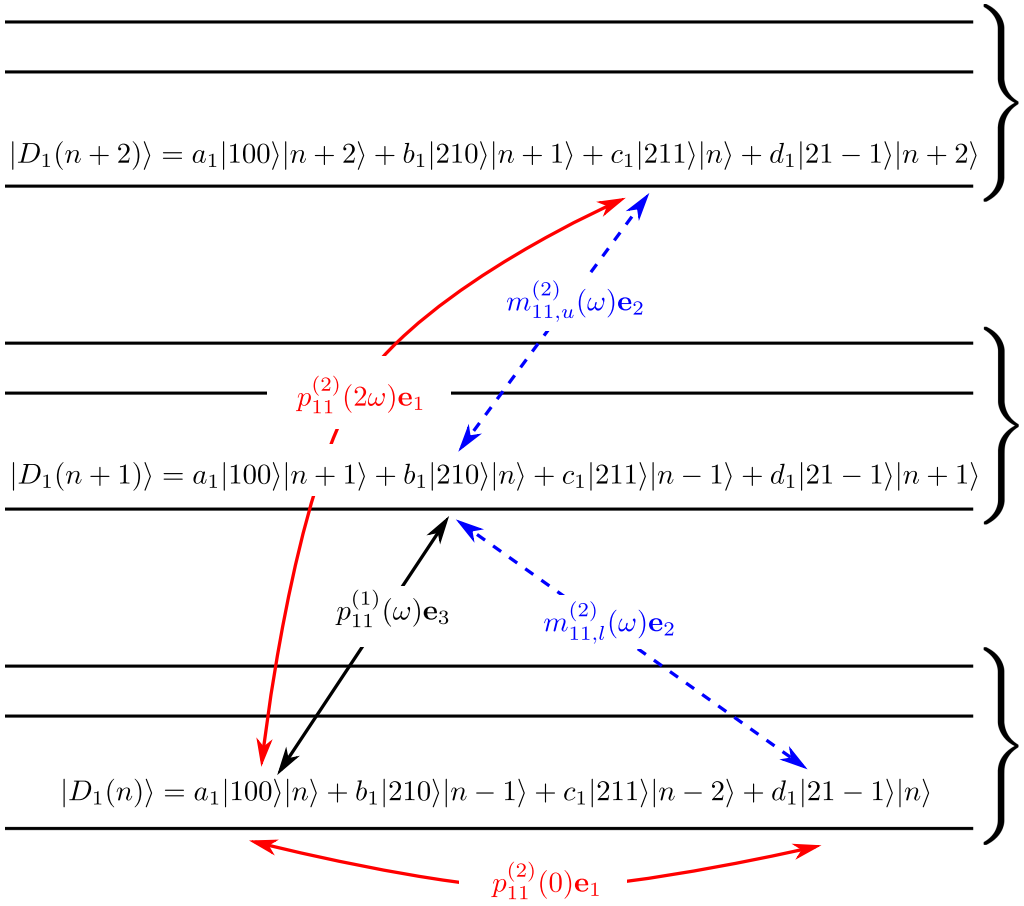

Figure 2.7: Schematic representation of nonlinear dipole moments calculated between dressed states of index $i = 1$. Solid arrows represent allowed electric dipole transitions and dashed arrows represent allowed magnetic dipole transitions.

The linear electric dipole moment is calculated to be

$$\begin{aligned}\left\langle \hat{p}_{ii}^{(1)}(\omega) \right\rangle &= \langle D_i(n+1)| \, e\hat{r} \, |D_i(n)\rangle + h.c. \\ &= a_i b_i^* \, \langle n| \, \langle 2,1,0| \, e\hat{r} \, |1,0,0\rangle \, |n\rangle + h.c. \\ &= \mu_\ell^{(e)} \, (a_i b_i^* + c.c.) \, \mathbf{e}_3 \, , \end{aligned} \tag{2.63}$$

which has a form identical to that shown for the singly-dressed atom. The electric moment at zero-frequency is

$$\begin{aligned}\left\langle \hat{p}_{ii}^{(2)}(0) \right\rangle &= \langle D_i(n)| \, e\hat{r} \, |D_i(n)\rangle + h.c. \\ &= (a_i d_i^* \, \langle n| \, \langle 2,1,-1| \, e\hat{r} \, |1,0,0\rangle \, |n\rangle + a_i^* d_i \, \langle n| \, \langle 1,0,0| \, e\hat{r} \, |2,1,-1\rangle \, |n\rangle) + h.c. \\ &= \frac{\mu_\ell^{(e)}}{\sqrt{2}} \, \{[a_i d_i^* \, (\mathbf{e}_1 + i\mathbf{e}_2) + a_i^* d_i \, (\mathbf{e}_1 - i\mathbf{e}_2)] + c.c.\} \\ &= \mu_\ell^{(e)} \frac{2}{\sqrt{2}} \, (a_i d_i^* + c.c.) \, \mathbf{e}_1 \, . \end{aligned} \tag{2.64}$$

In the last two steps of the above equation, the Hermitian conjugate terms cancel, leaving a static moment oriented purely along $\mathbf{e}_1$ (the direction of optical field propagation).The matrix product $\langle 1,0,0| \, \hat{r} \, |2,1,-1\rangle$ and its conjugate have been evaluated via integration over the hydrogenic wavefunctions and the details for this and subsequent inner product calculations may be found in Appendix B. The fact that a zero-frequency moment may arise confirms that inversion symmetry of the unperturbed atom has been lost as a result of dynamic symmetry breaking by the 2-field optical interaction (and is true regardless of the size of the basis set). A second-harmonic generation (SHG) polarization also arises and is calculated in the same way as the electric moment at zero-frequency,

$$\begin{aligned}\left\langle \hat{p}_{ii}^{(2)}(2\omega) \right\rangle &= \langle D_i(n+2)| \, e\hat{r} \, |D_i(n)\rangle + h.c. \\ &= a_i c_i^* \, \langle n| \, \langle 2,1,1| \, e\hat{r} \, |1,0,0\rangle \, |n\rangle + h.c. \\ &= \mu_\ell^{(e)} \frac{1}{\sqrt{2}} \, [a_i c_i^* \, (\mathbf{e}_1 + i\mathbf{e}_2) + c.c.] \, . \end{aligned} \tag{2.65}$$

Numerical evaluation shows that the conjugate terms in the above expression along $\mathbf{e}_2$ cancel, giving a polarization oriented purely along $\mathbf{e}_1$.

Lastly, we calculate the induced magnetic dipole moments. As is apparent from Fig. 2.7, there are two induced magnetizations in the doubly-dressed atom. The second-order

magneto-electric moment relies physically on the initiation of motion by the electric field in the first step of the interaction process, so the moment must be proportional to the coherences established between states $|1\rangle$ & $|2\rangle$. The expression to evaluate is

$$\hat{m} = a_i b_i^* \frac{e}{2m_e} \hat{L} \, , \tag{2.66}$$

which yields the two terms

$$\begin{aligned} \left\langle \hat{m}_{ii}^{(2)}(\omega) \right\rangle_l &= a_i b_i^* \left\langle D_i(n+1) \right| \frac{e}{2m_e} \hat{L} \left| D_i(n) \right\rangle + h.c. \\ &= a_i b_i^* b_i d_i^* \left\langle n \right| \left\langle 2,1,0 \right| \frac{e}{2m_e} \hat{L} \left| 2,1,-1 \right\rangle \left| n \right\rangle + h.c. \\ &= \mu_\ell^{(m)} \frac{1}{\sqrt{2}} a_i b_i^* b_i d_i^* \left(\mathbf{e}_1 - i\mathbf{e}_2 \right) + c.c. \end{aligned} \tag{2.67}$$

and

$$\begin{aligned} \left\langle \hat{m}_{ii}^{(2)}(\omega) \right\rangle_u &= a_i b_i^* \left\langle D_i(n+2) \right| \frac{e}{2m_e} \hat{L} \left| D_i(n+1) \right\rangle + h.c. \\ &= a_i b_i^* b_i c_i^* \left\langle n \right| \left\langle 2,1,0 \right| \frac{e}{2m_e} \hat{L} \left| 2,1,1 \right\rangle \left| n \right\rangle + h.c. \\ &= \mu_\ell^{(m)} \frac{1}{\sqrt{2}} a_i b_i^* b_i c_i^* \left(\mathbf{e}_1 + i\mathbf{e}_2 \right) + c.c. \, . \end{aligned} \tag{2.68}$$

In experiments only the component of $\hat{m}(\omega)$ along $\mathbf{e}_2$ is projected out (see Chapter 3), so the moment of interest here lies only along $\mathbf{e}_2$. There is also a third-order magnetic contribution which comes about due to a second set of coherence terms which establish a magnetization over the same initial and final states as the process above but is driven purely by a 1-photon magnetic process,

$$\left\langle \hat{m}_{ii}^{(3)}(\omega) \right\rangle_l = -i\mu_\ell^{(m)} \frac{1}{\sqrt{2}} \left(a_i b_i^* a_i d_i^* + c.c. \right) \mathbf{e}_2 \, , \tag{2.69}$$

$$\left\langle \hat{m}_{ii}^{(3)}(\omega) \right\rangle_u = i\mu_\ell^{(m)} \frac{1}{\sqrt{2}} \left(a_i b_i^* a_i c_i^* + c.c. \right) \mathbf{e}_2 \, . \tag{2.70}$$

The justification of this additional term is explained in the extension to the molecular model given in the following section. Because these terms are third-order in the optical field, they are negligible in comparison to the second-order effects at low intensities but are left in the current analysis for the sake of direct comparison between atomic and molecular models.

We will see that they contribute in the molecular picture when the 2-photon detuning is always nearly zero.

The new electric polarizations are thus

$$\left\langle \hat{p}_{ii}^{(2)}(0) \right\rangle = \mu_\ell^{(e)} \frac{2}{\sqrt{2}} \left(a_i d_i^* + h.c. \right) \mathbf{e}_1 \, , \tag{2.71}$$

$$\left\langle \hat{p}_{ii}^{(2)}(2\omega) \right\rangle = \mu_\ell^{(e)} \frac{1}{\sqrt{2}} \left(a_i c_i^* + h.c. \right) \mathbf{e}_1 \, , \tag{2.72}$$

and the magnetizations are

$$\left\langle \hat{m}_{ii}^{(2)}(\omega) \right\rangle_l = -i\mu_\ell^{(m)} \frac{1}{\sqrt{2}} \left[a_i b_i^* \left(b_i d_i^* + a_i d_i^* \right) + c.c. \right] \mathbf{e}_2 \, , \tag{2.73}$$

$$\left\langle \hat{m}_{ii}^{(2)}(\omega) \right\rangle_u = i\mu_\ell^{(m)} \frac{1}{\sqrt{2}} \left[a_i b_i^* \left(b_i c_i^* + a_i c_i^* \right) + c.c. \right] \mathbf{e}_2 \, . \tag{2.74}$$

The induced magnetization at ω can be found by computing the direct (or coherent) sum of the moments for the upper and lower transitions. The coherent sum is taken only over terms of the same dressed state index to allow for out-of-phase terms to cancel. The total magnetization for index i is then,

$$\left\langle \hat{m}_{ii}^{(2)}(\omega) \right\rangle = -i\mu_\ell^{(m)} \frac{1}{\sqrt{2}} \left[a_i b_i^* \left(b_i d_i^* + a_i d_i^* - b_i c_i^* - a_i c_i^* \right) + c.c. \right] \mathbf{e}_2 \, . \tag{2.75}$$

where the aforementioned simplifications have been imposed on the final form of the moments. The moments shown in Eqs. (2.71)-(2.74) are to lowest-order all second-order in the optical field and these constitute a new family of magneto-electric nonlinear effects. Just as in the singly-dressed case, the net moments must be computed using an incoherent sum over all values of dressed state index i. The electric moments are defined as

$$\left| \hat{p}_{net}^{(2)}(0) \right| = \frac{2\mu_\ell^{(e)}}{\sqrt{2}} \left[\sum_{i=1}^{4} \left| \left(a_i d_i^* + c.c. \right) \right|^2 \right]^{1/2} \, , \tag{2.76}$$

$$\left| \hat{p}_{net}^{(2)}(2\omega) \right| = \frac{\mu_\ell^{(e)}}{\sqrt{2}} \left[\sum_{i=1}^{4} \left| \left(a_i c_i^* + c.c. \right) \right|^2 \right]^{1/2} \, , \tag{2.77}$$

and the quadratic magnetic moment is

$$\left|\hat{m}^{(2)}_{net}(\omega)\right| = \frac{\mu^{(m)}_{\ell}}{\sqrt{2}} \left\{ \sum_{i=1}^{4} \left| [a_i b_i^* \left(b_i d_i^* + a_i d_i^* - b_i c_i^* - a_i c_i^*\right) + c.c.] \right|^2 \right\}^{1/2} . \tag{2.78}$$

The orientations of these moments relative to the optical field orientation is useful to point out. The linear electric moment at the fundamental frequency is oriented along the direction of electric field polarization. Likewise, the two induced magnetic dipole moments are oriented along the direction of magnetic field polarization. The two second-order electric polarizations are induced along the axis parallel to the propagation axis, which is in complete agreement with the classical theory presented earlier. The dependences of these induced moments on intensity and frequency will be discussed in the results chapter. Moments of the form $\langle D_i(n)| \hat{p}(0) |D_j(n')\rangle$, $\langle D_i(n)| \hat{p}(2\omega) |D_j(n')\rangle$, and $\langle D_i(n)| \hat{m}(\omega) |D_j(n')\rangle$ where $i \neq j$ have been omitted due to being either negligible or redundant.

2.3 Molecules dressed by two fields (E and B)

Results of the doubly-dressed atomic model (or excited state model) described above predict the frequency dependence, intensity dependence, and polarization of induced magnetic dipole scattering intensities as measured in scattering experiments. However the model fails to explain the apparent enhancement of the strong magnetic response measured in experiments. Here we show that by extending the atomic model to account for molecular degrees of freedom, the moments are readily enhanced and both qualitative and quantitative agreement between experiment and theory is found. A key shortcoming of the atomic model is that the atomic states which are coupled via the magnetic interaction are essentially degenerate, meaning the 2-photon detunings associated with the joint magneto-electric process are far from resonant. Here instead we intentionally construct our model to have states accessible via the magnetic transition that have excited state character but ground state energy [37]. This removes the weak 2-photon resonant condition present in the atomic model and also introduces the rotational frequency as a key physical quantity. A new interaction Hamiltonian is constructed in order to properly describe the couplings between atomic and molecular states of this system. It is shown that inclusion of magnetic torque accounts for an enhancement mechanism by which the magnetic response can rival that of the electric response. A 3-state basis is used for this model to allow for an analytic solution to be written down.

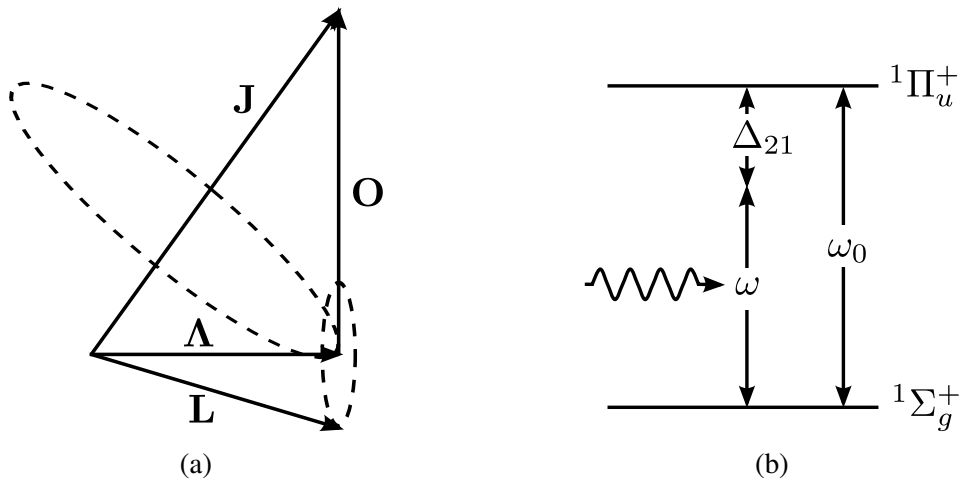

Figure 2.8: (a) Specification of angular momentum components in molecular system. (b) Simplified schematic of energy level structure in molecular system. The ground and excited state are separated by the atomic resonance ω_0.

We assume a rigid, homonuclear diatomic molecule with a 1-photon resonance at ω_0. The total angular momentum $\hat{J}$ is taken to be the sum of internal (orbital) angular momentum $\hat{L}$ and external (rotational) angular momentum $\hat{O}$ so that $\hat{J} = \hat{L} + \hat{O}$ (see Fig. 2.8(a)) [38]. We again neglect spin of the electron. Orbital angular momentum ℓ and rotational angular momentum o are assumed to be good quantum numbers, and the ground (excited) state is taken to be $^1\Sigma_g^+$ ($^1\Pi_u$) with $\ell = 0, o = 0$ ($\ell = 1, o = 1$), as shown in Fig. 2.8(b). The projections of angular momenta yield magnetic substates denoted by $m_\ell = \{-1, 0, 1\}$ and $m_o = \{-1, 0, 1\}$ and the ket notation $|\alpha, \ell, m_\ell\rangle\,|o, m_o\rangle$ is used to define the $|\text{internal}\rangle\,|\text{external}\rangle$ electronic states. The basis then consists of product combinations of the sets $\{|1,0,0\rangle, |2,1,0\rangle, |2,1,1\rangle, |2,1,-1\rangle\}$ and $\{|0,0\rangle, |1,0\rangle, |1,1,\rangle, |1,-1\rangle\}$ with the single-mode Fock state state $|n\rangle$. The uncoupled molecule-field states are then written as $|\alpha, \ell, m_\ell\rangle\,|o, m_o\rangle\,|n\rangle$ and we assume

$$|1\rangle \equiv |1,0,0\rangle\,|0,0\rangle\,|n\rangle\ , \tag{2.79}$$

$$|2\rangle \equiv |2,1,0\rangle\,|1,0\rangle\,|n-1\rangle\ , \tag{2.80}$$

$$|3\rangle \equiv |2,1,-1\rangle\,|1,1\rangle\,|n\rangle\ . \tag{2.81}$$

These states are eigenstates of the molecule-field Hamiltonian[4]

[4]The additional $\hat{O}^2/2I$ term comes from the kinetic energy of the molecule. There is also a term which is proportional to $\hat{L}\cdot\hat{O}$ but is assumed to be small and is not included in the molecule-field Hamiltonian.

$$\hat{H}_{mf} = \hat{H}_{mol} + \hat{H}_{field} = \frac{\hbar\omega_0}{2}\hat{\sigma}_z + \frac{\hat{O}^2}{2I} + \hbar\omega\hat{a}^+\hat{a}^- \ , \tag{2.82}$$

with eigenenergies

$$E_1 = -\frac{\hbar\omega_0}{2} + n\hbar\omega \ , \tag{2.83}$$

$$E_2 = \frac{\hbar\omega_0}{2} + (n-1)\,\hbar\omega \ , \tag{2.84}$$

$$E_3 = -\frac{\hbar\omega_0}{2} + \hbar\omega_\varphi + n\hbar\omega \ . \tag{2.85}$$

The moment of inertia about the rotational axis is defined as

$$I = \frac{\hbar}{\omega_\varphi} \ , \tag{2.86}$$

and the operator $\hat{O}^2$ on molecular states follows the usual

$$\hat{O}^2\,|o, m_o\rangle = o\,(o+1)\,\hbar^2\,|o, m_o\rangle \ . \tag{2.87}$$

The assignment of the energy of $|3\rangle$ in Eq. (2.85) anticipates the removal of orbital angular momentum from the excited state as the result of magnetic torque which causes it to exchange for rotational angular momentum (described in the following section). Removal of orbital angular momentum forces the molecule into the electronic ground state. It is also consistent with the mixing diagram of Fig. 2.9. This shows that when rotational degrees of freedom are accounted for in simple molecular systems such as a diatomic molecule, there is a splitting of p-orbital energy levels $2p\pi$ and $2p\sigma$ depending on rotational character. As the nuclei increase in mass, the state $2p\sigma$ descends toward the ground state $2s\sigma$, while the $2p\pi$ state ascends in energy (see Fig. 2.9). Thus rotational mixing creates a state with p-orbital character, but ground-state energy.

The initial uncoupled basis states permit a single electric and a single magnetic transition to occur between adjacent states via a magneto-electric interaction potential, which is derived in the following subsection. Figure 2.10 depicts these transitions in the molecular energy basis and illustrates the near-resonant interactions of *both* electric and magnetic transitions. The 1- and 2-photon detunings are defined (respectively) as

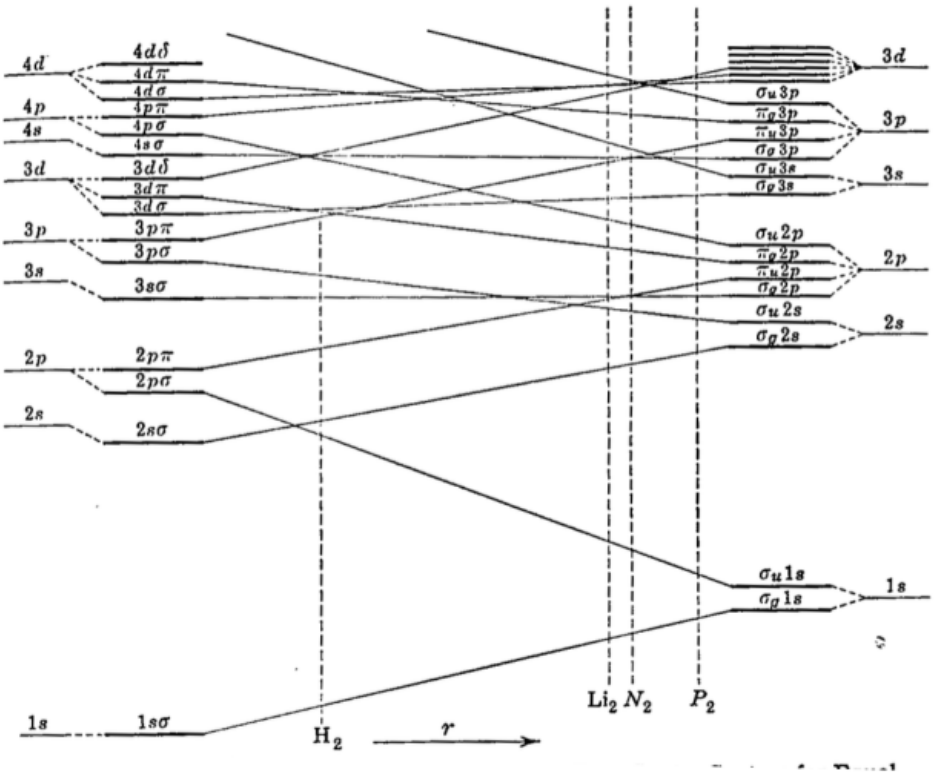

Figure 2.9: Splitting of rotationally-coupled energy levels in homonuclear diatomic molecules. Figure taken from Herzberg *Molecular Spectra and Molecular Structure: I. Diatomic Molecules*.

$$\Delta_{21} \equiv (E_2 - E_1)/\hbar = \omega_0 - \omega \,, \tag{2.88}$$

$$\Delta_{31} \equiv (E_3 - E_1)/\hbar = \omega_\varphi \,. \tag{2.89}$$

Here ω_φ is the rotational (librational) frequency of some molecular liquid (crystalline solid). This term is analogous to the resonant denominator ω_z from the CLOM which was described in Chapter 1. The 2-photon condition is unique in that it shows no dependence on the input optical field oscillation; it is purely a property of the material. As will be shown in Chapter 4, this near-resonant magnetic transition permits very strong magnetic effects to take place in molecular systems.

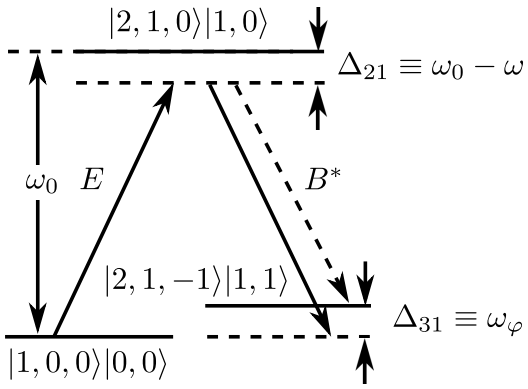

Figure 2.10: Depiction of electric and magnetic transitions driven between uncoupled states of the system. The dashed curve on the magnetic transition represents a completely resonant, inelastic transition that may account for nonlinear depolarization as explained later on.

2.3.1 Derivation of torque-driven magnetic interaction Hamiltonian

A new magnetic interaction potential is derived to describe terms which may couple the internal and external angular momentum states. This interaction will vary slightly from the customary $-\boldsymbol{\mu}_\ell^{(m)} \cdot \mathbf{B}$ used in the previous section for the atomic system. By accounting for torque, terms which go as $\hat{L}_+\hat{O}_-$ and its conjugate appear in the interaction potential and allow for an exchange of angular momentum between magnetic substates of the molecular system. This also provides a mechanism for the enhancement of the induced magnetic moments, as is described below.

We begin with an expression for the kinetic energy of molecular rotation,

$$H = \frac{1}{2}\boldsymbol{\omega} \cdot \mathbf{O} \,, \tag{2.90}$$

where $\boldsymbol{\omega}$ is the vector representing rotation at angular frequency ω about an axis perpendicular to the internuclear axis and $\mathbf{O}$ is the angular momentum vector of the rigid rotor. Once the electric field has driven a transition between the ground and excited states, there is an internal angular momentum $\mathbf{L}$ associated with the electron. If the magnetic field is then allowed to act on this charge distribution such that $\mathbf{B} \perp \mathbf{L}$, then a torque $\mathbf{T}$ is exerted on the system, and a rotation is initiated which may be described by $\mathbf{O}$. Classically, the molecule accumulates rotational angular momentum according to

$$\mathbf{O} = \int_0^t \left(\frac{d\mathbf{O}}{dt}\right) dt \,. \tag{2.91}$$

Since total angular momentum $\mathbf{J} = \mathbf{L} + \mathbf{O}$ is conserved in an isolated system, its time

derivative is zero. Then,

$$\frac{d\mathbf{J}}{dt} = \frac{d\left(\mathbf{L}+\mathbf{O}\right)}{dt} = 0\,, \tag{2.92}$$

and

$$\mathbf{O} = -\int_0^t \left(\frac{d\mathbf{L}}{dt}\right) dt\,. \tag{2.93}$$

The equation of motion for rotations is taken to be

$$\mathbf{T} = \frac{d\mathbf{L}}{dt}\,, \tag{2.94}$$

which ignores precession of the rotational axis described by the $\boldsymbol{\omega}\times\mathbf{L}$ contribution. Magnetic torque is given by $\mathbf{T}=\mathbf{m}\times\mathbf{B}$, where $\mathbf{m}$ is the magnetic moment due to circulation of charge at the optical frequency. The positive (negative) frequency component of $\mathbf{m}$ combines with the negative (positive) frequency component of $\mathbf{B}$ to yield a slowly-varying amplitude of the rotational angular momentum. The expression for $\mathbf{O}$ is then

$$\mathbf{O} = -\int_0^t \left(\mathbf{m}\times\mathbf{B}\right) dt\,. \tag{2.95}$$

For molecules, the various momenta are referenced to the molecular COM. We may therefore specify the electron position as $\mathbf{R}\equiv\mathbf{r}+\mathbf{h}$ in cylindrical coordinates (r,φ,h) centered on an origin halfway between the nuclei of the diatomic, homonuclear rigid rotor. Then the charge circulation responsible for $\mathbf{L}$ in the excited state is azimuthal as depicted in Fig. 2.11. The orbital angular momentum

$$\mathbf{L} = \mathbf{R}\times m_e\frac{\partial\mathbf{R}}{\partial t} \tag{2.96}$$

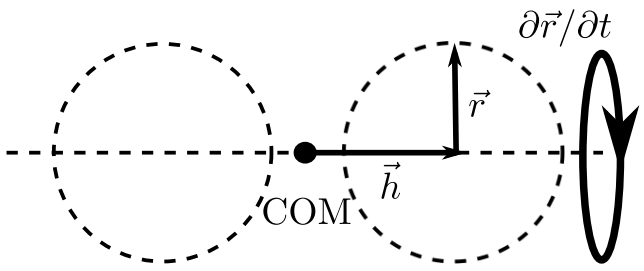

Figure 2.11: Orbital angular momentum $\hat{L}$ of an electron about the internuclear axis of a diatomic molecule, visualized in cylindrical coordinates reference to the COM. Here angular momentum is determined by the local coordinate r.

contains four terms, three of which are zero. The two terms

$$\mathbf{r} \times m_e \frac{\partial \mathbf{h}}{\partial t} \quad \text{and} \quad \mathbf{h} \times m_e \frac{\partial \mathbf{h}}{\partial t} \tag{2.97}$$

are both zero because the axial component of $\mathbf{R}$ is time-invariant. Also, the term

$$\mathbf{h} \times m_e \frac{\partial \mathbf{r}}{\partial t} \tag{2.98}$$

averages to zero since the product is directed radially along $\mathbf{r}$ and rotates at ω_0. The remaining term yields

$$\mathbf{L} = m_e \mathbf{r} \times \frac{\partial \mathbf{r}}{\partial t} \tag{2.99}$$

and its magnitude is

$$L = m_e r^2 \omega_0 \, . \tag{2.100}$$

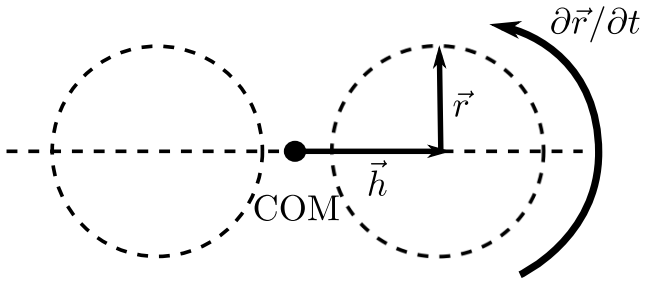

Figure 2.12: After application of the magnetic torque, electron motion is in a plane orthogonal to that in Fig. 2.11. It consists of rotation about an axis perpendicular to the internuclear axis, normal to the plane of the drawing. Angular momentum is determined chiefly by the coordinate h of the electron since $h \gg r$.

Rotational angular momentum due to end-over-end motion of the molecule arises after the application of the magnetic torque (see Fig. 2.12). In this case the electron motion rotates into a plane orthogonal to the initial plane. The leading contribution to rotational angular momentum is

$$\mathbf{O} = \mathbf{R} \times m_e \frac{\partial \mathbf{R}}{\partial t} \, , \tag{2.101}$$

which can be written as

$$\mathbf{O} = \mathbf{h} \times m_e \frac{\partial \mathbf{h}}{\partial t} \tag{2.102}$$

or as

$$\mathbf{O} = m_e h^2 \hat{h} \times \frac{\partial \hat{r}}{\partial t} = m_e h^2 \omega_0 \hat{r}_0 \ , \tag{2.103}$$

where $\hat{r}_0 = \hat{L} \times \hat{B}$ is a unit vector perpendicular to the internuclear axis. The magnitude of the rotational term is

$$O = m_e h^2 \omega_0 \ . \tag{2.104}$$

The average value of h is exactly 1/2 of the internuclear separation, where the average value of r is on the order of the Bohr radius ($h \gg r$). The relative magnitudes of $\mathbf{O}$ and $\mathbf{L}$ for the same electron velocity are therefore described by an enhancement factor η obtained by combining Eqs. (2.100) and (2.104),

$$\eta \equiv \frac{O}{L} = \frac{h^2}{r^2} \ . \tag{2.105}$$

This factor is the same as the ratio of areas enclosed by charge motion during "external" molecular rotation as opposed to "internal" orbital angular momentum. An immediate consequence of this is that the magnetic moment is enhanced to a value of

$$\mathbf{m} = \eta \left(\frac{e\mathbf{L}}{2m_e} \right) \ . \tag{2.106}$$

Using this definition, the rotational angular momentum is given by the integral

$$\mathbf{O} = -\int_0^t \left(\frac{e\eta}{2m_e} \right) (\mathbf{L} \times \mathbf{B}) \, dt \ , \tag{2.107}$$

which may be integrated (assuming constant torque) to yield

$$\mathbf{O} = -\left(\frac{e\eta}{2m_e} \right) (\mathbf{L} \times \mathbf{B}) \, t \ . \tag{2.108}$$

Substituting this result for $\mathbf{O}$ into the expression for the kinetic energy yields

$$H = -\frac{1}{2I} \mathbf{O} \cdot \frac{e\eta}{2m_e} (\mathbf{L} \times \mathbf{B}) \, t \ , \tag{2.109}$$

$$= -\frac{1}{2I} \boldsymbol{\mu}_o \cdot (\mathbf{L} \times \mathbf{B}) \, t, \tag{2.110}$$

where the rotational magnetic moment is defined as

$$\boldsymbol{\mu}_o \equiv \frac{e\eta}{2m_e} \mathbf{O} \ . \tag{2.111}$$

This is slightly different from the standard form for the induced magnetic moment by a factor of the enhancement term η.

The momentum transfer time t may be estimated by setting the time-integrated torque equal to the angular momentum available for transfer, which is $\hbar$ (for $\ell = 1$). That is to say,

$$\Delta \mathbf{L} = \left(\frac{e}{2m_e} \right) (\mathbf{L} \times \mathbf{B})\, t = \hbar \mathbf{O} \; . \tag{2.112}$$

Solving for t, one finds that

$$t = \frac{4m_e}{eB_0} = \frac{4}{\omega_c} \; , \tag{2.113}$$

where $\omega_c = eB_0/m_e$ is the cyclotron frequency for the component of

$$B = \frac{1}{2} B_0 \left(e^{i\omega t} + e^{-i\omega t} \right) \tag{2.114}$$

that counter-rotates with respect to the electric field. This yields for the interaction energy,

$$H = -\left(\frac{2\omega_\varphi}{\omega_c} \right) \boldsymbol{\mu}_o \cdot (\mathbf{L}' \times \mathbf{B}) = -\mu^{(m)} \mathbf{O}' \cdot (\mathbf{L}' \times \mathbf{B}) \; , \tag{2.115}$$

where the magnetic moment is defined as

$$\boldsymbol{\mu}^{(m)} \equiv \eta \left(\frac{2\omega_\varphi}{\omega_c} \right) \left(\frac{e\hbar}{2m_e} \right) \mathbf{O}' = \mu^{(m)} \mathbf{O}' \; . \tag{2.116}$$

and the primed notation again represents division by $\hbar$. Due to conservation of angular momentum,

$$I_{\mathbf{L}} \omega_0 = I_{\mathbf{O}} \omega_\varphi \; , \tag{2.117}$$

the overall enhancement factor can be replaced by a ratio of the corresponding frequencies,

$$\eta \left(\frac{2\omega_\varphi}{\omega_c} \right) = \left(\frac{2m_N h^2}{m_e r^2} \right) \left(\frac{m_e}{2m_N} \right) \left(\frac{2\omega_\varphi}{\omega_c} \right) = \frac{m_e \omega_0}{m_N \omega_c} \; . \tag{2.118}$$

We may now evaluate the quantum mechanical analogue of the new interaction potential,

$$\hat{H}^{(m)}_{int} = -\boldsymbol{\mu}^{(m)} \cdot \left(\hat{L}' \times \mathbf{B} \right) \; , \tag{2.119}$$

where the magnetic moment is now established over the entire molecule and

$$\boldsymbol{\mu}^{(m)} = \left(\frac{m_e\omega_0}{m_N\omega_c}\right)\left(\frac{e}{2m_e}\right)\hat{O} = \mu^{(m)}\hat{O}' \,, \tag{2.120}$$

where the primed operators $\hat{L}' \equiv \hat{L}/\hbar$ and $\hat{O}' \equiv \hat{O}/\hbar$ are defined for notational convenience. Expanding the Hamiltonian yields

$$\begin{aligned}
\hat{H}_{int}^{(m)} &= -\boldsymbol{\mu}^{(m)} \cdot \left(\hat{L}' \times \mathbf{B}\right) \\
&= -\left[\mu^{(m)}\hat{O}'\right] \cdot \left\{\left[\hat{L}'\right] \times \left[\sqrt{\frac{\hbar k^2}{2\epsilon_0\omega\mathcal{V}}}\,(\boldsymbol{\kappa}\times\boldsymbol{\varepsilon})\left(\hat{a}^- + \hat{a}^+\right)\right]\right\} \\
&= -\mu^{(m)}\sqrt{\frac{\hbar k^2}{2\epsilon_0\omega\mathcal{V}}}\left[\hat{O}' \cdot \left(\hat{L}' \times (-\mathbf{e}_2)\right)\right]\left(\hat{a}^- + \hat{a}^+\right) \,,
\end{aligned} \tag{2.121}$$

where in evaluating the cross-product $(\boldsymbol{\kappa} \times \boldsymbol{\varepsilon})$ we took the electric field polarization to be along $\mathbf{e}_3$ and the propagation axis to lie along $\mathbf{e}_1$[5], thereby giving that

$$\boldsymbol{\kappa} \times \boldsymbol{\varepsilon} = \mathbf{e}_1 \times \mathbf{e}_3 = -\mathbf{e}_2 \,. \tag{2.122}$$

We can now evaluate the term in square brackets from the equation above. First we compute the cross product,

$$\hat{L}' \times \mathbf{e}_1 = \begin{vmatrix} \mathbf{e}_1 & \mathbf{e}_2 & \mathbf{e}_3 \\ \hat{L}'_x & \hat{L}'_y & \hat{L}'_z \\ 0 & -1 & 0 \end{vmatrix} = \hat{L}'_z\mathbf{e}_1 - \hat{L}'_x\mathbf{e}_3 \,, \tag{2.123}$$

which as we can see has components along both $\mathbf{e}_1$ and $\mathbf{e}_3$[6]. However, for z-axis quantization, the term along $\mathbf{e}_1$ must vanish. This is because the operator $\hat{L}_z$ does not change the projection of the quantum system and therefore will not contribute to any off-diagonal entries in the Hamiltonian matrix. We are then left just with $-\hat{L}'_x\mathbf{e}_3$. Dotted into $\hat{O}'$ we see,

$$\hat{O}' \cdot \left(\hat{L}' \times (-\mathbf{e}_1)\right) = \hat{O}' \cdot \left(-\hat{L}'_x\mathbf{e}_3\right) = -\hat{O}'_z\hat{L}'_x \,. \tag{2.124}$$

The quantization axis $\mathbf{e}_3$ defines the axis about which $\hat{L}$ has a well-defined projection.

[5]The *only* restriction on the system up to this point was that the electric field interaction has defined the quantization axis to lie along $\mathbf{e}_3$. The choice for propagation axis is still free to lie along *either* $\mathbf{e}_1$ or $\mathbf{e}_2$ (or some linear combination). It can be shown that the choice has no overall effect on the outcome of this theoretical model.

[6]Note that if the propagation axis were taken to lie along $\mathbf{e}_2$ instead then $\boldsymbol{\kappa} \times \boldsymbol{\varepsilon} = \mathbf{e}_2 \times \mathbf{e}_3 = \mathbf{e}_1$ and then the cross product with $\hat{L}'$ would be $\hat{L}' \times \mathbf{e}_2 = \hat{L}'_z\mathbf{e}_2 - \hat{L}'_y\mathbf{e}_3$.

That is to say, a measurement of $\hat{L}_z$ returns a well-defined eigenvalue, while measurements of $\hat{L}$ in directions orthogonal to $\mathbf{e}_3$ change the state of the system, as described in the previous section. This allows us to write $\hat{L}_x$ and $\hat{L}_y$ in terms of the raising and lowering operators $\hat{L}_+$ and $\hat{L}_-$. However, we have defined $\hat{O} \perp \hat{L}$, so the axis about which $\hat{O}$ has a well-defined projection must be orthogonal to $\mathbf{e}_3$, meaning that a measurement of $\hat{O}_z$ will put the system into a different rotational state. By virtue of this fact, we may represent $\hat{O}_z$ in terms of raising and lowering operators,

$$\hat{O}'_z = \frac{1}{2}\left(\hat{O}'_+ + \hat{O}'_-\right) . \tag{2.125}$$

The product $-\hat{O}'_z\hat{L}'_x$ is then found to be

$$\begin{aligned} -\hat{O}'_z\hat{L}'_x &= -\left[\frac{1}{2}\left(\hat{O}'_+ + \hat{O}'_-\right)\right]\left[\frac{1}{2}\left(\hat{L}'_+ + \hat{L}'_-\right)\right] \\ &= -\frac{1}{4}\left(\hat{O}'_+ + \hat{O}'_-\right)\left(\hat{L}'_+ + \hat{L}'_-\right) . \end{aligned} \tag{2.126}$$

and the magnetic interaction Hamiltonian is now

$$\begin{aligned} \hat{H}^{(m)}_{int} &= \frac{1}{4}\mu^{(m)}\sqrt{\frac{\hbar k^2}{2\epsilon_0\omega\mathcal{V}}}\left(\hat{O}'_+ + \hat{O}'_-\right)\left(\hat{L}'_+ + \hat{L}'_-\right)\left(\hat{a}^- + \hat{a}^+\right) \\ &= \frac{1}{4}\mu^{(m)}\sqrt{\frac{\hbar k^2}{2\epsilon_0\omega\mathcal{V}}}\left(\hat{O}'_+ + \hat{O}'_-\right)\left(\hat{L}'_+\hat{a}^- + \hat{L}'_-\hat{a}^+\right) \\ &= \hbar f\left(\hat{O}'_-\hat{L}'_+\hat{a}^- + \hat{O}'_+\hat{L}'_-\hat{a}^+\right) , \end{aligned} \tag{2.127}$$

where the RWA has been made and

$$f = \frac{\mu^{(m)}}{4\hbar}\sqrt{\frac{\hbar k^2}{2\epsilon_0\omega\mathcal{V}}} = \frac{\mu^{(m)}_{eff}}{\hbar}\sqrt{\frac{\hbar k^2}{2\epsilon_0\omega\mathcal{V}}} . \tag{2.128}$$

Here an effective magnetic moment has been defined in terms of the enhancement factor and $\mu^{(m)}$ as

$$\mu^{(m)}_{eff} \equiv \left(\frac{m_e\omega_0}{4m_N\omega_c}\right)\mu^{(m)} . \tag{2.129}$$

We can write f in terms of ω instead of wavenumber k by using that $k/\omega = 1/v$ and $v = c/n_\omega$, where n_ω is the real part of the refractive index. Then we see

$$f = \frac{\mu_{eff}^{(m)}}{\hbar}\sqrt{\frac{\hbar}{2\epsilon_0\omega\mathcal{V}}\cdot\frac{n_\omega^2\omega^2}{c^2}} = \frac{\mu_{eff}^{(m)}}{\hbar}\sqrt{\frac{\hbar n_\omega^2\omega}{2\epsilon_0\mathcal{V}c^2}}\ . \tag{2.130}$$

In simulations and for all practical purposes, n_ω should be set to unity since the refractive index only makes sense in the limit that we have a dense collection of scattering centers; it does not make sense to talk about an "effective refractive index" for a single molecule.

2.3.2 Analytic solution to the secular cubic equation

The goal here is to solve the eigenvalue problem

$$\hat{H}\left|D_i(n)\right\rangle = E_{Di}\left|D_i(n)\right\rangle\ , \tag{2.131}$$

for "doubly-dressed" states $|D_i(n)\rangle$ and energies E_{Di}. Here $\hat{H}$ is the full Hamiltonian,

$$\hat{H} = \hat{H}_{mf} + \hat{H}_{int}\ , \tag{2.132}$$

where the second term is the interaction Hamiltonian and is composed of the electric and magnetic interaction terms derived in the previous subsection,

$$\begin{aligned}\hat{H}_{int} &= \hat{H}_{int}^{(e)} + \hat{H}_{int}^{(m)} \\ &= \hbar g\left(\hat{\sigma}^+\hat{a}^- + \hat{\sigma}^-\hat{a}^+\right) + \hbar f\left(\hat{O}'_-\hat{L}'_+\hat{a}^- + \hat{O}'_+\hat{L}'_-\hat{a}^+\right)\end{aligned} \tag{2.133}$$

We can now determine the elements of the Hamiltonian matrix, which in general looks like

$$\begin{pmatrix} H_{33} & H_{32} & H_{31} \\ H_{23} & H_{22} & H_{21} \\ H_{13} & H_{12} & H_{11} \end{pmatrix}\ , \tag{2.134}$$

where the H_{ij} elements are determined in the customary way by evaluating

$$H_{ij} = \left\langle i\right|\hat{H}\left|j\right\rangle\ . \tag{2.135}$$

The diagonal elements of the matrix are simply the bare-state energies shown above, but the off-diagonal elements are related to the coupling of the individual states by the electromagnetic interaction Hamiltonian. The electric interaction on the ground state gives

$$\begin{aligned}\hat{H}_{int}^{(e)}\left|1\right\rangle &= \hbar g\left(\hat{\sigma}^{+}\hat{a}^{-}+\hat{\sigma}^{-}\hat{a}^{+}\right)\left|1,0,0\right\rangle\left|0,0\right\rangle\left|n\right\rangle \\ &= \hbar g\sqrt{n}\left|2,1,0\right\rangle\left|1,0\right\rangle\left|n-1\right\rangle\ ,\end{aligned} \tag{2.136}$$

and taking its inner product with $\langle 2| = \langle n-1|\langle 1,0|\langle 2,1,0|$, we see that $H_{21} = \hbar g\sqrt{n}$ and so $H_{12} = \hbar g^{*}\sqrt{n} = \hbar g\sqrt{n}$ since g is real. The electric transition changes the values of both ℓ and o from $\ell = 0, o = 0$ in the ground state to $\ell = 1, o = 1$ in the excited state. Now we consider the magnetic interaction on state $|2\rangle$,

$$\begin{aligned}\hat{H}_{int}^{(m)}\left|2\right\rangle &= \hbar f\left(\hat{O}'_{-}\hat{L}'_{+}\hat{a}^{-}+\hat{O}'_{+}\hat{L}'_{-}\hat{a}^{+}\right)\left|2,1,0\right\rangle\left|1,0\right\rangle\left|n-1\right\rangle \\ &= 2\hbar f\sqrt{n-1}\left|2,1,1\right\rangle\left|1,-1\right\rangle\left|n-2\right\rangle + 2\hbar f\sqrt{n}\left|2,1,-1\right\rangle\left|1,1\right\rangle\left|n\right\rangle\ ,\end{aligned} \tag{2.137}$$

and taking the inner product with state $\langle 3| = \langle n|\langle 1,1|\langle 2,1,-1|$ we find that $H_{32} = 2\hbar f\sqrt{n}$ and so $H_{23} = 2\hbar f^{*}\sqrt{n} = 2\hbar f\sqrt{n}$ since f is real. Note that the RWA is used to throw away the state $|2,1,1\rangle|1,-1\rangle|n-2\rangle$, though we will come back to this issue in a later discussion in Chapter 4. We have also used that

$$\hat{O}'_{\pm}\left|o,m_o\right\rangle = \sqrt{o(o+1)-m_o(o\pm 1)}\left|o,m_o\pm 1\right\rangle\ . \tag{2.138}$$

It is then easy for us to write down the Hamiltonian including the interaction terms,

$$\hat{H} = \begin{pmatrix} E_3 & 2\hbar f\sqrt{n} & 0 \\ 2\hbar f\sqrt{n} & E_2 & \hbar g\sqrt{n} \\ 0 & \hbar g\sqrt{n} & E_1 \end{pmatrix}\ , \tag{2.139}$$

and solve the eigenvalue equation $\hat{H}\left|D_i(n)\right\rangle = E_{Di}\left|D_i(n)\right\rangle$ for "doubly-dressed" eigenvalues E_{Di} and eigenstates $|D_i(n)\rangle$. In full form, this equation is

$$\begin{pmatrix} E_3 & 2\hbar f\sqrt{n} & 0 \\ 2\hbar f\sqrt{n} & E_2 & \hbar g\sqrt{n} \\ 0 & \hbar g\sqrt{n} & E_1 \end{pmatrix}\begin{pmatrix} c_i \\ b_i \\ a_i \end{pmatrix} = E_{Di}\begin{pmatrix} c_i \\ b_i \\ a_i \end{pmatrix}\ , \tag{2.140}$$

where the new eigenstates of the system can be expressed in terms of the dressed state coefficients a_i, b_i, and c_i as

$$\left|D_i(n)\right\rangle = a_i\left|1,0,0\right\rangle\left|0,0\right\rangle\left|n\right\rangle + b_i\left|2,1,0\right\rangle\left|1,0\right\rangle\left|n-1\right\rangle + c_i\left|2,1,-1\right\rangle\left|1,1\right\rangle\left|n\right\rangle\ . \tag{2.141}$$

For all intents and purposes, the system is easily solved using numerical techniques. However, because the the secular equation is cubic, an analytic solution does exist that we can write down. We include it here for completeness.

2.3.2.1 Determining eigenvalues

For the analytic solution, we search for eigenvectors which satisfy the equation

$$(H - E_{Di}I)\,|D_i(n)\rangle = 0\,, \tag{2.142}$$

and look to write the dressed state coefficients a_i, b_i, and c_i in terms of the new eigenenergies, the initial bare state energies, and the electric and magnetic coupling strengths. To find the eigenvalues, we must solve the secular determinant

$$\begin{vmatrix} E_3 - E_{Di} & 2\hbar f\sqrt{n} & 0 \\ 2\hbar f\sqrt{n} & E_2 - E_{Di} & \hbar g\sqrt{n} \\ 0 & \hbar g\sqrt{n} & E_1 - E_{Di} \end{vmatrix} = 0\,. \tag{2.143}$$

After some manipulation, the above equation becomes

$$\begin{aligned} E_{Di}^3 - (E_1+E_2+E_3)E_{Di}^2 + (E_1E_2 + E_2E_3 + E_3E_1 - 4n\hbar^2f^2 - n\hbar^2g^2)E_{Di} \\ + (-E_1E_2E_3 + 4n\hbar^2f^2E_1 + n\hbar^2g^2E_3) = 0\,, \end{aligned} \tag{2.144}$$

and has the general form

$$y^3 + py^2 + qy + r = 0\,, \tag{2.145}$$

where $y = E_{Di}$ and the coefficients are

$$p \equiv -(E_1+E_2+E_3) \tag{2.146}$$

$$q \equiv (E_1E_2 + E_2E_3 + E_3E_1 - 4n\hbar^2f^2 - n\hbar^2g^2) \tag{2.147}$$

$$r \equiv (-E_1E_2E_3 + 4n\hbar^2f^2E_1 + n\hbar^2g^2E_3)\,. \tag{2.148}$$

Upon the substitution $y = x + p/3$, the equation reduces to

$$x^3 + ax + b = 0\,, \tag{2.149}$$

where the coefficients are

$$
\begin{aligned}
a &= \frac{1}{3}(3q - p^2) \\
&= (E_1E_2 + E_2E_3 + E_3E_1 - 4n\hbar^2 f^2 - n\hbar^2 g^2) - \frac{1}{3}(E_1 + E_2 + E_3)^2
\end{aligned} \tag{2.150}
$$

and

$$
\begin{aligned}
b =& \frac{1}{27}(2p^3 + 27r - 9pq) \\
=& -\frac{2}{27}(E_1 + E_2 + E_3)^3 + (-E_1E_2E_3 + 4n\hbar^2 f^2 E_1 + n\hbar^2 g^2 E_3) \\
&+ \frac{1}{3}(E_1 + E_2 + E_3)(E_1E_2 + E_2E_3 + E_3E_1 - 4n\hbar^2 f^2 - n\hbar^2 g^2) \, .
\end{aligned} \tag{2.151}
$$

There are a handful of methods for solving Eq. (2.149), though one simple solution is in the case of three real and unequal roots. This solution is obtained via a trigonometric method, whereby the cubic equation

$$
x^3 + ax + b = 0 \tag{2.152}
$$

is transformed into

$$
u^3 \cos^3\varphi + au\cos\varphi + b = 0 \tag{2.153}
$$

when x is replaced with $u\cos\varphi$. The goal is to make Eq. (2.153) take the form of the trigonometric identity

$$
4\cos^3\varphi - 3\cos\varphi - \cos 3\varphi = 0 \, , \tag{2.154}
$$

which is known as the triple angle formula. Choosing $u = 2\sqrt{-a/3}$ and dividing Eq. (2.153) by $u^3/4$ we get

$$
4\cos^3\varphi - 3\cos\varphi - \frac{3b}{2a}\sqrt{\frac{-3}{a}} = 0 \, . \tag{2.155}
$$

Combining with the identity from Eq. (2.154), we get

$$
\cos 3\varphi = \frac{3b}{2a}\sqrt{\frac{-3}{a}} \tag{2.156}
$$

and so the roots of the cubic polynomial are

$$x_k = 2\sqrt{-\frac{a}{3}}\cos\left[\frac{1}{3}\cos^{-1}\left(\frac{3b}{2a}\sqrt{-\frac{3}{a}}\right) - k\frac{2\pi}{3}\right] \tag{2.157}$$

for $k = 0, 1, 2$, or equivalently

$$x_k = 2\sqrt{-\frac{a}{3}}\cos\left(\varphi - k\frac{2\pi}{3}\right), \tag{2.158}$$

where

$$\varphi = \frac{1}{3}\cos^{-1}\left(\frac{3b}{2a}\sqrt{\frac{-3}{a}}\right) . \tag{2.159}$$

Hence, the analytic solutions for the doubly-dressed system are therefore

$$\begin{aligned} E_{D1} &= 2\sqrt{-\frac{a}{3}}\cos\left(\varphi - \frac{4\pi}{3}\right) + \frac{1}{3}(E_1 + E_2 + E_3) \\ E_{D2} &= 2\sqrt{-\frac{a}{3}}\cos\left(\varphi - \frac{2\pi}{3}\right) + \frac{1}{3}(E_1 + E_2 + E_3) \\ E_{D3} &= 2\sqrt{-\frac{a}{3}}\cos\left(\varphi\right) + \frac{1}{3}(E_1 + E_2 + E_3) , \end{aligned} \tag{2.160}$$

where the subscript labeling is chosen so that E_{D1} and E_{D2} reduce to the eigenenergies of the singly-dressed atom (i.e. E_{D-} and E_{D+}, respectively) and E_{D3} is only coupled when the magnetic contribution is considered.

2.3.2.2 Finding eigenvectors

We seek to determine eigenvectors $|D_i(n)\rangle$ which satisfy the equation $(H - E_{Di}I)\,|D_i(n)\rangle = 0$, where $i = 1, 2, 3$ and have the form

$$|D_i(n)\rangle = a_i\,|1\rangle + b_i\,|2\rangle + c_i\,|3\rangle \ . \tag{2.161}$$

We require that coefficients a_i, b_i, c_i satisfy the standard normalization condition

$$1 = |a_i|^2 + |b_i|^2 + |c_i|^2 . \tag{2.162}$$

Of course, the standard way of determining the new eigenvectors is to write out the the explicit formula

$$\begin{pmatrix} E_3 - E_{Di} & 2\hbar f\sqrt{n} & 0 \\ 2\hbar f\sqrt{n} & E_2 - E_{Di} & \hbar g\sqrt{n} \\ 0 & \hbar g\sqrt{n} & E_1 - E_{Di} \end{pmatrix} \begin{pmatrix} a_i \\ b_i \\ c_i \end{pmatrix} = \begin{pmatrix} 0 \\ 0 \\ 0 \end{pmatrix} , \tag{2.163}$$

and do the matrix multiplication on the LHS and then solve for values of a_i, b_i, and c_i which satisfy the condition on the RHS for each of the three eigenenergies. However, because of the complexity of the cubic roots, it is more convenient to write the solution down in a more general form which is expressed in terms of the dressed state energies, bare state energies, and coupling strengths. Here the eigenvectors may be expressed in the form

$$\begin{aligned} |D_i(n)\rangle = \frac{1}{\Xi_i} \Bigg\{ \left[\frac{(E_{Di} - E_2)}{\hbar g\sqrt{n}} - \frac{4\hbar f^2\sqrt{n}}{g(E_{Di} - E_3)} \right] |1\rangle \\ +(1)\,|2\rangle + \frac{2\hbar f\sqrt{n}}{(E_{Di} - E_3)}\,|3\rangle \Bigg\} , \end{aligned} \tag{2.164}$$

where the normalization factor Ξ_i is given as the unitless quantity

$$\Xi_i = \sqrt{\left(\frac{(E_{Di} - E_2)}{\hbar g\sqrt{n}} - \frac{4\hbar f^2\sqrt{n}}{g(E_{Di} - E_3)} \right)^2 + 1^2 + \left(\frac{2\hbar f\sqrt{n}}{(E_{Di} - E_3)} \right)^2} . \tag{2.165}$$

The state coefficients a_i, b_i, and c_i are of course

$$a_i = \frac{1}{\Xi_i} \left[\frac{(E_{Di} - E_2)}{\hbar g\sqrt{n}} - \frac{4\hbar f^2\sqrt{n}}{g(E_{Di} - E_3)} \right] , \tag{2.166}$$

$$b_i = \frac{1}{\Xi_i} , \tag{2.167}$$

$$c_i = \frac{1}{\Xi_i} \left[\frac{2\hbar f\sqrt{n}}{(E_{Di} - E_3)} \right] . \tag{2.168}$$

We note here that in the limit that the magnetic coupling term is taken to zero (i.e. $f \longrightarrow 0$), the eigenvector solution is reduced to that of the singly-dressed state. In other words, an identical solution can be written down for the singly-dressed case which is in agreement with what we have derived here but for $f = 0$.

2.3.3 Evaluation of induced dipole moments

Given that we now have a way of obtaining solutions for the dressed state coefficients a_i, b_i, and c_i, we may proceed to calculate the nonzero electric and magnetic dipole moments that arise between the mixed states of the driven system. As shown in Fig. 2.13 there are only three moments which arise in the simplified basis: a linear electric moment at ω, a quadratic electric moment at 0-frequency, and a nonlinear magnetic moment at ω.

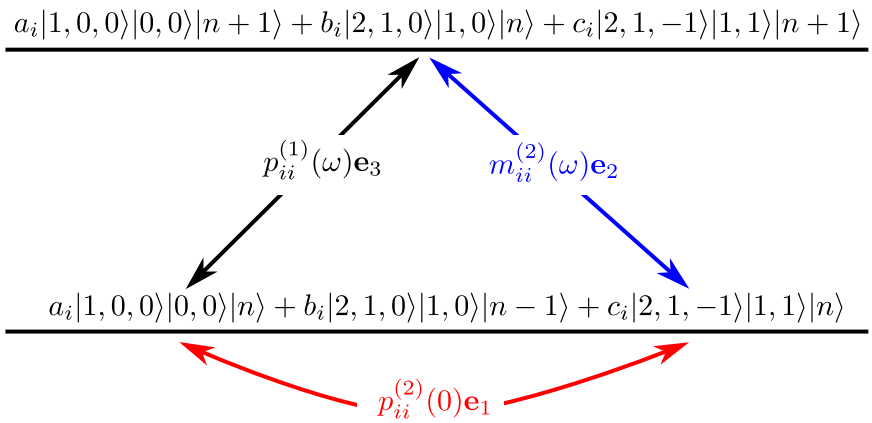

Figure 2.13: Induced electric and magnetic dipole moments between dressed states of the driven molecular system. The induced nonlinear electric moment is shown by the red curved arrow and the induced nonlinear magnetic moment is shown by the blue straight arrow.

The linear electric moment is of course

$$\begin{aligned}\left\langle \hat{p}_{ii}^{(1)}(\omega) \right\rangle &= \langle D_i(n+1)|\, e\hat{r}\, |D_i(n)\rangle + h.c. \\ &= a_i b_i^* \langle n| \langle 1,0| \langle 2,1,0|\, e\hat{r}\, |1,0,0\rangle |0,0\rangle |n\rangle + h.c. \\ &= \mu_\ell^{(e)} \left(a_i b_i^* + c.c.\right) \mathbf{e}_3 \,, \end{aligned} \tag{2.169}$$

which is the same as we had in the atomic system. There is also a zero-frequency moment which arises within each individual dressed state. We see

$$\begin{aligned}\left\langle \hat{p}_{ii}^{(2)}(0)\right\rangle &= \langle D_i(n)|\, e\hat{r}\, |D_i(n)\rangle + h.c. \\ &= (a_i c_i^* \langle n| \langle 1,1| \langle 2,1,-1|\, e\hat{r}\, |1,0,0\rangle |0,0\rangle |n\rangle + \\ &\quad a_i^* c_i \langle n| \langle 0,0| \langle 1,0,0|\, e\hat{r}\, |2,1,-1\rangle |1,1\rangle |n\rangle) + h.c. \\ &= \mu_\ell^{(e)} \left\{ \left[a_i c_i^* \frac{1}{\sqrt{2}} (\mathbf{e}_1 + i\mathbf{e}_2) + a_i^* c_i \frac{1}{\sqrt{2}} (\mathbf{e}_1 - i\mathbf{e}_2) \right] + c.c. \right\} \\ &= \frac{2\mu_\ell^{(e)}}{\sqrt{2}} (a_i c_i^* + c.c.)\, \mathbf{e}_1 \,, \end{aligned} \tag{2.170}$$

where we have used the fact that

$$\langle 1,1| \langle 2,1,-1|\, e\hat{r}\, |1,0,0\rangle |0,0\rangle = \mu_\ell^{(e)} \frac{1}{\sqrt{2}} (\mathbf{e}_1 + i\mathbf{e}_2) \ . \tag{2.171}$$

As promised in the previous section, here we provide further details on the analysis of the induced magnetization terms. The magnetic dipole moments considered here involve motion initiated by the electric field that is then deflected by the magnetic field. The expectation value of the magnetization is therefore expected to be proportional to the electric field polarization, as was the case for the atomic system described earlier. There are again two contributions to the nonlinear magnetic moments. The first originates in second-order as the $\mathbf{e}_2$-directed projection of a mixed magneto-electric moment and the second originates as a third-order purely magnetic moment. We can identify these two contributions to the magnetic moment by examining the trace elements of the magneto-electric moment $\mu^{(me)}$ (or the direct magnetic moment $\mu^{(m)}$) with the slowly-varying amplitude of the density matrix $\tilde{\rho}$.

The contribution to the magnetic moment which is second-order is given by,

$$\begin{aligned}\left\langle \hat{m}^{(2)}\right\rangle &= \text{Tr}\left(\mu^{(me)}, \tilde{\rho}\right) \\ &= \left(\mu_{21}^{(me)} \tilde{\rho}_{12}^{(2)} + \mu_{31}^{(me)} \tilde{\rho}_{13}^{(2)} + \mu_{32}^{(me)} \tilde{\rho}_{32}^{(2)}\right) + c.c. \,. \end{aligned} \tag{2.172}$$

Now the 2-photon magneto-electric moment is non-vanishing only between states $|1\rangle$ and $|3\rangle$. These states are connected by the sequence of an electric dipole transition between states $|1\rangle$ and $|2\rangle$ followed by a magnetic dipole transition between states $|2\rangle$ and $|3\rangle$. Therefore, in the above we see that $\mu_{21}^{(me)} = \mu_{32}^{(me)} = 0$, leaving only

$$\left\langle \hat{m}^{(2)}\right\rangle = \mu_{31}^{(me)} \tilde{\rho}_{13}^{(2)} + c.c. \,. \tag{2.173}$$

The solution for the off-diagonal density matrix element is

$$\tilde{\rho}_{13}^{(2)} = \frac{\tilde{\rho}_{12}^{(1)}\tilde{V}_{23}^{(1)}}{\Delta_{13} + i\Gamma_{13}} \,, \tag{2.174}$$

where $\Delta_{13} \equiv (\omega_1 - \omega_3) - \omega$. The correspondence between density matrix elements and mixing coefficients in the dressed state picture is

$$\tilde{\rho}_{12}^{(1)} \longleftrightarrow a_i b_i^* \tag{2.175}$$

and

$$\frac{\tilde{\rho}_{12}^{(1)}\tilde{V}_{23}^{(1)}}{\Delta_{13} + i\Gamma_{13}} \longleftrightarrow \langle D_i(n)| \, \mu_{21}^{(e)} \mu_{eff}^{(m)} \hat{L}'_{-} \hat{O}'_{+} \hat{\sigma}_{+} \, |D_i(n)\rangle \ . \tag{2.176}$$

Although $\tilde{\rho}_{13}^{(2)}$ is a second-order coherence with no time dependence, the act of projecting out the component along $\mathbf{e}_2$ with an analyzer (as described in Chapter 3) restores the time dependence of the magnetic quadrature of the 2-photon moment. The moment then evaluates to

$$\begin{aligned} \left\langle \hat{m}^{(2)} \right\rangle &= \left(a_i b_i \, \langle D_i(n)| \, \mu_{21}^{(e)} \mu_{eff}^{(m)} \hat{L}'_{-} \hat{O}'_{+} \hat{\sigma}_{+} \, |D_i(n)\rangle + h.c. \right)_{\mathbf{e}_2} \\ &= a_i b_i^* \, \langle n| \, \langle 1,1| \, \langle 2,1,-1| \, c_i^* \mu_{eff}^{(m)} \hat{L}'_{-} \hat{O}'_{+} b_i \, |2,1,0\rangle \, |1,0\rangle \, |n\rangle + h.c. \\ &= 2\mu_{eff}^{(m)} \left(a_i b_i^* b_i c_i^* + c.c. \right) \ . \end{aligned} \tag{2.177}$$

The additional contribution to the magnetization arises from the third-order terms in the expectation value. In this case, a pure 1-photon magnetic dipole moment is $\mu^{(m)}$ is considered,

$$\left\langle \hat{m}^{(3)} \right\rangle = \left(\mu_{21}^{(m)} \tilde{\rho}_{12}^{(3)} + \mu_{31}^{(m)} \tilde{\rho}_{13}^{(3)} + \mu_{32}^{(m)} \tilde{\rho}_{23}^{(3)} \right) + c.c. \ . \tag{2.178}$$

The solution for the off-diagonal density matrix element in this case is

$$\tilde{\rho}_{23}^{(3)} = \frac{\tilde{V}_{21}^{(1)}\tilde{\rho}_{13}^{(2)}}{\Delta_{23} + i\Gamma_{23}} \,, \tag{2.179}$$

where $\Delta_{23} \equiv (\omega_2 - \omega_3) - \omega$. In the above, $\mu_{21}^{(m)} = 0$ and $\mu_{31}^{(m)} = 0$ since there is no direct magnetic coupling between state $|1\rangle$ and states $|2\rangle$ or $|3\rangle$. Here the magnetic moment forms on a separate 1-photon transition in third-order and we have the following correspondence between density matrix and dressed state picture,

$$\tilde{\rho}_{13}^{(2)} \longleftrightarrow a_i c_i^* \tag{2.180}$$

and

$$\frac{\tilde{V}_{21}^{(1)}\tilde{\rho}_{13}^{(2)}}{\Delta_{23}+i\Gamma_{23}} \longleftrightarrow \langle D_i(n)|\, \mu_{21}^{(e)} 2\mu_{eff}^{(m)}\hat{\sigma}_+ \,|D_i(n)\rangle \ . \tag{2.181}$$

One finds that

$$\begin{aligned}\left\langle \hat{m}^{(3)} \right\rangle &= \left(a_i c_i^* \,\langle D_i(n)|\, \mu_{21}^{(e)} 2\mu_{eff}^{(m)}\hat{\sigma}_+ \,|D_i(n)\rangle + h.c. \right)_{\mathbf{e}_2} \\ &= 2a_i c_i^* \,\langle n|\,\langle 2,1,0|\, b_i^* \mu_{eff}^{(m)}\hat{\sigma}_+ a_i \,|1,0,0\rangle\,|0,0\rangle\,|n\rangle + h.c. \\ &= 2\mu_{eff}^{(m)}\left(a_i^* b_i a_i c_i^* + c.c.\right) \ . \end{aligned} \tag{2.182}$$

The total magnetic moment is the sum of these two moments which are both at the oscillation frequency ω and are both oriented along $\mathbf{e}_2$. Since the leading behavior is quadratic, the total magnetic moment for individual dressed state indices will be represented as

$$\left\langle \hat{m}_{ii}^{(2)}(\omega) \right\rangle = 2\mu_{eff}^{(m)}\left[a_i b_i^*\left(b_i c_i^* + a_i c_i^*\right) + c.c.\right]\mathbf{e}_2 \ . \tag{2.183}$$

Once again, the incoherent sum must be taken for each of the induced effects to give the net measurable moment. The linear electric is the same as defined in previous sections. We have for the 0-frequency electric moment,

$$\left|\hat{p}_{net}^{(2)}(0)\right| = \frac{2\mu_\ell^{(e)}}{\sqrt{2}}\left[\sum_{i=1}^{3}\left|\left(a_i c_i^* + c.c.\right)\right|^2\right]^{1/2} \tag{2.184}$$

and for the quadratic magnetic moment

$$\left|\hat{m}_{net}^{(2)}(\omega)\right| = 2\mu_{eff}^{(m)}\left\{\sum_{i=1}^{3}\left|\left[a_i b_i^*\left(b_i c_i^* + a_i c_i^*\right) + c.c.\right]\right|^2\right\}^{1/2} \ . \tag{2.185}$$

When the magnetization is evaluated numerically, the value of the effective magnetic moment reference value may be replaced according to $\mu_{eff}^{(m)} = c\mu_\ell^{(e)}$. This value is twice the upper bound on $\mu_{eff}^{(m)}$ derivable from Faraday's law for a single component of angular momentum [2]. This represents a *limitation* on the maximum magnetic value which may be achieved using the dressed-state analysis.

2.3.4 Magnetic torque dynamics

Because torque is the mechanism which is responsible for coupling the ground state to the rotationally-excited molecular state, it is worthwhile to consider the time required for this process to go to completion. During the B^* transition in which the magnetic interaction is applied, the principal quantum number changes due to magnetic torque,

$$\left\langle \hat{T} \right\rangle = \left\langle \frac{d\hat{L}}{dt} \right\rangle = \frac{i}{\hbar} \left\langle \left[\hat{H}_{int}^{(m)}, \hat{L} \right] \right\rangle \ , \tag{2.186}$$

transferring all orbital angular momentum of the excited state into rotational motion. The expectation value of the torque is

$$\begin{aligned} \left\langle \hat{T} \right\rangle &= i\hbar \mathbf{e}_3 \tilde{\rho}_{32} \left\langle 1,0 \right| \left\langle 2,1,0 \right| f \hat{L}'_+ \hat{O}'_- \left| 2,1,-1 \right\rangle \left| 1,1 \right\rangle + h.c. \\ &= 2i\hbar \mathbf{e}_3 f \tilde{\rho}_{32} + c.c. \ , \end{aligned} \tag{2.187}$$

and in the high-intensity limit, the coherence evaluates as $\tilde{\rho}_{32} \approx 1$ and so $|\langle \hat{T} \rangle| \approx \hbar f$ is the total amount of torque exerted about an axis perpendicular to the molecule over some time. Since there are no atoms on the internuclear axis in the diatomic model, the orbital angular momentum $\hat{L}$ and its kinetic energy $L^2/2\mu$ are clearly exchanged for end-over-end rotation of the molecule with energy $O^2/2I$. The speed of transfer can be estimated by finding the time interval τ necessary for m_ℓ to change by unity. From Eq. (2.186) we see

$$\tau = \frac{\hbar c}{\mu_{eff}^{(m)} B} \ . \tag{2.188}$$

Using $\mu_{eff}^{(m)} = c\mu_\ell^{(e)}$ and assuming a field strength of $E \approx 10^8$ W/cm^2 as such is used in our experiments, we find

$$\tau = \frac{\hbar}{\mu_\ell^{(e)} E} \approx 125 \text{ fs} \ . \tag{2.189}$$

This calculation shows that the torque mechanism is an ultrafast process and goes to completion for typical field strengths and pulse durations of our experiments, as will be described in the following chapter.

CHAPTER 3

Methods for Measuring Magnetic Dipole Scattering

This chapter outlines the methods used for measuring induced second-order ME magnetization. The experimental approach described herein is a straight-forward extension to the methods described in Section 1.4 that were used in the initial scattering experiments. This approach improves on the initial experimental methods in several ways. For one, complete automation of the rotation stages and light detection instruments was implemented which allowed for the experiment to be run without the need for the experimenter to be present in the lab. Automation of the experiment also allowed for longer count periods, which provided better signal averaging as well as the ability to map out full angular patterns of the detected signal for each input intensity point. The focusing lenses before the sample were also removed and replaced with a beam expander to allow for easier alignment and a more homogeneous beam cross-section. A dispersion compensation unit was also introduced which provided a consistent method for achieving transform-limited pulses at the interaction point of the sample as well as a method for keeping track of the pulse duration. A "light-tight" box was built to isolate the detector from ambient light and a thermo-electrically cooled photomultiplier tube was used in place of the less sensitive detectors used in earlier experiments.

As was previously described in Chapter 1, this experiment aims to measure the relative amplitudes of the induced electric and magnetic dipole moments in a dielectric material. In this experiment, pulsed light of moderate optical intensity (of the order 10^8 W/cm^2) is incident on either the sample cell or sample volume and scattered light is collected at 90° relative to the path of the input light. The 90° geometry is a fundamental feature of this experiment since only at this angle is it possible to distinguish between induced electric and magnetic moments; electric and magnetic dipole moments are indistinguishable in the forward direction. This fact is apparent in Fig. 3.1, where we note that if the incident electric (magnetic) field is oriented vertically, then the induced electric (magnetic) dipole

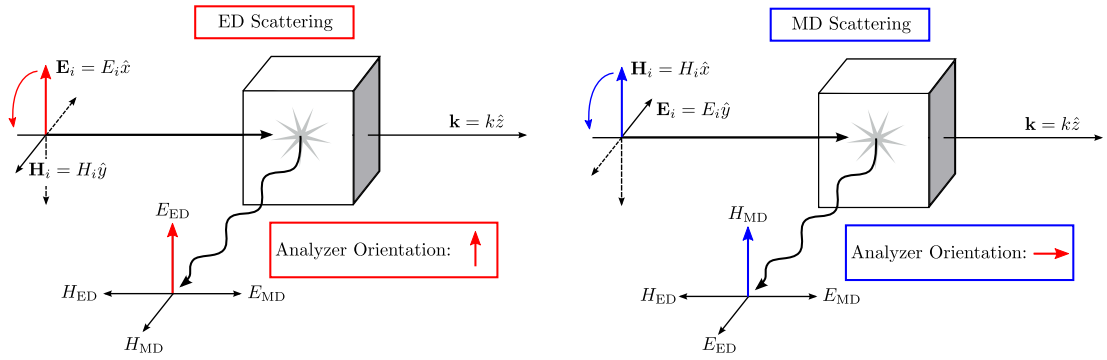

(a) Electric scattering (b) Magnetic scattering

Figure 3.1: Schematic for (a) electric and (b) magnetic dipole scattering. For the ED (MD) scattering, the initial incident electric (magnetic) field is oriented along $\hat{x}$ and the input polarization is rotated through 2π to map out the scattered light intensity. To measure ED (MD) scattering, the analyzer is fixed along $\hat{x}$ ($\hat{z}$).

will also be oriented vertically. Then a measurement of the electrically (magnetically) scattered light requires the analyzer to be oriented vertically (horizontally) in order to pass the electric component of the scattered field. When the analyzer is vertical it measures electric dipole radiation and when horizontal it measures magnetic dipole radiation. Rotating the input field using a $\lambda/2$ plate allows for the construction of "dipole radiation patterns" which describe the angular dependence of the input signal.

For the remainder of this chapter we discuss the experimental design, the methods for data collection and analysis, and the sample selection and preparation. The first section describes the components used in the experimental approach and how they were assembled into a system. This section also includes a description of the alignment procedure as well as an overview of the detection scheme used for measuring the scattered light. We then describe the approach used for collecting and analyzing data, including how the signals were measured and stored as data arrays and how these files were processed to extract physically significant parameters. We conclude with a discussion of the selection procedure for the molecular liquids and crystalline solids that were measured in this experiment. This includes a description of procedures for cleaning, storing, and handling the molecular liquids.

3.1 Experimental design

Figure 3.2 is a schematic which shows the experimental approach. The incident laser light is the pulsed output from a linearly-polarized, chirp-pulse amplified (CPA) Clark-MXR CPA-2001 system. This system has a repetition rate of 1 kHz, average power 800 mW,

center wavelength 775 nm, and FWHM bandwidth of 5 nm. The output from the laser is directed into the dispersion compensation box before traveling through a series of optical components which either control or monitor the light in some way. A $\lambda/2$ plate is used in combination with a 10^5:1 quartz polarizer to control the input optical intensity as well as reject any light polarized orthogonal to the transmission axis (this extinguishes orthogonal polarizations to 1 part in 10^5). A non-polarizing 70:30 (T:R) beam splitter is used to send 30% of the input beam to a Thor Labs S401C thermal power meter which monitors the laser power as a function of time and provides a method for obtaining an average power value. A temporary flip mirror is used to direct the light into the dispersion feedback loop (explained in detail in a later subsection). A second $\lambda/2$ plate controls the orientation of the input optical field before the beam is expanded using a $3\times$ telescope. The full $1/e^2$ width of the beam is measured to be 21 mm $\times$ 16 mm (width $\times$ height) after the telescope and a pinhole centered on the beam and set to a diameter of 3.5 mm is used to aperture the beam. This creates an approximate "flat-top" beam before the sample, in which the variation from the middle of the beam to the edges is no more than 5% of the total beam power, as is explained in Appendix F.

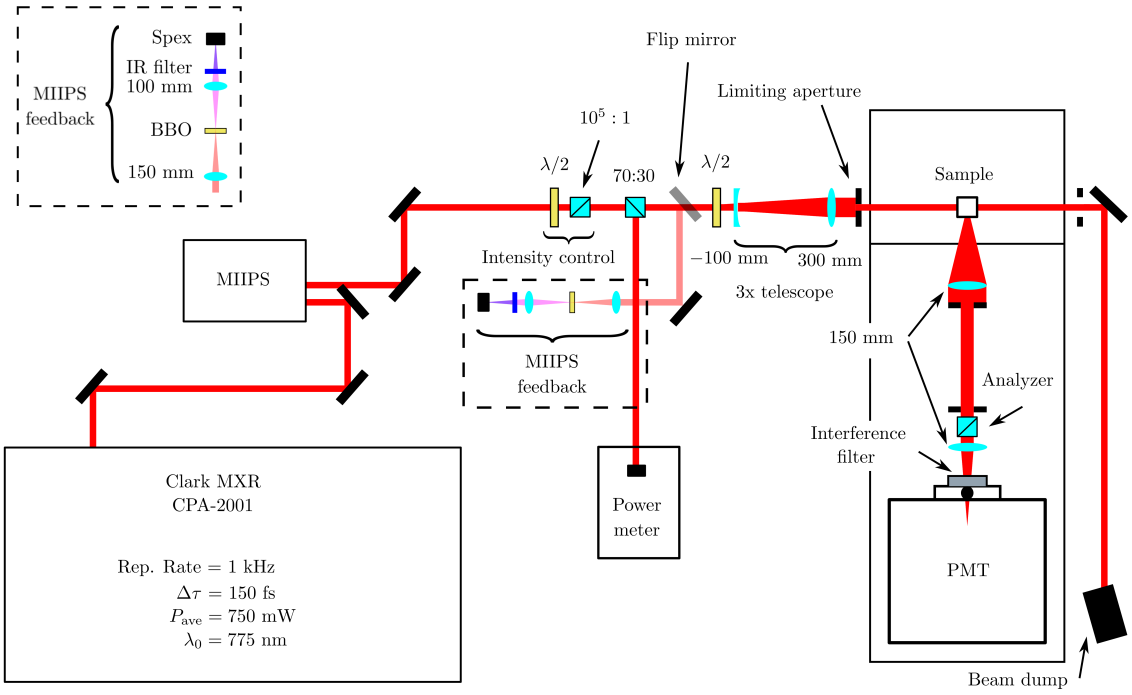

Figure 3.2: Schematic showing the footprint of the experimental scattering setup. The black dashed inset box shows the components of the MIIPS feedback loop.

After being apertured, the laser enters a light-tight box through a 1/2" diameter hole. The box has removable sides and a lid constructed of plywood which have been painted

with a flat black paint to aid in light absorption. During experiments a black tarp is draped over the entire box in order to further reduce the amount of ambient light which may otherwise enter the box during signal detection. Inside the box, the light is incident on the sample and is allowed to pass through the length of either the cuvette cell or bulk crystal before exiting the box through a second 1/2" hole. This light is then sent to a beam dump which is angled off-axis relative to the beam path in order to minimize reflections back into the detection box. As a further redundancy to prevent ambient light from entering the detector, a custom-built filter mount was used to attach the interference filter directly to the face of the detector. Given these measures, the photons counted with the detector shutter closed versus open (laser off) were indistinguishable at about 3-5 counts/s.

The scattered light is collected into a cooled photomultiplier tube (PMT) at 90° relative to the input beam line using a 1:1 imaging system consisting of two 150 mm lenses, two pinholes, a quartz analyzer, and an interference filter. The pinholes were both apertured to 3.5 mm in order to exclude the amount of out-of-plane polarized light to below 1% (see Appendix C). Alignment of the collection optics relative to the input beam is critical to ensure that any out-of-plane electric signal is sufficiently attenuated. This is achieved by first establishing orthogonal beam paths for the input beam and collection beam over the lengths of the table using only turning mirrors and standard alignment techniques. The technique used here consisted of using a beam height tool which could be secured in any two adjacent 1/4"-20 holes of the optical table to either align the beam directly over a set of holes or directly in between a set of holes. The orientation of each turning mirror was checked using the alignment tool at three locations: near the mirror, as far from the mirror as possible given the available table space, and at a location in between. The placement of each mirror was used to adjust the nearby alignment and the mirror tilt was used for the far alignment. Once a particular beam path was established, alignment pinholes with 1" diameter were placed in the beam line and were centered using a Thor Labs CCD beam camera. This provided a consistent method of checking the beam alignment during everyday use.

Alignment of the input probe laser was achieved by attenuating the beam to an eye-safe level and using index cards or fluorescent infrared cards and the Thor Labs CCD camera. All of the turning mirrors for the amplified pulses were anti-reflection coated dielectric mirrors from Newport. The beam path for the collection optics was aligned using a 5 mW HeNe laser and metallic turning mirrors following the same procedure described above. This method achieved two well-defined beam paths whose orthogonality was dependent on the precision of the holes of the optical table. A precision right-angle prism was placed at the interaction point of the sample in order to obtain a more definitive measure of the orthogonality of the two beams. With the prism, the orthogonality of the two beams could

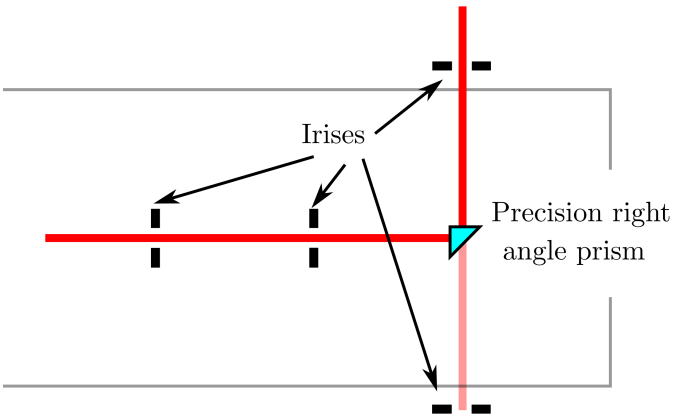

Figure 3.3: Depiction of alignment check using precision right angle prism to confirm orthogonality of pump beam and collection optics.

be defined to within 3 arcmin. The prism was aligned such that the incident light from the CPA system was deflected at a right angle through the pinholes that established the collection optics while the back reflection from the entrance face of the prism was simultaneously aligned back through the pinholes which established the probe beam path. This is depicted in Fig. 3.3. Placement of the prism on a 3D translation stage plus goniometer allowed for all necessary adjustments. This check was performed whenever any change in the alignment of the system was made. It is worth noting that this check could have also been done using the HeNe beam. The only difference is that the deflected light from the HeNe must be aligned back through the pinholes which establish the pump beam path while then the back reflection from the entrance surface of the prism is simultaneously aligned back through the HeNe optics.

Only after establishing and aligning the two beam paths were the other optical components added into the probe and collection beam lines. Alignment of each component was checked by aligning the back-reflected light while minimizing the deflection of the center of the beam in the forward direction. The forwardly-deflected light was monitored with the CCD placed directly behind a slightly-closed and aligned pinhole. Adjustment of the $3\times$ telescope was performed by placing the 300 mm lens on a translation stage and minimizing the beam divergence over a distance of approximately 1 m. Alignment of the collection optics was achieved by simulating diffusely-scattered light at the interaction plane of the sample. This was done by passing the HeNe laser through a thin diffuser[1] placed along the plane bisecting the input probe beam. The first 150 mm lens was positioned on a translation stage and the collimation was checked by placing a mirror after the lens to retro-reflect the

[1]For this, several layers of frosted Scotch tape were used.

collimated beam back through the lens and focus it onto the diffuser. The second lens in the imaging system was positioned such that its focal plane was coincident with the position of the detector cathode.

3.1.1 Dispersion compensation using MIIPS

Providing a way to pre-compensate for dispersive elements in an optical system is useful in that it allows one to deliver transform-limited pulses to the interaction region of the sample. This not only allows the experimenter to maintain the peak intensity of ultrashort pulses, but it allows for an accurate and reproducible method by which the pulse duration may be measured before each experimental run without needing an autocorrelator. Our experiment used a multiphoton intrapulse interference phase scan (MIIPS)-HD system from Biophotonics, Inc. to compress the output pulses from the Clark-MXR laser system.

The MIIPS system consists of only a few optical components (some mirrors, a diffraction grating, a cylindrical lens, and a spatial light modulator (SLM)) and a compression algorithm that retrieves spectral information from a second-harmonic (SH) signal. The basic operating procedure of the system is relatively straight-forward. Light enters the MIIPS box and is guided toward a diffraction grating using a series of metallic turning mirrors. After reflecting off the grating, the spectral components of the pulse are angularly distributed in space. The cylindrical lens then collimates the light and directs it toward the surface of the SLM, which is used to impart nonlinear phase corrections to the individual spectral components of the pulse. This is achieved by applying a desired voltage to a given pixel in the crystal which in turn causes local deformations on the surface of the SLM due to electrostriction. Since the spectral components are distributed over the length of the SLM, a "best-compressed" voltage mask is determined using an iterative algorithm in LabVIEW which uses spectral information retrieved from the SH signal.

The SH signal is generated by focusing the light into a Beta Barium Borate (BBO) crystal and then filtering and directing this light into a fiber-coupled Ocean Optics spectrometer (see inset in Fig. 3.2). Our experimental approach used a temporary turning mirror (see Fig. 3.2 above) to direct this light out of the main beam path. Once the SH spectrum is fed into the spectrometer, the compression algorithm is run for 6 iterations until convergence to a best-compressed value of the pulse is achieved. All of the pulse shaping is achieved by altering the pixels of the liquid crystal modulator to impart some specific phase on each wavelength component. In other words, this yields a best-fit phase mask which is maintained on the face of the SLM so long as it remains powered up. The flip mirror can then be removed from the beam line and the compressed pulse travels to the sample.

A typical compression from this device will yield pulse durations of the order 150 fs full-width at half-max (FWHM). However, a measurement using the built-in autocorrelator function of the MIIPS box shows that the actual pulse duration is typically closer to 180 fs. Regardless of this, the temporal width used in data analysis was always taken as the compressed pulse width, not the measured value from the built-in autocorrelator. The MIIPS system was run whenever the laser was turned on or whenever the laser output was optimized or adjusted. This is because the phase mask on the SLM for optimal compression will be different if there are any shifts in the laser spectrum.

3.1.2 Interference filter

A narrowband filter was used in the detection arm of the apparatus to select light in a narrow band centered on the fundamental frequency of the laser. Our experiments used a 780 nm filter with a passband of 5 nm tilted at an angle of 14° relative to the input beam path. An interference filter consists of a stack of multiple layers of dielectric material with varying refractive indices. The multilayer design allows one to engineer the filter such that only select frequency bands are transmitted, while all others are reflected. These filters are designed for normal incidence but the central passband can be effectively tuned lower if the angle of incidence is increased from zero. The tilt angle of 14° was tested and found to transmit light centered on the central laser wavelength of 775 nm.

Figure 3.4 shows the transmission of the interference filter at normal incidence (blue dashed curve) centered at 780 nm and a predicted shift in transmission centered on 775 nm (solid blue curve). The transmission peak of the interference filter is about 50%. Here the red curve represents an approximation to the Clark-MXR laser which is just a normalized Gaussian curve with a FWHM of 5 nm centered at 775 nm. The light reaching the detector is a product of the blue and red curves, so unless the filter passband and laser bandwidth are lined up, only a portion of the scattered light will be detected. This was confirmed in two experimental runs of scattering in the liquid sample CCl_4. There was an increase in signal of about 160% when the filter was tilted. Overlapping the two spectra is also important so that vibrational Raman scattering is not detected.

A filter mount was machined out of a 1.25" diameter aluminum rod cut to a length of 1.25". The front and back surfaces of the rod were faced off using the lathe and one side of the rod was turned down to a diameter of 1.00". This lower diameter went only to a depth of 0.75", leaving 0.50" still at the original 1.25" diameter. The rod was then fixed in place at 14° relative to normal and a 1.00" diameter hole was milled into the side of the rod with the 1.25" diameter. This hole was meant to hold the interference filter in place. A drilled

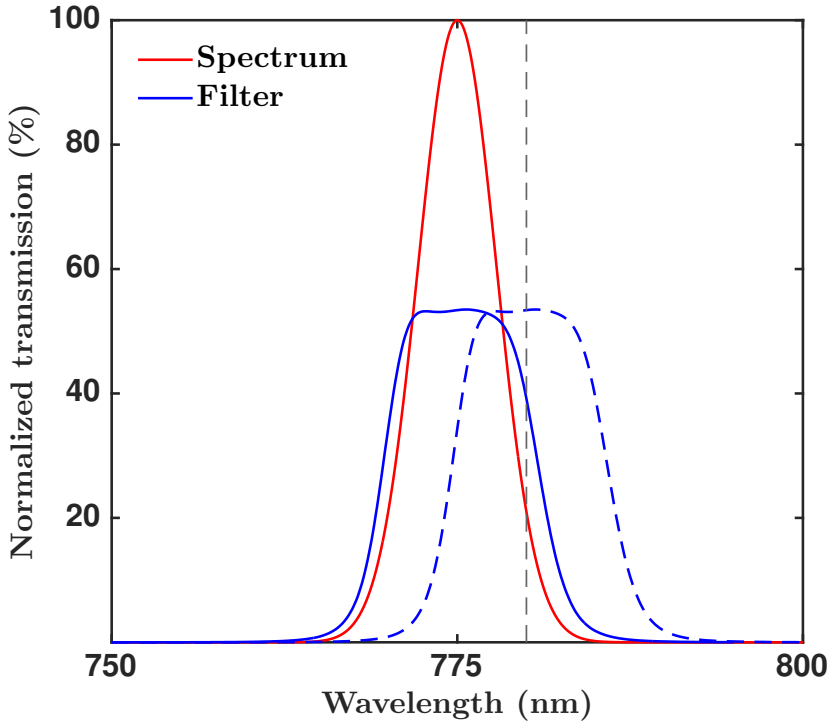

Figure 3.4: Plot showing the interference filter transmission as a function of laser wavelength overlaid with a Gaussian curve of 5 nm bandwidth to approximate the laser spectrum. The dashed blue curve represents the filter transmission at normal incidence, which is centered at 780 nm (depicted by dashed grey curve). The solid blue curve represents the estimated shift in the filter transmission when tilted at 14° incidence.

and tapped hole on the edge of the mount was used to keep the filter from moving. A hole of approximately 0.50" diameter was drilled through the entire rod to allow light to pass through. This fixture was then mounted to the face of the PMT.

3.1.3 Signal detection using photomultiplier tube

A thermo-electrically cooled PMT was used to detect light at the single-photon level. This sensitive detection scheme was required due to the low cross-section for incoherent scattering at 90°. A PMT works by converting a signal photon into an electrical signal which is then amplified via reflection off several dynodes arranged in a cascade-like fashion. Here an incoming photon is incident on the cathode and ejects a single electron due to the photoelectric effect. The electrons are then directed through the amplification stage after which the signal reaches the anode and is large enough to be detected by an electronic circuit. The cathode, dynodes, and anode are arranged in a vacuum tube in which each subsequent

electrode is maintained at a pre-determined potential. A discriminator voltage is set so that counts from the cathode which have the amplitude of single-photon events are transmitted and lower amplitude events due to $1/f$ noise are filtered out. Thermo-electric cooling of the device further reduces unwanted signals at the detection anode.

Alignment of the PMT required both transverse and longitudinal measurements of the cathode position. This was to ensure that the cathode was centered on the optical beam line and that the imaging optics focused the light onto the cathode. The position of the cathode along the optical axis was determined by removing the tube and physically measuring its location relative to its housing. The focusing lens from the collection optics was then placed such that its focal plane was coincident with the plane of the cathode. The PMT was then affixed to a machined translation stage which allowed for the device to be adjusted horizontally and vertically in a plane perpendicular to the beam path of the collected light. Alignment of the cathode in the beam path was achieved by measuring the detected signal as a function of horizontal and vertical translation and then determining the position where the response peaked. The adjustments on the translation stage were then set to this optimal position.

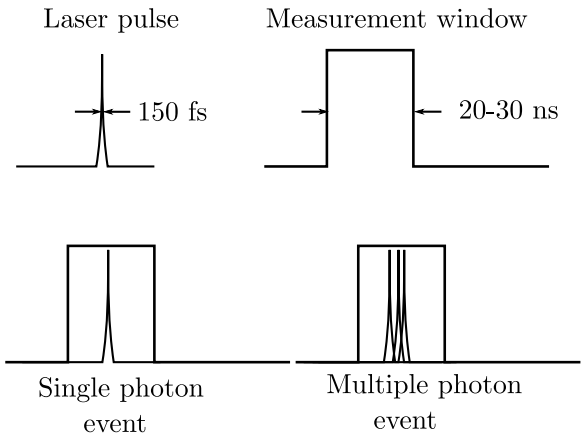

Figure 3.5: Schematic depiction of the limitation of photon-counting devices. If the device measurement window is greater than the temporal duration of the signal being measured, then the device may only count a single photon per cycle of signal. A multiple photon event would saturate the detector and result in a nonlinear response.

A major shortcoming of any single-photon detection scheme is that the device will saturate if too many photons are coincident at once. Essentially, if more than one signal photon reaches the cathode within a specific time interval, the detector will not be able to properly count how many photons are present due to the speed of the electronics. This is known as "detector paralyzability" and the time interval over which the detector is paralyzed is known as "dead time" [39]. Most PMTs are limited to a dead time on the order of 10 ns,

which for our experiments means that we are limited to detecting no more than one photon per 150 fs pulse. This is depicted in Fig. 3.5, where the detector is only able to accurately record "single photon events," while "multiple photon events" will result in detector saturation. For a 1 kHz repetition rate laser, a count rate greater than 1000 counts/s will result in detector saturation. This in turn limits the dynamic detection range to between 10 and 1000 counts/s (noise to saturation). This observation became obvious when a simple measurement of Rayleigh scattered light gave a nonlinear curve for input optical intensities $\lesssim 10^6$ W/cm^2. A detailed discussion of detector saturation is accounted for in Appendix D, but the solution to this problem used in our experimental approach was to attenuate the amount of light reaching the detector. This was done by placing a neutral density (ND) filter of appropriate density to limit the maximum scattered signal to below 1000 counts/s.

3.2 Data collection and analysis

Complete polar radiation patterns were recorded for both vertical and horizontal orientations of the analyzer over a series of input intensities. This allowed for mapping of the intensity dependence of the scattering amplitudes over a decade of intensity inputs at equally-spaced intervals. Computer control of the input intensity, polarization state, and analyzer position make the experiment relatively simple to run while allowing for long averaging times to be used. This also allows for the experiment to be done in a completely dark laboratory without the experimenter being present to potentially act as a reflector of ambient light or as a source of thermal radiation. Calibration and mechanical reproducibility of the rotation stages is a critical component of the experiment, so special care was taken to set up these devices. Appendix E provides a detailed explanation of the methods used for confirming the operation of the rotational stages along with a discussion regarding mechanical backlash.

A standard arrangement was to use a $\lambda/2$-plate + analyzer pair to systematically control the throughput intensity which reaches the sample. With such a pair, the transmission through the analyzer follows a cosine-squared pattern as the $\lambda/2$-plate is rotated about the propagation axis of the input light. The experiment begins by zeroing the $\lambda/2$-plate before the analyzer to maximize light transmission. This reference value for zero angle is entered into the MATLAB program used to run the experiment. The maximum input power to the sample is then selected using a reflecting gradient attenuator wheel. If necessary, an appropriate ND filter is selected for attenuating the scattered light in the detection arm which reaches the PMT. Over the course of a typical collection of data, several intensity points are recorded using a step size determined by the arccosine-squared of the azimuthal

orientation of the $\lambda/2$-plate. This determines the appropriate angular rotation to correspond to equally-spaced intervals of the transmitted light intensity. Figure 3.6 shows that the input optical power over each experimental run has an equal spacing. The analyzed data does not rely on the accuracy of this calibration, instead the measured scattering amplitudes are paired with the measured power value for each intensity point.

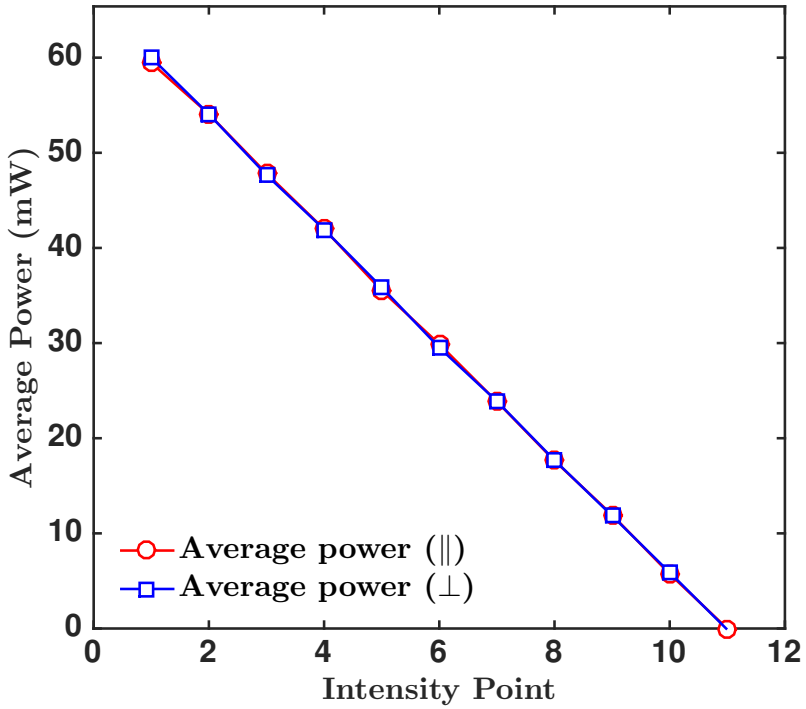

Figure 3.6: A measurement of the input optical power as a function of the equally-spaced intensity points due to the rotation of the $\lambda/2$ + analyzer pair. This procedure is done for the analyzer in both parallel and perpendicular orientations. This plot confirms that the intensity control does in fact yield equally-spaced power increments between each intensity run.

The second waveplate that controls the polarization orientation of the input beam must be calibrated so that zero corresponds to a purely horizontal orientation of the input optical field. This calibration is done by placing an analyzer set to pass only horizontally-polarized light in the beam line after the $3\times$ telescope. A power meter can then be used to record the transmission of light through the analyzer as a function of rotation angle of the $\lambda/2$ plate in the input beam. The data is then fitted with a cosine-squared curve and the corrected phase offset of this curve is used to determine the zero point of the waveplate.

The analyzer before the PMT is set to pass either vertically or horizontally polarized light that has scattered in a direction perpendicular to the propagation axis of the input

beam (as explained in the experimental design section above). Zeroing of this component is critical to ensure the correct polarization state is passed to the detector. This is done by taking the rejected light from the analyzer and sending it across the optics table to an iris or beam tool set at the height of the plane of the optical beam. The zeroing of this component should be checked once every 4-5 experimental runs to avoid mechanical walk-off/backlash that may be acquired with the rotation mounts. The sample is then placed at the interaction point and is centered and aligned using the input pump beam from the Clark-MXR and the alignment beam from the HeNe laser. Once both the pump and alignment beams are centered through their adjacent faces of the sample, the goniometer tilt for the sample platform is adjusted to align surface back reflections to lie along the input beam axes.

After calibration and alignment, the room lights are turned off and the PMT shutter is opened. After this, an experiment may be run. A typical experimental run will measure the light scattered in both vertical and horizontal orientations of the analyzer as a function of input polarization orientation. The step size is usually set to 12° increments and measurements are made for 10 equally-spaced intensity points. A desired exposure time (or count time) for the PMT as well as a number of periods (or intervals) for which the device should count are then selected. The exposure time is usually set to 4-8 s for ED scattering and 20-40 s for MD scattering, with 4-5 periods. Experiments with these parameters typically take 8-12 hours to complete. These values are chosen so that any angular features of the signals can be resolved above any random background signal. A measurement of the background signal is first made with the laser blocked via the mechanical shutter. This is later subtracted from the measured signals. Next, the amount of scattered light passed by the analyzer in the vertical orientation is recorded at the first intensity point, which is followed by the same measurement for light passed by the analyzer in the horizontal orientation. These measurements are recorded over the range of input intensities and the values are saved as individual text files to be processed once the experiment has finished.

The analyzer used for the intensity control has an extinction ratio of 10^5:1, so the light exiting this optic has a strong, horizontal linear polarization. The orientation of the electric field polarization is controlled using the second $\lambda/2$-plate, which rotates by 180° to give a 360° rotation of the field polarization vector[2]. This allows us to map out complete dipole patterns of the electric and magnetic signals at some fixed incremental spacing of waveplate orientation. This technique is different from previous experiments [15, 1, 2] which compared the light scattered from only two points on the dipole for each orientation of the analyzer. This earlier method is less reliable because it assumes the orientation of the

[2]This is because a rotation by θ of the waveplate corresponds to a rotation of 2θ of the field.

induced dipoles are known and it does not allow for tracing out full radiation patterns. This technique would not be able to measure any rotation of the induced dipoles. Using our improved method, we are able to record enough points along the dipole to have sufficient points for fitting a curve and then extracting both the polarized and unpolarized responses. Figure 3.7 depicts a typical set of data we might collect at any given intensity point, which shows the data follows a cosine-squared pattern with two independent fitting parameters for both the ED and MD curves.

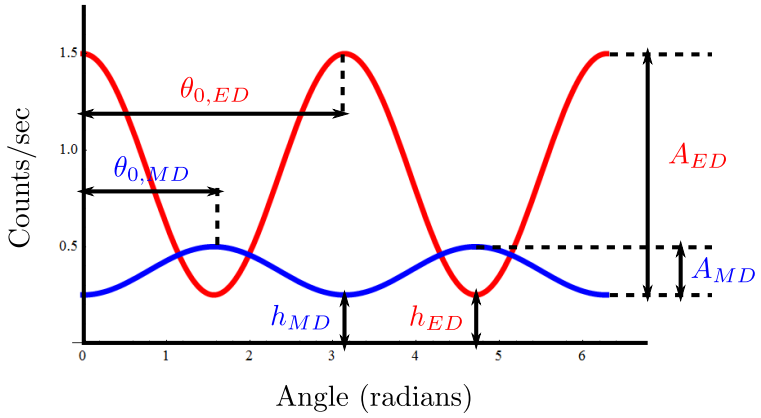

Figure 3.7: Cartesian representation of a typical set of data collected in the scattering experiment. Here we see the independent fitting parameters are the amplitude (polarized component) and vertical offset (unpolarized component).

The measured intensity curves are fitted according to

$$I_{ED} = A_{ED}\cos^2(\theta+\theta_0)+h_{ED}\,, \tag{3.1}$$

$$I_{MD} = A_{MD}\sin^2(\theta+\theta_0)+h_{MD}\,, \tag{3.2}$$

where A_{ED} (A_{MD}) is the amplitude and h_{ED} (h_{MD}) is the vertical offset for the electric (magnetic) signal. Here θ_0 is not an independent fitting parameter, but rather an arbitrary rotation that may be used to zero the input field orientation[3]. The fitting parameters A and h are the values of most interest when analyzing a particular sample. Here the amplitude A is referred to as the "polarized component" while the offset or waist h is referred to as the "unpolarized component." These parameters also afford us to define a second useful quantity for both electric and magnetic signals,

[3]In later experiments, this variable was not required since zeroing the $\lambda/2$ used for polarization control was perfomed.

$$\delta_{ED} = \frac{h_{ED}}{A_{ED} + h_{ED}} \quad \text{and} \quad \delta_{MD} = \frac{h_{MD}}{A_{MD} + h_{MD}}\,, \tag{3.3}$$

which we call the "depolarization ratio." This quantity allows us to make several qualitative and quantitative statements regarding the measured signals with a single plot. For instance, we can show the relative amount of polarized to unpolarized signal, the dependence on field of the unpolarized signal relative to the polarized signal, and the degree of sample saturation. This depolarization is different from the traditional definition, which considers only two measurements to compute the depolarization ratio.

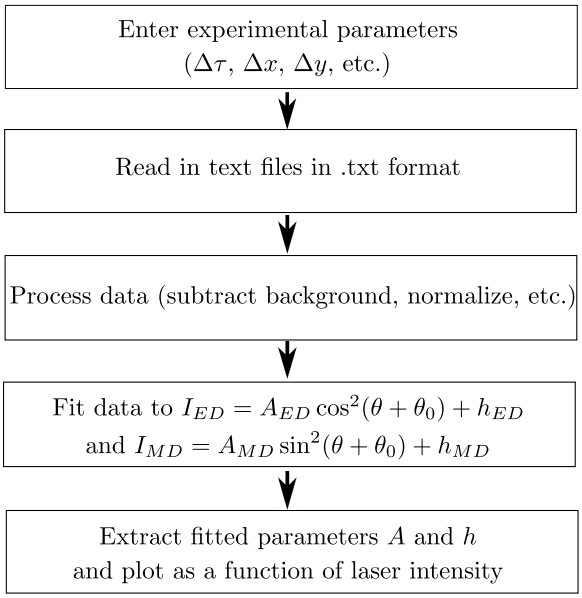

Figure 3.8: Flow chart showing the basic components of the data processing script. Experimental parameters are entered, the text files are read in, processed, and fitted, and the fitted parameters are extracted and plotted.

Figure 3.8 shows the basic outline of the MATLAB script used to process the data. The user first enters experimental parameters specific to the sample data. This includes the laser pulse duration, center wavelength, beam diameter, number of intensity points, and ratio of beam splitter power. The text files are then read into the script and saved into a cell so that they can be accessed using the intensity index. The detector dark counts are then subtracted from the raw measured counts and the signals are normalized according to the ED and MD collection times. After this, the data is represented in terms of the count rate in "counts/s." The data is then fitted according to the cosine- and sine-squared functions from Eqs. (3.1) and (3.2) and the fitted parameters for the polarized and unpolarized components are plotted as a function of input laser intensity. Least-squared polynomial fits of either order 1 or order 2 are used to fit the extracted parameters. The generated plots are then

exported in .eps format and can be easily compiled with a LaTeX script to produce a .pdf of all of the relevant results from any given experiment.

3.3 Samples

The three molecular liquids that were measured in earlier studies [2, 15] were H_2O, C_6H_6, and CCl_4, whose structures are shown in Fig. 3.9. These materials were initially chosen due to the fact that they were non-chiral, had no optical resonances near the laser probe wavelength, and because their liquid nature prohibited any $\chi^{(2)}$ response driven by EE or EE^* processes. CCl_4 was a particularly good candidate in these initial studies because it offered the further symmetry property of being a "spherical top" molecule with charge distributed equally about the central carbon atom. Spherical top molecules have no permanent internal dipole that could potentially contribute to the measured signals and are isotropic. A comparison performed by W. Fisher of the induced magnetic response in these three molecular liquids showed that C_6H_6 provided the largest signal[4]. This result suggested that molecules with delocalized π-electron orbitals might be good candidates for obtaining a large magnetic response.

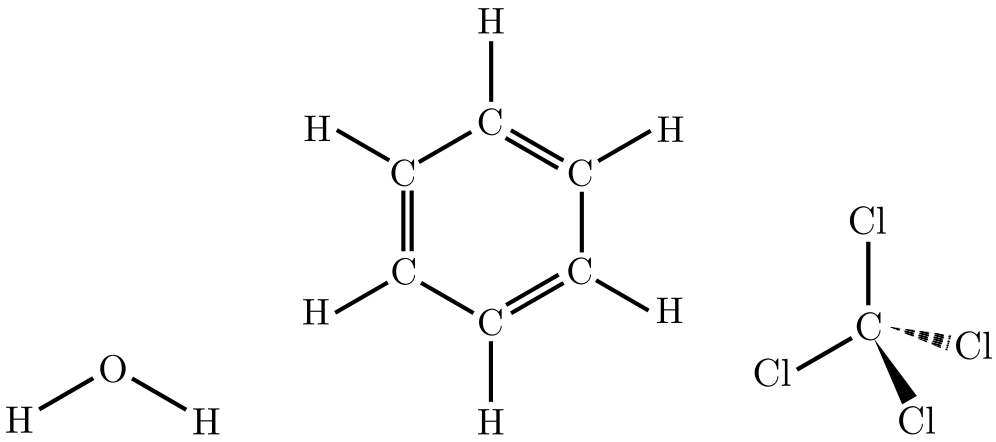

(a) Water (b) Benzene (c) Carbon tetrachloride

Figure 3.9: Molecular diagrams of the three liquids studied in the initial magnetic scattering experiments.

[4]It was later uncovered that W. Fisher may have neglected to take into consideration detector saturation, and so the experiment that compared the three liquids had to be redone.

3.3.1 Liquid sample selection and handling

In view of these previous studies, the initial aim of this thesis work was to systematically vary the electronic and/or molecular structure in a series of transparent molecular liquids in order to determine which physical characteristics provided the largest magnetic response. Based on the previous work suggesting that benzene-like structures may provide a good platform for this study, a series of this type of molecule was determined and tested. This first series consisted of C_6H_6, $C_6H_5NH_2$ (aniline), C_6H_5CN (benzonitrile), and C_6D_6 (deuterated benzene). The addition of aniline and benzonitrile was intended to provide a push-pull comparison for the benzene, as the NH_2 of the aniline pushed some of the charge into the π-orbital while benzonitrile pulled some charge out of the π-orbital. However as we will discuss in Chapter 4, the relevant variation between these molecular liquids is the magnitude of the internal dipole. The comparison between benzene and deuterated benzene allowed us to test for an isotope effect between regular and "heavy" benzene.

The experiments undertaken in the present work sought to explore additional tetrahedral structures more systematically. As will be apparent in Chapter 4, these molecules offered a better platform for comparing the induced magnetic effects since they had a fixed geometry, unlike the benzene series. The first set to be studied consisted of CCl_4, $SiCl_4$ (silicon tetrachloride), $SiBr_4$ (silicon tetrabromide), and $SnCl_4$ (tin tetrachloride) [40]. In the series of

$$CCl_4 \longrightarrow SiCl_4 \longrightarrow SnCl_4 \ ,$$

the moment of inertia increase from left to right and only the central atom is substituted while the peripheral atoms are kept the same. A second comparison was made between the set of molecules

$$SiCl_4 \longrightarrow SiBr_4 \ ,$$

for which the central atom is kept the same and the peripheral chlorine atoms are substituted for the heavier bromide atoms with a greater number of electrons. A systematically-varied series of molecules such as this provided a means to better understand which physical properties are relevant predictors for achieving high magnetic response. The molecules $TiCl_4$ (titanium tetrachloride), $GeCl_4$ (germanium tetrachloride), and $GeBr_4$ (germanium tetrabromide) were not studied in this work, but would also be good candidates for testing the importance of molecular structure. The tetrahedral structures become increasingly dangerous to work with as the mass increases, so safe handling and storage procedures were

developed.

The liquid samples were sealed in quartz cuvettes purchased from Starna Cells with either a push-cap lid (DLC-23-Q-10) or a screw-cap lid and septum (DLC-3-Q-10-ST-C). The push cap cuvettes were used for the benzene series and the screw-cap cuvettes with the septum were used for the more dangerous tetrahedral series. The cells had exterior dimensions of 12.5 mm $\times$ 12.5 mm $\times$ 45 mm and inner dimensions of 10 mm $\times$ 10 mm $\times$ 45 mm, providing a volume of 3.5 mL. All four sides of the cells were polished to a fine tolerance to achieve surface smoothness across the face of each cell. Minimizing the surface roughness was necessary in order to minimize light scattered from the air-glass and glass-sample boundaries. A cleaning procedure was used to remove debris from inside the cuvette cells before being filled with a sample. The procedure followed the steps shown below:

1. Fill the cuvette with a mixture consisting of 2-3 drops of Starna Cells cleaning detergent and deionized water.
2. Cap and shake the cells vigorously for approximately 30 seconds.
3. Rinse the cells 2-3 times with deionized water.
4. Rinse the cells 2-3 times with acetone.
5. Rinse the cells 2-3 times with isopropyl alcohol (IPA).
6. Bake cells in oven at 181° F (boiling point of IPA) under vacuum to burn off contaminants.
7. Fill cells in nitrogen glovebox using a syringe[5].
8. Cap cells and seal with parafilm wax.

The samples were then stored in the fume hood and in later experiments (when working with highly-reactive tetrahedral structures) in a desiccator under vacuum. A glass ball jar desiccator was used and was evacuated using a mechanical pump.

The outer walls of each cuvette were cleaned using lens tissue and photometric grade methanol. Standard cleaning practice was used in which the tissue was folded several times, held with a plastic hemostat, and wetted with a drop of photometric methanol. In some cases when there was a lot of debris, several passes using the same lens tissue were made. However only a single tissue per wipe was used for the last pass on each cell wall.

[5]In some cases for which the cleanliness of the sample container was suspect, the liquid was prefiltered through double 0.2 μm millipore mesh filters as was done in previous experiments.

A lab coat was worn when working with the tetrahedral series. The cells were handled with nitrile gloves to avoid contaminating the surface with oils or dirt. Once the outside of the cell was cleaned, it was placed in a machined sample holder inside the light-tight detection box. The holder consisted of a square notch milled into a 1/2" thick piece of aluminum which was sized to exactly fit the cell. A 3-dimensional translation stage as well as goniometer mount were used to allow for alignments of the sample. The cell was aligned first using the HeNe laser of the collection optics. This procedure consisted of first translating the cell to be in the center of the beam and then adjusting the tilt and rotation to align the back-reflected light. The probe beam was then used to finalize the alignment. First the cell was translated so that the probe passed through the center of the cell and then the tilt was used to align the back-reflected light. Both beams were then simultaneously incident on the sample and alignment was double-checked.

3.3.2 Crystalline samples

Previous ME scattering experiments were performed in clear liquids, which are easier to prepare for sensitive scattering experiments than solids[6]. However due both to safety and practical purposes, working with solids is more desirable. Studies of the cubic crystal $Gd_3Ga_5O_{12}$ (gadolinium gallium garnet or cubic GGG) were therefore performed. This is a rare earth garnet of the space group Ia$\bar{3}$d (or point group O_h or m$\bar{3}$m, depending on notation). Most importantly, this crystal has cubic symmetry so that $\chi^{(2)}$-driven quadratic nonlinearities of the type EE or EE^* are forbidden. Hence any observed second-order nonlinearities must be of a (new) unexpected type. Additionally, the composition of garnet crystals can be varied widely while maintaining the same general formula as GGG.

The GGG crystal used in this study was polished on 4 of the 6 sides, allowing a choice between two different entrance and exit faces in the horizontal scattering plane. The same cleaning procedure described above was used to prepare samples, consisting of lens tissue and photometric grade methanol. The dimensions of the sample were of the order 1 cm^3, which allowed for a large enough entrance face that the beam was not clipped by the edges and a large enough exit/detection face so that the signal was not clipped by the edges. This was important for reducing unwanted reflections of incident laser light into the detection arm and thereby minimizing background light levels. Alignment of the probe and collection beams were completed in the same way as described above for the liquid cuvette samples.

[6]This is because solid samples require precision cutting and polishing.

CHAPTER 4

Experimental and Theoretical Results

In this chapter we present the main experimental and theoretical results of this thesis. We first present results on light scattering in the forward direction through a crystalline solid to show that no induced ellipticity is occurring as laser light interacts with the sample. These results are recorded over an intensity regime consistent with those used for the scattering measurements made at 90°.

The second section is devoted to discussing the results of the magneto-electric scattering experiment described in Chapter 3. Experimental results are discussed for two classes of systematically-varied molecular liquids as well as a solid cubic garnet crystal. The first class of systematically-varied structures are of tetrahedral structure and consist of the liquids CCl_4, $SiCl_4$, $SiBr_4$, and $SnCl_4$. The second class of systematically-varied structures are π-delocalized electronic molecules, consisting of the liquids C_6H_6, $C_6H_5NH_2$, C_6H_5CN, and C_6H_6. Analysis of unpolarized scattering in these different samples in particular shows that the moment of inertia plays an important role in predicting the magnitude of induced magneto-electric response. Some conclusions are also drawn regarding the effect of large internal dipole moments in the π-delocalized structures and their effect on enhancing the scattered response. We then show the first results of strong magnetic dipole scattering in the cubic garnet crystal GGG. Here the nonlinear magnetic scattering is shown to be of the order of the electric scattering.

The results of the two different theoretical models that were developed in Chapter 2 are presented in the third section of this chapter. Here the magnitudes of the magneto-electric nonlinear moments $m(\omega)$, $p(2\omega)$, and $p(0)$ are plotted as a function of either photon number (i.e. laser intensity) or detuning (i.e. laser frequency). Of particular interest is the predicted nonlinear magnetization, as this is the quantity being measured by the scattering experiment. The atomic picture is shown to correctly predict three qualitative features seen in the experiments: (1) transverse orientation of induced magnetization relative to the propagation axis, (2) second-order dependence on input field, and (3) dependence on the laser frequency ω. All three of these features are surprising because they contradict

conventional nonlinear optics. The atomic picture does have a shortcoming because it does not provide quantitative agreement with experimental scattering results. However, the results of the molecular picture developed in Chapter 2 achieve quantitative agreement between theory and experiment by taking into account the effects of magnetic torque on molecular rotation. General summaries of the experimental and theoretical results and their comparisons are left for discussion in Chapter 5.

4.1 Light scattering in the forward direction

A measurement was made in the forward direction to confirm that the samples used in the scattering experiments did not permit any XPW generation or other forms of induced ellipticity. XPW generation is a four-wave mixing process that takes place in media with large $\chi^{(3)}$ susceptibilities to generate a polarization that is third-order and is oriented perpendicular to the linearly polarized input field [23, 24],

$$\omega_{\perp} = \omega_{\parallel} + \omega_{\parallel} - \omega_{\parallel} \, . \tag{4.1}$$

To confirm that no induced ellipticity was taking place in the samples studied in this work, two measurements were taken using the sample GGG. This sample was used because XPW generation has been measured in crystalline solids with similar structure as GGG [23, 24]. The first experiment confirmed that the angular distribution of polarized light components in the forward direction does not change as a result of passing through the crystal. The second experiment verified that the intensity of light passed through the crystal increased linearly with the intensity of the input beam. Both of these measurements were made in the forward direction and light was detected using a Thor-Labs S401C thermal power meter with a sensitivity of approximately 10 μW. The detection scheme for this measurement is shown in Fig. 4.1.

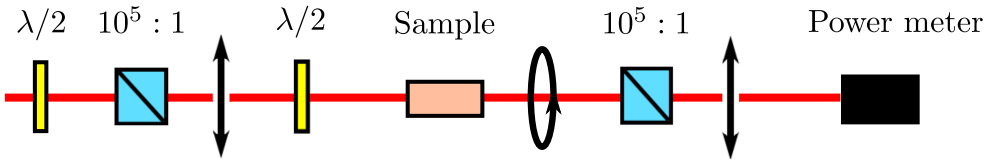

Figure 4.1: Schematic for measuring light scattering in the forward direction. The input polarization to the sample is linearly polarized with extinction of 10^5:1. A second polarizer with a power meter is set to pass polarization along the horizontal axis to check for ellipse rotation.

The first experiment was done as follows. A polarizer with an extinction of 10^5:1 was

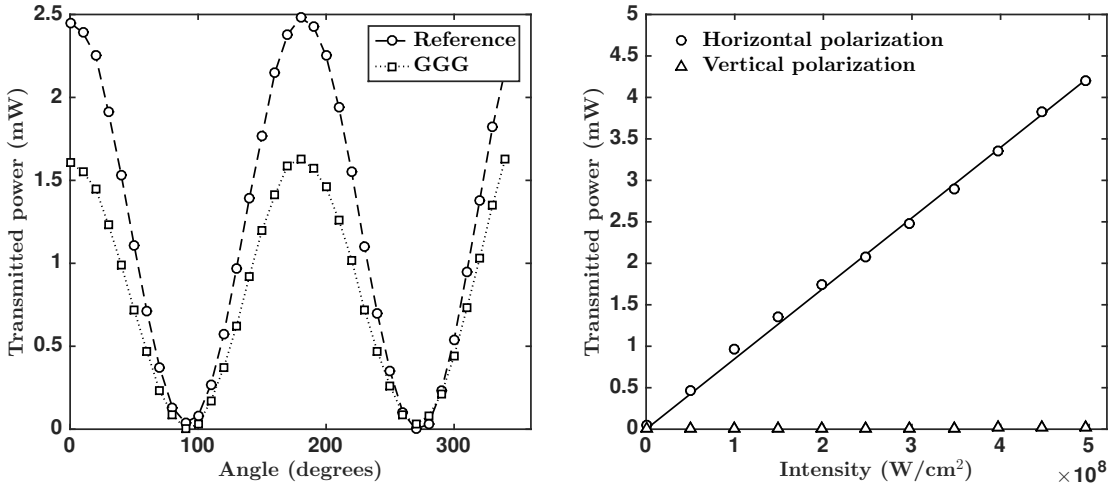

(a) (b)

Figure 4.2: (a) Dependence of the transmitted intensity as a function of angle for linearly-polarized light passing through a bulk cystal of GGG. The dashed curve shows the same but with no GGG. (b) The transmitted power through GGG as a function of input intensity for horizontal and vertical polarizations of light. Measurements were made after a horizontal analyzer in both (a) and (b).

placed in the beam path directly after the sample (see Fig. 3.2) with its transmission axis aligned horizontally. The $\lambda/2$-plate for controlling the polarization orientation was then zeroed and rotated through 360° and power measurements were recorded over 10° increments. This measurement was performed first without any sample (to obtain a reference curve) and then with the sample of GGG. The input intensity of light was 2×10^8 W/cm^2. The results are shown in Fig. 4.2(a) and show no indication of induced ellipse rotation or depolarization. In fact, both curves have a cosine-squared dependence on angle with extinction into the noise floor of the detector. This angular dependence is what one would expect if no ellipse rotation is present.

The second measurement was performed in a similar fashion. Again, a polarizer placed after the sample with its transmission axis oriented horizontally was used. The $\lambda/2$-plate before the sample was then set to rotate the field to be either horizontal (parallel to the polarizer transmission axis) or vertical (perpendicular to the polarizer transmission axis) while the input intensity was varied. The range of intensity points were chosen to be the same as those used in the scattering experiments described in the following section. The results of these measurements are shown in Fig. 4.2(b). The measurements show that for horizontally-polarized input light, the measured power increases linearly with input intensity while for the vertically-polarized light, there is no detectable signal. Again, these

results are consistent with the conclusion that no induced ellipticity is taking place.

Furthermore, the 90° detection geometry and full $\lambda/2$-plate rotation used in the experimental approach outlined in Chapter 3 allows us to directly determine if ellipse rotation has occurred. For one, the rotation of input field through 360° allows for tracking of any rotation in the measured signals. This would show up in the polar plots as off-axis rotations or tilts in the dipole signals. More importantly, however, is the fact that XPW generation cannot generate a complete 90° polarization rotation, which is the angle at which we are measuring the magnetic signals. It will be shown in the following section that in some samples (including GGG) we measure scattering amplitudes in the co- and cross-polarized orientation of the analyzer that are comparable in amplitude and are aligned according to the zeroed input field. The large scattering amplitudes and orthogonal orientation of the measured signals relative to the linear Rayleigh scattering cannot be explained by ellipse rotation.

4.2 Experimental scattering results

All data recorded in this section were obtained following the approach discussed in Chapter 3. The only laser used for measurements was the Clark-MXR CPA-2001 system with a center wavelength of 775 nm and bandwidth of approximately 5 nm. Daily variations in the pulse duration, laser power, and central wavelength were recorded and accounted for in the analysis procedure. The same interference filter was used in all measurements with a 5 nm passband effectively centered at 775 nm[1]. All of the experimental results shown here were recorded using the same thermo-electrically cooled PMT. Precautions were taken to limit the amount of signal light reaching the detector to avoid saturating the device by placing ND filters in the detection arm. The experimental geometry remained constant with the same input pinhole size of 3.5 mm, the same solid angle pinhole size of 3.5 mm, and the same $3\times$ telescope before the sample cuvette. The angle made between the outermost ray and the optical axis was 0.7°, which provided extinction of out-of-plane scattering to approximately 1 part in 10^4 (for details see Appendix C). There were variations in the number of points collected per angular sweep as well as the type of neutral density filter used before the PMT and the PMT count time. All of these parameters were taken into account and normalized for in the analysis procedure.

The results presented in this section constitute only a subset of the experimental data collected from the magneto-electric scattering experiment. The primary features of the in-

[1]Recall that the filter used was centered at 780 nm but affixing it to a mount at 14° effectively shifted the center λ to 775 nm.

duced magnetic response are best summarized by plotting the dependence of the polarized and unpolarized components as a function of input laser intensity. As mentioned in Chapter 3, the measured response is fit using the formulæ,

$$I_{ED} = A_{ED}\cos^2(\theta+\theta_0) + h_{ED} \quad \text{and} \quad I_{MD} = A_{MD}\sin^2(\theta+\theta_0) + h_{MD}\ , \tag{4.2}$$

and the fitted parameters A_{ED} (A_{MD}) and h_{ED} (h_{MD}) constitute the polarized and unpolarized response for the electric (magnetic) scattering. The "Total Response" is the sum of the polarized and unpolarized components. Plots showing the depolarization ratio

$$\delta_{ED} = \frac{h_{ED}}{A_{ED}+h_{ED}} \quad \text{and} \quad \delta_{MD} = \frac{h_{MD}}{A_{MD}+h_{MD}}\ , \tag{4.3}$$

are also provided for several of the samples. These provide a mechanism for quantifying the degree of depolarization. To avoid redundancy, plots showing the full angular dependence of the magnetically or electrically scattered light are only provided for select samples. Plots showing the relative amplitudes of the measured response for each systematically-varied set of molecular liquids are provided.

We are primarily interested in analyzing and understanding electric and magnetic response that has a nonlinear dependence on the input optical intensity. This is in accord with the earlier experimental results, which showed strong magnetic scattering as a function of intensity. Our experimental results show nonlinear dependence for the polarized magnetic response as well as nonlinear dependence of the unpolarized response for *both* the electric and magnetic components. In all cases, the polarized electric response should show a linear dependence, in accord with linear Rayleigh scattering. These features are apparent in most of the plots shown below. The plots showing comparisons of these nonlinear effects allow us to confirm the role of moment of inertia and the importance of molecular rotations for enhancing these moments.

4.2.1 Scattering in tetrahedral molecules

Here we present data on magnetic scattering in the tetrahedral structures CCl_4, $SiCl_4$, $SiBr_4$, and $SnCl_4$. Results are first shown for CCl_4, which was the first material shown to exhibit a strong nonlinear magnetic response [1, 2]. Aside from repeating the initial observations, we also observe nonlinear dependence on the unpolarized response for both electric and magnetic signals. The sample of $SiCl_4$ shows only a slight nonlinear dependence in the unpolarized magnetic signal and the results shown here represent only initial measurements

which ought to be repeated. $SiBr_4$ shows the same qualitative features as CCl_4 and $SnCl_4$ shows no apparent quadratic magnetic dependence, but does show nonlinear dependence on the unpolarized electric scattering. A comparison is then made between the unpolarized nonlinear electric response in CCl_4, $SiBr_4$, and $SnCl_4$ and we determine that the heavier molecules appear to exhibit a larger magneto-electric response at lower input intensities.

4.2.1.1 Scattering in CCl_4

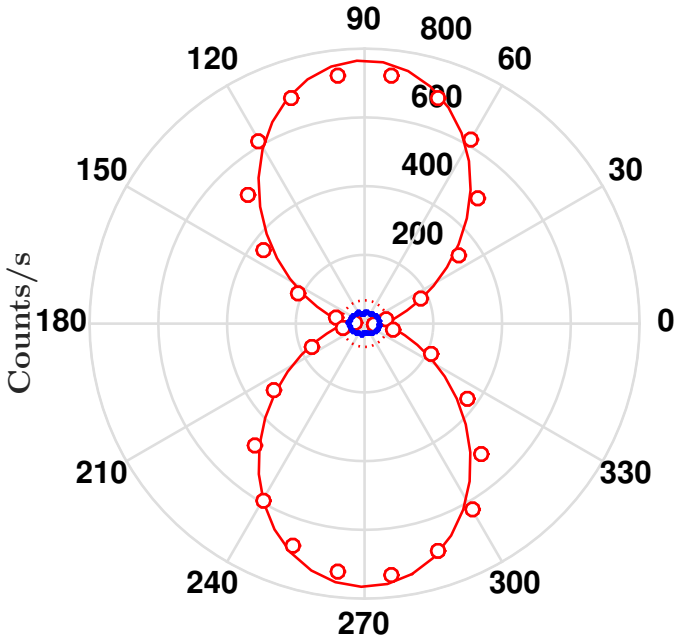

Figure 4.3: Polar plot showing electric (red open circles) and magnetic (blue closed circles) scattering intensities in CCl_4 at $I = 3.3 \times 10^8$ W/cm^2. Solid lines represent best fit lines to the data. The dotted red line represents the (small) unpolarized center in the ED scattering.

It was crucial to first repeat the measurements done by earlier researchers using the sample CCl_4 before beginning new experiments. This provided a consistent baseline for measurement and experimentation. Figure 4.3 shows one set of measurements recorded for CCl_4 at an input intensity of $I = 3.3 \times 10^8$ W/cm^2. The count interval was the same for both parallel and perpendicular orientations of the analyzer at 8 s per interval over 4 periods. Here the red open circles (blue filled circles) represent the electric (magnetic) scattering amplitudes. Figure 4.4(a) shows a blown-up view of the magnetic scattering amplitude. The solid curves in both plots represent the fitted cosine-squared (or sine-squared) functions

to the raw, normalized data. The unpolarized centers are denoted by the dotted lines. In Fig. 4.4(b) the fitted unpolarized waist has been removed from the magnetic data to show only the polarized component. It is apparent that both sets of data follow the fitted curves quite well. This fitting is especially good considering the low count rate of the magnetically-scattered light, which has an amplitude of no more than 15 counts/s. This number is very close to the detector background noise of 3-4 counts/s. Better averaging can be achieved by counting photons for longer intervals or allowing more signal light to reach the PMT for the case of the magnetic scattering.

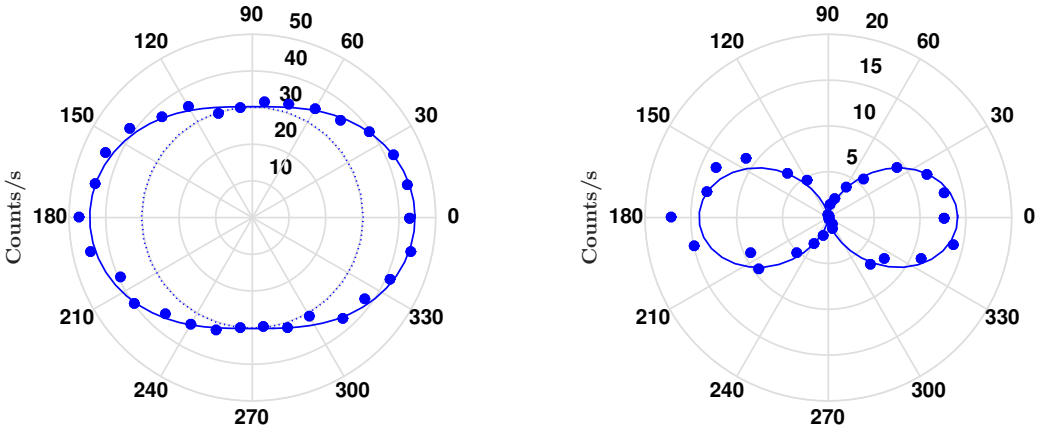

(a) Total MD

(b) Polarized MD

Figure 4.4: The magnetic scattering intensities in liquid CCl_4 from Fig. 4.3 blown up to show the orthogonal orientation relative to the the ED scattering. (a) Shows the total magnetic scattering with the dotted line representing the unpolarized magnetic component. In (b) the unpolarized component has been subtracted to show just the polarized component.

A measurement was also done to show the dependence of the electric and magnetic scattering amplitudes as a function of input intensity. The dependence of the polarized and unpolarized components are shown in Fig. 4.5. This data is different from the one shown in Figs. 4.3 and 4.4. Here the ED collection time was 2 s and the MD collection time was 12 s[2] over 4 periods. In Fig. 4.5(a) the magnetic signal has a quadratic dependence but has been multiplied by a numerical factor of 10 so it may appear on the same axes as the electric signal. In the same plot, the electrically-scattered light is shown to grow linearly with intensity before beginning to saturate around 850 counts/s. This linear dependence is expected and represents elastic Rayleigh scattering. The solid curves through both sets of

[2]The PMT cannot count for intervals of more than one significant digit, so entering 12 s was rounded to 10 s and a multiplicative correction factor of 6/5 then was used to correct the MD data.

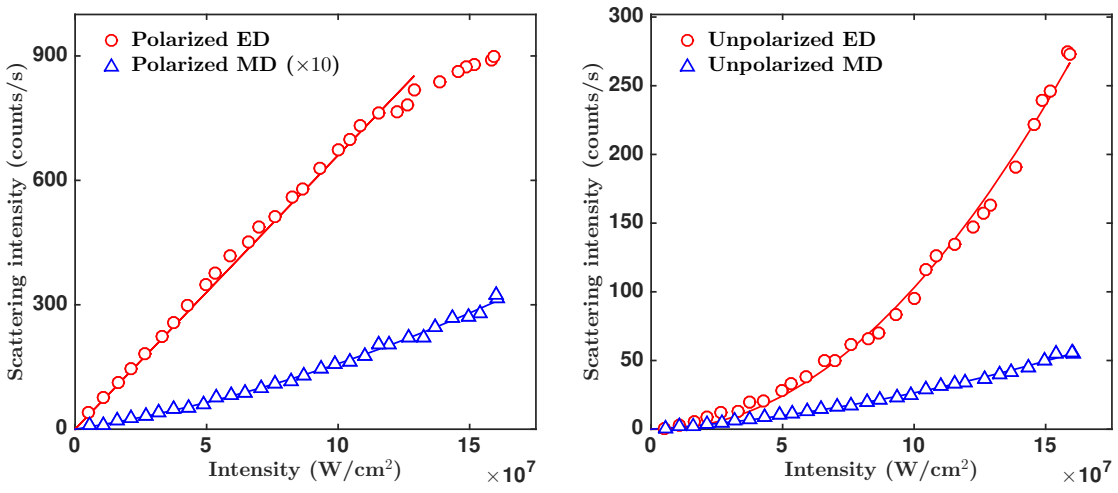

(a) Polarized (b) Unpolarized

Figure 4.5: The (a) polarized and (b) unpolarized components of electrically- and magnetically-scattered light in liquid sample CCl_4. In (a) the magnetic signal is multiplied by a numerical factor of 10 so that it appears on the same set of axes as the electric signal. The polarized ED data is partly saturated above 1.2×10^8 W/cm^2 so these points are not included in the fit.

data represent least-squared polynomial fits with a zero-intercept. The saturated points are not included in the linear fit to the electric signal.

The dependence of the unpolarized signals for the electric and magnetic scattering are shown in Fig. 4.5(b). These curves are fit using polynomials of order 2. It is evident that both curves have a quadratic dependence on the input field intensity. No numerical factor has been used to make the electric and magnetic signals appear on the same scale. This is the first known observation of nonlinear unpolarized scattering in both parallel and perpendicular orientations of the analyzer. This result suggests that a second nonlinear mechanism may be present. This may be attributed to a completely resonant, slightly inelastic transition driven by a quadratic magneto-electric mechanism as we discuss later in Chapter 5. The depolarization ratios δ_{ED} and δ_{MD} for this same set of data are shown in Fig. 4.6. Both curves are fit using a linear polynomial and for the magnetic signal the first 3 points were not included in the curve fitting. These points represent measured signals that were too far into the noise of the PMT. The slope of the electric depolarization is more pronounced than the magnetic, which is not surprising since the unpolarized electric response has a higher-degree of nonlinearity as shown in Fig. 4.5(b).

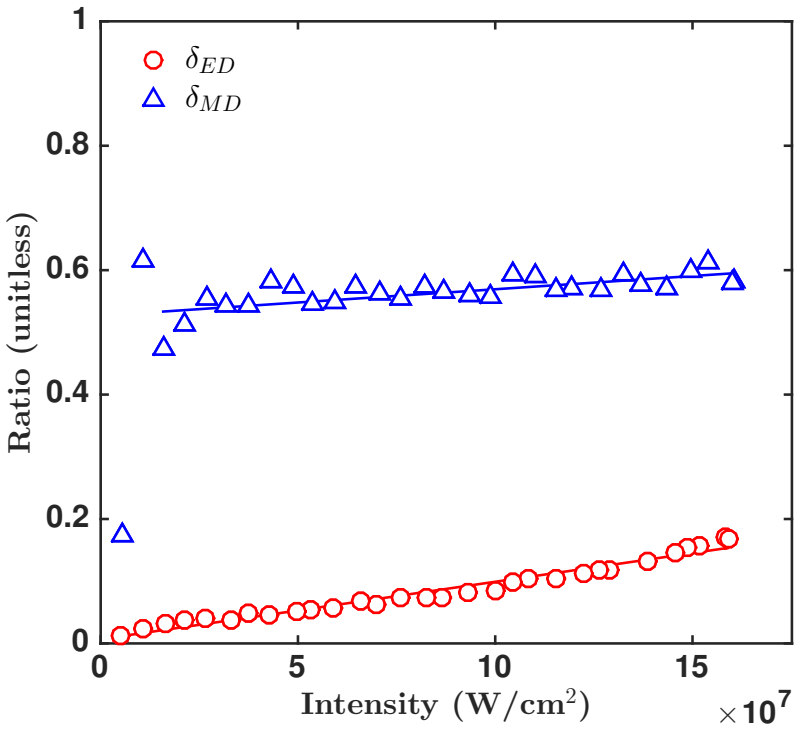

Figure 4.6: Depolarization ratios δ_{ED} and δ_{MD} for molecular liquid CCl_4. The solid curves represent first-order polynomial fits to the data. The first three points were not included in the magnetic fit to the data.

4.2.1.2 Scattering in $SiCl_4$

Silicon is the next element below carbon in the periodic table, so naturally the next liquid to compare to CCl_4 is $SiCl_4$. This sample was particularly difficult to work with since for some reason it was difficult to keep the outer walls of the cuvette clean. Cleanliness of the outer walls is important because any surface blemishes or changes in refractive index will greatly increase the amount of spurious scattered light in the box. Regardless of the number of times a lens tissue with methanol was used to clear away debris or oil, there appeared to always be streaks on the outer walls of the cuvette. This problem was noticed this with $SnCl_4$ too, but a concerted effort proved to be adequate to avoid leaving streaks.

It is important to exercise caution when working with these CCl_4 isomorphs, since they become increasingly dangerous to work with as we move down the periodic table. The major health hazards of this molecule include respiratory track burns, skin burns, eye burns, and mucous membrane burns. For these reasons, it is recommended to avoid handling the samples more than absolutely necessary even if this necessitates making measurements with slightly dirty outer cell walls.

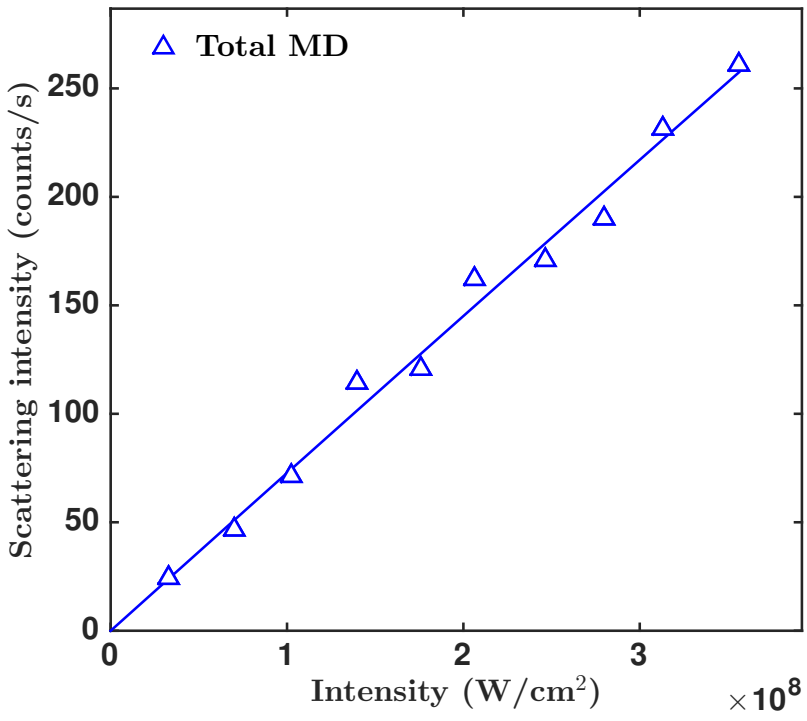

Figure 4.7: The total measured magnetic response in molecular liquid $SiCl_4$ as a function of laser intensity. The solid curve represents a linear fit to the experimental data.

The results of the measured magnetic response are shown in Fig. 4.7 for $SiCl_4$ with

a linear polynomial fit represented by the solid line. There is no corresponding electric response to show since during this run the scattering intensity was much greater than anticipated and the electric signal saturated the PMT. The count time for the magnetic signal was 8 seconds and 4 periods were used. The total magnetic signal appears to be linear with intensity, but Fig. 4.8 shows the polarized and unpolarized components of this response. From Fig. 4.8(b), it is apparent that the unpolarized response has a slightly nonlinear dependence on intensity, while in Fig. 4.8(a) the polarized response is linear versus intensity within experimental error. More experimentation should be done to examine this sample further, but these results are included here to show that the nonlinear unpolarized response, is consistent with the results of the CCl_4 scattering.

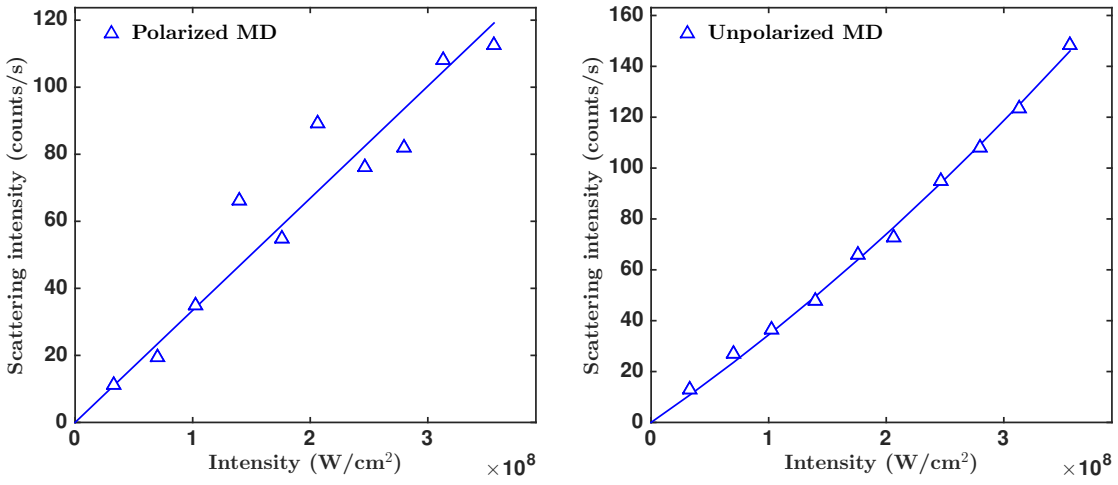

(a) Polarized (b) Unpolarized

Figure 4.8: The (a) polarized and (b) unpolarized magnetic scattering intensities as a function of laser intensity for the liquid sample $SiCl_4$. The polarized component is seen to grow linearly while the unpolarized component has a slight nonlinear dependence on intensity.

4.2.1.3 Scattering in $SiBr_4$

Next in line to study for the CCl_4 isomorphs is $SiBr_4$ which is slightly heavier than $SiCl_4$, since Br is the next element below Cl in the periodic table. The measurements shown here used 8 second count intervals for both the ED and MD data and 4 periods of the PMT were used. The measured total response for electric and magnetic signals is shown in Fig. 4.9 as a function of intensity. Here the magnetic signal is multiplied by a numerical factor of 5 so that it appears on the same vertical axis as the electric signal. The electric dipole data has been fitted with a linear function and the magnetic data has been fitted with a second-order polynomial. The linear behavior of the electric signal is consistent with elastic Rayleigh scattering and the quadratic magnetic response is consistent with a nonlinear optical process having a quadratic dependence on the incident field.

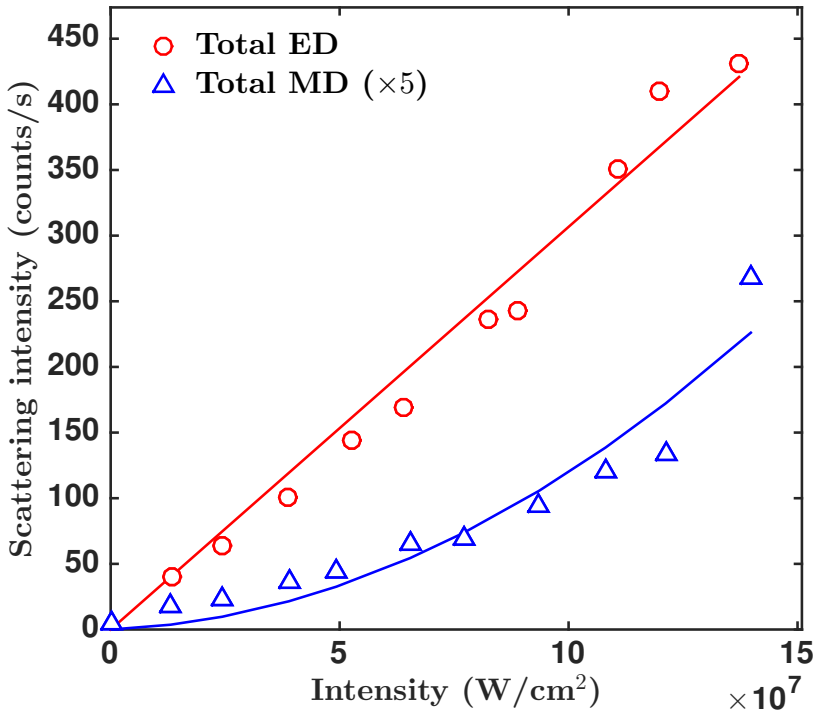

Figure 4.9: The total measured signal in $SiBr_4$ for electric and magnetic orientations of the analyzer. The electric response follows a linear fit while the magnetic response is quadratic.

In Fig. 4.10 the polarized and unpolarized components are plotted separately as a function of intensity for both electric and magnetic signals. In Fig. 4.10(a) the polarized electric response is linear as anticipated and the magnetic response is quadratic. The magnetic response is again multiplied by a numerical factor of 5 so it appears on the same axes as the electric signal. In Fig. 4.10(b) the unpolarized response for both electric and magnetic

signals is shown to have a quadratic dependence on intensity. In this case, no factors were used to scale the magnetic signal. The fact that the electric unpolarized response is so small compared to the polarized response accounts for why the leading behavior of the electric signal is predominantly linear.

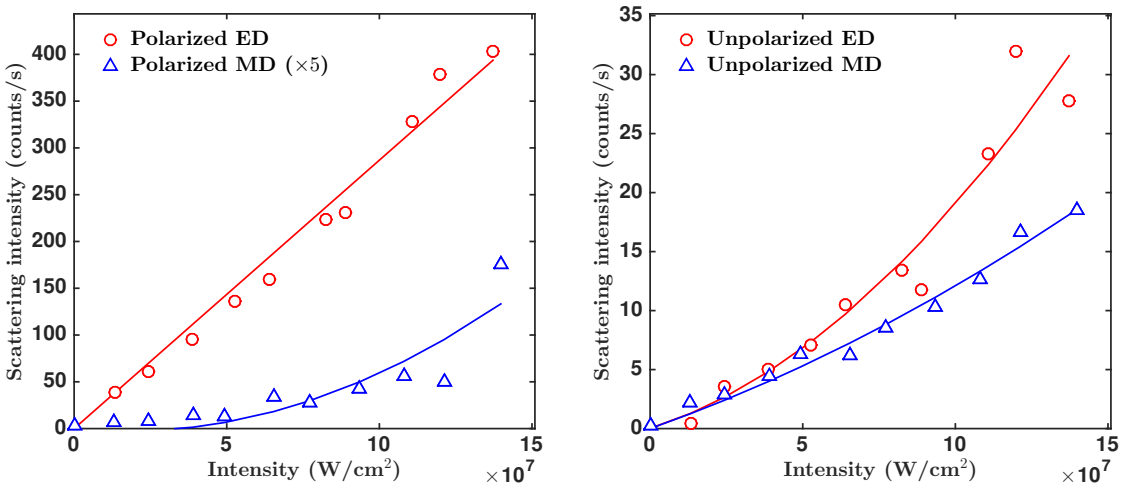

(a) Polarized (b) Unpolarized

Figure 4.10: The (a) polarized and (b) unpolarized response for the electric and magnetic scattering intensities in liquid sample $SiBr_4$. The polarized electric response is linear while the polarized magnetic response is nonlinear, as are the unpolarized responses for both electric and magnetic signals.

The quadratic nature of the polarized magnetic response in $SiBr_4$ is more apparent in Fig. 4.11, which shows the same measurement done in the previous plots except the input intensity range was increased by about a factor of 2. The measurement of the electric response was not included in this plot since the intensity of Rayleigh scattering was sufficient to saturate the PMT.

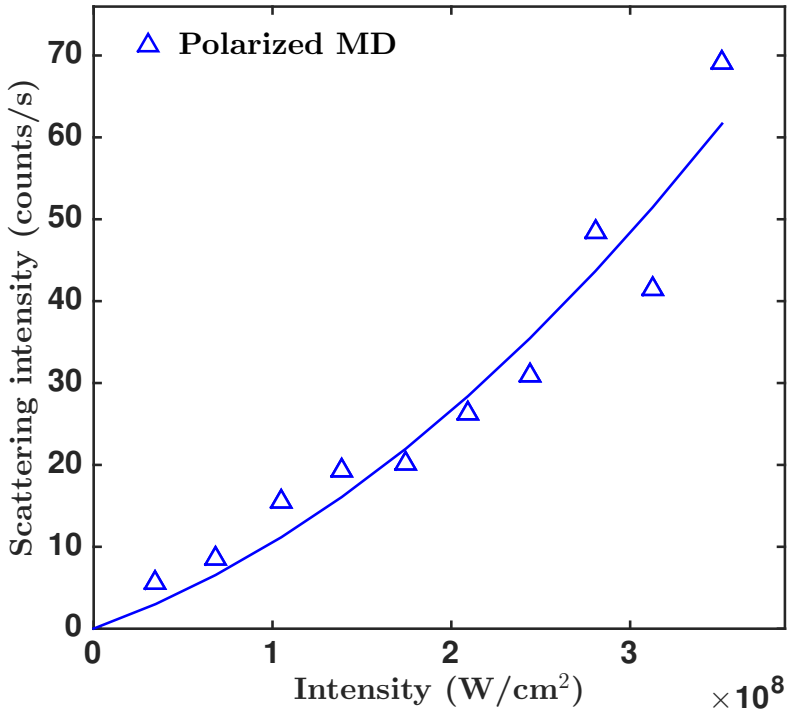

Figure 4.11: Plot showing the quadratic response of the polarized component of the magnetically-scattered light in liquid sample $SiBr_4$.

4.2.1.4 Scattering in $SnCl_4$

The primary results of the magnetic scattering measurements in $SnCl_4$ are provided in Fig. 4.12. The electric and magnetic count intervals were both set at 8 s and measurements were done for 4 periods of the PMT. Figure 4.12(a) shows that both the electric and magnetic response increased linearly with intensity. In Fig. 4.12(b) the unpolarized electric response is quadratic with respect to input intensity while the magnetic response is predominantly linear. This suggests that any nonlinear magnetic response may have saturated while the nonlinear mechanism responsible for the unpolarized electric response is still at work. Further experiments are needed to explore this sample in more depth.

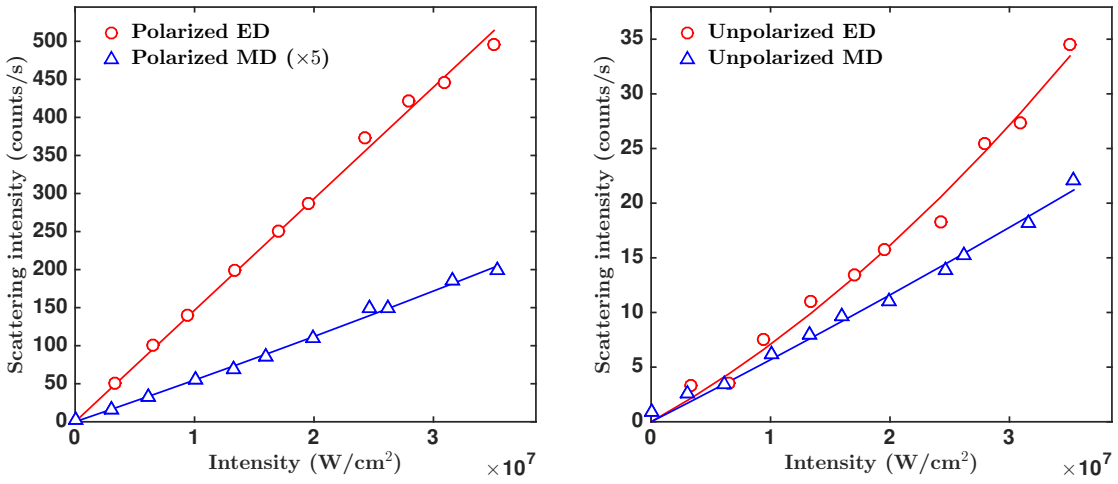

(a) Polarized (b) Unpolarized

Figure 4.12: The (a) polarized and (b) unpolarized response for the electric and magnetic scattering intensities in liquid sample $SnCl_4$. There is no apparent nonlinear magnetic response but the unpolarized electric response is quadratic.

4.2.1.5 Comparative analysis in tetrahedral liquids

Each of the samples described above displays at least a small nonlinear component in its response, so naturally it is useful to make a comparative analysis of these measured quantities. This will allow us to draw some conclusions regarding the relevant molecular properties responsible for enhancing the measured moments. Due to the issues with cleaning the $SiCl_4$ cuvette, this sample will not be included in the comparative analysis. Instead, we see that there is a clear quadratic dependence of the unpolarized electric signal in the samples of CCl_4, $SiBr_4$, and $SnCl_4$. We focus our comparative analysis on the unpolarized response of these three samples.

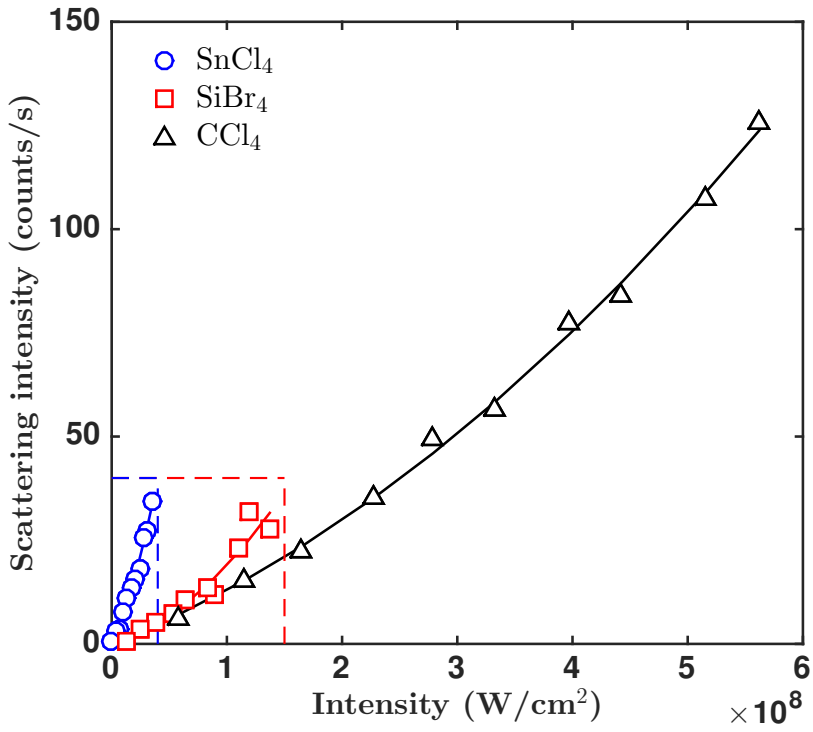

Figure 4.13: Comparison of quadratic unpolarized electric response in CCl_4, $SiBr_4$, and $SnCl_4$ as a function of input intensity. The steepest slope is for $SnCl_4$ and the shallowest slope is for CCl_4, suggesting that moment of inertia plays a role in the magnitude of the measured response.

Figure 4.13 shows the measured unpolarized electric scattering for the three samples CCl_4, $SiBr_4$, and $SnCl_4$ as a function of input intensity. Due to limitations of the detector, we are restricted to stitching together data collected over several ranges of the input intensity range. Therefore the largest range shown here is for scattering in CCl_4, while smaller plot ranges are depicted by the red and blue dashed curves in the lower left corner of the

plot. These dashed areas are blown up in Fig. 4.14 to show the curves for $SiBr_4$ and $SnCl_4$ more clearly. Although only small ranges were taken for these samples, it is clear that $SnCl_4$ has the steepest slope and therefore largest response, while CCl_4 has the shallowest slope and therefore weakest response.

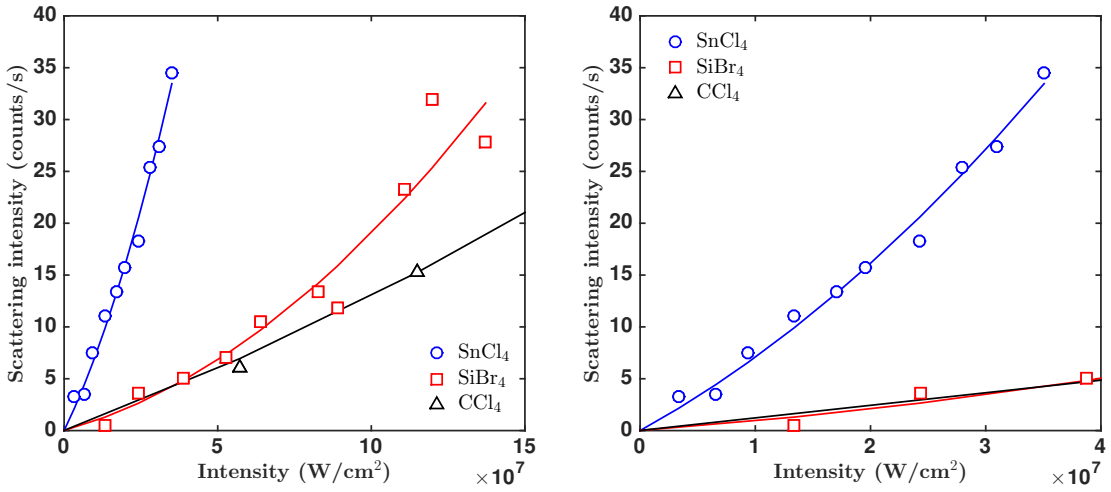

Figure 4.14: Expanded plot windows of Fig. 4.13 for (a) the red dashed box and (b) the blue dashed box.

These features can be seen more clearly in a log-log plot of the measured response as is shown in Fig. 4.15. It is clear that the $SnCl_4$ sample requires a lower input intensity than the other samples to reach a given arbitrary count rate. For example, CCl_4 requires nearly an order of magnitude higher intensity to reach the same count rate. This result is consistent with the idea that the moment of inertia plays an important role in predicting the magnitude of the induced ME phenomena. As we will discuss in Chapter 5, a higher moment of inertia means a lower rotational frequency, which leads to enhancement of the nonlinear magnetic response. Table 4.1 provides values of the rotational frequencies measured by Raman spectroscopy following the work of Ref. [41]. The rotational frequency is lowest for $SnCl_4$ and highest for CCl_4 which is consistent with the results of Fig. 4.15.

Molecule	Mass (g/mol)	Rot. Freq. (cm^{-1})	B (poise^{-1})
CCl_4	153.82	775	13.4
$SiCl_4$	169.90	625	12.6
$SiBr_4$	347.47	525	5.5
$SnCl_4$	260.50	367	9.0

Table 4.1: Table showing physical values relevant to tetrahedral structures.

The enhancement mechanism for large magnetic response is not limited to the rotational frequency. The damping, or viscosity, of the molecular liquid should also be considered. This is because the magnetic response should have inverse proportionality with respect to both the rotational frequency and the damping, as

$$m(\omega) \propto \frac{1}{\Delta^2 + \Gamma^2} \,, \tag{4.4}$$

where Δ represents the rotational frequency and Γ is a damping term. Hildebrand and Lamoreaux provide several tables of damping parameters in their paper *Fluidity: A General Theory* [42]. The relevant damping parameter provided in their work is given as B in units of inverse "poise," which is a unit of viscosity. These values are also tabulated in Tab. 4.1. The damping in CCl_4 is largest, while the damping in $SiBr_4$ is lowest. There is an apparent correlation between the mass of the molecule and the damping. It is worth noting that, although both damping and rotational frequency appear as resonant denominators, the dominant factor in causing enhancement is the rotational frequency.

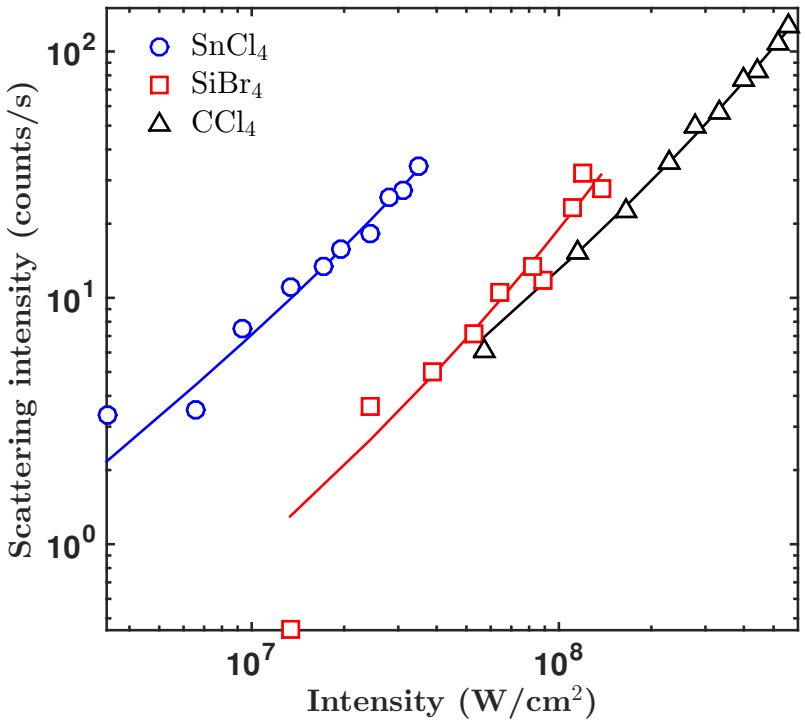

Figure 4.15: Log-log plot showing the amplitudes of the unpolarized electric scattering as a function of intensity in the liquid samples CCl_4, $SiBr_4$, and $SnCl_4$. Solid curves represent fits to second-order polynomials. The response in $SnCl_4$ is much higher than CCl_4, which suggests that molecules with a larger moment of inertia will more readily display this quadratic nonlinearity.

4.2.2 Scattering in molecules with delocalized π-electron orbitals

Here we present the first comparative analysis of several molecular liquids with π-delocalized electronic orbitals. These measurements included C_6H_6 (benzene), $C_6H_5NH_2$ (aniline), C_6H_5CN (benzonitrile), and C_6H_6 (deuterated benzene).

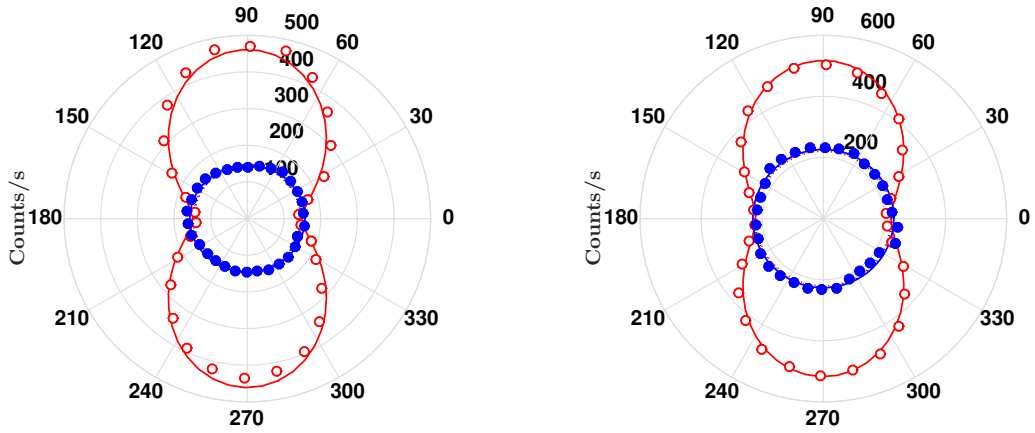

(a) Benzene

(b) Aniline

(c) Benzonitrile

(d) Deuterated benzene

Figure 4.16: Experimental intensity patterns for delocalized π-electronic benzene structures at $I = 1.9 \times 10^8$ W/cm^2. The red open circles (blue filled circles) represent electric (magnetic) dipole response. The unpolarized centers have not been subtracted, and there is no apparent polar response for any of the magnetic scattering.

The benzene and deuterated benzene only differ by having the outer hydrogen atoms of the benzene ring be replaced by deuterium atoms (heavy hydrogen). Because only the mass was changed while the structure remained the same, this provided a means to draw

some conclusions regarding the role of moment of inertia in the magnitude of the scattering intensities. Comparison of benzene with aniline and benzonitrile was intended to evaluate the importance of charge density inside the benzene ring in determining the ME response. The substitution of NH_2 in aniline pushed extra charge into the electron cloud, while the substitution of CN in benzonitrile pulled some of the charge out of the electron cloud. All measurements shown here are for an ED collection time of 5 s and MD collection time of 10 s with 4 periods.

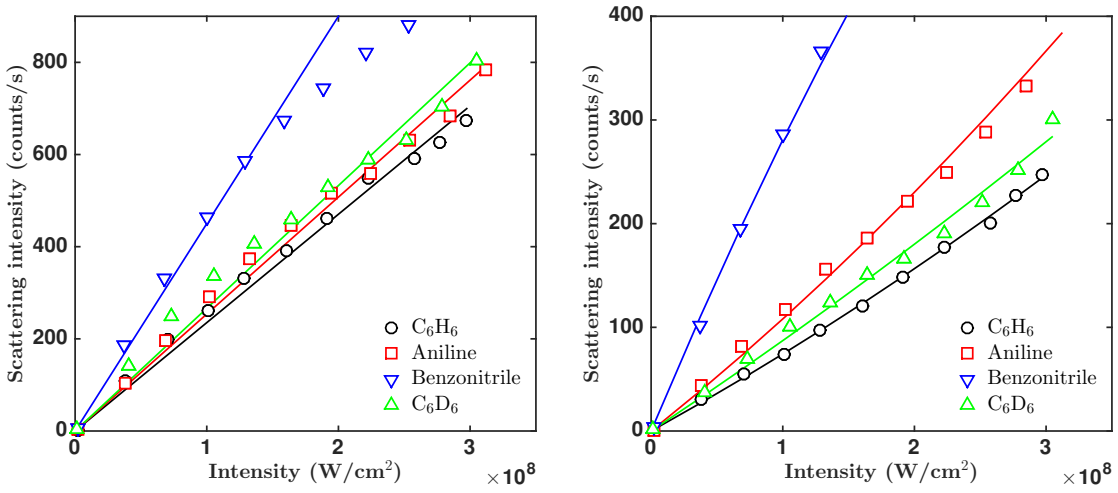

(a) Electric total

(b) Electric unpolarized

Figure 4.17: Experimental plots showing (a) the total electric response and (b) the unpolarized electric response in C_6H_6 (benzene), $C_6H_5NH_2$ (aniline), C_6H_5CN (benzonitrile), and C_6H_6 (deuterated benzene) as shown in the plot legends. The solid curves represent linear fits in (a) and quadratic fits in (b). The plot axes limit the response in benzonitrile because it was high and saturated the detector.

Experimental plots of the measured intensity patterns of the electric and magnetic response for the four benzene structures are shown in Fig. 4.16 at an input intensity of $I = 1.9\times10^8$ W/cm^2. The red open circles (blue filled circles) represent electric (magnetic) scattering amplitudes and the solid curves represent best fit lines according to Eq. (4.2). A striking feature of these plots is that there is no apparent polarized magnetic response in any of the data shown here. This may indicate that the intensity regime for measuring quadratic magnetic response is different from the range of intensities used here, or that the unpolarized electric response overwhelms any polarized magnetic response because a different mechanism is at work here. It is also apparent that the unpolarized electric response shown in these plots is much greater than was found in the tetrahedral molecules. The ratio of unpolarized to polarized electric response is lowest in benzene ($\sim$25%) and largest

in benzonitrile (∼70%). The unpolarized components of aniline, benzene, and deuterated benzene are closely grouped.

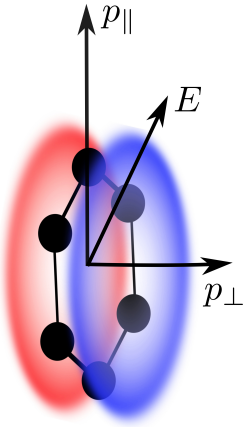

Figure 4.18: The anisotropy of a benzene ring leads to two different molecular polarizabilities and hence large depolarization.

Plots showing the measured dependence of the total electric signal and the unpolarized electric signal in the four benzene structures are shown in Fig. 4.17. This is from the same set of data shown in Fig. 4.16. No comparative analysis was done for the magnetic scattering since no polarized MD component was observed experimentally and the measured unpolarized waist was equal to the electric unpolarized waist. The total response was fitted using a polynomial of degree one and the unpolarized response was fitted using a polynomial of degree two. The response from benzonitrile was much larger than the other samples and caused saturation of the PMT above $\sim 1.5 \times 10^8$ W/cm^2, so the intensity range in the plots of Fig. 4.17 is limited to showing only unsaturated points. The curves through the benzonitrile data are just guides to the eye through the lowest intensity points. Not much can be concluded from the total electric response in Fig. 4.17(a) since the three curves from benzene, aniline, and deuterated benzene nearly overlap. However it is possible to draw some conclusions from the curves shown in Fig. 4.17(b).

We can see that deuterated benzene has a larger response than regular benzene, which is a confirmation that the moment of inertia plays a role in scattering, where rotations cause depolarization; C_6D_6 has a higher moment of inertia than C_6H_6. The average difference between the curves for benzene and heavy benzene can be calculated by taking the ratio of scattering intensities at each individual intensity point and then averaging over them. Ignoring the first set of points that are within the detector noise, this average gives 0.8396, or about 16%. This can be compared to the ratio of measured moments of inertia in the same two molecules from Ref. [43], as shown in Tab. 4.2,

$$R = \frac{\omega_{\varphi,\mathrm{C_6H_6}}}{\omega_{\varphi,\mathrm{C_6D_6}}} = \frac{147.59 \times 10^{-40}\ \mathrm{g{\cdot}cm^2}}{178.45 \times 10^{-40}\ \mathrm{g{\cdot}cm^2}} = 0.8271\ , \tag{4.5}$$

which is about 17%. Because these two numbers are in agreement with each other (within experimental uncertainty), this confirms that the moment of inertia is responsible for the response we are seeing. A larger moment of inertia corresponds to a lower rotational frequency through the relation $\omega_\varphi = \hbar/I$. Hence it takes less energy to initiate rotations of C_6D_6 than C_6H_6.

Molecule	Molar mass (g/mol)	Moment of inertia (g·cm^2)
C_6H_6	78.11	$(147.59 \pm 0.04) \times 10^{-40}$
C_6D_6	84.19	$(178.45 \pm 0.09) \times 10^{-40}$

Table 4.2: Table showing physical values relevant to benzene structures.

In molecules with anisotropy or permanent internal dipole moments, the electric field will readily induce rotations through a third-order, all-electric torque mechanism [7]. This differs from the second-order, electro-magnetic torque mechanism developed in Chapter 2. These two mechanisms are competing effects and the data from Figs. 4.16 and 4.17 suggest that for benzene structures the electric-torque effect overwhelms any magnetic-torque effect. This is due primarily to the anisotropy of the molecule, as there is no evidence of this effect in the tetrahedral structures where the electric-torque interaction cannot occur. This is obvious when we consider the polarizability of the benzene structures. Due to the distribution of charge in the π-delocalized orbitals, the induced polarizability along the plane of the structure $p_\parallel$ and normal to the plane $p_\perp$ will differ, as depicted in Fig. 4.18. This leads to huge depolarization and masking of any quadratic ME signal.

A comparison may also be made between benzene, aniline, and benzonitrile using Fig. 4.17(b). As mentioned above, the difference between these molecular liquids is the amount of charge centered on the benzene ring. One might naïvely suspect that when more charge is removed from the π-delocalized electron cloud (as in the case of benzonitrile), then the measured response would decrease, while at the same time, when more charge is introduced to the electron could (as in the case of aniline), then the measured response would increase. The prediction would then be that aniline would have the largest response, followed by benzene, and then finally benzonitrile. This is consistent with the idea that a denser electron cloud would be more susceptible to induced magneto-electric effects. However, we see instead (as is apparent in Fig. 4.17(b)) that benzonitrile has the largest response, followed by aniline, and then benzene.

It may not be initially obvious, but this is precisely the behavior that one would expect

for these three molecular liquids. As we described above, there is no measurable ME interaction taking place in this series of molecules and instead the response is overwhelmed by the all-electric torque mechanism. Since this mechanism relies on inducing rotations by virtue of acting on an internal dipole moment, the measured response will be largest in the molecule that has the greatest internal dipole moment. The effect of pushing charge into the π-delocalized orbital as in aniline or taking charge out as in benzonitrile will effectively increase the ratio of $p_{\parallel}/p_{\perp}$. The molecules ordered by increasing dipole moment are then benzene, aniline, and benzonitrile, which is exactly the trend shown in Fig. 4.17. A proper study of the dependence on the electron density will require benzene structures with symmetrically-substituted molecules so that no extra dipole moment is created.

The depolarization ratios for the four benzene derivatives are shown in Fig. 4.19. Fits to the magnetic data were constant lines and fits to the electric data were polynomials of order one. For each molecule the magnetic depolarization ratio is close to unity, indicating complete lack of observable polarized magnetic response, as seen in Fig. 4.16. The electric depolarization curves all have a positive linear slope, which indicates that the degree of depolarization is larger for higher input intensities. The same features that were discussed above are also apparent from these curves. We see that benzonitrile has the largest depolarized response, followed by aniline, and then benzene and deuterated benzene. It seems clear that the magnitude of the internal static dipole moment determines the effectiveness of electron torque-mediated depolarization in symmetric molecules like benzonitrile. This is in close agreement with previous experiments and theory on benzene derivatives [44]. On the other hand, the results of this chapter show that in spherical top molecules, depolarization takes place by a different mechanism, since electric torque interactions are absent.

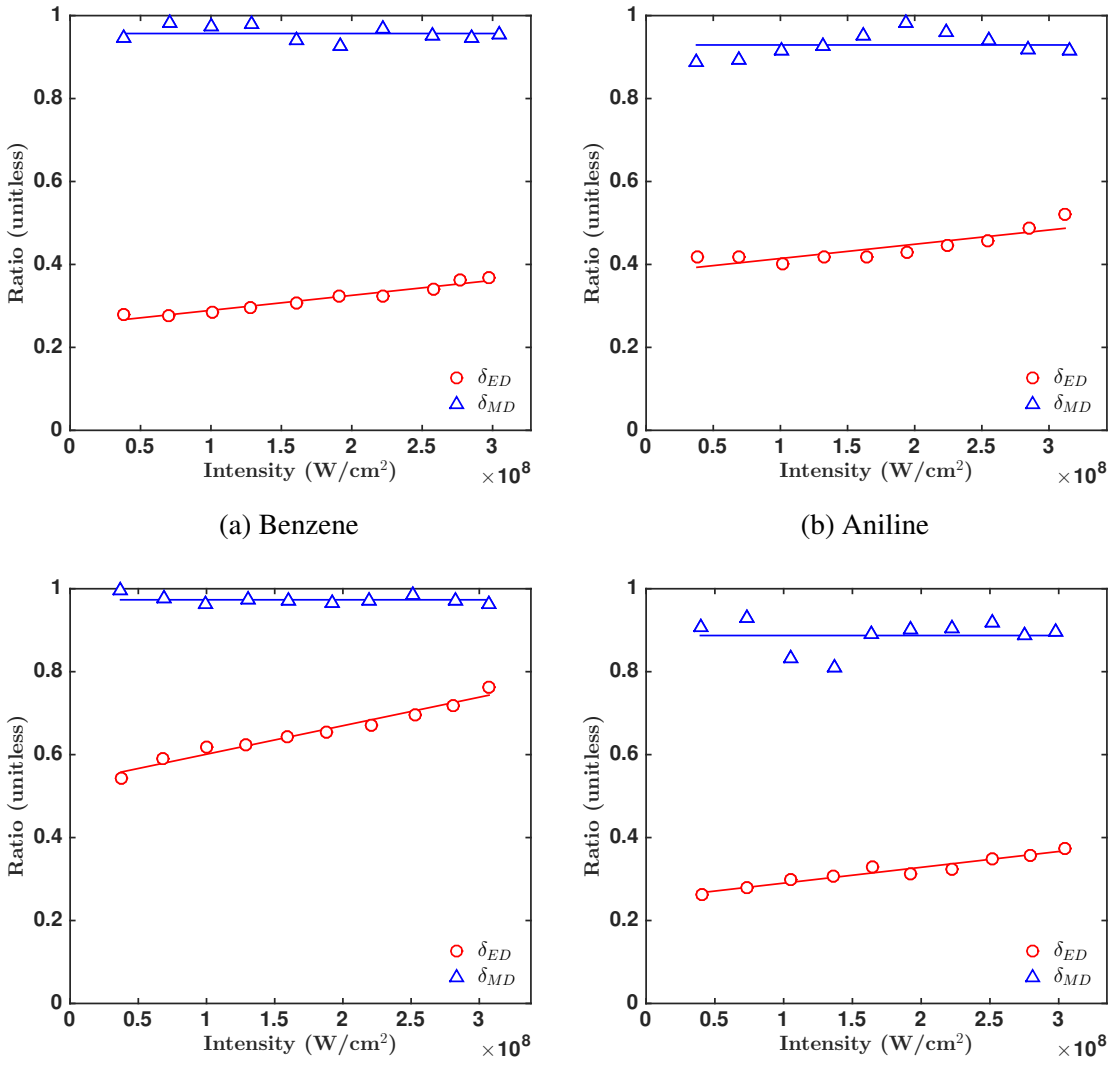

(a) Benzene

(b) Aniline

(c) Benzonitrile

(d) Deuterated benzene

Figure 4.19: The measured depolarization ratios for π-delocalized benzene structures. δ_{MD} is close to unity in each sample which indicates lack of a polarized MD component, while δ_{ED} in each sample is linear which indicates nonlinear unpolarized response.

4.2.3 Scattering in cubic solids

During the course of this research, the first observations were made of strong magnetic dipole scattering in the solid cubic garnet crystal GGG. The sample used had dimensions of approximately 1.5 cm $\times$ 1 cm $\times$ 1 cm and was polished on four of the six sides: the two 1 cm $\times$ 1 cm faces were polished and two of the 1.5 cm $\times$ 1 cm sides were polished. The incident beam was directed through the 1 cm $\times$ 1 cm face and traversed the full length of the crystal before exiting to a beam dump. The same techniques were used as described in Chapter 3 in which the intensity of the scattered light was mapped out for the analyzer in the vertical and horizontal positions over a range of input optical intensities. These curves were fit according to cosine-squared functions and the fitted parameters for the polarized and unpolarized components were extracted and plotted as a function of input optical intensity. The ED and MD collection times were both 10 s and 4 periods were used.

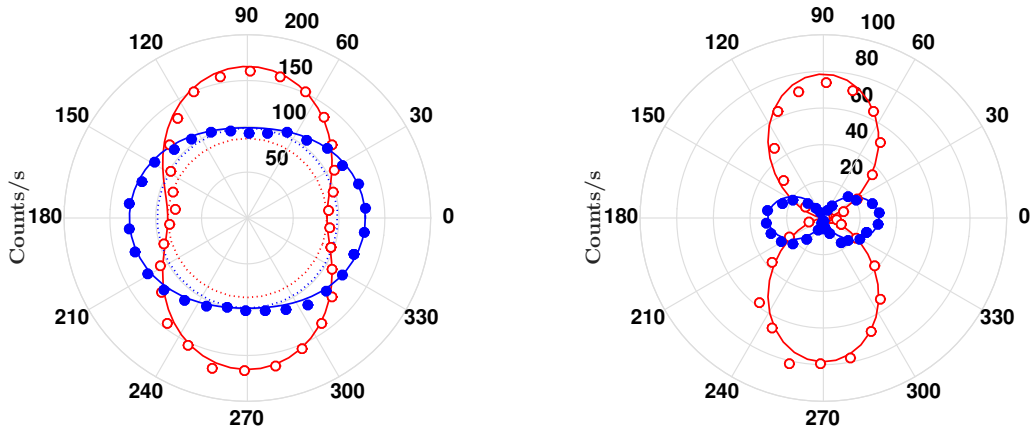

(a) Total signal

(b) Polarized signal

Figure 4.20: Dipole plots showing the measured electric (red open circles) and magnetic (blue filled circles) scattering intensities in the solid sample GGG at intensity $I = 10^8$ W/cm^2. (a) Shows the total signal (polarized + unpolarized) and (b) shows only the polarized component.

Figure 4.20 shows the measured dipole patterns for the electric and magnetic scattered light at $I = 10^8$ W/cm^2. The total signal, consisting of both the polarized and unpolarized components, is shown in Fig. 4.20(a), while Fig. 4.20(b) shows only the polarized components. The red open circles (blue filled circles) represent measured scattering amplitudes of the induced electric (magnetic) dipole moments. The solid curves represent least-squared fits to the data according to Eq. (4.2). Both electric and magnetic signals fit the cosine-squared patterns to a high-degree, indicating the precise dipolar nature of the

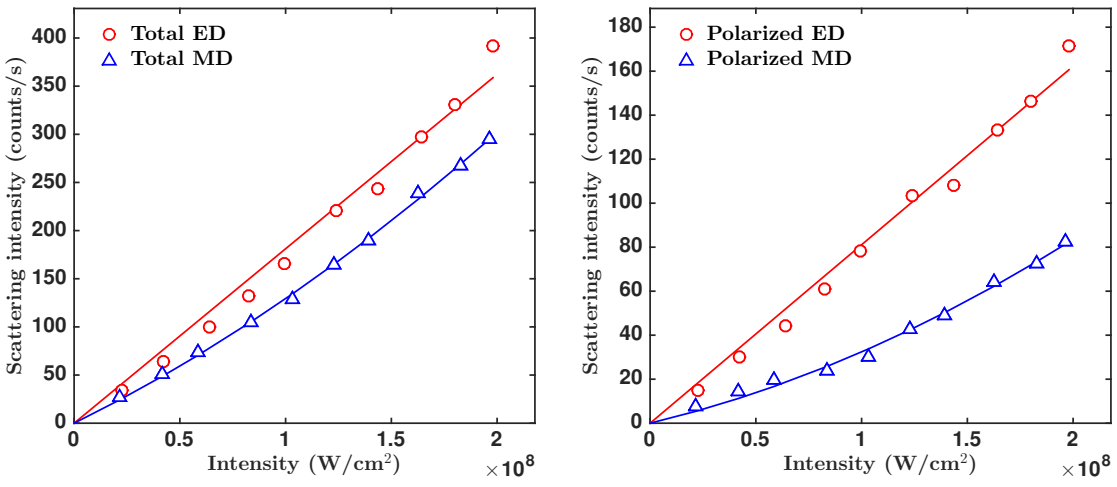

(a) Total response

(b) Polarized response

Figure 4.21: (a) Polarized + unpolarized and (b) polarized scattering intensities as a function of input optical intensity in solid garnet crystal GGG. Red circles represent electric scattering and blue triangles represent magnetic scattering.

signals. Surprisingly, the total magnetic and electric signals have a comparable amplitude as is evident in Fig. 4.20(a). Even with the removal of the unpolarized center, the ratio of the magnetic to electric signal strength is still much larger than the $\alpha^2 = 1/137^2$ expected from classical electrodynamics [12]. It is also evident that the unpolarized response for both electric and magnetic components is quite large.

The dependence of the amplitudes of the electric and magnetic scattering intensities on the input optical intensity are shown in Fig. 4.21. The total signal consisting of the polarized + unpolarized response is given in Fig. 4.21(a) while just the polarized component is shown in Fig. 4.21(b). The electric (magnetic) data was fit according to a least-squared polynomial of order one (two), indicated by the solid red (blue) curves. In both cases, the electric component has a linear dependence on optical intensity, which is not surprising due to the fact that this is linear Rayleigh scattering. The magnetic signal has an apparent quadratic dependence on intensity, which is evident in both plots. This result is in accord with the theoretical predictions of a second-order magneto-electric magnetization.

In Fig. 4.22 the unpolarized response for both the electric and magnetic signals is shown as a function of optical intensity. As expected, both signals are nonlinear. This result is in agreement with the scattering results obtained in experiments on tetrahedral molecules and will be discussed in further detail in Chapter 5.

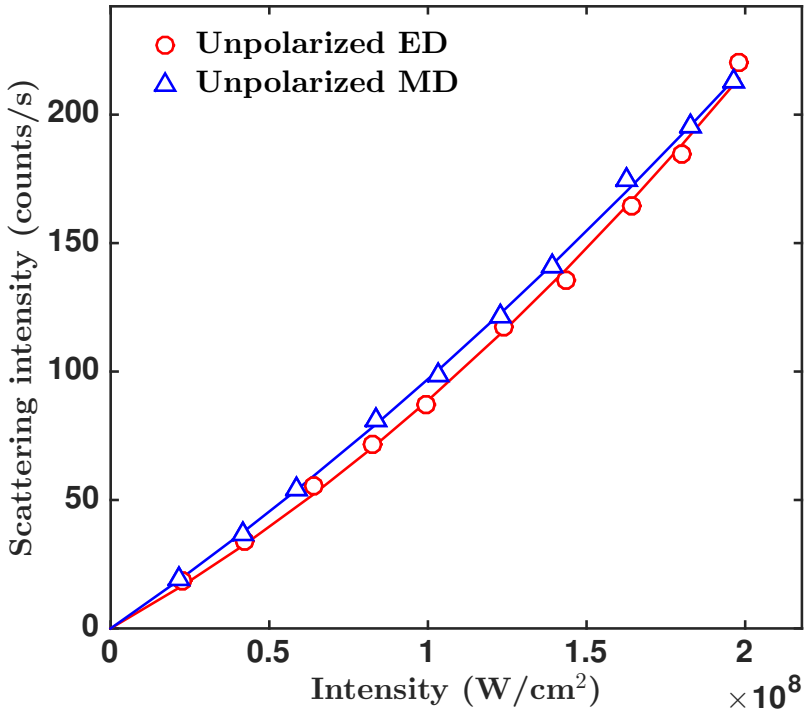

Figure 4.22: The unpolarized electric and magnetic scattering intensities as a function of input optical intensity for the cubic garnet crystal GGG. Solid curves represent second-order polynomial fits.

4.3 Theoretical results

The fundamental results of the two dressed state theoretical models are best summarized by plotting the dependence of the induced electric and magnetic moments on photon number n and frequency ω. The photon number is linearly proportional to the field intensity, so these plots provide a mechanism to easily determine the order to which the dipole moments depend on the optical field. The plots showing the dependence on the frequency ω (and in the molecular model ω_φ as well) allow us to confirm the detuning behavior for the 1- and 2-photon transitions. As per the discussion in Chapter 2, the moments may either be analyzed in terms of their individual dressed state components i, or as the net incoherent sum over all dressed state terms. Here we will show the intensity dependence for both cases, as it allows one to see more transparently which transitions are primarily responsible for the net induced effects.

Another set of useful variables to plot are the individual dressed state coefficients for each index (a_i, b_i, c_i, and d_i for the atomic case or just a_i, b_i, and c_i for the molecular case). Showing these moments as a function of n allows us to essentially measure the effect of turning on the interaction potential: as n becomes larger, the interaction is essentially stronger and the populations of the dressed state coefficients begin to change. These plots are also a confirmation that the ordering was done correctly in the numerical code. For example, we know that dressed state index $i = 1$ should correspond to the bare state $|1\rangle$, so a plot of a_1, b_1, c_1, and (in the case only of the atomic model) d_1 should show $a_1 = 1$ for $n = 0$ and all other coefficients starting at 0 before the interaction is turned on. These plots are perhaps the most straightforward way of predicting the end behavior of the induced moments.

Hence, in the following two subsections we show plots of the intensity dependence on the dressed state coefficients and the induced electric and magnetic moments, as well as plots of the detuning behavior. We do this first for the atomic model and then for the molecular model. Both models are able to correctly predict the qualitative features as measured in the scattering experiments, but only in the molecular model when a mechanism for enhancement is introduced can we predict quantitative agreement as well. The predicted magnetic response has the following four characteristics which agree with experimental results: (1) transverse orientation, (2) quadratic dependence on field, (3) oscillation at the laser fundamental frequency, and (4) amplitude equal or comparable to induced electric dipole effects. Points (1) and (3) are apparent from the derivations of Chapter 2, while points (2) and (4) are shown in the following plots.

4.3.1 Excited state atomic model

For the simulations shown in this subsection, atomic hydrogen was used to obtain the numerical values $\mu_\ell^{(e)} = ea_0\sqrt{2}\,(243/128)$ and $\mu_\ell^{(m)} = (e\hbar/2m_e)(1/\sqrt{2})$. Here the atomic detuning is specified by the first Lyman transition to be $\omega_0 = 15.5 \times 10^{15}$ s^{-1}. The interaction strengths were specified to be $g = 10^9$ s$^{1/2}$ and $f = (\mu_\ell^{(m)}/c\mu_\ell^{(e)})g$, where g is calculated from Eq. (2.9) and $\mathcal{V} = 10^{-16}$ is the mode volume. The detuning from 1- or 2-photon resonances is specified for each plot and all other physical constants are taken in SI units.

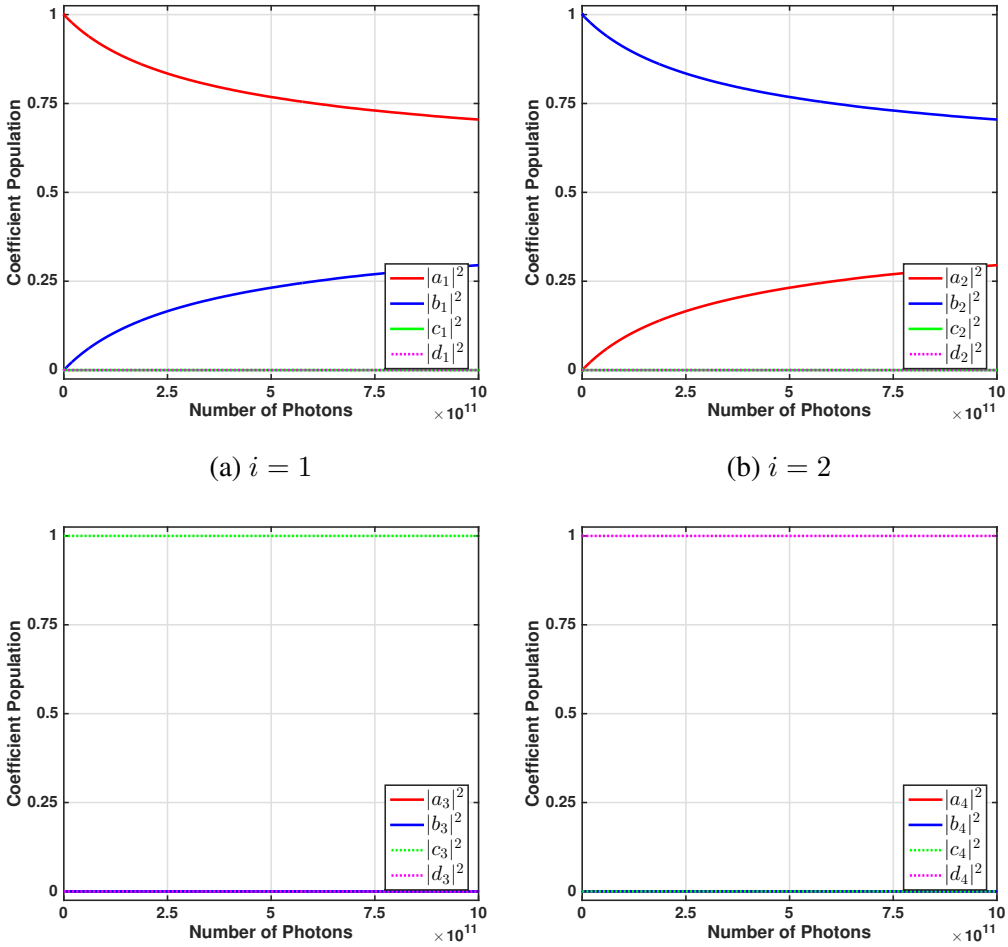

(a) $i = 1$ (b) $i = 2$

(c) $i = 3$ (d) $i = 4$

Figure 4.23: Dependence of dressed state coefficient populations on n for individual dressed state indices in the atomic model. Here $\omega/\omega_0 = 0.9$.

The dressed state coefficient amplitudes $|a_i|^2$, $|b_i|^2$, $|c_i|^2$, and $|d_i|^2$ are shown in Fig. 4.23 for each individual dressed state index. For instance, Fig. 4.23(a) shows the depen-

dence of the coefficient amplitudes for $i = 1$, which corresponds to the bare state $|1\rangle$. As one would expect, $|a_1|^2 = 1$ for $n = 0$ and only once the interaction is increased does the population begin to transfer to the other states. One can see that most of the population transfer goes to the coefficient b_1, while very little population is transferred to coefficients c_1 or d_1. This is not surprising in light of the fact that the populations $|c_1|^2$ and $|d_1|^2$ depend on the coupling from state $|2\rangle$ via the weak magnetic interaction (i.e. $f \ll g$).

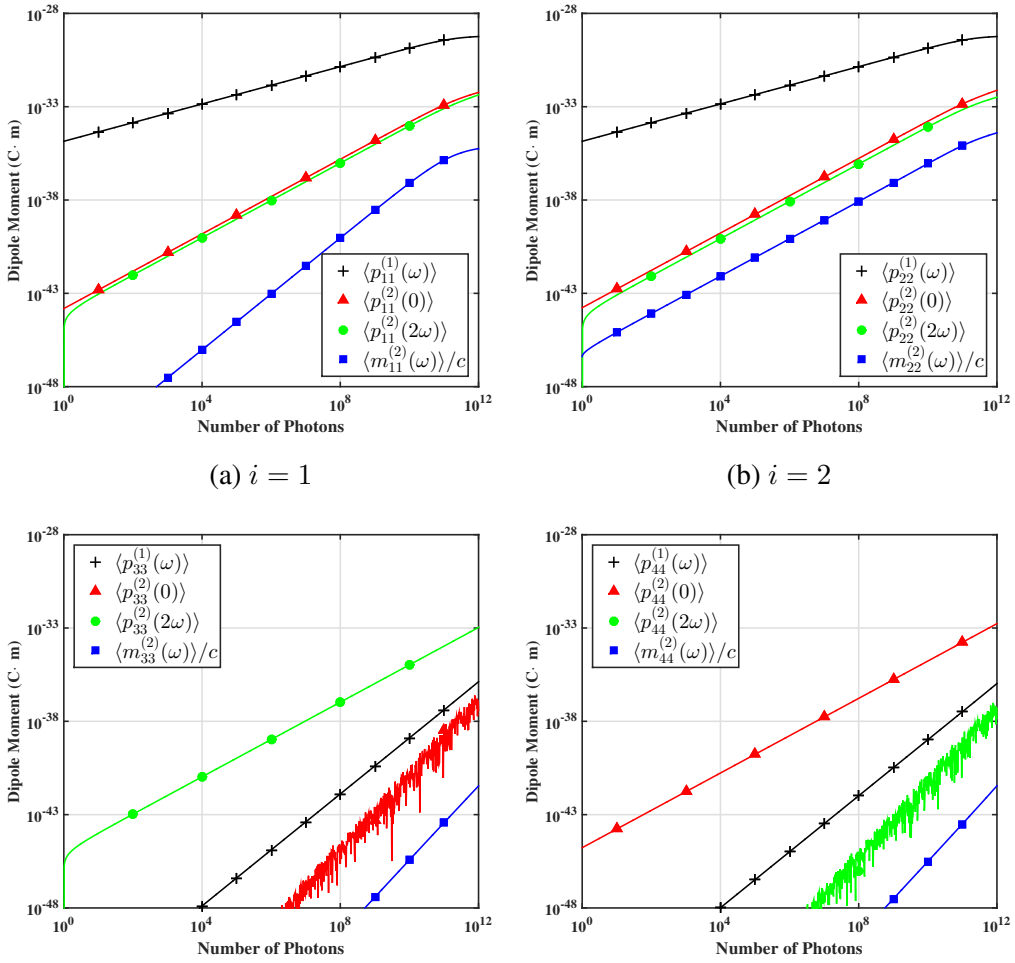

(a) $i = 1$ (b) $i = 2$

(c) $i = 3$ (d) $i = 4$

Figure 4.24: Log-log plots of the absolute magnitudes of induced electric and magnetic moments as a function of photon number in the atomic dressed-state picture. The magnetic moments were divided by a factor of the speed of light to make the units for all dipole moments C·m. The detuning was fixed at $\omega/\omega_0 = 0.9$.

The same behavior is seen for $i = 2$ except states $|1\rangle$ and $|2\rangle$ flip-flop. For indices 3 and 4, the population remains mostly in the initial state since the transfer to the adjacent states is mediated by the weak magnetic coupling. One may conclude just by looking

at these plots that induced dipole moments which terminate in states coupled to by the magnetic interaction will be quite weak. We can see this most directly by plotting the induced moments as a function of intensity.

From Chapter 2 we have several electric and magnetic moments which arise as a result of the magnetic interaction term in the Hamiltonian for $\omega/\omega_0 = 0.9$. Recall that these include the electric moments $\langle p_{ii}^{(1)}(\omega)\rangle$, $\langle p_{ii}^{(2)}(0)\rangle$, and $\langle p_{ii}^{(2)}(2\omega)\rangle$ as well as two individual magnetic moments whose sum gave $\langle m_{ii}^{(2)}(\omega)\rangle$. Plots of these moments are shown in Fig. 4.24 for each dressed state index. Computational precision errors are responsible for the erratic behavior seen in some of the curves. For indices 1 and 2, the electric moment shown by the black curve is in complete agreement with the linear electric moment from the 2-level system. These plots also show that the sum- and difference-frequency electric moments are both quadratic in the input field, while the magnetic moment is quadratic only for $i = 2$. The magnetization for $i = 1$ is fourth-order in the optical interaction, which means that this term requires a higher number of successive field couplings to reach its terminal state.

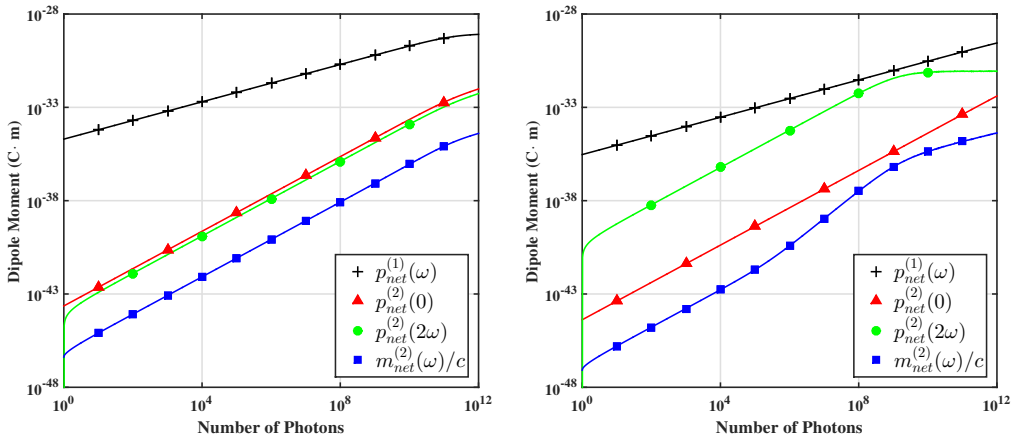

(a) $\omega/\omega_0 = 0.9$ (b) $\omega/\omega_0 = 0.49999$

Figure 4.25: Log-log plot of the incoherent sum of induced electric and magnetic dipole moments in the atomic picture. (a) A detuning of $\omega/\omega_0 = 0.9$ was used, while (b) shows enhancement of the second-harmonic effect and magnetization for the near-resonant 2-photon detuning of $\omega/\omega_0 = 0.49999$ (i.e. $\Delta_{31} \approx 0$).

The moments for indices 3 and 4 simply reflect additional higher-order contributions to the overall induced moments. These higher-order effects simply arise by virtue of the fact that the dressed state formalism includes dynamics originating from states other than the unperturbed ground state. It should be noted that as the driving field is tuned above the resonance condition (i.e. when $\omega > \omega_0$), the behavior of the moments for indices 1 and

2 flip character. This is because of the anti-crossing and exchange of character of levels $|D_1(n)\rangle$ and $|D_2(n)\rangle$. From these individual plots, we conclude that the magneto-electric moments are each of quadratic character to lowest-order.

It is more instructive to consider the incoherent sum over the dressed state index as a predictor of the measurable behavior from this model. A plot showing the net magnitudes for each of the dipole moments is shown in Fig. 4.25(a) for $\omega/\omega_0 = 0.9$. Here we see that the leading behavior of each of the magneto-electric moments is in fact second-order in the optical field. It is useful to point out that the curves $p(0)$ and $p(2\omega)$ differ by a numerical factor of 2 which comes from the additional inner-state coupling when the 0-frequency moment is evaluated. A 2-photon resonance which peaks at the condition $\Delta_{31} = 0$ is apparent in both $p(2\omega)$ and $m(\omega)$, as is shown in Figure 4.25(b). This is because these effects are mediated by the coupling of states $|1\rangle$ and $|3\rangle$. Here the input frequency was set to $\omega/\omega_0 = 0.49999$. The 2-photon resonance for the rectification moment relies on the detuning $\Delta_{41} \equiv \omega_0$, which cannot be shown by the results of this model. A 2-photon enhancement for the $p(0)$ moment is apparent in the molecular model, as will be described shortly.

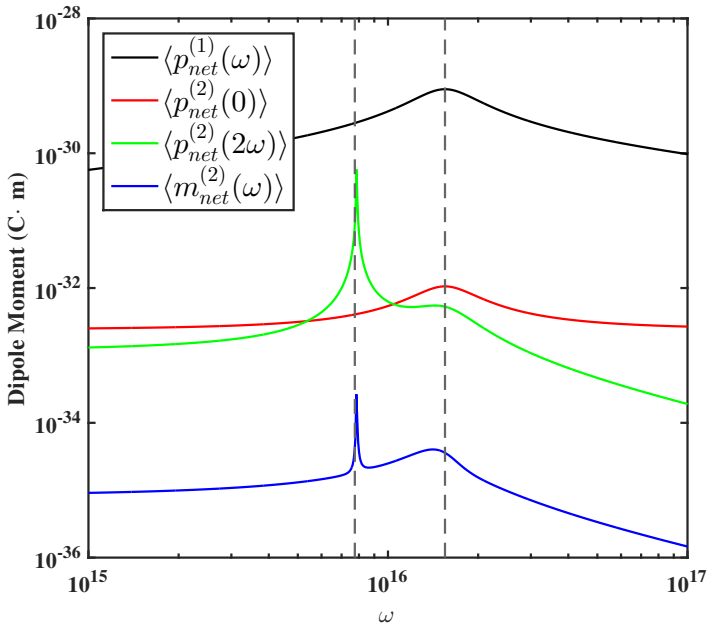

Figure 4.26: The resonant behavior for the dipole moments from the atomic model. The rightmost dashed curve is for the 1-photon resonance condition $\omega = \omega_0$ and the leftmost curve is for the 2-photon resonance condition $\omega = \omega_0/2$. Here $n = 10^{12}$.

The dependence on frequency detuning for the four moments of from this model are shown in Fig. 4.26. Here the photon number was taken to be $n = 10^{12}$ and ω was allowed

to vary over the range of approximately $0.1\omega_0$ to $10\omega_0$. Such a large input intensity was considered here so the detunings were more pronounced; a lower photon number means the interaction is effectively less intense and so the magnetically-driven resonant structures will not be as apparent. The grey dashed curves represent the conditions for 1- and 2-photon detunings. All four moments exhibit the 1-photon resonance condition when $\omega = \omega_0$ (rightmost grey curve). The second-harmonic also has an obvious resonance for the 2-photon resonance condition $\omega = \omega_0/2$ (leftmost grey curve). The magnetization also has a dependence on this detuning, which comes from the magnetization on the upper transition. This upper magnetic response is mediated by the $a_i c_i^*$ coherence.

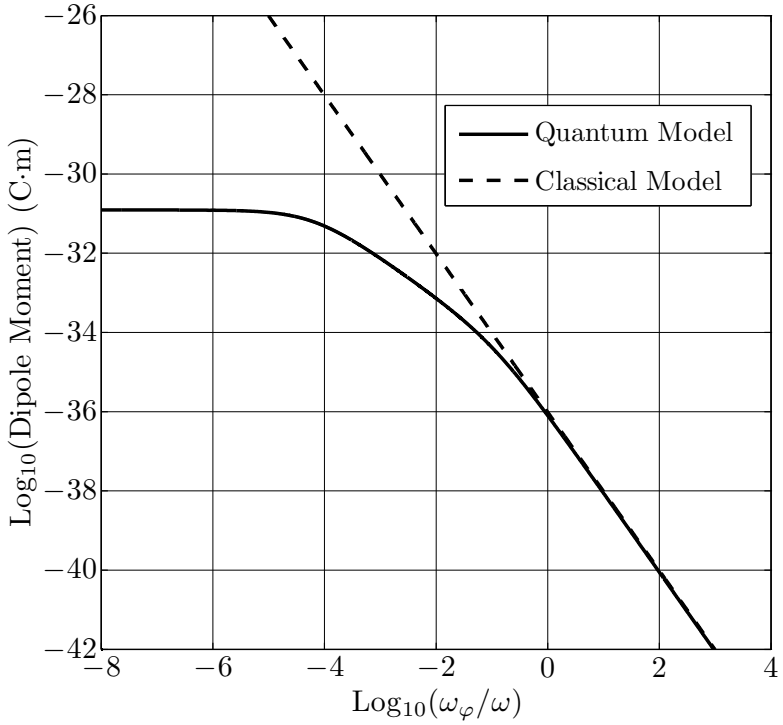

Figure 4.27: Comparison between classical and quantum models of the 0-frequency rectification moment. Due to normalization, the classical model has a physical limitation to how large it can grow.

It is also apparent from the figures showing the dependence of the induced ME moments on photon number that there is a physical limit to their magnitudes. This is due to the normalization that occurs when the matrix is diagonalized: the predicted moments each depend on a coherence product of two or more dressed state coefficients, all of which may at most be unity. This puts a physical limit to the size of the predicted effects, which is a shortcoming of the classical approach described in Chapter 1. In the classical model there is no mechanism for regulating the predicted response in the rectification term, so this can

be infinitely large. A comparison between the quantum and classical models is shown in Fig. 4.27.

The fact that all three types of nonlinear moment display the same inverse proportionality to the 1-photon detuning as the linear moment reflects the fact that these moments all require the first-order electric coupling of states $|1\rangle$ and $|2\rangle$ prior to any magnetic coupling. Combined with the fact that to lowest-order the nonlinear moments are quadratic in the field, this result confirms that the moments are in fact initiated by the joint action of sequential electric and then magnetic couplings. Regardless of the initial symmetry of the system, the inclusion of the magnetic coupling term in the Hamiltonian effectively breaks the symmetry of the system, thereby rendering quadratic moments of the type EB and $EB*$ possible. When the molecular model is considered quantitative agreement with experiments may also be found.

4.3.2 Ground state molecular model

For the simulations shown in this subsection, diatomic hydrogen was used to obtain numerical values for the atomic detuning and the electric and magnetic moment reference values. The atomic detuning is now $\omega_0 = 16.2 \times 10^{15}$ s^{-1}. The electric dipole amplitude was again taken to be $\mu_\ell^{(e)} = ea_0\sqrt{2}(243/128)$ and the effective magnetic dipole moment amplitude was taken to be $\mu_{eff}^{(m)} = c\mu_\ell^{(e)}$, in accord with the discussions of Chapter 2. The field coupling amplitudes were then $g = 10^9$ 1/s and $f = g$ with a mode volume of $\mathcal{V} = 10^{-16}$. The detuning from 1- or 2-photon resonances are specified in each plot and all other physical constants are evaluated in SI units. Full analysis is provided for the 3-state molecular system for which an analytic solution exists. This model will achieve quantitive agreement with the experimental results to within a factor of $\sqrt{2}$, and only when a fourth state is included in the basis is there complete quantitative agreement. Here we discuss both results.

The dressed state coefficient amplitudes $|a_i|^2$, $|b_i|^2$, and $|c_i|^2$ are shown in Fig. 4.28 where the detunings were taken to be $\omega/\omega_0 = 0.9$ and $\omega_\varphi/\omega_0 = 10^{-3}$. Contrary to the results of the atomic model, we immediately see that the states which are accessed via the magnetic interaction are more strongly coupled into the system. This is most obvious in Fig. 4.28(a) for which the population begins in state $|1\rangle$ and as soon as the interaction is turned on all three states are equally populated. The strong coupling via the magnetic interaction is explained by two key features of this model: (1) the assignment of the bare energy for state $|3\rangle$ which yields the 2-photon detuning $\Delta_{31} \equiv \omega_\varphi$, and (2) the choice of magnetic moment reference value $\mu_{eff}^{(m)} = c\mu_\ell^{(e)}$ which causes $f = g$.

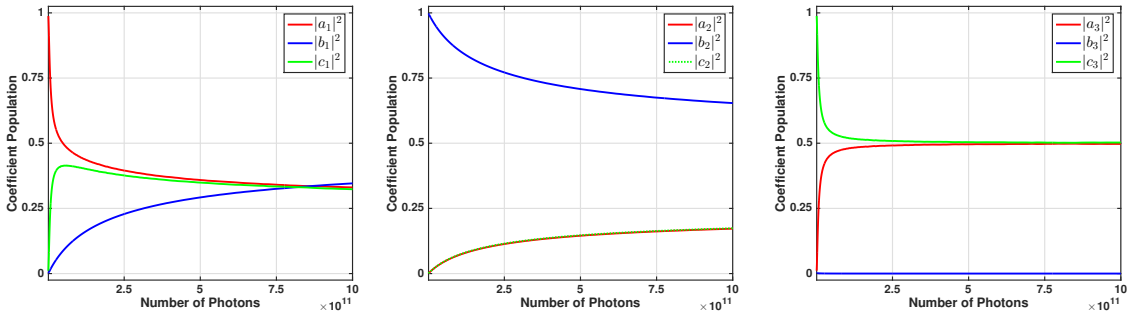

(a) $i = 1$ (b) $i = 2$ (c) $i = 3$

Figure 4.28: Dependence of dressed state coefficient populations on n for individual dressed state indices in the molecular model. Here $\omega/\omega_0 = 0.9$ and $\omega_\varphi/\omega_0 = 10^{-3}$.

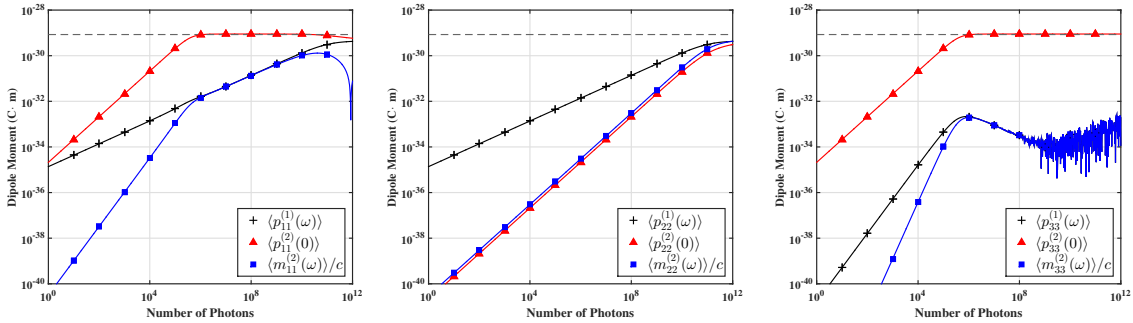

(a) $i = 1$ (b) $i = 2$ (c) $i = 3$

Figure 4.29: Log-log plot of the electric and magnetic dipole moments in the molecular model for individual dressed state index. The detunings were $\omega/\omega_0 = 0.9$ and $\omega_\varphi/\omega_0 = 10^{-7}$. The grey dashed curve is for the value ea_0.

The implications of strong magnetic coupling is more obvious when plots of the induced moments are given. For our choice of basis only two nonlinear moments are predicted: the 0-frequency electric moment $\langle p_{ii}^{(2)}(0)\rangle$ and the magnetic moment $\langle m_{ii}^{(2)}(\omega)\rangle$[3]. Plots of these moments along with the linear electric moment are shown in Fig. 4.29 for each individual dressed state index with $\omega/\omega_0 = 0.9$ and $\omega_\varphi/\omega_0 = 10^{-7}$. Again, for indices 1 and 2 the electric moment at ω is linear in the optical field and is in complete agreement with the results of the 2-level model. The leading behavior of the 0-frequency electric moment is quadratic for all three indices before the effect saturates at the value of ea_0 as shown in the grey dashed curve. The dependence on the magnetic term is quadratic for index 2 while higher-order for indices 1 and 3. Just as with the atomic model, the behavior of indices 1 and 2 flip-flop when the detuning is taken to be above the atomic detuning (i.e.

[3]The inclusion of additional terms in the basis would permit solutions for a second-harmonic electric signal, though it can be shown to be small compared to the other nonlinear effects predicted by this model.

$\omega > \omega_0$). This is due to the anti-crossing of states $|D_1(n)\rangle$ and $|D_2(n)\rangle$.

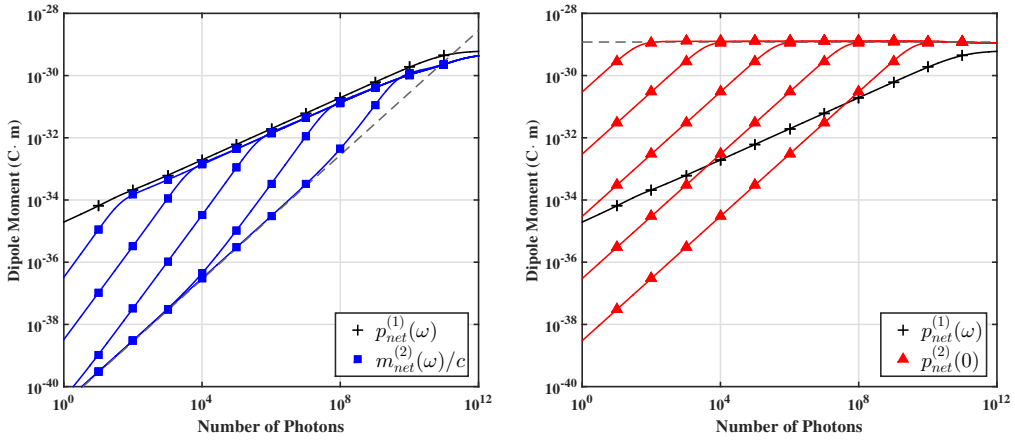

(a) Magnetization (b) Rectification

Figure 4.30: Log-log plot of the incoherent sum of (a) $\langle m^{(2)}_{net}(\omega)\rangle$ and (b) $\langle p^{(2)}_{net}(0)\rangle$ in the molecular model. The series of curves are for 2-photon detunings of $\omega_\varphi/\omega_0 = 10^{-11}, 10^{-9}, 10^{-7}, 10^{-5}, 10^{-3}$ from left to right in both plots. The 1-photon detuning is $\omega/\omega_0 = 0.9$. In (a) the dashed curve represents a quadratic dependence on input field while in (b) the dashed curve is for $ea_0\sqrt{2}$.

It is again more useful to plot the incoherent sum over dressed state index of the induced moments. Plots showing the net magnitudes of the magnetic and electric nonlinear moments are shown in Fig. 4.30 for the various 2-photon detunings of $\omega_\varphi/\omega_0 = 10^{-11}, 10^{-9}, 10^{-7}, 10^{-5}, 10^{-3}$. The 1-photon detuning is again kept at $\omega/\omega_0 = 0.9$. The effect of the 2-photon resonance is apparent in both plots: as $\Delta_{31} \equiv \omega_\varphi \longrightarrow 0$, the amplitudes of the induced effects are significantly enhanced. In Fig. 4.30(a) the magnetization has a quadratic dependence at low intensities before saturating, after which point it tracks the electric dipole. The agreement between the magnetic and linear electric curve is within a factor of $\sqrt{2}$, which is accounted for by including a fourth state in the basis, as explained shortly. In Fig. 4.30(b) the 0-frequency moment is seen to be readily enhanced and saturate at the value of $\sqrt{2}ea_0$, which is the physical limitation of this dressed state model.

Curves showing the resonance behavior of the three moments are shown in Fig. 4.31. For these curves the photon number was set to $n = 10^9$. Figure 4.31(a) shows the dependence on the input optical frequency. Here we see that all three moments have the same 1-photon detuning $\omega_0 - \omega$, again confirming that the other nonlinear effects implicitly rely on the coherence established in the first stage of the interaction. In Fig. 4.31(b) the dependence on the rotational frequency ω_φ is shown. There is a clear maximum for each of the nonlinear moments $p(0)$ and $m(\omega)$ for $\omega_\varphi \longrightarrow 0$, while the linear moment $p(\omega)$ shows no

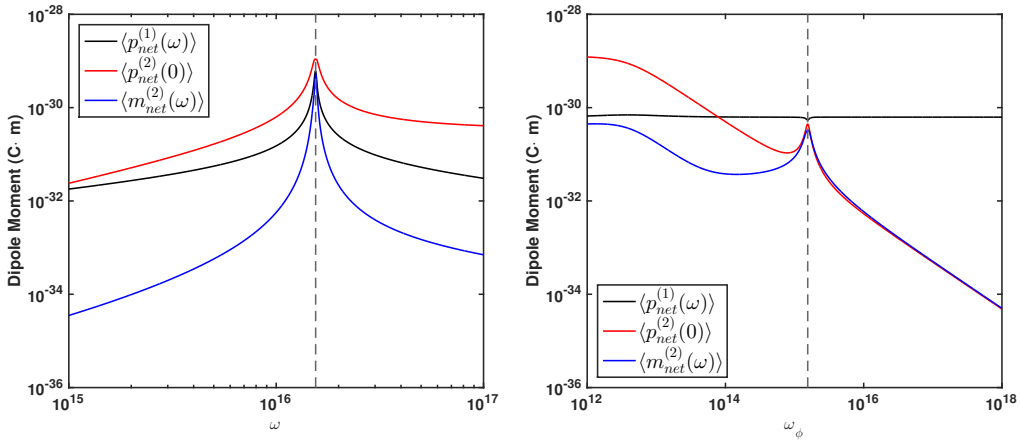

(a) 1-photon detuning (b) 2-photon detuning

Figure 4.31: The resonant behavior for (a) the 1-photon detuning and (b) the 2-photon detuning for the molecular model. In (a) the dashed curve represents the value $\omega = \omega_0$ and in (b) the dashed curve represents the value $\omega_\varphi = \omega_0 - \omega = 0.1\omega_0$.

dependence on this variable. The curves also reflect the 1-photon resonance which occurs at the condition $\omega_\varphi = \omega_0 - \omega$.

Finally, it is useful to compare the results of the 3-state molecular system with the 4-state molecular system. If the RWA is not made for the molecular model, then there is a fourth state in the system which has the electronic character $|2,1,1\rangle$. When included in the calculation, a fourth molecule-field product state defined as $|4\rangle \equiv |2,1,1\rangle\,|1,-1\rangle\,|n\rangle$ is defined and the eigenvalue equation is solved for the four coefficients a_i, b_i, c_i, and (now) d_i. The resulting fourth state permits another magnetic term to contribute to the overall magnetic moment, whose result yields complete quantitative agreement with the linear electric moment. These results are shown in Fig. 4.32. Both plots assume the same input parameters and the result of adding the fourth state apparently accounts for the factor of $\sqrt{2}$ between the $p(\omega)$ and $m(\omega)$ curves in the 3-state model.

Just as in the atomic case, all of the qualitative features – quadratic dependence on field, transverse orientation, and oscillation at ω – are present in this model. Only in the molecular model, however, can the quantitative agreement with large magnetic response as measured by the scattering experiments be explained. The enhancement to the magnetic response is only possible due to the unique property of the interaction Hamiltonian in that it couples internal (orbital) states to external (rotational) states via $\hat{L}_-\hat{O}_+$ coupling terms. This interaction process justifies the assignment of bare energy states which yield the unique 2-photon detuning of $\Delta_{31} \equiv \omega_\varphi$ and the choice of the magnetic moment reference value $\mu^{(m)}_{eff} = c\mu^{(e)}_\ell$. Both of these facts allow for near-resonant behavior in this model,

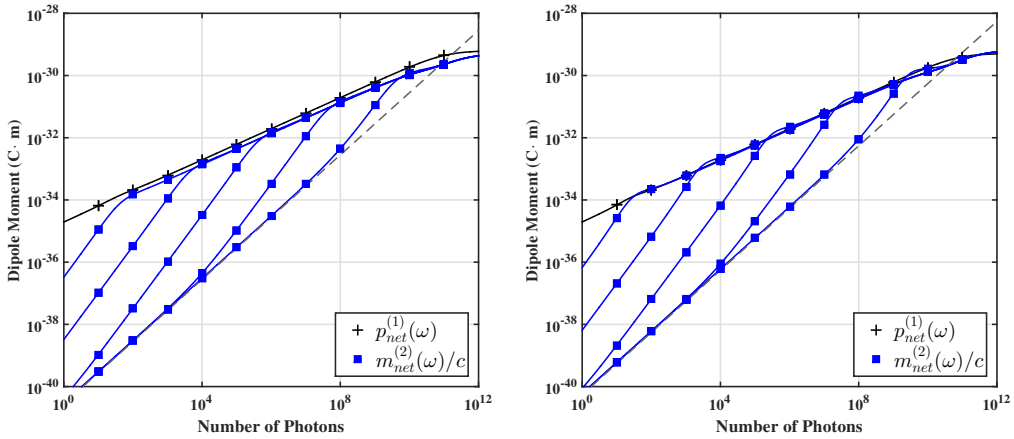

(a) 3-state model (b) 4-state model

Figure 4.32: Results for the magnetization in (a) the 3-state model and (b) the 4-state model. Complete quantitative agreement is found with the linear electric moment for the 4-state model. The series of curves are for 2-photon detunings of $\omega_\varphi/\omega_0 = 10^{-11}, 10^{-9}, 10^{-7}, 10^{-5}, 10^{-3}$ from left to right in both plots and $\omega/\omega_0 = 0.9$.

regardless of the 1-photon detuning, thereby permitting incredibly large magnetic response at modest input intensities.

CHAPTER 5

Conclusions

The final chapter of this thesis is split into five sections. In sections 1 and 2 we summarize the main qualitative and quantitative features from the experimental results and the theoretical models, respectively. In the third section we then draw comparisons between the experiment and theory and describe what these conclusions imply for high-frequency magnetism. The fourth section outlines several other experimental platforms that are either currently in use or in development for measuring this family of ME nonlinear effects. In the fifth and final section, we discuss the outlook for further experiments using the magnetic-scattering system that was developed for this thesis.

5.1 Summary of experimental results

The main experimental results of this thesis may be summarized as follows. The intensity of elastically-scattered light polarized perpendicular to Rayleigh scattered light in non-chiral, non-polar, symmetric dielectric media was measured using a 90° detection geometry. The chosen class of materials avoids all mechanisms which can give rise to spurious signals from the rotation of any initial electric dipole polarization. The choice of geometry also eliminates signal contributions from other nonlinear optical phenomena such as the Raman-induced Kerr effect [45]. The measured signals had a quadratic dependence on intensity, the same frequency as the laser, and in some instances had amplitudes which rivaled that of linear Rayleigh scattering. It was found in most samples that the unpolarized components of the signals measured in both co- and cross-polarized analyzer positions had a nonlinear dependence on input intensity, as expected. In others, a nearly linear dependence was observed which appeared to be saturated. The qualitative features of these signals point to their origin as being magnetic, in accord with previous experimental findings [2] and theoretical predictions [5, 6, 46].

Two series of molecular liquids were studied to provide insight as to which physical

parameters are important for achieving large magnetic response. In the study of non-polar, "spherical-top" tetrahedral molecules, it was found that the polarized magnetic response increased with heavier molecules which had larger central atoms or larger moments of inertia. The same trend was observed for the unpolarized response of ED and MD signals, which increased nonlinearly with input intensity and was largest for the most massive molecular liquid. These results are consistent with the expectation that molecules with a smaller rotational frequency and lower damping [47] will more readily exhibit resonantly-enhanced behavior. This is true because both the rotational frequency and the damping show up as theoretical contributions to the denominator for this type of effect. The dressed state model accounts for the dependence on rotational frequency but ignores the possible contribution from damping.

In the second study of systematically-varied molecular liquids, we studied a series of benzene-like molecules which had varying degrees of differential polarizability and in some cases internal dipoles. In these molecules, there was very little polarized magnetic response and the unpolarized electric scattering was shown to be up to 70% of the total measured signal. The relative weakness of magnetic signal strength can be attributed to the preponderance of a third-order all-electric interaction that is responsible for intense rotationally-averaged (unpolarized) scattering in anisotropic liquids [7]. This effect also explains why benzonitrile, with the largest permanent dipole of the series, showed the largest percentage of unpolarized signal, while benzene, with no static dipole whatsoever, showed the smallest response. The dependence of the measured response on the rotational frequency was consistent with the ratio of moments of inertia when benzene and deuterated (heavy) benzene were compared. The relative slopes of unpolarized scattering for these two molecules differed by 17%, with C_6D_6 having the higher cross-section for unpolarized scattering. This is consistent with the ratio of moments of inertia [43],

$$R = \frac{\omega_{\varphi,\mathrm{C_6H_6}}}{\omega_{\varphi,\mathrm{C_6D_6}}} = \frac{147.59 \times 10^{-40}\ \mathrm{g{\cdot}cm^2}}{178.45 \times 10^{-40}\ \mathrm{g{\cdot}cm^2}} = 0.8271\ , \tag{5.1}$$

of these two molecules.

It was also shown for the first time that intense, nonlinear magnetic response is present in solid garnet crystals which have centrosymmetry. The crystal studied was $Gd_3Ga_5O_{12}$ which is a rare-earth garnet crystal from the space group $Ia\bar{3}d$ (or point group O_h or $m\bar{3}m$, depending on notation). Most important is that this crystal has cubic symmetry so that $\chi^{(2)}$-driven quadratic nonlinearities of the type EE or EE^* were forbidden, meaning that any second-order response measured in our experiments must be driven by the (new) process anticipated by our model of ME dynamics. Here the polarized magnetic response and the

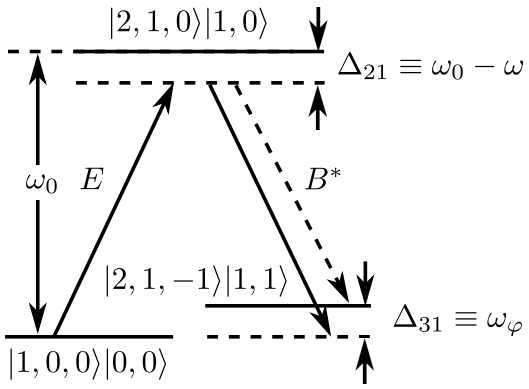

Figure 5.1: Depiction of electric and magnetic transitions driven between uncoupled states of the molecular dressed-state system. The dashed curve on the magnetic transition represents a completely resonant, inelastic transition that may account for nonlinear unpolarized scattering.

unpolarized response for both electric and magnetic signals had a nonlinear dependence on field that was best fitted by a quadratic component, albeit over a limited range. Furthermore, the total magnetic (polarized + unpolarized) signal was shown to be comparable in amplitude to the linear Rayleigh signal. A series of measurements were also made of light in the forward-direction to confirm that no XPW generation [23, 24] was taking place over the range of intensities shown in the plots of Chapter 4.

The third-order, all-electric interaction responsible for the depolarizing molecular rotations in benzene cannot take place in either GGG or any of the tetrahedral structures. In optically isotropic GGG, free rotations are prevented by the rigid crystal structure and in molecules isomorphic to CCl_4, the presence of spherical top symmetry prohibits polarization anisotropy. Consequently our observations of polarized quadratic components in these samples suggest a very different origin of the scattering, consistent with magnetic torque from the second-order, magneto-electric interaction. The presence of unpolarized background scattering with quadratic intensity dependence can be accounted for as well by second-order magneto-electric torque dynamics. This was shown by predictions of the exact dressed state model. The presence of polarized and unpolarized components in the magnetic scattering is made possible by the use of ultrashort pulses with sufficient bandwidth to excite both solid and dashed downward transitions in Fig. 5.1, offering a new explanation of librational excitation and depolarization. That is, depolarized scattering can be mediated by the magneto-electric process, pointing to a novel, universal mechanism for generating rotations and magnetism in natural materials.

5.2 Summary of theoretical results

An exact, fully-quantized model was developed in two stages to explain these unexpected experimental results. In stage 1 (dubbed the atomic model) and stage 2 (dubbed the molecular model) it was shown that by accounting exactly for a sequence of electric and magnetic interactions of light, dynamic symmetry breaking takes place in an initially centrosymmetric system. Interestingly, these results are in general accord with classical calculations of bound electron motion driven jointly by E and B fields [16] which showed that the electron distribution is no longer centered on the nucleus when the magnetic field acts, thereby causing an asymmetry in the system and allowing quadratic nonlinearities to form. Similarly in the dressed state approach, inversion ceases to be a symmetry of optically-driven charge systems subjected to strong Lorentz forces, thereby enabling new nonlinear processes. From this theory, three second-order optical nonlinearities that are magneto-electric in origin were predicted: longitudinal rectification at 0-frequency, longitudinal harmonic generation at 2ω, and transverse magnetization at the fundamental frequency. These effects exist purely due to the inclusion of the dynamic magnetic interaction term. The transverse magnetization in particular is not compatible with any static symmetry analysis of the medium. Consequently, dynamic symmetry breaking indicates that these phenomena may be observed universally, in natural materials. Specifically, all transparent dielectric materials and semiconductors (in the forbidden energy gap) are predicted to support these quadratic ME nonlinearities.

The theory presented in Chapter 2 effectively explained the four key features of the magnetization observed in the scattering experiments: (1) transverse orientation with respect to the propagation axis, (2) quadratic dependence on the input field intensity, (3) oscillation at the fundamental frequency, and (4) amplitude equal or comparable to electric-dipole scattering. Both atomic and molecular models correctly predicted the first three features, but only the molecular model was able to explain the unusually large amplitude of the magnetic response (quantitatively equal to that of Rayleigh scattering). The amplitudes of the predicted magnetic response in the atomic model were very small because of the large 2-photon detuning factors. The small magnitudes of induced moments in turn derived from the choice of bare-state energies, which forced the magnetic transitions to take place in the excited state far off resonance. This resulted in weak mixing of magnetic states into the system [46]. Much better agreement with the experimental results was found using the molecular model in which rotational degrees of freedom were included and a magnetic torque interaction was introduced. This permitted enhancement in two ways. First, the terminal state was chosen to have energy close to the electronic ground state, recogniz-

ing that magnetic torque transfers angular momentum into rotational angular momentum, thereby causing electronic de-excitation of the molecule. This enables a nearly-resonant 2-photon magneto-electric transition. Second, the magnetic interaction coupled internal atomic states to external molecular states with much larger cross sectional areas and therefore larger effective magnetic moments.

It should also be emphasized that in both of the dressed state approaches, standard quantum mechanical selection rules were obeyed in all matrix elements that contributed to the magneto-electric state mixing by the E and B fields or the induced moments. Consider for example the atomic system, for which the customary rules for ED and MD interactions are ($\Delta\ell_{ij} = \pm 1$; $\Delta m_{ij} = 0$) and ($\Delta\ell_{ij} = 0$; $\Delta m_{ij} = \pm 1$), respectively. Here the subscript notation refers to the dressed state components (not the dressed state index), as $1 \leftrightarrow |1\rangle$, $2 \leftrightarrow |2\rangle$, and so on. For example, the non-zero contribution to the magnetic moment between dressed states $|D_1(n)\rangle$ and $|D_1(n+1)\rangle$ is $\langle \hat{m} \rangle \propto \langle n|\langle 2,1,0|\hat{L}|2,1,-1\rangle|n\rangle$, which obeys the rules $\Delta\ell_{24} = 0$ and $\Delta m_{24} = +1$ for an MD transition. The same was true for the other nonlinear moments of the atomic model as well as the predictions of the molecular model.

5.3 Comparison of experiment and theory

The main results of this thesis are most obvious when we compare the experimental results with the predictions of the theoretical model, namely the observation and explanation of intense high-frequency magnetic radiation induced by the passage of light through transparent, dielectric media. Scattered light with the polarization of induced magnetic dipoles was found to be transverse to the direction of propagation, oscillated at the fundamental frequency, and increased with a nonlinear dependence on the input field. We experimentally demonstrated in both solid and liquid samples that the magnetic component of scattering was purely dipolar in nature, was nonlinear in origin, and was comparable in intensity to electric-dipole scattering under non-relativistic conditions.

These unprecedented results are in full quantitative agreement with the exact dressed state model with quantized energy levels and fields. Resonant enhancement of the ME nonlinearities was more than sufficient to make up for the usual factor distinguishing electric from magnetic moments, namely the fine structure constant, $\alpha \doteq 1/137$. This was shown to arise due to a magnetic torque mechanism. The experiments also showed that unpolarized scattering components grew nonlinearly as a function of intensity, again consistent with the molecular quantum picture, and pointed to the presence of two possible magnetic transitions as in Fig. 5.1. The comparisons of systematically-varied molecular

systems also provided evidence for the importance of moment of inertia and damping as key physical parameters for enhancing the magnetic response. A second systematic study using anisotropic molecular liquids showed that when an internal electric dipole moment is present, ME response is most likely overwhelmed by an electric torque mechanism through which the electric field induces depolarizing molecular rotations.

The dressed-state models which were developed to explain these unusual experimental findings provided a more detailed picture of the ME nonlinear effects than the earlier classical approach [5] or Heisenberg picture [6]. The dressed state approach is able to predict the same trio of nonlinear effects as these earlier methods, and is exact within the Born-Oppenheimer, dipole-, and rotating-wave approximations. The predicted trio of optical processes from the dressed state approach all share a common 1-photon detuning, as well as a 2-photon detuning which depends on the terminal state accessed by the magnetic interaction. These detunings reflect the fact that the trio of nonlinear effects are sequential electro-magnetic processes, whereby the electric field must first establish a charge distribution and then the magnetic field may act on it. Most importantly, the theoretical model developed herein provides a convincing explanation for how high-frequency magnetic response may be initiated and measured in natural, unstructured media at moderate optical intensities.

The findings of this thesis research suggest that several other magneto-optical phenomena should be observable at low intensities. This includes the rectification moment $p(0)$ and ME second-harmonic generation $p(2\omega)$ which are predicted by the theoretical model. Several experimental platforms are already in use or being developed to study these effects, the details of which are described in the next section of this chapter. Several less-obvious magneto-optical effects may also be observable. Magneto-electric contributions to the nonlinear index n_2, optically-induced Faraday rotation, and negative permeability are among some of the anticipated effects, as described in Ref. [2]. Of these, perhaps most impactful would be negative permeability which could greatly advance the fields of dielectric metamaterials [8] and and the development of dynamic magnetic materials [48]. Negative permeability in natural materials could provide low-loss approaches to the fields of subwavelength imaging [49], magnetic mirrors [50], nanolithography [51], and electromagnetic cloaking [52]. Findings in this field may shed ligh on the general class of phenomena known as Hall effects, [53, 54], of relevance to energy conversion. It has been suggested that the rectification term $p(0)$ may allow for conversion of sunlight to electricity with near-unit efficiency [16]. These are just a few of the areas which may see advances due to the experimental and theoretical work of this thesis; essentially *any* known electro-optic effect may have a magneto-optic counterpart and a corresponding enhancement mechanism.

5.4 Alternative platforms for measuring ME effects

Analysis presented earlier in this thesis predicts that magnetization is just one of three magneto-electric nonlinear processes which may be induced by light in *any* dielectric medium, regardless of symmetry. This family of effects includes the rectification moment $p(0)$, magneto-electric second-harmonic generation $p(2\omega)$, and magnetization $m(\omega)$. Naturally, other platforms could be developed to study each of these nonlinear effects using techniques different from those described above. In this section we briefly describe some of the current efforts along these lines.

5.4.1 Rectification effect

The rectification term $p(0)$ is predicted to be large by the molecular quantum model presented in this thesis. This effect consists of a net charge displacement in a dielectric medium in the forward direction, parallel to the path of the incident light. The action of the optical field to separate charge along the direction of the beam is due to light pressure and two distinct approaches can be imagined to measure this effect. The first approach uses direct detection of a static field created by a cw or long-pulse laser passing through a bulk crystal. The second approach uses an ultrafast pulsed laser to impulsively excite the sample, leading to the formation of a transient electric dipole moment that will radiate single-cycle THz pulses.

5.4.1.1 Direct detection of DC field

In direct detection of the rectification moment, a static voltage must be established over the interaction length of the entire sample. This voltage would need to be measured using a high-sensitivity circuit design [16, 4]. There are two way of theoretically achieving an end-to-end rectification moment such as this: either using cw illumination in a bulk crystal or using pulsed illumination with an ultra-thin sample. In either case, an optically-transparent coating such as indium tin oxide (ITO) must be deposited on the entrance and exit faces to allow for the passage of light while also conducting the generated electrical signal. The dimensions of the electrodes and the spacing between them are both critical factors for maximizing the detectable signal, but these are limited by the choice of light source. This is because a minimum intensity of the order 10^7 W/cm^2 is required to see these effects [16], so either a cw source must be focused through the sample or the thickness of the sample must be chosen so an optical pulse completely fills it from end-to-end.

To give an example, if a 10 W cw laser is used then the cross sectional area of the

electrode must be of the order 100 μm^2 which is small enough to make its alignment with the beam difficult. It is more desirable to have larger electrodes, but this requires using a pulsed laser[1] to achieve a higher power density. The primary concern in this case is that the thickness of the sample L is related to the pulsewidth τ_p of the laser through the relation $L < c\tau_p$. With either the cw or pulsed approach, electro-magnetic interference (EMI) may overwhelm the small signals, although the closely-related photon-drag effect [55, 56] has been shown to produce Lorentz-driven signals in layers of graphene as well as THz signals from conductors irradiated with short pulses [57].

5.4.1.2 Impulsive detection of DC field

A promising approach for measuring ME rectification is to impulsively excite a dipole and then measure the field radiated by the time-varying charge distribution it creates. This can be done by sending an ultrafast optical pulse (with duration $<$ 1 ps) into an insulating dielectric medium. Inside the medium a quasi-static rectification moment is generated each time an optical pulse passes a fixed point. This in turn generates a local time-varying current density, which in turn produces an electromagnetic signal. Due to the ultrashort nature of the light, the generated signal will be a THz electric field [58]. This electric field can be calculated from the polarization by first noting how the current density relates to the polarization,

$$\mathbf{J}(t) = \frac{\partial \mathbf{P}(t)}{\partial t} \ , \tag{5.2}$$

Then the current density becomes a source term for the THz electric field,

$$\mathbf{E}_{\text{THz}}(\mathbf{r}, t) \propto \frac{\partial \mathbf{J}(t)}{\partial t} \ . \tag{5.3}$$

Substituting Eq. (5.2) into Eq. (5.3) shows that the THz field is proportional to the second time derivative of the quasi-static polarization according to

$$\mathbf{E}_{\text{THz}}(\mathbf{r}, t) \propto \frac{\partial^2 \mathbf{P}(t)}{\partial t^2} \ . \tag{5.4}$$

From Eq. (5.4) one can estimate the shape of the THz electric field given that the input optical pulse is a Gaussian in time. Then $\mathbf{P}(t)$ will have a Gaussian distribution and the THz field will be a single-cycle electric signal as shown in Fig. 5.2. This is easier to see in the frequency-domain by mixing two optical fields since $p(0) \propto EB^*$. If the input fields

[1] This is the case because cw lasers with output power greater than 10 W or so are not practical or typically available in laser labs.

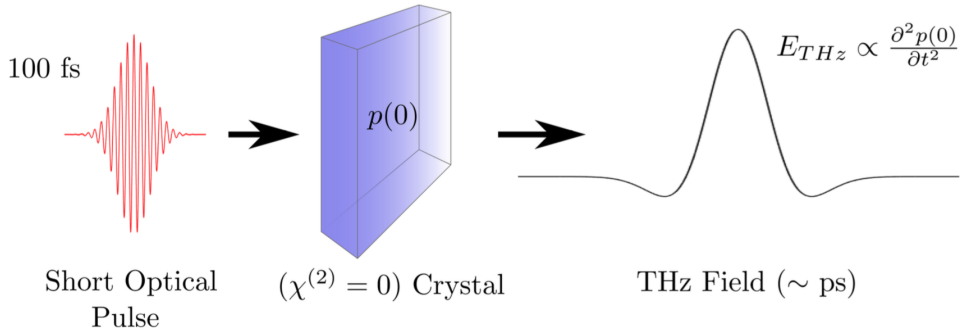

Figure 5.2: The generated THz field is proportional to the second time derivative of the envelope of the input electric field.

are from one and the same spectral mode then the fields will mix to yield $\omega - \omega = 0$. When an ultrafast pulse is used, all of the spectral components in the laser bandwidth $\Delta\omega$ are mixed, and the resulting spectrum extends from 0-frequency to a few THz.

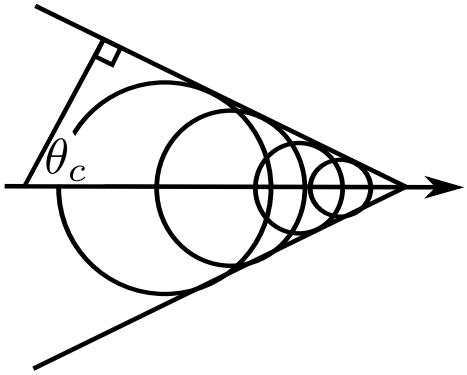

Figure 5.3: Wavefront diagram of Cherenkov-like cone produced by the difference in THz and optical refractive indices [3].

This technique of generating a THz signal from the magneto-electric polarization $p(0)$ is analogous to optical rectification (OR), which is one of two standard techniques used for converting an optical pulse to a single-cycle THz field [59]. In conventional OR, the rectification term is only possible due to difference frequency generation (DFG) in which two electric fields are mixed in a non-centrosymmetric medium. In other words, $p(0) \propto EE^*$. To be distinguishable from an all-electric process, ME rectification must be performed in centrosymmetric media. In either case the THz electric field will radiate in the forward direction. Due to this fact, the same approach used for detecting THz radiation via traditional OR may be used to detect the ME THz signal. This also means that the same issues which the conventional OR signal detection apply in the ME case. The two crucial conditions which must be met to maximize the measured signal are phase- and index-matching.

Phase-matching puts limitations on the distance over which the THz signal may accumulate constructively. Index-matching determines the ease with which the signal may be coupled into free space due to total internal reflection (TIR).

TIR may occur because there is a mismatch between the THz refractive index and the optical refractive index, with $n_{\text{THz}} > n_{\text{opt}}$. This creates a lag in the THz wavefront and causes it to have a shallow angle (see Fig. 5.3), which is defined by

$$\theta_c = \cos^{-1}\left(\frac{n_{\text{opt}}}{n_{\text{THz}}}\right) . \tag{5.5}$$

The critical angle for TIR can be found by considering Snell's law

$$n_i \sin\theta_i = n_t \sin\theta_t , \tag{5.6}$$

and finding the value[2] of θ_i for which $\theta_t = \pi/2$. Rearranging Snell's law we see

$$\theta_{\text{TIR}} = \theta_i|_{\theta_t=\pi/2} = \sin^{-1}\left(\frac{n_t}{n_i}\sin\theta_t\right)\Bigg|_{\theta_t=\pi/2} = \sin^{-1}\left(\frac{n_t}{n_i}\right) . \tag{5.7}$$

Assuming the index of the transmitted medium is air, we can take $n_t = 1$ and $n_i = n_{\text{THz}}$ to give

$$\theta_{\text{TIR}} = \sin^{-1}\left(\frac{1}{n_{\text{THz}}}\right) . \tag{5.8}$$

The angle made between the generated THz wavefront and a plane perpendicular to the direction of pump propagation (i.e. the arrow in Fig. 5.3) is θ_c. Therefore, when $\theta_c > \theta_{\text{TIR}}$ there will be no output coupling of the THz signal. A solution for this condition in terms of the refractive indices can be given by solving the inequality,

$$\sin^{-1}\left(\frac{1}{n_{\text{THz}}}\right) < \cos^{-1}\left(\frac{n_{\text{opt}}}{n_{\text{THz}}}\right) \tag{5.9}$$

to find

$$n_{\text{THz}} < \sqrt{n_{\text{opt}}^2 + 1} , \tag{5.10}$$

which is found using the *Mathematica* solve function.

One of the most common techniques for detecting the generated THz signal is to use a photoconductive receiver in a pump-probe geometry [60]. This receiver consists of an optically-gated switch deposited on the surface of a semiconductor substrate with a short

[2]This is the angle at which all light is reflected back inside of the medium and can only occur when $n_i > n_t$.

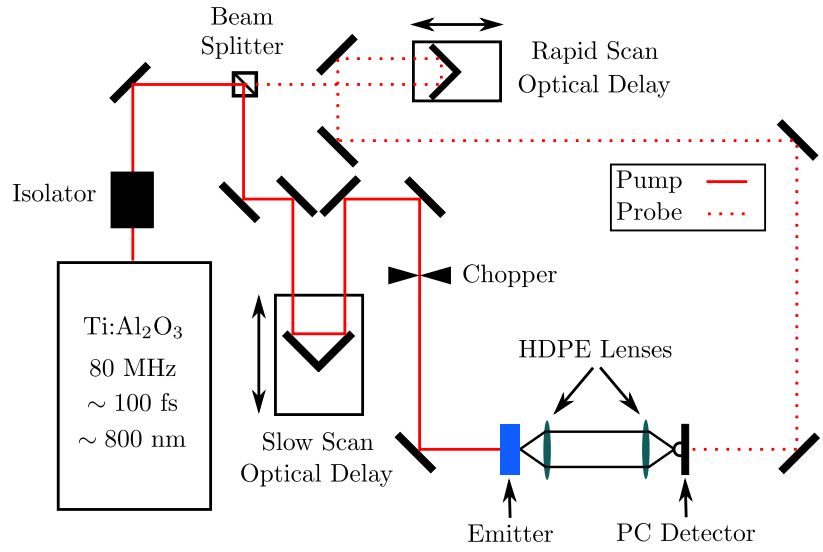

Figure 5.4: A typical pump-probe THz generation/detection scheme.

carrier lifetime such as low-temperature grown gallium arsenide (lt-GaAs). The gate is typically made of gold and is patterned either as a bowtie or Hertzian dipole antenna. Incident optical pulses from the probe beam (about 5-10% of the total beam power) are focused on the gap between the electrodes, thereby exciting carriers into the conduction band of the semiconductor substrate. The THz electric field then acts as a bias and moves the photocurrent through an electrical circuit, which is sent through a current pre-amplifier. The optical pump beam is modulated using an optical chopper so that the signal from the current pre-amp can be detected using a lock-in amplifier. The pump and probe beams are aligned using a collinear geometry and several delay rails (as shown in Fig. 5.4) can be adjusted to permit the two pulses to arrive at the detector at the same time. The electric field is sampled by scanning the delay rail so the short probe pulse (duration $\sim$ 100 fs) sweeps through the long THz signal (duration $\sim$ 10 ps). This sampling procedure allows one to reconstruct the temporal profile of the generated electric field.

A major drawback to the collinear geometry is that the generated THz signal has a limited amplitude (due to phase-matching) and is difficult to extract from the sample (due to index-matching). Several techniques can be implemented to increase the bulk interaction length of the nonlinear medium without compromising the phase-matching condition. The most common technique is to use periodically-poled structures such as periodically-poled lithium niobate (PPLN) [61], but the issue of TIR due to index-matching still persists. One method for overcoming TIR consists of machining the nonlinear crystal so that the output faces match the angle of the Cherenkov cone [62]. A second method consists of imaging a

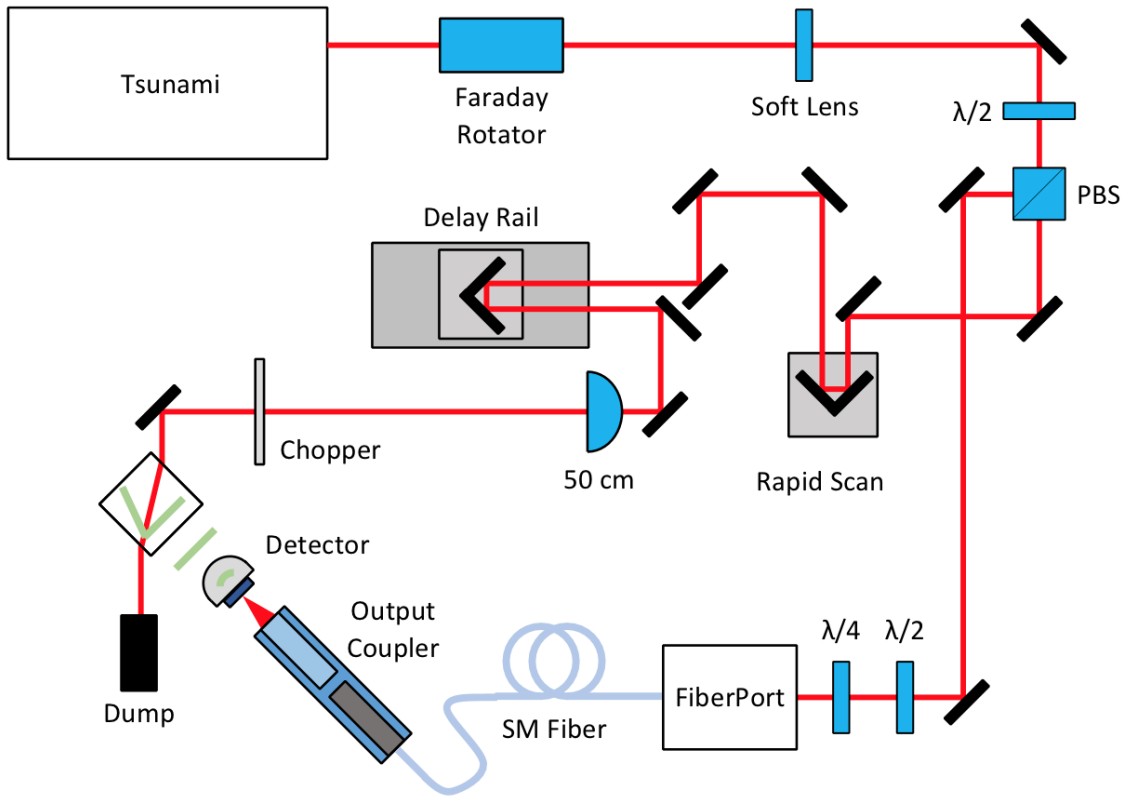

Figure 5.5: Proposed fiber-coupled receiver for THz detection via ME rectification. The receiver and the sample are both free to rotate independent of each other and the probe beam.

diffraction grating into a bulk nonlinear medium so the generated THz wavefront is parallel to the output face of the crystal [63]. In either case, the goal is to either alter the geometry or the orientation of the generated THz wave such that the coherent THz signal is normal to the output face, making extraction of the signal much more efficient.

In order to measure the THz rectification field from the magneto-electric polarization, a more sensitive antenna [64] and new experimental design will be needed which relies on a non-collinear geometry with a fiber-coupled plasmonic receiver. The THz receiver will be affixed to a high-precision rotation/translation stage and the free-space probe beam will be coupled into a short single-mode optical fiber. Using this design, the angle of the receiver optics relative to the pump beam can be easily changed since it is no longer fixed by free-space mirrors. If the sample is then rotated relative to the input pump beam, it will be possible to match the k-vector of the generated THz beam to be normal to the exit face of the crystal. The fiber-coupled receiver can then be placed at the output face of the crystal to maximize detection sensitivity. A schematic setup is shown in Fig. 5.5 that achieves the same goal of other methods, but requires neither machining the crystal nor imaging a

grating into the medium.

5.4.2 Harmonic generation

The magneto-electric second-harmonic moment $p(2\omega)$ is predicted to be smaller than the rectification term by both classical [5] and quantum models [46] of ME dynamics. This is because the 2-photon resonance condition $2\omega - \omega = 0$ is not met. The scientific literature contains many references to Lorentz-force driven SHG, where "Lorentz-force driven" means the $\mathbf{v} \times \mathbf{B}$ term is retained in the model. Shen explains in the first few pages of his text on nonlinear optics how an electron gas can respond nonlinearly to some incident light due to the Lorentz term [65]. A Lorentz-mediated SHG signal has also been reported by Klein et. al., who detected the light as transversely-polarized signals in split ring resonator (SRR) structures where light propagated at an angle relative to the SRR plane [66]. These latter observations, however, required a structured medium and it is the electric field which is responsible for inducing high-frequency magnetic response. These earlier observations of Lorentz-mediated SHG in metamaterials are therefore not the same as the ME process discussed in this thesis. Unpublished results from T. Heinz and collaborators have recently shown that Lorentz-driven SHG is in fact possible *without* the use of structured materials. For their experiment, s-polarized light was incident on a single layer of graphene at some angle and p-polarized light oscillating at 2ω was detected through a filter. The polarization of the incident and measured beams was found to be consistent with a Lorentz-driven harmonic signal: the input E-field must lie in the plane of the graphene to initiate charge motion and then the B-field must be out of plane to deflect the motion, producing a second-order polarization with a nonzero component along the third axis.

5.4.3 Magnetization in micro resonators

There are three main drawbacks to the ME scattering experiment described in Chapter 3. First, the system is limited to high-peak power lasers. Second, large volumes of liquid are required. Third, the low repetition rate of the laser limits the detector range. This subsection describes a second platform based on light scattering to measure magnetic response which offers a solution to these problems in micro-resonators. The use of micro-resonators has become widespread in the study of nonlinear phenomena such as high-harmonic generation [67], parametric oscillation [68], and laser cooling [69] (all at very low input powers). These structures work by confining optical energy from a relatively weak input beam inside a resonant cavity so the light is recirculated, causing the local optical intensity to be very high. Typically the input beam is a low-power tunable cw source. The resonators can either

be constructed by a nano-imprinting technique [70] or by an etching process which creates a hollow-core resonator that can be filled with a fluid [71, 72]. Only a small amount of liquid is needed for the hollow-core structures, which makes the task of synthesizing the required volume of test compounds much easier.

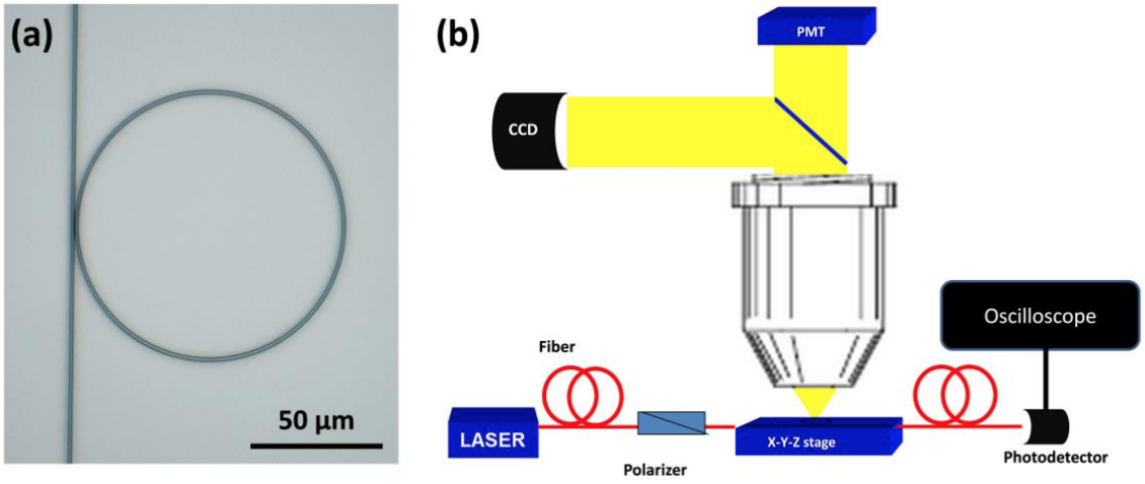

Figure 5.6: (a) Optical image of fabricated polymer micro-ring with a coupling waveguide. The diameter of the ring is 100 μm and cross-section is 1 μm $\times$ 1 μm. (b) Experimental setup for measuring optical scattering. The sample is placed on a high-precision translation stage and light is collected at 90° relative to the plane of the resonator. Light is coupled into the waveguide using a single-mode fiber and its transmission is measured using a multi-mode fiber and photodetector.

An example of a high-Q resonator in close proximity to a straight waveguide used to evanescently couple in the light is shown in Fig. 5.6(a). The resonator may be fabricated from polystyrene by nano-imprinting and using a silicon mold fabricated by electron beam lithography [70]. The resonator may be mounted on a high-precision translation stage and laser light coupled into it via the waveguide from a single-mode fiber. The transmitted light is typically collected using a multimode fiber, which is then sent to a photodetector and displayed on an oscilloscope (see Fig. 5.6(b)). In practice, the pump laser is located by observing a dip in transmitted intensity. The resonantly-coupled light will occupy either a transverse electric (TE) or transverse magnetic (TM) mode of the ring resonator. The order in which resonances appear and the separation between them can be used to distinguish between TE or TM modes. The fabricated ring has a rectangular cross-section which prohibits more than one of these modes from being excited at once, and also provides a means by which the TE and TM modes are spectrally separated.

Because nano-imprinting is adaptable to other polymers, this technique could easily be used to study the nonlinear response in several other materials. The use of hollow-core

structures is also a possible direction for future work, since they require very little sample volume and can be reused many times. The typical hollow-core resonators have a cross-section of 20 μm $\times$ 40 μm and a diameter of about 320 μm, which yields a volume of about 260 pL [71], much less than the several mL of sample volumes that were required for this dissertation research.

5.5 Future work in magnetic scattering

Despite the major advances made by the work of this thesis, there are still several experimental avenues to explore in order to better understand these magneto-optical phenomena. In this last section of the thesis we discuss the outlook for the magnetic scattering experiment. We begin with a few suggestions of potential material candidates for studying systematic variations in molecular and electronic structure. We then briefly discuss a second experimental setup which uses a high-repetition rate, broad bandwidth laser and a different detection scheme to overcome the issue of detector saturation. We conclude with a few words on how to temporally resolve these magnetic phenomena.

5.5.1 Conditions for future systematic studies

There are several more studies which can be done of systematically-varied molecular liquids. The immediate study to be done is of the series $CCl_4 \longrightarrow SiCl_4 \longrightarrow GeCl_4 \longrightarrow SnCl_4 \longrightarrow TiCl_4$, which are ordered from lightest to heaviest central atom while the halogens remain the same. This analysis will provide a better understanding of how rotational frequency and damping contribute to the magnetic response. A second series of tetrahedral molecules will be either $SiCl_4 \longrightarrow SiBr_4$ or $GeCl_4 \longrightarrow GeBr_4$, in which the halogen atom is changed while the central atom remains constant. These studies should provide feedback as to the role of increasing charge density, as Br has several more electrons than Cl.

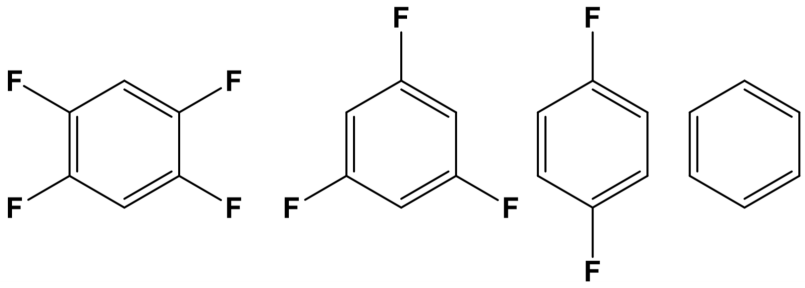

Figure 5.7: Molecular structure of tetrafluorobenzene, trifluorobenzene, difluorobenzene, and benzene, as shown from left to right in order of increasing electron density.

It may also be worthwhile to consider another series of benzene structures with varying electron density, but no intrinsic dipole moment. This would require choosing a series which has substituted atoms that equally balance the charge distribution such as the fluorobenzene series $C_6H_2F_4 \longrightarrow C_6H_3F_3 \longrightarrow C_6H_4F_2 \longrightarrow C_6H_6$, which are listed in order of increasing electron density and shown in Fig. 5.7. These molecules are still anisotropic, but the lack of internal dipole moments eliminates the possibility of direct torque on the dipole to cause rotations and may allow for a compelling assessment of the role of charge.

Other solid samples should also be studied using this experimental approach. The GGG crystal studied here is only one material from a class of garnets with the general formula $A_3B_5O_{12}$, where A is a rare earth cation such as Y^{3+} or Gd^{3+} and B is Al^{3+}, Ga^{3+}, or Fe^{3+} [73, 74]. Future studies of garnets might include YAG, GSAG, GSGG, etc.. Studies of simpler systems such as fused silica should also be performed because their robust mechanical properties, which are relevant to energy conversion applications of ME nonlinearities.

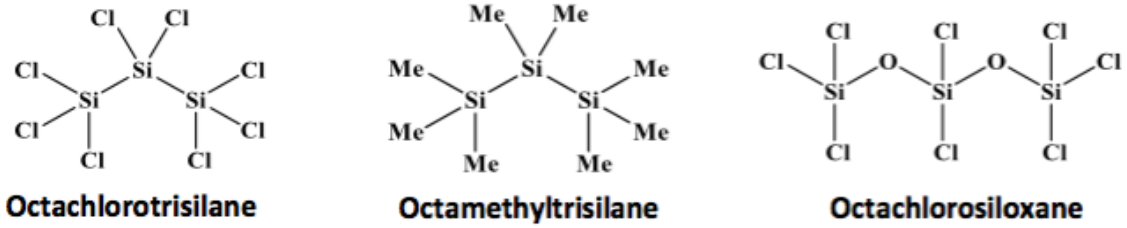

Figure 5.8: Structure of non-polar, symmetric molecular liquids.

Conjugated molecular systems offer high density, delocalized electron clouds which may be the best suited electronic structures to support ME rectification. Hence compounds with fused benzene rings, bi/tetra phenyl rings, and thiophene structures may all be considered. A final set of molecular structures that should be investigated is shown in Fig. 5.8. These compounds are non-polar liquids at room temperature that consist of elaborated tetrahedral structures with large moments of inertia, suitable for experimental tests via scattering experiments of the influence of rotational frequency and damping on magnetization.

5.5.2 Magnetic scattering using high-repetition rate laser

A major shortcoming of magneto-electric scattering experiments to date is the limited dynamic range of the detector due to the combination of relatively long dead time and low repetition rate of the laser. If a low repetition rate laser is to be used, the only way to increase the dynamic range is to effectively stretch the pulse several orders of magnitude more than the detector dead time. This could be done using an optical "storage" device such

as an "optical bottle." Alternatively, a high-repetition rate laser may be used in conjunction with the same photon-counting device to increase the effective dynamic range simply by virtue of having more pulses per second that produce less than one scattered photon each. With a high repetition rate laser, the total number of detectable scattered photons increases dramatically, making signal detection possible with a sensitive photodiode. For these reasons, a second magnetic scattering experiment with a layout identical to the one described in Chapter 3 is under construction. It uses an 80 MHz Vitara laser oscillator from Coherent and an EG&G FND-100 photodetector. This system features incredibly broad, tunable pulses (with up to 150 nm bandwidth) of duration < 10 fs which should allow for studies of the spectral and temporal response of these magnetic effects.

5.5.3 Time-resolved measurements

It is also of great interest to perform time-resolved studies of the dynamics responsible intense magnetization. ME nonlinearities are thought to arise from a process of sequential electric and magnetic interactions on charge distributions in dielectric media. Physically, the picture is that the electric field first initiates motion of the electron distribution and then the magnetic field is allowed to either deflect that motion (in a solid) or induce rotations (in a liquid). The dressed state molecular model shows that the time required for the magnetic interaction to go to completion is on the order of several hundred femtoseconds under the conditions of our experiments (see Subsection 2.3.4). However no tests tests of temporal behavior have been performed to date.

To study transient behavior, one could simply change the pulse duration (which may be done using the MIIPS system) while keeping the intensity range constant. A comparison could then be made, for instance, of the measured response for durations of 150 fs, 300 fs, 450 fs, and 600 fs. In order to resolve single optical-cycle dynamics, however, a different approach and altogether different laser system has to be used. Measurements with femtosecond precision are possible when a carrier-envelope phase (CEP) stabilized laser system is used. With CEP, measurement and control of the phase between the optical carrier wave and the pulse intensity envelope is possible [75] both in oscillators [76] and amplified laser systems [77]. It has been shown that very long-term phase coherence is possible [78], thus facilitating pump-probe experiments on ultrafast times scales. Construction of such a system for magnetic scattering experiments would allow us to resolve the dynamics of the induced magnetic response on femtosecond timescales.

APPENDIX A

Non-RWA Contributions in Dressed State Model

When the non-secular terms are included in the magnetic interaction Hamiltonian for the case of the atomic (excited state) model, doubly-dressed eigenstates that are accurate to any order in the optical interaction may be computed using progressively larger and larger sets of basis states. In other words, since both secular and non-secular terms in the magnetic interaction Hamiltonian couple to different atom-field product states of the quantum system with about the same coupling strength, the RWA cannot be readily made for this interaction. When this is true, the set of basis states used for the problem grows indefinitely (i.e. is no longer a closed set). Fortunately, more than one application of the magnetic field has negligible effects at small 1-photon detunings. We show that an eight-state basis permits computation of second-order magneto-electric moments with negligible errors from higher-order effects. This approach is outlined in Ref. [46], but the following analysis is provided to discuss this problem in greater detail.

The RWA is valid when the optical frequency is slightly detuned from the atomic frequency. In the atomic picture, the detuning that corresponds to the secular terms in the electric dipole transition goes as $\omega_0 - \omega$ while the detuning from the non-secular terms goes as $\omega_0 + \omega$. Since the 1-photon detuning is typically chosen to be relatively small (i.e. near resonance), only the secular terms will contribute to the overall effect and the RWA may be made. However in the case of the magnetic interaction for the atomic model, both of the relevant 2-photon detunings are far from resonant and the RWA cannot be readily made. These additional terms are accounted for in the full interaction Hamiltonian,

$$\hat{H}_{int} = \hbar g \left(\hat{a}^- \hat{\sigma}^+ + \hat{a}^+ \hat{\sigma}^- \right) + f \left(\hat{a}^- \hat{L}_+ + \hat{a}^+ \hat{L}_- + \hat{a}^- \hat{L}_- + \hat{a}^+ \hat{L}_+ \right) , \tag{A.1}$$

and the set of atom-field product states no longer consists of the original closed set,

$$\{ |1,0,0\rangle |n\rangle , |2,1,0\rangle |n-1\rangle , |2,1,1\rangle |n-2\rangle , |2,1,-1\rangle |n\rangle \} , \tag{A.2}$$

and basis grows indefinitely.

First we provide an iterative approach to explain the growth of the basis upon successive applications of the optical field. We then solve the eigenvalue problem for the case of 4-, 6-, and 8-state bases and provide plots showing the dependence of these moments as a function of intensity. From these computations we can make the general conclusion that the net effect of including the two extra states in the 6-state basis simply doubles the magnitude of the induced nonlinear dipole moments, while including the higher-order couplings can be essentially ignored. This result is easily explained in terms of higher-order field coupling to additional states.

A.1 Growth of basis

The simplest way of understanding the growth of the basis is to track the order of the field interaction required to couple successive states to the initial or ground state. Given that the initial state is $|1,0,0\rangle\,|n\rangle$, the only term in the interaction Hamiltonian from Eq. (A.1) which can couple to an adjacent state is the electric interaction term that goes as $\hat{a}^{-}\hat{\sigma}^{+}$, which couples to $|2,1,0\rangle\,|n-1\rangle$. Then the basis to first-order in the interaction consists only of the two states

$$\left\{|1,0,0\rangle\,|n\rangle\,,|2,1,0\rangle\,|n-1\rangle\right\}\ . \tag{A.3}$$

To determine which states are coupled to via a second-order optical interaction requires us to apply the full interaction Hamiltonian to the current set of two basis states and count which *new* states are generated as a result of the interaction terms. Application of the electric interaction to either of the two states does not generate any new states since the counter-rotating terms have been removed from $\hat{H}_{int}^{(e)}$. However, because there is now a state with nonzero ℓ, the magnetic interaction can act to generate four new states from $|2,1,0\rangle\,|n-1\rangle$. Each term in the magnetic interaction contributes and the new basis is now

$$\begin{aligned}\{&|1,0,0\rangle\,|n\rangle\,,|2,1,0\rangle\,|n-1\rangle\,,\\ &|2,1,1\rangle\,|n-2\rangle\,,|2,1,-1\rangle\,|n\rangle\,,|2,1,1\rangle\,|n\rangle\,,|2,1,-1\rangle\,|n-2\rangle\}\ .\end{aligned} \tag{A.4}$$

Another iteration of this same procedure to the set of states above shows that two additional states may be coupled to via magnetic interaction terms and the basis to third-order in the interaction grows to

$$\{|1,0,0\rangle|n\rangle, |2,1,0\rangle|n-1\rangle,$$
$$|2,1,1\rangle|n-2\rangle, |2,1,-1\rangle|n\rangle, |2,1,1\rangle|n\rangle, |2,1,-1\rangle|n-2\rangle$$
$$|2,1,0\rangle|n-3\rangle, |2,1,0\rangle|n+1\rangle\} \ . \tag{A.5}$$

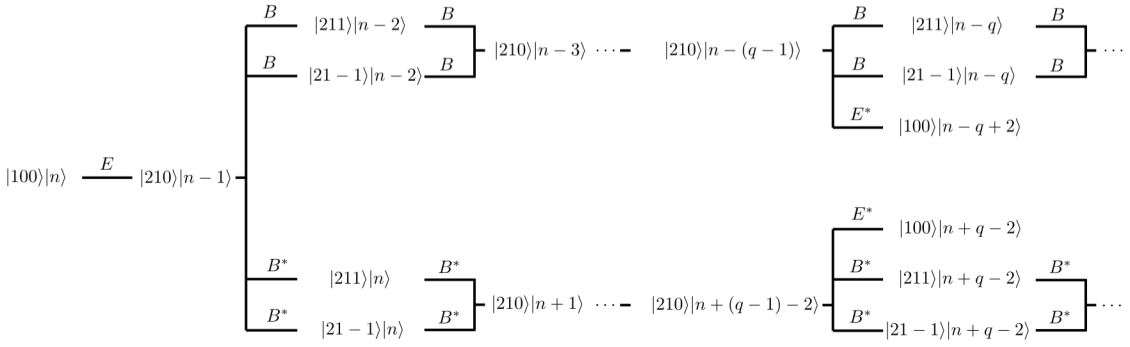

Figure A.1: Expansion of the basis due to iterations of the interaction Hamiltonian. One can easily count the orders in the field to see how strong the coupling may be for different states.

This iterative procedure of looking for states which are coupled to the initial ground state via higher-order applications of the optical field will of course proceed indefinitely. Upon the next iteration (i.e. to fourth-order in the field) a total of six additional states are to be included in basis. The fifth iteration then shows two more states must be added, and then the pattern of adding 6 and then 2 additional states will continue. A general expression can then be written down to show the growth of the basis for arbitrarily-ordered coupling to the initial ground state. This can also be represented diagrammatically as shown in Fig. A.1 where $q+1$ is the order in the field interaction. The details of these derivations are not relevant to this discussion, as we will show that even terms beyond third-order in the optical interaction are completely negligible.

A.2 Diagonalizing the matrix

We are interested in seeing how expanding the basis to include more terms will affect the overall magnitudes of the induced nonlinear moments. Here the main question we are interested in asking is whether or not the rotating wave approximation can be made for the magnetic interaction Hamiltonian. So instead of looking at the system in orders of the

optical interaction (i.e. 2-, 6-, then 8-state bases), we instead compare the results of the 4-state basis which comes about due to making the RWA with the 6- and 8-state bases. The eigenvalue to solve in either case is the standard

$$\hat{H}\left|D_i(n)\right\rangle = E_{Di}\left|D_i(n)\right\rangle \ , \tag{A.6}$$

and we seek solutions for the dressed energies E_{Di} and states $|D_i(n)\rangle$.

A.2.1 4-state basis

The four-state basis consists of the set

$$\begin{aligned}
|1\rangle &\equiv |1,0,0\rangle\,|n\rangle \ , && \text{(A.7)}\\
|2\rangle &\equiv |2,1,0\rangle\,|n-1\rangle \ , && \text{(A.8)}\\
|3\rangle &\equiv |2,1,1\rangle\,|n-2\rangle \ , && \text{(A.9)}\\
|4\rangle &\equiv |2,1,-1\rangle\,|n\rangle \ , && \text{(A.10)}
\end{aligned}$$

which have the bare-state energies

$$\begin{aligned}
E_1 &= -\frac{\hbar\omega_0}{2} + n\hbar\omega \ , && \text{(A.11)}\\
E_2 &= \frac{\hbar\omega_0}{2} + (n-1)\,\hbar\omega \ , && \text{(A.12)}\\
E_3 &= \frac{\hbar\omega_0}{2} + (n-2)\,\hbar\omega \ , && \text{(A.13)}\\
E_4 &= \frac{\hbar\omega_0}{2} + n\hbar\omega \ . && \text{(A.14)}
\end{aligned}$$

The eigenvalue problem for the 4-state basis is written as

$$\begin{pmatrix} E_4 & 0 & q & 0 \\ 0 & E_3 & p & 0 \\ q & p & E_2 & r \\ 0 & 0 & r & E_1 \end{pmatrix} \begin{pmatrix} d_i \\ c_i \\ b_i \\ a_i \end{pmatrix} = E_{Di} \begin{pmatrix} d_i \\ c_i \\ b_i \\ a_i \end{pmatrix} \ , \tag{A.15}$$

where we have defined $p = \hbar f\sqrt{2\,(n-1)}$, $q = \hbar f\sqrt{2n}$, and $r = \hbar g\sqrt{n}$ for convenience. We can numerically solve this problem for coefficients a_i, b_i, c_i, and d_i which must obey the normalization condition

$$1 = |a_i|^2 + |b_i|^2 + |c_i|^2 + |d_i|^2 \ . \tag{A.16}$$

The dressed states can then be written in terms of these coefficients as

$$|D_i(n)\rangle = a_i\,|1\rangle + b_i\,|2\rangle + c_i\,|3\rangle + d_i\,|4\rangle \tag{A.17}$$

and the nonlinear electric and magnetic dipole moments may then be calculated between the adjacent states.

The induced moments are the same as were derived in Section 2.2. We of course have the linear electric moment,

$$\left\langle \hat{p}_{ii}^{(1)}(\omega) \right\rangle = \mu^{(e)}\left(a_i b_i^* + c.c.\right)\mathbf{e}_3 \ , \tag{A.18}$$

along with an electric moment at zero-frequency and an electric moment at the harmonic frequency,

$$\left\langle \hat{p}_{ii}^{(2)}(0) \right\rangle = \mu_\ell^{(e)}\frac{2}{\sqrt{2}}\left(a_i d_i^* + c.c.\right)\mathbf{e}_1 \ , \tag{A.19}$$

$$\left\langle \hat{p}_{ii}^{(2)}(2\omega) \right\rangle = \mu_\ell^{(e)}\frac{1}{\sqrt{2}}\left(a_i c_i^* + c.c.\right)\mathbf{e}_1 \ , \tag{A.20}$$

two nonlinear magneto-electric moments,

$$\left\langle \hat{m}_{ii}^{(2)}(\omega) \right\rangle_l = -i\mu_\ell^{(m)}\frac{1}{\sqrt{2}}\left[a_i b_i^*\left(b_i d_i^* + a_i d_i^*\right) + c.c.\right]\mathbf{e}_2 \ , \tag{A.21}$$

$$\left\langle \hat{m}_{ii}^{(2)}(\omega) \right\rangle_u = i\mu_\ell^{(m)}\frac{1}{\sqrt{2}}\left[a_i b_i^*\left(b_i c_i^* + a_i c_i^*\right) + c.c.\right]\mathbf{e}_2 \ . \tag{A.22}$$

The induced magnetization at ω can be found by computing the direct (or coherent) sum of the moments for the upper and lower transitions. The coherent sum is taken only over terms of the same dressed state index to allow for out-of-phase terms to cancel. The total magnetization for index i is then,

$$\left\langle \hat{m}_{ii}^{(2)}(\omega) \right\rangle = -i\mu_\ell^{(m)}\frac{1}{\sqrt{2}}\left[a_i b_i^*\left(b_i d_i^* + a_i d_i^* - b_i c_i^* - a_i c_i^*\right) + c.c.\right]\mathbf{e}_2 \ . \tag{A.23}$$

The net moments must again be calculated by computing an incoherent sum over the dressed state index. This yields, for the linear electric moment

$$\left|\hat{p}^{(1)}_{net}(\omega)\right| = \mu^{(e)}_{\ell}\left[\sum_{i=1}^{4}\left|(a_i b_i^* + c.c.)\right|^2\right]^{1/2} , \tag{A.24}$$

for the quadratic electric moments,

$$\left|\hat{p}^{(2)}_{net}(0)\right| = \frac{2\mu^{(e)}_{\ell}}{\sqrt{2}}\left[\sum_{i=1}^{4}\left|(a_i d_i^* + c.c.)\right|^2\right]^{1/2} , \tag{A.25}$$

$$\left|\hat{p}^{(2)}_{net}(2\omega)\right| = \frac{\mu^{(e)}_{\ell}}{\sqrt{2}}\left[\sum_{i=1}^{4}\left|(a_i c_i^* + c.c.)\right|^2\right]^{1/2} , \tag{A.26}$$

and for the quadratic magnetic moment

$$\left|\hat{m}^{(2)}_{net}(\omega)\right| = \frac{\mu^{(m)}_{\ell}}{\sqrt{2}}\left[\sum_{i=1}^{4}\left|[a_i b_i^*\left(b_i d_i^* + a_i d_i^* - b_i c_i^* - a_i c_i^*\right) + c.c.]\right|^2\right]^{1/2} . \tag{A.27}$$

A.2.2 6-state basis

The six-state basis now includes the additional states

$$|5\rangle \equiv |2,1,1\rangle\,|n\rangle\ , \tag{A.28}$$

$$|6\rangle \equiv |2,1,-1\rangle\,|n-2\rangle\ , \tag{A.29}$$

with bare-state energies

$$E_5 = \frac{\hbar\omega_0}{2} + n\hbar\omega\ , \tag{A.30}$$

$$E_6 = \frac{\hbar\omega_0}{2} + (n-2)\,\hbar\omega\ . \tag{A.31}$$

The eigenvalue problem is now

$$\begin{pmatrix} E_6 & 0 & 0 & 0 & p & 0 \\ 0 & E_5 & 0 & 0 & q & 0 \\ 0 & 0 & E_4 & 0 & q & 0 \\ 0 & 0 & 0 & E_3 & p & 0 \\ p & q & q & p & E_2 & r \\ 0 & 0 & 0 & 0 & 0 & E_1 \end{pmatrix} \begin{pmatrix} f_i \\ e_i \\ d_i \\ c_i \\ b_i \\ a_i \end{pmatrix} = E_{Di} \begin{pmatrix} f_i \\ e_i \\ d_i \\ c_i \\ b_i \\ a_i \end{pmatrix} , \tag{A.32}$$

and the coefficients are numerically evaluated and normalized according to

$$1 = |a_i|^2 + |b_i|^2 + |c_i|^2 + |d_i|^2 + |e_i|^2 + |f_i|^2 \ , \tag{A.33}$$

so that the dressed eigenstates may be written as

$$|D_i(n)\rangle = a_i\,|1\rangle + b_i\,|2\rangle + c_i\,|3\rangle + d_i\,|4\rangle + e_i\,|5\rangle + f_i\,|6\rangle \ . \tag{A.34}$$

The inclusion of these two additional states produces four more contributions to the nonlinear dipole moments, two electric

$$\left\langle \hat{p}^{(2)}_{ii}(0) \right\rangle' = \mu^{(e)}_\ell \frac{2}{\sqrt{2}} \left(a_i e_i^* + c.c.\right) \mathbf{e}_1 \ , \tag{A.35}$$

$$\left\langle \hat{p}^{(2)}_{ii}(2\omega) \right\rangle' = \mu^{(e)}_\ell \frac{1}{\sqrt{2}} \left(a_i f_i^* + c.c.\right) \mathbf{e}_1 \ , \tag{A.36}$$

and two magnetic

$$\left\langle \hat{m}^{(2)}_{ii}(\omega) \right\rangle'_l = -i\mu^{(m)}_\ell \frac{1}{\sqrt{2}} \left[a_i b_i^* \left(b_i e_i^* + a_i e_i^*\right) + c.c.\right] \mathbf{e}_2 \ , \tag{A.37}$$

$$\left\langle \hat{m}^{(2)}_{ii}(\omega) \right\rangle'_u = i\mu^{(m)}_\ell \frac{1}{\sqrt{2}} \left[a_i b_i^* \left(b_i f_i^* + a_i f_i^*\right) + c.c.\right] \mathbf{e}_2 \ , \tag{A.38}$$

where the measured signal is again projected along $\mathbf{e}_2$[1]. Their coherent sum yields

$$\left\langle \hat{m}^{(2)}_{ii}(\omega) \right\rangle' = -i\mu^{(m)}_\ell \frac{1}{\sqrt{2}} \left[a_i b_i^* \left(b_i e_i^* + a_i e_i^* - b_i f_i^* - a_i f_i^*\right) + c.c.\right] \mathbf{e}_2 \ . \tag{A.39}$$

[1]Notice that depending on the signs in front of the individual magnetic contributions and whether a coherent or incoherent sum is taken, the net magnetic response can either add completely in or out of phase. A solution to avoid this altogether is to sum the magnitudes of the induced magnetic terms so out-of-phase components do not destructively interfere.

Here the primed notation is used to designate contributions to the overall nonlinear moments due to including the counter-rotating terms in the basis. To compute the net induced effects, a coherent sum over moments of the same type and with the same dressed state index is first taken, and then an incoherent sum is taken over the dressed state index from $i = 1$ to $i = 6$. For example, $\langle \hat{p}_{ii}^{(2)}(0) \rangle'$ is a correction to the term $\langle \hat{p}_{ii}^{(2)}(0) \rangle$, and so these expressions are first summed directly before the incoherent sum is taken. The net nonlinear electric moments are now

$$\left| \hat{p}_{net}^{(2)}(0) \right| = \frac{2\mu_\ell^{(e)}}{\sqrt{2}} \left[\sum_{i=1}^{6} \left| (a_i d_i^* + c.c. + a_i e_i^* + c.c.) \right|^2 \right]^{1/2} , \tag{A.40}$$

$$\left| \hat{p}_{net}^{(2)}(2\omega) \right| = \frac{\mu_\ell^{(e)}}{\sqrt{2}} \left[\sum_{i=1}^{6} \left| (a_i c_i^* + c.c. + a_i f_i^* + c.c.) \right|^2 \right]^{1/2} , \tag{A.41}$$

and the net magnetization is

$$\left| \hat{m}_{net}^{(2)}(\omega) \right| = \frac{\mu_\ell^{(m)}}{\sqrt{2}} \left\{ \sum_{i=1}^{6} \left| [a_i b_i^* (b_i d_i^* + a_i d_i^* + b_i e_i^* + a_i e_i^* - b_i c_i^* - a_i c_i^* - b_i f_i^* - a_i f_i^*) + c.c.] \right|^2 \right\}^{1/2} . \tag{A.42}$$

A.2.3 8-state basis

The eight-state basis now includes the additional states

$$|7\rangle \equiv |2,1,0\rangle \, |n+1\rangle , \tag{A.43}$$

$$|8\rangle \equiv |2,1,0\rangle \, |n-3\rangle , \tag{A.44}$$

with bare-state energies

$$E_7 = \frac{\hbar\omega_0}{2} + (n+1)\,\hbar\omega , \tag{A.45}$$

$$E_8 = \frac{\hbar\omega_0}{2} + (n-3)\,\hbar\omega . \tag{A.46}$$

The eigenvalue problem is now

$$\begin{pmatrix} E_8 & 0 & t & 0 & 0 & t & 0 & 0 \\ 0 & E_7 & 0 & s & s & 0 & 0 & 0 \\ t & 0 & E_6 & 0 & 0 & 0 & p & 0 \\ 0 & s & 0 & E_5 & 0 & 0 & q & 0 \\ 0 & s & 0 & 0 & E_4 & 0 & q & 0 \\ t & 0 & 0 & 0 & 0 & E_3 & p & 0 \\ 0 & 0 & p & q & q & p & E_2 & r \\ 0 & 0 & 0 & 0 & 0 & 0 & 0 & E_1 \end{pmatrix} \begin{pmatrix} h_i \\ g_i \\ f_i \\ e_i \\ d_i \\ c_i \\ b_i \\ a_i \end{pmatrix} = E_{Di} \begin{pmatrix} h_i \\ g_i \\ f_i \\ e_i \\ d_i \\ c_i \\ b_i \\ a_i \end{pmatrix} , \tag{A.47}$$

where we have defined $s = \hbar f \sqrt{2\,(n+1)}$ and $t = \hbar f \sqrt{2\,(n-2)}$. The coefficients are numerically evaluated and normalized according to

$$1 = |a_i|^2 + |b_i|^2 + |c_i|^2 + |d_i|^2 + |e_i|^2 + |f_i|^2 + |g_i|^2 + |h_i|^2 \ , \tag{A.48}$$

so that the dressed eigenstates may be written as

$$|D_i(n)\rangle = a_i\,|1\rangle + b_i\,|2\rangle + c_i\,|3\rangle + d_i\,|4\rangle + e_i\,|5\rangle + f_i\,|6\rangle + g_i\,|7\rangle + h_i\,|8\rangle \ . \tag{A.49}$$

Once again there are several additional contributions to the net induced dipole moments. First there is a linear electric moment at the fundamental frequency given by

$$\left\langle \hat{p}_{ii}^{(3)}(\omega) \right\rangle'' = \mu^{(e)}\,(a_i g_i^* + c.c.)\,\mathbf{e}_3 \ , \tag{A.50}$$

though this term is induced by the mixing of $\omega - \omega + \omega$ to give ω. This term is responsible for mediating two additional nonlinear magnetization terms,

$$\left\langle \hat{m}_{ii}^{(4)}(\omega) \right\rangle_{l,1}'' = -i\mu_\ell^{(m)} \frac{1}{\sqrt{2}} \left[a_i g_i^* \left(g_i d_i^* + a_i d_i^* \right) + c.c. \right] \mathbf{e}_2 \ , \tag{A.51}$$

$$\left\langle \hat{m}_{ii}^{(4)}(\omega) \right\rangle_{l,2}'' = -i\mu_\ell^{(m)} \frac{1}{\sqrt{2}} \left[a_i g_i^* \left(g_i e_i^* + a_i e_i^* \right) + c.c. \right] \mathbf{e}_2 \ , \tag{A.52}$$

which we see are fourth-order in the field. A second electric moment is initiated as well which is also cubic but is the result of combining $\omega + \omega + \omega = 3\omega$. This term is given as

$$\left\langle \hat{p}_{ii}^{(3)}(3\omega) \right\rangle'' = \mu^{(e)}\,(a_i h_i^* + c.c.)\,\mathbf{e}_3 \ , \tag{A.53}$$

and like the other cubic term, this mediates two additional nonlinear magnetization terms,

$$\left\langle \hat{m}_{ii}^{(4)}(\omega) \right\rangle''_{u,1} = i\mu_\ell^{(m)} \frac{1}{\sqrt{2}} \left[a_i h_i^* \left(h_i c_i^* + a_i c_i^* \right) + c.c. \right] \mathbf{e}_2 \,, \tag{A.54}$$

$$\left\langle \hat{m}_{ii}^{(4)}(\omega) \right\rangle''_{u,2} = i\mu_\ell^{(m)} \frac{1}{\sqrt{2}} \left[a_i h_i^* \left(h_i f_i^* + a_i f_i^* \right) + c.c. \right] \mathbf{e}_2 \,. \tag{A.55}$$

The terms in these expressions represent just the lowest-order contributions to these magnetic moments, as there are other pathways over which a coherence may be established between the initial $|1\rangle$ state and the final state $|7\rangle$ or $|8\rangle$; the higher-order terms will be even more negligible since they contain successively more coefficient products. Again, an incoherent sum must be taken over all of the terms in order to determine the net resulting moment. The third-order electric polarization at ω can be added to $p(\omega)$ term which comes from the 4-state basis,

$$|\hat{p}_{net}(\omega)| = \mu_\ell^{(e)} \left[\sum_{i=1}^{8} \left| \left[\left(a_i b_i^* + a_i g_i^* \right) + c.c. \right] \right|^2 \right]^{1/2} , \tag{A.56}$$

and the third-order electric polarization at 3ω is simply

$$\left| \hat{p}_{net}^{(3)}(3\omega) \right| = \mu_\ell^{(e)} \left[\sum_{i=1}^{8} \left| \left(a_i h_i^* + c.c. \right) \right|^2 \right]^{1/2} . \tag{A.57}$$

In the above, expression for the linear electric moment, the superscript (1) has been removed since the moment now consists of higher-order terms as well. The net magnetization is then going to be the sum of *all* contributions up to this point at frequency ω. We have,

$$\begin{aligned} |\hat{m}_{net}(\omega)| = \frac{\mu_\ell^{(m)}}{\sqrt{2}} \Bigg(\sum_{i=1}^{8} \Big| \{ & [a_i b_i^* (b_i d_i^* + a_i d_i^* + b_i e_i^* + a_i e_i^* - b_i c_i^* - a_i c_i^* - b_i f_i^* - a_i f_i^*) \\ & + a_i g_i^* \left(g_i d_i^* + a_i d_i^* + g_i c_i^* + a_i e_i^* \right) - a_i h_i^* \left(h_i c_i^* + a_i c_i^* + h_i f_i^* + a_i f_i^* \right)] \\ & + c.c. \} \Big|^2 \Bigg)^{1/2} . \end{aligned} \tag{A.58}$$

where we have again dropped the superscript (2) since the moments here reflect a sum of mixed-order processes.

There are a number of nonzero moments which arise between states of different dressed state index i, but it should be noted that these terms are of little interest here. The terms

are due the the degeneracy of states $|3\rangle$, $|4\rangle$, $|5\rangle$, and $|6\rangle$, but the result of including them in the calculation merely multiplies the amplitudes of *all* moments by a small numerical factor. We essentially care about the magnitudes of the induced moments relative to the linear electric moment, so including these terms is redundant.

A.3 Intensity dependence of nonlinear moments

The effect of including more states in the basis is obvious when plots of the induced moments as a function of photon number are created. The most straight-forward way of quantifying the effect of including the additional basis states is to plot on the same set of axes the net induced moments from the 4-state basis and the net induced moments when the primed and double-primed corrections are added to the moments. This result is shown explicitly in Fig. A.2. Here the higher-order corrections to $p(\omega)$, $p(0)$, $p(2\omega)$ and $m(\omega)$ have been included up to the 8-state basis. The dashed curves in grey represent the values of the moments in the 4-state basis. From here it is obvious that the net result of including the additional states to the basis is to simply double the induced moments. These corrections come primarily through the addition of states $|5\rangle$ and $|6\rangle$; the cubic and quartic corrections to $p(\omega)$ and $m(\omega)$ from states $|7\rangle$ and $|8\rangle$ are negligible.

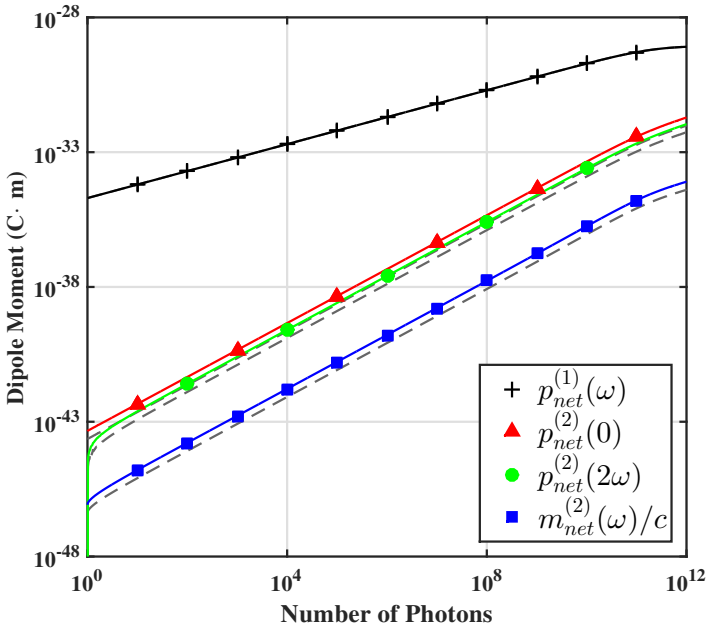

Figure A.2: The net induced moments with corrections up to the 8-state basis for $p(\omega)$, $p(0)$, $p(2\omega)$ and $m(\omega)$. The grey dashed curves represent the values of the moments in the 4-state basis.

To see how the additional terms individually contribute to the moments, it is most useful to look at plots for p and m at each dressed state index i in the 4-, 6-, and 8-state bases. To avoid cluttering the plots, only select moments are given for each set of basis states. In the 4-state basis, we plot $p(\omega)$, $p(0)$, $p(2\omega)$ and $m(\omega)$, in the 6-state basis we plot $p'(0)$, $p'(2\omega)$ and $m'(\omega)$, and in the 8-state basis we plot $p''(\omega)$, $p''(3\omega)$ and $m''(\omega)$. Here the plotted magnetizations represent the direct sum over each additional magnetic contribution. Figure A.3 shows the electric and magnetic contributions which come from the 4-state basis, as are discussed in detail in Chapter 4.

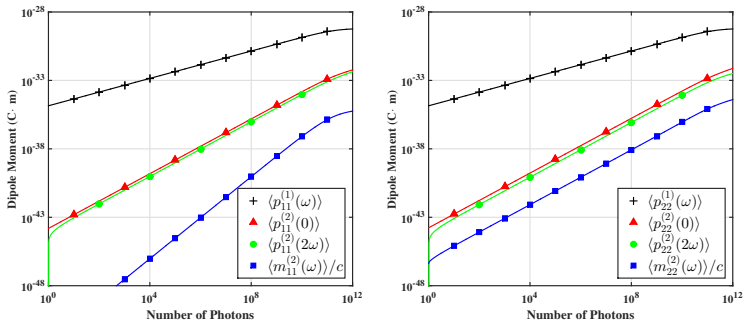

(a) $i = 1$ (b) $i = 2$

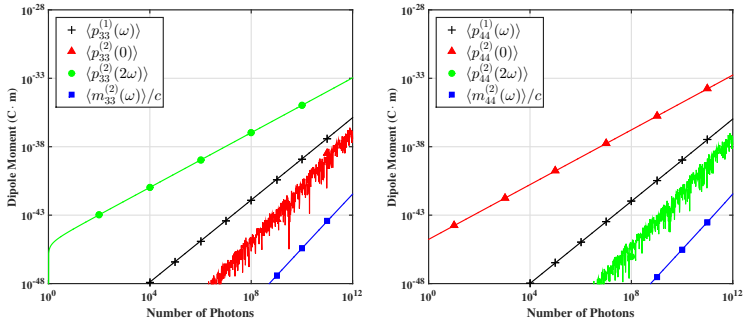

(c) $i = 3$ (d) $i = 4$

Figure A.3: Induced electric and magnetic dipole moments in the 4-state basis for individual dressed state indices. Shown are the linear electric moment $\langle p_{ii}^{(1)}(\omega)\rangle$, the nonlinear electric moments $\langle p_{ii}^{(2)}(0)\rangle$ and $\langle p_{ii}^{(2)}(2\omega)\rangle$, and the nonlinear magnetization $\langle m_{ii}^{(2)}(\omega)\rangle$.

In Fig. A.4 the additional contributions to the induced electric and magnetic moments are shown. The moments shown here are only the ones with the single prime notation as defined above. We can see by looking at the plots for indices $i = 1$ and $i = 2$ that the moments are essentially repeated from the results of the 4-state basis, this is the root of the factor of 2 discussed in Fig. A.2. The plots for indices $i = 3 - 6$ reflect small quadratic contributions to the 0-frequency and second-harmonic electric moments, and negligible quartic contributions to the magnetization.

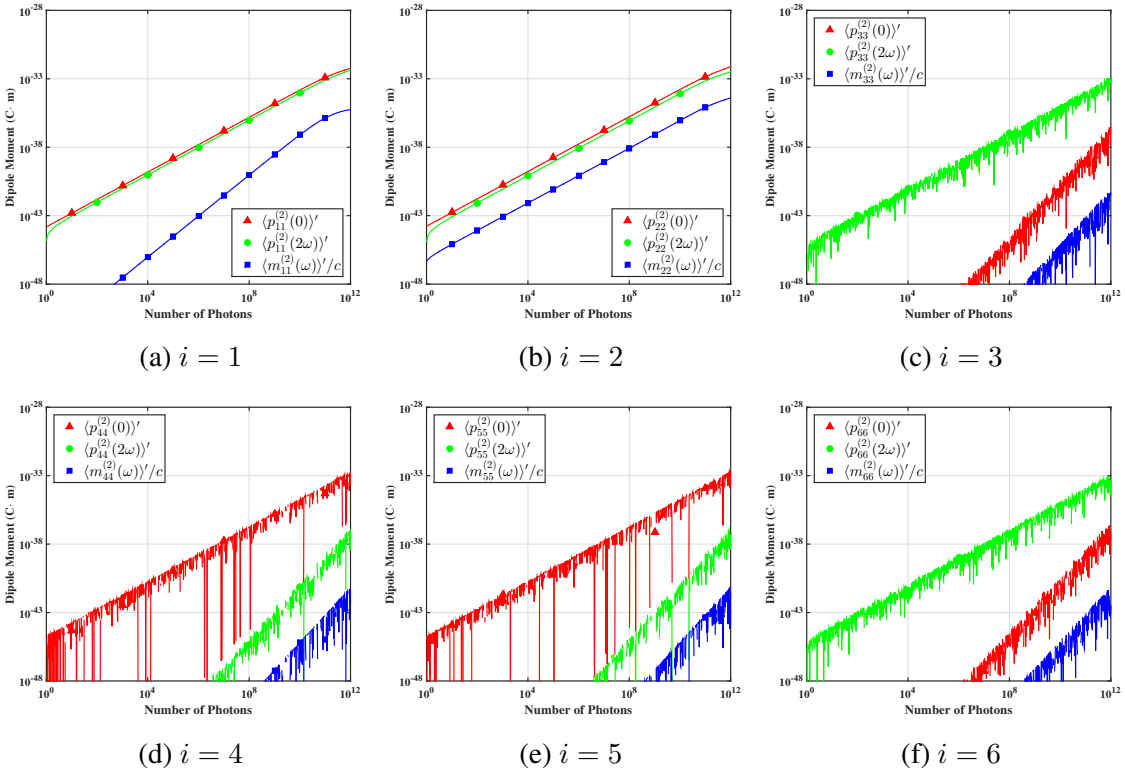

(a) $i = 1$ (b) $i = 2$ (c) $i = 3$

(d) $i = 4$ (e) $i = 5$ (f) $i = 6$

Figure A.4: Induced electric and magnetic dipole moments in the 6-state basis for individual dressed state indices. Shown are the corrections to the nonlinear electric moments $\langle p^{(2)}_{ii}(0)\rangle'$ and $\langle p^{(2)}_{ii}(2\omega)\rangle'$, and the nonlinear magnetization $\langle m^{(2)}_{ii}(\omega)\rangle'$.

Figure A.5 shows the additional contributions to several of the induced moments when the 8-state basis is considered. Only the double-primed contributions as defined above are shown, which constitute the third-order electric moments $\langle p^{(3)}_{ii}(\omega\rangle''$ and $\langle p^{(3)}_{ii}(3\omega\rangle''$ and the fourth-order magnetic moment $\langle m^{(4)}_{ii}(\omega\rangle''$. Not surprisingly, all of the plots show that these contributions are in fact negligible when added to the existing electric and magnetic moments driven between the first two stages of the quadratic EB or EB^* process; in other words, because these moments are higher-order in the field, they are less significant.

From this analysis, it is simple to conclude the effect of including the counter-rotating terms in the magnetic interaction Hamiltonian: the states which can be accessed via a similar process from the ground state will contribute equally, while states which require additional applications of the interaction will be less important. This is why including states $|5\rangle$ and $|6\rangle$ shows a net increase in the induced moments by 2, while including states $|7\rangle$ and $|8\rangle$ yield a negligible contribution. It is easy to see how including higher-order states from the growth of the basis shown in Fig. A.1 will have a small impact on the net outcome of the induced moments. This reasoning allows us to solve the problem in the

original 4-state basis so that a closed set of states may be used, while maintaining that the result of including additional terms is to simply double the induced nonlinear moments.

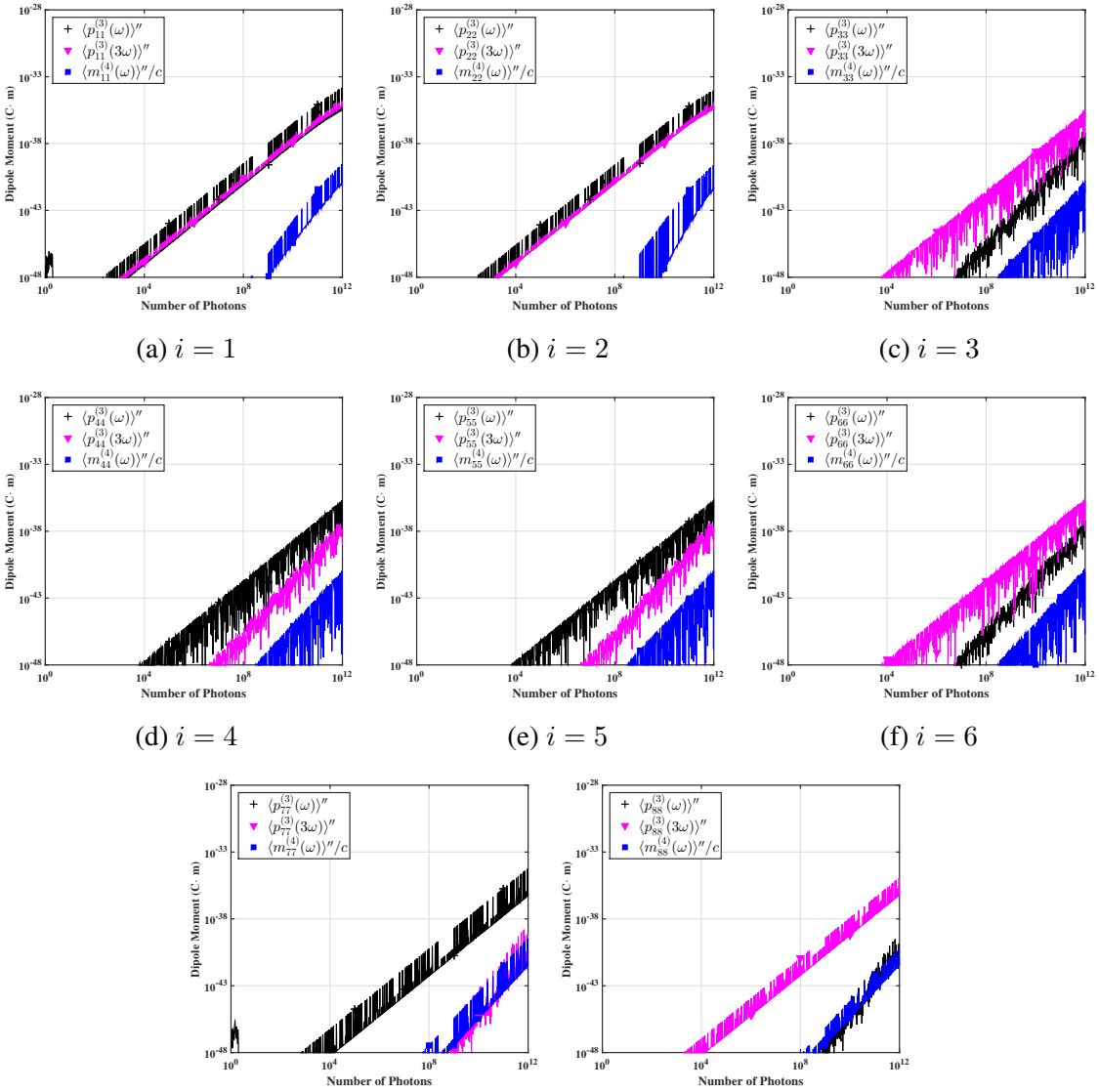

(a) $i = 1$ (b) $i = 2$ (c) $i = 3$

(d) $i = 4$ (e) $i = 5$ (f) $i = 6$

(g) $i = 7$ (h) $i = 8$

Figure A.5: Higher-order contributions to electric and magnetic dipole moments when 8-states are considered for the basis. Shown are the cubic moments $\langle p_{ii}^{(3)}(\omega)\rangle''$ and $\langle p_{ii}^{(3)}(3\omega)\rangle''$ and the fourth-order moment $\langle m_{ii}^{(4)}(\omega)\rangle''$.

APPENDIX B

Evaluation of Operators in Atomic Hydrogen

The primary results of the dressed state theory rely on evaluating the electric and magnetic dipole moment operators between electronic states of the driven system. The operators of interest are

$$\hat{p} = e\hat{r} \quad \text{and} \quad \hat{m} = \frac{e}{2m_e}\hat{L}\,, \tag{B.1}$$

and so the quantum observables we wish to measure are $\hat{r}$ and $\hat{L}$. Our atomic and molecular systems assume hydrogenic wavefunctions and the transitions of interest all occur between the $1s$ and $2p$ states. Here we show explicit calculation of $\hat{r}$ and $\hat{L}$ between the relevant states in our system. The position operator is evaluated using the normalized position wavefunctions composed of Laguerre polynomials and spherical harmonics for atomic hydrogen, while the angular momentum operator is evaluated using ladder operators. In all calculations the quantization axis is taken to be along $\mathbf{e}_3$.

The wavefunctions for the $1s$ and $2p$ states in atomic hydrogen are

$$|1,0,0\rangle = \frac{1}{\sqrt{\pi a_0^3}} e^{-r/a_0} = \xi_1 e^{-r/a_0}\,, \tag{B.2}$$

$$|2,1,0\rangle = \frac{1}{4\sqrt{2\pi a_0^3}} \frac{r}{a_0} e^{-r/2a_0}\cos\theta = \xi_2 r e^{-r/2a_0}\cos\theta\,, \tag{B.3}$$

$$|2,1,1\rangle = \frac{1}{8\sqrt{\pi a_0^3}} \frac{r}{a_0} e^{-r/2a_0}\sin\theta e^{i\varphi} = \xi_3 r e^{-r/2a_0}\sin\theta e^{i\varphi}\,, \tag{B.4}$$

$$|2,1,-1\rangle = \frac{1}{8\sqrt{\pi a_0^3}} \frac{r}{a_0} e^{-r/2a_0}\sin\theta e^{-i\varphi} = \xi_3 r e^{-r/2a_0}\sin\theta e^{-i\varphi}\,, \tag{B.5}$$

where ξ_i (for $i = 1,2,3$) are defined for convenience and a_0 is the Bohr radius. We are interested in measuring $\hat{r}$ between the ground and excited states of this basis. Using that

$$\hat{r} = \hat{x}\mathbf{e}_1 + \hat{y}\mathbf{e}_2 + \hat{z}\mathbf{e}_3 \tag{B.6}$$

the nonzero moments with $|1,0,0\rangle$ are

$$\langle 2,1,0|\,\hat{r}\,|1,0,0\rangle = \langle 2,1,0|\,\hat{z}\,|1,0,0\rangle\,\mathbf{e}_3\ , \tag{B.7}$$

$$\langle 2,1,1|\,\hat{r}\,|1,0,0\rangle = \langle 2,1,1|\,\hat{x}\,|1,0,0\rangle\,\mathbf{e}_1 + \langle 2,1,1|\,\hat{y}\,|1,0,0\rangle\,\mathbf{e}_2\ , \tag{B.8}$$

$$\langle 2,1,-1|\,\hat{r}\,|1,0,0\rangle = \langle 2,1,-1|\,\hat{x}\,|1,0,0\rangle\,\mathbf{e}_1 + \langle 2,1,-1|\,\hat{y}\,|1,0,0\rangle\,\mathbf{e}_2\ . \tag{B.9}$$

There are five more nonzero terms computed between $\langle 1,0,0|$ and the $2p$ states, which are related to those in the above set of equations by

$$\langle 2,1,0|\,\hat{z}\,|1,0,0\rangle = \langle 1,0,0|\,\hat{z}\,|2,1,0\rangle\ , \tag{B.10}$$

$$\langle 2,1,1|\,\hat{x}\,|1,0,0\rangle = \langle 1,0,0|\,\hat{x}\,|2,1,-1\rangle\ , \tag{B.11}$$

$$\langle 2,1,1|\,\hat{y}\,|1,0,0\rangle = \langle 1,0,0|\,\hat{y}\,|2,1,-1\rangle\ , \tag{B.12}$$

$$\langle 2,1,-1|\,\hat{x}\,|1,0,0\rangle = \langle 1,0,0|\,\hat{x}\,|2,1,1\rangle\ , \tag{B.13}$$

$$\langle 2,1,-1|\,\hat{y}\,|1,0,0\rangle = \langle 1,0,0|\,\hat{y}\,|2,1,1\rangle\ . \tag{B.14}$$

Thus we need to evaluate only half of the above terms.

We see

$$\begin{aligned}
\langle 2,1,0|\,\hat{z}\,|1,0,0\rangle &= \int d^3\mathbf{r}\ \xi_1\xi_2 r e^{-r/2a_0}\cos\theta\,(r\cos\theta)\,e^{-r/a_0} \\
&= \xi_1\xi_2\int_0^\infty r^4 e^{-3r/2a_0}dr\int_0^\pi \cos^2\theta\sin\theta d\theta\int_0^{2\pi} d\varphi \\
&= \left(\frac{1}{4\sqrt{2}a_0^4\pi}\right)\left(\frac{256a_0^5}{81}\right)\left(\frac{2}{3}\right)(2\pi) \\
&= \frac{128\sqrt{2}}{243}a_0\ ,
\end{aligned} \tag{B.15}$$

$$\begin{aligned}
\langle 2,1,1|\,\hat{x}\,|1,0,0\rangle &= \int d^3\mathbf{r}\;\xi_1\xi_3 r e^{-r/2a_0}\sin\theta e^{-i\varphi}\left(r\sin\theta\cos\varphi\right)e^{-r/a_0} \\
&= \xi_1\xi_3\int_0^\infty r^4 e^{-3r/2a_0}dr\int_0^\pi \sin^3\theta d\theta\int_0^{2\pi}\cos\varphi e^{-i\varphi}d\varphi \\
&= \left(\frac{1}{8a_0^4\pi}\right)\left(\frac{256a_0^5}{81}\right)\left(\frac{4}{3}\right)(\pi) \\
&= \frac{128}{243}a_0\;, \qquad \text{(B.16)}
\end{aligned}$$

$$\begin{aligned}
\langle 2,1,1|\,\hat{y}\,|1,0,0\rangle &= \int d^3\mathbf{r}\;\xi_1\xi_3 r e^{-r/2a_0}\sin\theta e^{-i\varphi}\left(r\sin\theta\sin\varphi\right)e^{-r/a_0} \\
&= \xi_1\xi_3\int_0^\infty r^4 e^{-3r/2a_0}dr\int_0^\pi \sin^3\theta d\theta\int_0^{2\pi}\sin\varphi e^{-i\varphi}d\varphi \\
&= \left(\frac{1}{8a_0^4\pi}\right)\left(\frac{256a_0^5}{81}\right)\left(\frac{4}{3}\right)(-i\pi) \\
&= -i\frac{128}{243}a_0\;, \qquad \text{(B.17)}
\end{aligned}$$

We are able to calculate $\langle 2,1,-1|\,\hat{x}\,|1,0,0\rangle$ and $\langle 2,1,-1|\,\hat{y}\,|1,0,0\rangle$ from the above expressions since the only difference is the sign of the imaginary argument of the exponential. We see

$$\begin{aligned}
\langle 2,1,-1|\,\hat{x}\,|1,0,0\rangle &= \xi_1\xi_3\int_0^\infty r^4 e^{-3r/2a_0}dr\int_0^\pi \sin^3\theta d\theta\int_0^{2\pi}\cos\varphi e^{i\varphi}d\varphi \\
&= \left(\frac{1}{8a_0^4\pi}\right)\left(\frac{256a_0^5}{81}\right)\left(\frac{4}{3}\right)(\pi) \\
&= \frac{128}{243}a_0 \qquad \text{(B.18)}
\end{aligned}$$

$$\begin{aligned}
\langle 2,1,-1|\,\hat{y}\,|1,0,0\rangle &= \xi_1\xi_3\int_0^\infty r^4 e^{-3r/2a_0}dr\int_0^\pi \sin^3\theta d\theta\int_0^{2\pi}\sin\varphi e^{i\varphi}d\varphi \\
&= \left(\frac{1}{8a_0^4\pi}\right)\left(\frac{256a_0^5}{81}\right)\left(\frac{4}{3}\right)(i\pi) \\
&= i\frac{128}{243}a_0 \qquad \text{(B.19)}
\end{aligned}$$

And so we now have all of the possible values for the inner products of $1s$ and $2p$ atomic hydrogen wavefunctions. These results are summarized in Tab. B.1.

Inner Product	Value		Inner Product	Value
$\langle 2,1,0\vert\,\hat{z}\,\vert 1,0,0\rangle$	$\frac{128\sqrt{2}}{243}a_0$		$\langle 1,0,0\vert\,\hat{z}\,\vert 2,1,0\rangle$	$\frac{128\sqrt{2}}{243}a_0$
$\langle 2,1,1\vert\,\hat{x}\,\vert 1,0,0\rangle$	$\frac{128}{243}a_0$		$\langle 1,0,0\vert\,\hat{x}\,\vert 2,1,-1\rangle$	$\frac{128}{243}a_0$
$\langle 2,1,1\vert\,\hat{y}\,\vert 1,0,0\rangle$	$-i\frac{128}{243}a_0$		$\langle 1,0,0\vert\,\hat{y}\,\vert 2,1,-1\rangle$	$-i\frac{128}{243}a_0$
$\langle 2,1,-1\vert\,\hat{x}\,\vert 1,0,0\rangle$	$\frac{128}{243}a_0$		$\langle 1,0,0\vert\,\hat{x}\,\vert 2,1,1\rangle$	$\frac{128}{243}a_0$
$\langle 2,1,-1\vert\,\hat{y}\,\vert 1,0,0\rangle$	$i\frac{128}{243}a_0$		$\langle 1,0,0\vert\,\hat{y}\,\vert 2,1,1\rangle$	$i\frac{128}{243}a_0$

Table B.1: All possible values of $\hat{r}$ between the $1s$ and $2p$ states of atomic hydrogen.

Next we calculate the inner products associated with the angular momentum operator $\hat{L}$. We need to evaluate the following

$$\langle 2,1,\pm 1\vert\,\hat{L}\,\vert 2,1,0\rangle \qquad \text{and} \qquad \langle 2,1,0\vert\,\hat{L}\,\vert 2,1,\pm 1\rangle \ , \tag{B.20}$$

for a total of four terms since the states with different m_ℓ projection will have different expectation values. Instead of using the expression for $\hat{L}$ in Cartesian coordinates, we instead use the raising and lowering representation of the angular momentum operators. Recall that in general,

$$\hat{L} = \hat{L}_x \mathbf{e}_1 + \hat{L}_y \mathbf{e}_2 + \hat{L}_z \mathbf{e}_3 \ , \tag{B.21}$$

and we recall that $\hat{L}_z$ operating on any state of the form $\vert\alpha,\ell,m_\ell\rangle$ *does not* change the state, but simply measures the projection of the angular momentum off the z-axis according to

$$\hat{L}_z\,\vert\alpha,\ell,m_\ell\rangle = \hbar m_\ell\,\vert\alpha,\ell,m_\ell\rangle \ . \tag{B.22}$$

Hence, the z-component of the operator $\hat{L}$ does not change the state and so all inner products of the form $\langle\Psi'\vert\,\hat{L}_z\,\vert\Psi\rangle$ with $\vert\Psi'\rangle \neq \vert\Psi\rangle$ will be orthogonal. We are then left just with the components of $\hat{L}$ along x and y. We can rewrite these operators in terms of the raising and lowering operators according to,

$$\hat{L}_x = \frac{1}{2}\left(\hat{L}_+ + \hat{L}_-\right) \ , \qquad \hat{L}_y = \frac{1}{2i}\left(\hat{L}_+ - \hat{L}_-\right) \ , \tag{B.23}$$

where the application of $\hat{L}_\pm$ on some state follows the usual prescription,

$$\hat{L}_\pm \left|\alpha, \ell, m_\ell\right\rangle = \hbar\sqrt{\ell\left(\ell+1\right) - m_\ell\left(m_\ell \pm 1\right)}\left|\alpha, \ell, m_\ell\right\rangle \ . \tag{B.24}$$

This is to say that the raising and lowering operator just changes the projection m_ℓ. For the states of interest here, we note

$$\begin{aligned}
\hat{L}_+ \left|2,1,0\right\rangle &= \hbar\sqrt{2}\left|2,1,1\right\rangle \ , & \text{(B.25)}\\
\hat{L}_- \left|2,1,0\right\rangle &= \hbar\sqrt{2}\left|2,1,-1\right\rangle \ , & \text{(B.26)}\\
\hat{L}_- \left|2,1,1\right\rangle &= \hbar\sqrt{2}\left|2,1,0\right\rangle \ , & \text{(B.27)}\\
\hat{L}_+ \left|2,1,-1\right\rangle &= \hbar\sqrt{2}\left|2,1,0\right\rangle \ . & \text{(B.28)}
\end{aligned}$$

Using the above definitions, we can now evaluate $\hat{L}$ between the different m_ℓ states. We see

$$\begin{aligned}
\left\langle 2,1,1\right|\hat{L}\left|2,1,0\right\rangle &= \left\langle 2,1,1\right|\left[\frac{1}{2}\left(\hat{L}_+ + \hat{L}_-\right)\mathbf{e}_1 + \frac{1}{2i}\left(\hat{L}_+ - \hat{L}_-\right)\mathbf{e}_2\right]\left|2,1,0\right\rangle \\
&= \left\langle 2,1,1\right|\left[\frac{\hbar\sqrt{2}}{2}\mathbf{e}_1 + \frac{\hbar\sqrt{2}}{2i}\mathbf{e}_2\right]\left|2,1,1\right\rangle \\
&= \frac{\hbar\sqrt{2}}{2}\left(\mathbf{e}_1 - i\mathbf{e}_2\right) \qquad \text{(B.29)}
\end{aligned}$$

$$\begin{aligned}
\left\langle 2,1,-1\right|\hat{L}\left|2,1,0\right\rangle &= \left\langle 2,1,-1\right|\left[\frac{1}{2}\left(\hat{L}_+ + \hat{L}_-\right)\mathbf{e}_1 + \frac{1}{2i}\left(\hat{L}_+ - \hat{L}_-\right)\mathbf{e}_2\right]\left|2,1,0\right\rangle \\
&= \left\langle 2,1,-1\right|\left[\frac{\hbar\sqrt{2}}{2}\mathbf{e}_1 - \frac{\hbar\sqrt{2}}{2i}\mathbf{e}_2\right]\left|2,1,-1\right\rangle \\
&= \frac{\hbar\sqrt{2}}{2}\left(\mathbf{e}_1 + i\mathbf{e}_2\right) \qquad \text{(B.30)}
\end{aligned}$$

$$\begin{aligned}\langle 2,1,0|\,\hat{L}\,|2,1,1\rangle &= \langle 2,1,0|\left[\frac{1}{2}\left(\hat{L}_+ + \hat{L}_-\right)\mathbf{e}_1 + \frac{1}{2i}\left(\hat{L}_+ - \hat{L}_-\right)\mathbf{e}_2\right]|2,1,1\rangle \\ &= \langle 2,1,0|\left[\frac{\hbar\sqrt{2}}{2}\mathbf{e}_1 - \frac{\hbar\sqrt{2}}{2i}\mathbf{e}_2\right]|2,1,0\rangle \\ &= \frac{\hbar\sqrt{2}}{2}\left(\mathbf{e}_1 + i\mathbf{e}_2\right) \end{aligned} \tag{B.31}$$

$$\begin{aligned}\langle 2,1,0|\,\hat{L}\,|2,1,-1\rangle &= \langle 2,1,0|\left[\frac{1}{2}\left(\hat{L}_+ + \hat{L}_-\right)\mathbf{e}_1 + \frac{1}{2i}\left(\hat{L}_+ - \hat{L}_-\right)\mathbf{e}_2\right]|2,1,-1\rangle \\ &= \langle 2,1,0|\left[\frac{\hbar\sqrt{2}}{2}\mathbf{e}_1 + \frac{\hbar\sqrt{2}}{2i}\mathbf{e}_2\right]|2,1,0\rangle \\ &= \frac{\hbar\sqrt{2}}{2}\left(\mathbf{e}_1 - i\mathbf{e}_2\right) \end{aligned} \tag{B.32}$$

These expectation values are summarized in Tab. B.2.

Inner Product	Value		Inner Product	Value
$\langle 2,1,1\|\,\hat{L}\,\|2,1,0\rangle$	$\frac{\hbar\sqrt{2}}{2}\left(\mathbf{e}_1 - i\mathbf{e}_2\right)$		$\langle 2,1,0\|\,\hat{L}\,\|2,1,1\rangle$	$\frac{\hbar\sqrt{2}}{2}\left(\mathbf{e}_1 + i\mathbf{e}_2\right)$
$\langle 2,1,-1\|\,\hat{L}\,\|2,1,0\rangle$	$\frac{\hbar\sqrt{2}}{2}\left(\mathbf{e}_1 + i\mathbf{e}_2\right)$		$\langle 2,1,0\|\,\hat{L}\,\|2,1,-1\rangle$	$\frac{\hbar\sqrt{2}}{2}\left(\mathbf{e}_1 - i\mathbf{e}_2\right)$

Table B.2: All possible values of $\hat{L}$ between adjacent $2p$ states of atomic hydrogen.

APPENDIX C

Out of Plane Scattering

After the orthogonality between the pump and detection beams is checked using the alignment prism (as described in Chapter 3) there is still work to be done to ensure that the signal measured by the detector is either purely electric or purely magnetic. This can be achieved by using pinholes to discriminate against out-of-plane scattering from reaching the detector. The angle subtended by the pinholes should be selected to be sufficiently small so as to extinguish unwanted scattering by several orders of magnitude. Misalignment of the the beams or the use of pinholes with too large of an aperture will give rise to a large out-of-plane signal, as we discuss below.

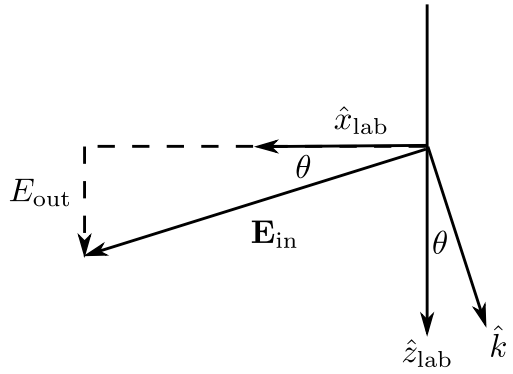

Figure C.1: A simplified geometry to determine the amount of out-of-plane scattering.

We consider a reference frame as that shown in Fig. C.1 in which the field $\mathbf{E}_{in}$ represents the field measured in our experiments and $\mathbf{E}_{out}$ represents an axial (out-of-plane) component due either to large pinholes or misalignment. The angle this ray makes with the optical axis of the input pump beam (i.e. $\hat{z}_{lab}$) can be written in terms of θ. The fields are then

$$\mathbf{E}_{\text{in}} = E_{\text{in}} \sin\theta \hat{z}_{\text{lab}} + E_{\text{in}} \cos\theta \hat{x}_{\text{lab}} \,, \tag{C.1}$$

$$E_{\text{out}} = \mathbf{E}_{\text{in}} \cdot \hat{z}_{\text{lab}} = E_{\text{in}} \sin\theta \,, \tag{C.2}$$

when $\mathbf{E}_{\text{in}}$ lies in the $\hat{x}_{\text{lab}} - \hat{z}_{\text{lab}}$ plane. If $\mathbf{E}_{\text{in}}$ also has a component along $\hat{y}_{lab}$ we get the more general expressions

$$\mathbf{E}_{\text{in}} = E_{\text{in}} \sin\theta \cos\varphi \hat{z}_{\text{lab}} + E_{\text{in}} \cos\theta \cos\varphi \hat{x}_{\text{lab}} + E_{\text{in}} \sin\varphi \hat{y}_{\text{lab}} \,, \tag{C.3}$$

$$E_{\text{out}} = \mathbf{E}_{\text{in}} \cdot \hat{z}_{\text{lab}} = E_{\text{in}} \sin\theta \cos\varphi \,. \tag{C.4}$$

We can easily calculate the relative proportion of axially polarized electric-dipole radiation coming from out-of-plane components by integrating E_{out}^2 over the desired solid angle. Assuming pinholes that define the scattering geometry are adjusted to the *same* size, the scattering solid angle is determined by the *second* pinhole alone, as depicted in Fig. C.2.

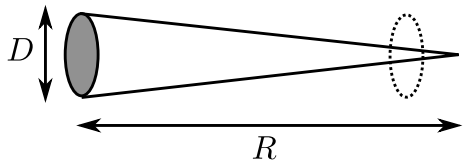

Figure C.2: The solid angle to be subtended by the choice of pinhole diameter.

Taking D to be the diameter of the second pinhole and R to be the distance to the sample scattering volume, the detection solid angle is

$$d\Omega = \frac{\pi(D/2)^2}{4\pi R^2} = \frac{D^2}{16R^2} \,. \tag{C.5}$$

The angular limits corresponding to the detection cone are the same for φ and θ,

$$d\varphi \leftrightarrow \pm\frac{D}{2R} \,, \tag{C.6}$$

$$d\theta \leftrightarrow \pm\frac{D}{2R} \,. \tag{C.7}$$

The intensity of the axially-polarized signal $\left|E_{\text{out},\|}\right|^2$ is then given by

$$\left|E_{\text{out},\parallel}\right|^2 = |E_{\text{in}}|^2 \cdot 2 \cdot 2 \int_0^{D/2R} d\theta R^2 \sin\theta \int_0^{D/2R} d\varphi \sin^2\theta \cos^2\varphi \,. \tag{C.8}$$

We wish to compare this to the maximum electric dipole signal measured with the same configuration. This is

$$|E_{\text{out},\perp}|^2 = |E_{\text{in}}|^2 \cdot 2 \cdot 2 \int_0^{D/2R} d\theta R^2 \sin\theta \int_{\pi/2}^{\pi/2+D/2R} d\varphi \cos^2\theta \sin^2\varphi \,. \tag{C.9}$$

Consequently, the ratio of axially-polarized to transversely-polarized intensity from the electric dipole alone is

$$\frac{\left|E_{\text{out},\parallel}\right|^2}{|E_{\text{out},\perp}|^2} = \frac{\int_{\theta=0}^{D/2R} d\theta \sin^3\theta \int_{\varphi=0}^{D/2R} d\varphi \cos^2\varphi}{\int_{\theta=0}^{D/2R} d\theta \sin\theta\cos^2\theta \int_{\varphi=0}^{D/2R} d\varphi \sin^2\varphi} \,. \tag{C.10}$$

The various integrals are

$$\int \sin^3\theta d\theta = -\cos\theta + \frac{1}{3}\cos^3\theta \,, \tag{C.11}$$

$$\int \cos^2\varphi d\varphi = \int \frac{1+\cos 2\varphi}{2} d\varphi = \frac{\varphi}{2} + \frac{1}{2}\left(\frac{\sin 2\varphi}{2}\right) \,, \tag{C.12}$$

$$\int \sin\theta\cos^2\theta d\theta = -\frac{\cos^3\theta}{3} \,, \tag{C.13}$$

$$\int \sin^2\varphi d\varphi = \int \frac{1-\cos 2\varphi}{2} d\varphi = \frac{\varphi}{2} - \frac{1}{2}\left(\frac{\sin 2\varphi}{2}\right) \,. \tag{C.14}$$

Hence

$$\frac{\left|E_{\text{out},\parallel}\right|^2}{|E_{\text{out},\perp}|^2} = \frac{\left[-\cos\theta + \frac{1}{3}\cos^3\theta\right]_0^{D/2R}\left[\frac{\varphi}{2} + \frac{1}{2}\left(\frac{\sin 2\varphi}{2}\right)\right]_0^{D/2R}}{\left[-\frac{1}{3}\cos^3\theta\right]_0^{D/2R}\left[\frac{\varphi}{2} - \frac{1}{2}\left(\frac{\sin 2\varphi}{2}\right)\right]_{\pi/2}^{\pi/2+D/2R}} \tag{C.15}$$

$$= 3 \cdot \frac{\left[\frac{2}{3} - \cos\left(\frac{D}{2R}\right) + \frac{1}{3}\cos^3\left(\frac{D}{2R}\right)\right]\left[\frac{D}{R} + \sin\left(\frac{D}{R}\right)\right]}{\left[1 - \cos^3\left(\frac{D}{2R}\right)\right]\left[\frac{D}{R} - \sin\left(\pi + \frac{D}{R}\right)\right]} \,. \tag{C.16}$$

A more simple form of this expression may be determined by using the small-angle approximation and reducing the trigonometric arguments. However, it is just as well to numerically evaluate the expression given some choice of D and R.

For the geometry used in our experiments, the pinhole was opened to $D = 3.5$ mm and

was placed after the collimating lens which had a focal length of150 mm. Using $D = 3.5$ mm and $R = 150$ mm, this provided an excellent extinction between in-plane and out-of-plane scattering to

$$\frac{\left|E_{\text{out},\parallel}\right|^2}{\left|E_{\text{out},\perp}\right|^2} = 6.8 \times 10^{-5} \, . \tag{C.17}$$

Also of use is the angle made between the optical axis and the outer-most ray. Using these same values, we find that θ is given by

$$\theta = \tan^{-1}\left(\frac{D}{2R}\right) = 0.67^\circ \, , \tag{C.18}$$

which is very small.

APPENDIX D

PMT Saturation

A major issue we encountered while building the ME scattering system was the effect of detector saturation. The time spent diagnosing and solving this problem is worth an appendix, especially because this effect may have been overlooked in previous experimental designs [15]. When using a photon-counting instrument, the detector will under-count the true number of incident photons and the observed count rate will become increasingly nonlinear as the intensity of incident light increases [39]. This occurs because the output signal pulse of the photomultiplier tube has a finite width associated with the speed of the electronics used to process the photocurrent generated by the incoming signal photons. The speed of these electronics sets a minimum time interval, often referred to as a "dead time," over which only a single photon can be accurately counted by the device. This type of device is often referred to as "paralyzable" or "semi-paralyzable" because there is a time interval over which the detector is frozen or not able to count more signal [79]. The degree of paralyzability determines the nonlinear saturation response, as we will discuss later.

Typical photon-counting devices have refresh rates of the order 10-100 MHz, corresponding to dead time intervals of the order 10-100 ns [39]. For observing continuous light sources such as light from stars or table-top optical experiments using continuous-wave lasers, the maximum count rate for such devices is still rather high (10^7-10^8 counts/s for devices with 10-100 MHz refresh rates). Count rates of this order still offer good signal averaging without having to use long exposure times and also have the added benefit of corresponding to low, but measurable, optical powers[1]. These signals may be detected using low-light power meters that are not subject to the same dead time saturation. A common high-sensitivity, low-light detector is the avalanche photodiode (APD), which is a semiconductor-based device which provides signal gain through avalanche multiplication. These devices work well for observing low-light signals from continuous or periodic sources with a high duty-cycle, but still have a minimum threshold for signal detection.

[1]For instance, 10^7 photons/second at 775 nm corresponds to about 2.5 pW of average power. Many sensitive power meters can detect down to single fW power levels.

However, when observing a weak signal from a periodic light source with a low duty-cycle, such as an amplified femtosecond laser, the maximum count rate is determined by the repetition rate of the laser and low-light power meters are no longer a viable option.

The temporal duration of pulses from the Clark CPA-2001 laser used in the scattering experiments were of the order 180 fs, therefore limiting the detected signal to a single photon per pulse since our PMT had a dead time of about 10 ns (180 fs $\ll$ 10 ns). This means that the device could not accurately detect more than one event during this time interval (see Fig. D.1). Because the laser repetition rate was 1 kHz, the maximum count rate in our experiment was limited to 1000 counts/s (i.e. 1 photon per pulse), as the time between subsequent laser pulses (1 ms) is many orders larger than the dead time window (see Fig. D.2). The lower range of the PMT is determined by the dark count rate, which should be between 0-10 counts/s for a good thermo-electrically cooled detector such as the one used in our experiment. Experimentally we had dark counts of the order 5 counts/s, which set the dynamic range of our PMT to 5-1000 counts/s. For measuring scattering from a typical liquid sample at modest input power (for example, CCl_4 at $I = 10^8$ W/cm^2) the actual count rate[2] of the electric signal was of the order 100,000 counts/s, clearly much higher than the allowed 1000 counts/s, which caused the detector to saturate.

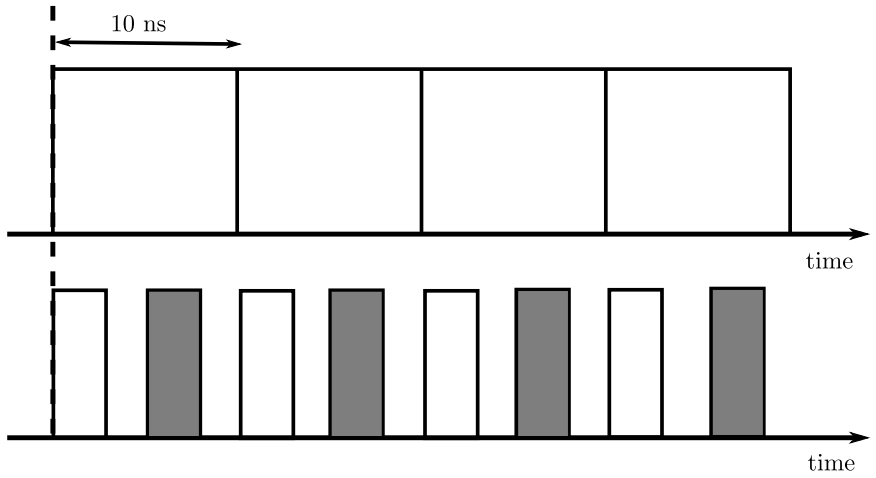

Figure D.1: A graphical representation of a 100 MHz photon-counting device being used to measure single photon events from a repetitious 200 MHz source. During the dead time window of 10 ns, only one of the signal photons will be counted and the resulting signal will be 50% of the true signal.

We discovered the issue of detector dead time and saturation while making measurements of electric Rayleigh scattering in several liquid samples. We noticed that for relatively low intensities (10^6 W/cm^2) the measured electric scattering was dipolar in nature

[2]Actual count rate here refers to what the counts would be without using filters to attenuate the signal.

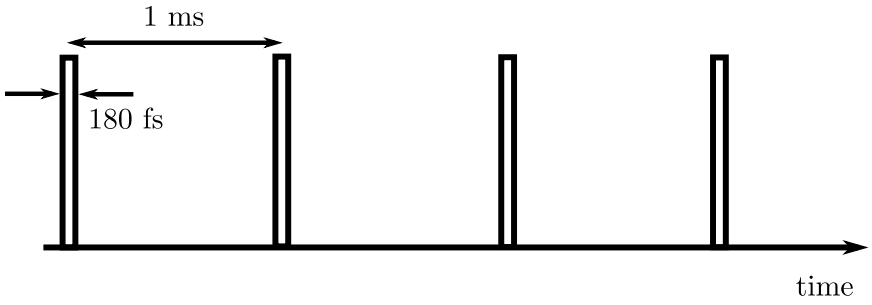

Figure D.2: A 1 kHz laser system with temporal pulses of the order 180 fs. The time between subsequent pulses is many times more than the dead time interval (1 ms $\gg$ 10 ns), so we are limited to a single photon per pulse.

(i.e. a cosine-squared fit), but as we increased the input intensity, the dipole would acquire a boxy-shape and its top would flatten out, as shown in Fig. D.3. Here we see that the dipole begins to flatten out around 600 counts/s which corresponds to an input power of about 10^7 W/cm^2, though this should be 1000 counts/s[3]. The fact that the input intensity was so low suggested that the saturation here was electronic and not optical in nature. To test this, we ran the experiment again but with a ND filter of 0.6 in the signal arm, with the expectation that lowering the signal into the detector would shift the saturation to a higher relative input intensity. The results of this are shown in Fig. D.4, in which we no longer see a flat-top saturation of the electric scattering. These two results are summarized in Fig. D.5(a-b) which shows the saturation cure with no attenuation and then when the attenuating filter is used.

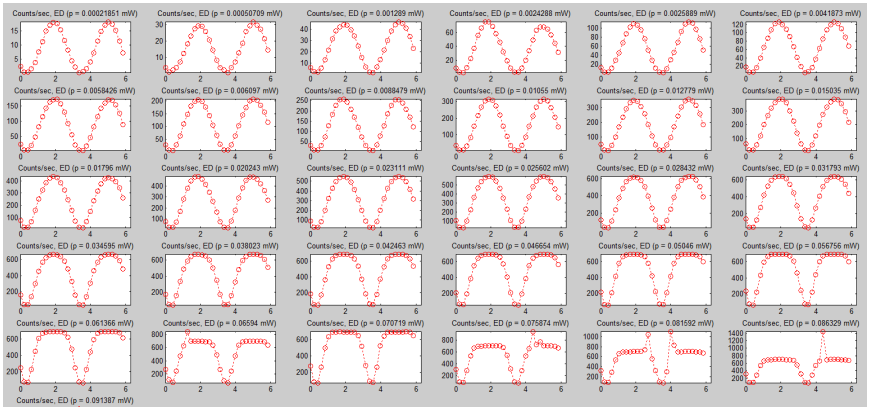

Figure D.3: Electric dipole scattering patterns for increasing input intensity. As the input power is increased, the dipole evolves into a boxy-shape. This was taken for CCl_4. The corresponding intensities should be up to about 2×10^7 W/cm^2 for the most intense plot.

[3]The code I was running did not normalize the count rate properly for these plots and should be multiplied by a factor of 3/2.

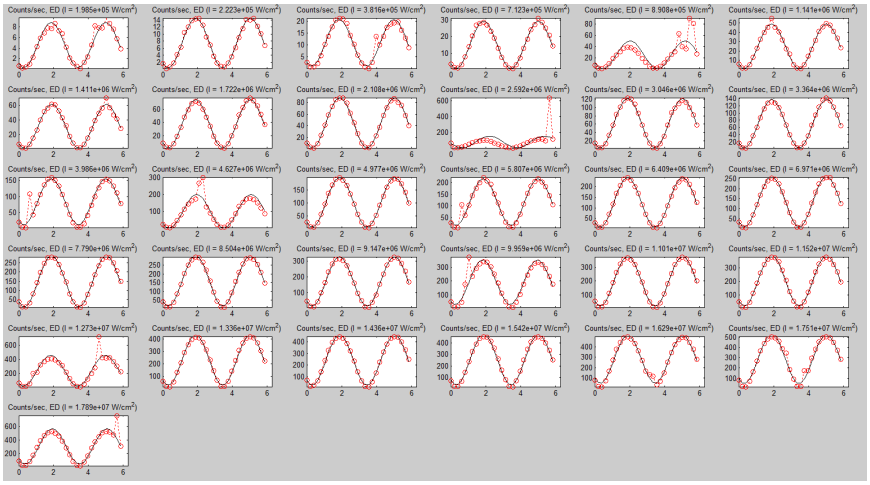

Figure D.4: Electric dipole scattering patterns in CCl_4 using an OD0.6 filter in the signal arm to attenuate the light reaching the PMT. The curves are no longer saturating at high intensities, suggesting that the effect of saturation is purely electronic.

As the input intensity is increased beyond the immediate saturation regime, the boxy nature of the measured scattering patterns begins to continually evolve into more obscure shapes (see Fig. D.6). This is because the PMT responds in an increasingly nonlinear fashion as more signal is sent to the cathode, meaning the device is semi-paralyzable. If the device were completely paralyzed over the entire dead time window, then the measured dipole patterns would flatten out completely and the saturation curve would be a plateau at 1000 counts/s for all input intensity. Instead, the detector is clearly measuring multiple signal events over a single dead time window, but in an unreliable fashion. The saturation curve for this higher intensity regime is shown in Fig. D.5 (right), though we will show later on a more complete measurement of this curve. The use of varying OD filters has been the simplest fix for the saturation issue, but it is worthwhile to consider other options in which we are not throwing away orders of magnitude of the signal.

There are essentially two options to consider when choosing an appropriate detector: we can either use single-photon counting devices or low-light power meters. The benefit of using a single-photon counting device is the extremely high sensitivity, however all devices of this nature are limited to the dead time issue discussed above. Low power light meters do not have the same saturation issue as photon-counting devices, but typically have minimum power requirements for measuring small signals. Devices of this nature can either be thermal, which are sensitive down to the μW level at best, or solid state, which can be as sensitive as a few fW[4]. We can establish a range of average power levels that we

[4]For example, Thor Labs Si photodiode model PDF10A can go down to 10 fW level on its own and sub-fW using a lock-in amplifier. Detectors like this, however, do not have appropriate bandwidth to use with low

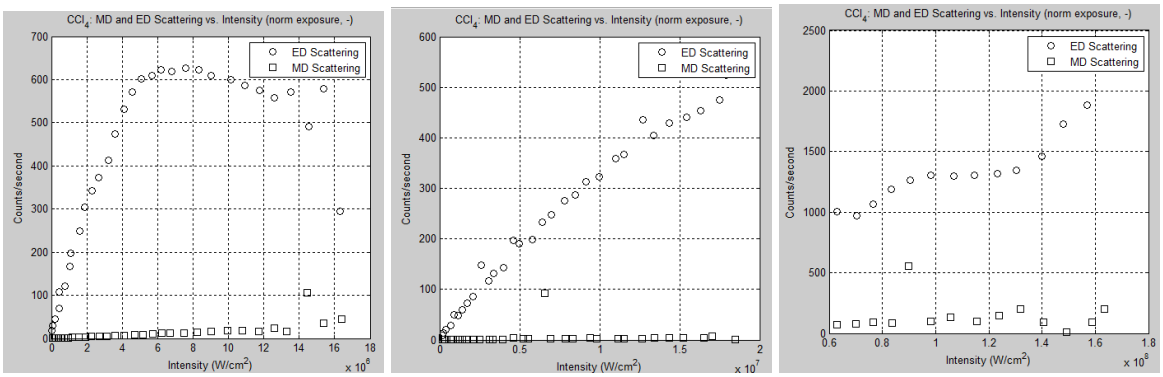

Figure D.5: Maximum electric dipole scattering (polarized fitted component) for no attenuation (left) and with attenuation of OD0.6 (middle) before the PMT. (Right) the response curve for the "highly-saturated" regime.

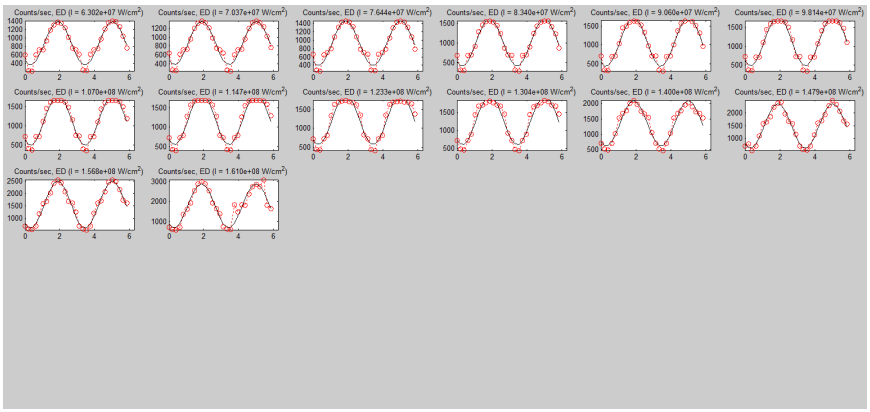

Figure D.6: Measured electric dipole scattering for "highly-saturated" PMT regime.

anticipate wanting to measure with a simple calculation. We start by calculating the energy of a single photon at the laser central wavelength, $\lambda_0 = 775$ nm, using

$$E = \hbar\omega = \frac{hc}{\lambda} = \frac{1240 \text{ eV} \cdot \text{nm}}{775 \text{ nm}} = 1.6 \text{ eV} , \tag{D.1}$$

which can be converted to J,

$$1.6 \text{ eV} \cdot \frac{1.6 \times 10^{-19} \text{ J}}{1 \text{ eV}} = 2.56 \times 10^{-19} \text{ J} . \tag{D.2}$$

This energy can also be thought of as the "energy per count." Next is to calculate the average power seen by the detector, which is the total energy deposited into the detector over a certain amount of time. For example, let's assume we have a single photon per pulse (1000 counts/s), so the average power is simply

repetition rate systems like the Clarks.

$$
\begin{aligned}
P_{ave} &= \frac{\Delta E}{\Delta t} \\
&= \frac{2.56 \times 10^{-19} \text{ J/count}}{1 \text{ s}} \cdot 1000 \text{ counts} \\
&= 0.256 \text{ fW} .
\end{aligned} \tag{D.3}
$$

The typical count ranges that we are trying to resolve are between 10 counts/s and about 10^6 counts/s, which is typical when the input intensity is of the order 10^9 W/cm^2. This range corresponds to average power measurements from 2.56 aW to 0.256 pW, which is still too low even for fW power meters to resolve. This suggests that the single-photon counting scheme is still the best approach.

In staying with a single photon counting device, we are left with four options to explore to potentially improve the dynamic range of our detector,

1. reduce the dark count rate,
2. increase the maximum allowed count rate,
3. apply a nonlinear correction to the saturated signal, or
4. reduce the signal level which reaches the detector.

The first of these options is perhaps the least fruitful in the sense that we are already at a very low dark count rate, while the second of these options is the most desirable since it would increase the dynamic range of the device up to $10^6 - 10^7$ counts/s. The third option is somewhat useful to think about, but would require us to implement a nonlinear correction to all of the measured data in our experiments. This approach would result in huge uncertainties in our data. The fourth option has been explained above and works fine but requires us to throw away a lot of signal. In the following sections we discuss solutions to each of these points.

D.1 Reducing the dark count rate

Reducing the dark count rate of our system would not result in much better dynamic range for our detector, but it is worth describing what could be done to improve the noise rejection. The most direct solution would be to add a second PMT to the detection scheme and run the pair of detectors in a coincidence circuit. This would give background noise rejection and would give good timing resolution to kill the random noise, as it would be possible

to set the detection scheme to only record a signal when both detectors see a photon. However, the signal averaging in the experiment can already be improved simply by using a longer exposure time for the PMT and averaging over more points in a given measurement.

D.2 Increasing the maximum count rate

The only way to increase the maximum count rate of our detector is to either stretch out the signal pulse in time several orders more than the detector dead time or to find a photon-counting detector that has a much faster refresh rate (or some combination of these two). There do exist photon-counting detectors with faster refresh rates (i.e. shorter dead time intervals), but at best these devices are only faster by an order of magnitude or so from our current device, so this alone would not solve the problem. The most realistic alternative would be to stretch the 180 fs signal pulses to many times more than the 10 ns detector dead time. Note that even if the 180 fs pulse was stretched to 10 ns, we would still be limited to 1 photon per pulse, so it must be much longer. The number of photons per pulse that could be detected would be given by the ratio

$$\#\text{ of photons detected per pulse} = \frac{\text{signal duration}}{\text{detector dead time}}\,, \tag{D.4}$$

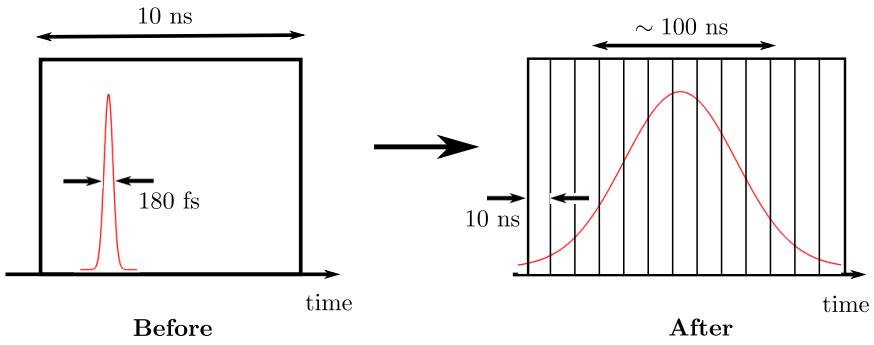

Figure D.7: *Left*: before being stretched, the ultrashort laser pulse fits inside the dead time window. *Right*: if the pulse is stretched to several orders more than the dead time then more counts per pulse can be recorded by the detector.

where the number of detected photons per pulse is rounded up to 1 if the ratio is less than unity. So, for example, a $10\times$ increase in count rate would mean that the signal pulse would have to be stretched to 100 ns, making the max count rate 10,000 counts/s (see Fig. D.7). Note that the maximum achievable count rate for a dead time-limited detector is the continuous source limit (i.e. the signal pulses are stretched so much that adjacent pulses overlap), which is 10^8 counts/s for a device with a 10 ns deadtime.

As we know from ultrafast optics there are several techniques which can be implored to lengthen the temporal duration of an optical pulse, which is really equivalent to increasing the temporal delay between spectral components of the ultrashort pulse. Some common techniques include diffractive gratings, prisms, or dispersion lines consisting of long segments of optical fiber. A less formal technique that can be used to separate the spectral components is simply reflecting the pulse off a highly-dispersive material, such as a white plastic (we see white because the material is dispersing the light). Following are brief discussions of these techniques.

D.2.1 Ping-pong ball trick

In this first approach to implementing a dispersive mechanism in our detection arm, we used a standard ping pong ball which we cut two ends from and inserted into one of our interference filter mounts. The first segment of the ping pong ball had a small aperture cut in the middle that was approximately the diameter of the focusing signal beam, while the second segment of the ping pong ball had no holes. These two pieces comprised a semi-permeable cavity into which the signal light would enter through the hole and then reflect multiple times before eventually exiting the second plastic membrane. Upon each reflection off one of the membranes, the spectral components of the pulse are assumed to spread more in time. A simple prediction of the amount of added delay in the signal can be calculated by knowing the separation of the two membranes, the transparency of the plastic used, and the effect of dispersion upon each reflection. This trick is very similar to the idea of an integrating sphere. The ping pong ball trick was tested using the liquid sample CCl_4 and looking at the electric Rayleigh scattering as a function of intensity to see if it still saturated at 1000 counts/s. Unfortunately, the electric scattering still saturated at the previous value of 1000 counts/s, suggesting that the semi-permeable plastic cavity did not sufficiently stretch the signal pulses out in time.

D.2.2 Fiber dispersion line

After the ping pong ball proved to be unsuccessful, we decided to explore more traditional methods for dispersing the optical pulse. At the top of this list was the inclusion of an optical fiber dispersion line, which would rely on the dispersive nature of the fiber core to separate the spectral components of the pulse in time. We consider two wavelength components λ_1 and λ_2 (for instance the two spectral components that coincide with the FWHM of the laser spectrum) of our ultrashort laser pulse and send them into the dispersive fiber at the same time. We wish to separate them by the time interval $\Delta\tau$ as they travel a

distance d through the fiber,

$$\begin{aligned}\Delta\tau &= \frac{d}{v_g(\lambda_1)} - \frac{d}{v_g(\lambda_2)} \\ &= d\left(\frac{1}{v_g(\lambda_1)} - \frac{1}{v_g(\lambda_2)}\right) ,\end{aligned} \tag{D.5}$$

where

$$v_g(\lambda) = v_p\left(1 + \frac{\lambda}{n}\frac{dn}{d\lambda}\right) , \tag{D.6}$$

is the group velocity and is essentially equal to the phase velocity, v_p. Given that $v_g \approx v_p = c/n$ and $n = n(\lambda)$, we can rewrite the expression for the time interval as

$$\Delta\tau = \frac{d}{c}\left[n(\lambda_1) - n(\lambda_2)\right] , \tag{D.7}$$

from which it is immediately obvious that the $\Delta\tau$ is caused entirely by the difference in refractive index at the different spectral components of our laser pulse. This is one way to calculate the temporal stretching of the pulse, but it requires that we know the refractive indices of the glass at two well-defined spectral components of our laser pulse. It is more common for fiber manufacturers to define the dispersive properties of the fiber by the "dispersion parameter," from which it is easy to determine the amount of fiber needed to stretch a pulse by a certain length of time.

The dispersion parameter is typically derived from the formula for the group-velocity dispersion (GVD) of an optical pulse, which is the phenomenon that the group velocity of light in a transparent medium depends on the optical frequency. The GVD is typically defined as[5]

$$\text{GVD} = \frac{\partial}{\partial\omega}\frac{1}{v_g} = \frac{\partial}{\partial\omega}\left(\frac{\partial k}{\partial\omega}\right) = \frac{\partial^2 k}{\partial\omega^2} , \tag{D.8}$$

where $k = \omega/v = n\omega/c$ is the wavenumber. From this, the dispersion parameter is defined as

$$D_\lambda = -\frac{2\pi c}{\lambda^2}\text{GVD} = -\frac{2\pi c}{\lambda^2}\frac{\partial^2 k}{\partial\omega^2} , \tag{D.9}$$

which has the units of s/m^2, but is often specified in terms of ps/(nm·km). This parameter depends on the wavelength and can be thought of as the ps increase in temporal duration

[5]The reference for this is RP-Photonics, GVD.

per nm wavelength difference and kilometer propagation distance.

Typical fibers offered by companies such as Thor Labs specify their fibers in terms of this dispersion parameter, which are all of the order 100-500 ps/(nm·km). For example, the dispersion for the fundamental mode of a large numerical aperture multimode fiber (for the FT-400 series fibers) is $D_\lambda = -117$ ps/(nm·km) at the Clark central wavelength of 775 nm. The desired temporal width can be calculated by computing

$$\Delta\tau = D_\lambda \cdot \Delta\lambda \cdot d \, . \tag{D.10}$$

So if we send our pulse, which has a bandwidth of about 5 nm, through a 1 km piece of optical fiber, the separation in time will be of the order

$$\Delta\tau = [-117 \text{ ps/(nm·km)}] \, (5 \text{ nm}) \, (1 \text{ km}) = -585 \text{ ps} \, , \tag{D.11}$$

which is still 20$\times$ shorter than the PMT dead time. This means that we would need at least 20 km of optical fiber just to stretch the signal pulse out to match the dead time window, and only then could we start to increase the maximum count rate of our detector. Fiber spools of this length are not practical to work with (something of the order 1-3 km might be manageable), and this does not even consider the losses we expect to have when propagating such long distances.

Hence, the only way we could implement a fiber dispersion line successfully into our detection scheme is if we were able to also get a photon-counting detector that recovered in tens of ps. This type of detector along with a dispersion line like the one described above may work, but the coupling and propagation losses through the fiber make it hard to justify. Other dispersive techniques such as gratings and prisms could possibly work, but we may need long working distances and very expensive optics.

D.3 Applying a nonlinear correction

Another approach for correcting the dead time issue is to apply a nonlinear correction to the measured signal. This is inherently a difficult thing to do, since nonlinear corrections to data will introduce huge uncertainties and could potentially wash out all useful quadratic information in the magnetic signals we are trying to measure. The first step in performing this correction is to precisely measure the detector saturation over a large range of input intensities. The detector saturation profile for a measurement of the analyzer set to pass vertically-polarized light is shown in Fig. D.8. The two curves are from the same set of data but are shown on (a) linear and (b) semilog-Y axes. The sample used as a scattering medium

was benzonitrile, which was chosen arbitrarily in order to simulate typical experimental conditions. For each intensity point, 20 points along each dipole were recorded, the PMT exposure time was 1 second, and the number of periods for the photon counting box was limited to 1. This data was taken using the original interference filter with $\lambda_0 = 780$ nm, $\Delta\lambda = 10$ nm, and tilted at 14° to pass the central laser wavelength of $\lambda_c = 775$ nm.

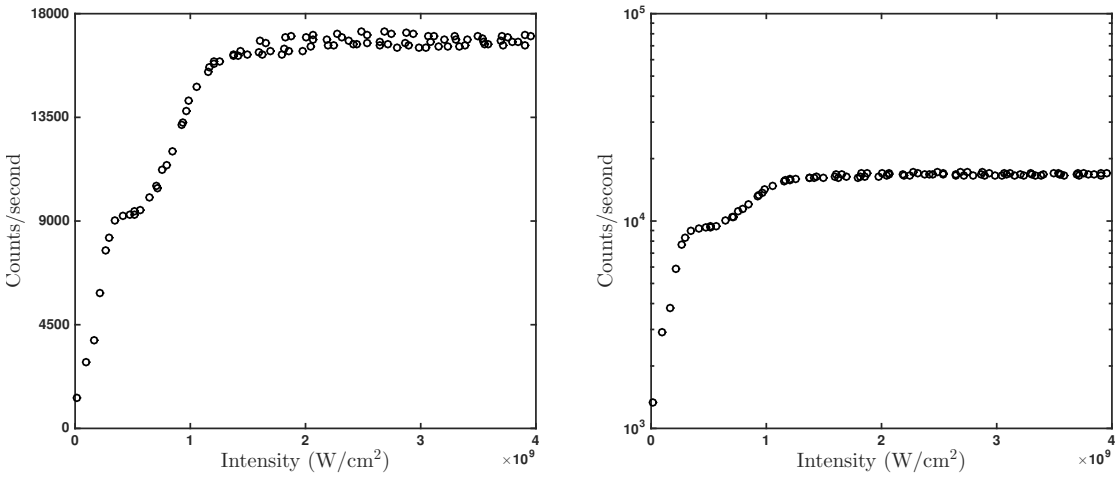

(a) (b)

Figure D.8: Saturation curves for the photomultiplier tube with the analyzer set to pass vertical polarization. Both plots show the same data but (a) is on linear axes and (b) is on a semilog-Y plot. In both curves it is possible to see at least two plateaus occurring at 9,000 and 17,000 counts/s. At least two more plateaus are present (at 1,000 and 3,000 counts/s) but it is difficult to make these out from this data.

From the plots, we can see three distinct regions of saturation followed by small segments over which the detector appears to be mostly linear. There appears to be constant (or saturated) segments at 3000, 9000, and 17,000 counts/s, each of which stay saturated over a consecutively broader range of intensities. What is not possible to see in these saturation curves is the initial saturation plateau, which occurs at 1000 counts/s (and can be seen in the plots at the beginning of this section). As we can see from the plots for the analyzer in the vertical position, the final saturation plateau at 17,000 counts/s does not appear to go linear again, suggesting that this value must be the true device saturation.

If we were to apply a correction to our data, we would have to first measure the saturation curve again, but with high enough precision to see the onset of the first saturation plateau at 1000 counts/s. We also require that the signal being used to generate the saturation curve is linear (such as electric Rayleigh scattering) and we have another technique that can simultaneously measure the signal (or in our case, the optical power of the throughput

beam) to confirm its linearity. We would then do a linear fit to a portion of the data below the first saturation plateau, and extend this for all input optical intensities: this would be the curve that we are trying to measure. We would then have to use a convolution in order to correct our measured, nonlinear signal and make it match the linear fitted line. This would have to be applied to every set of data that we process, and would have to be done in a way that it does not rely on the input intensity but rather the overall count rate and the slope of the linear portion of the measured signal (i.e. we would need to always be in a regime where we knew what the linear electric Rayleigh scattering should look like).

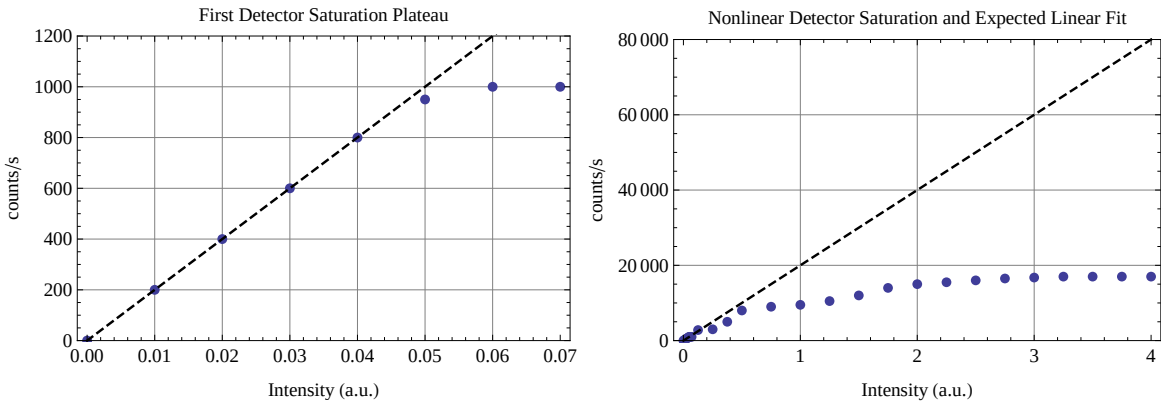

Figure D.9: (a) The first anticipated detector plateau occurs at a count rate of 1000 counts/s. (b) Multiple other saturation plateaus occur at higher intensities. In both plots the dashed black curve represents the actual linear signal we intend to measure.

Using the data from the above saturation curves, we can estimate the shape and onset of the first saturation plateau that would reach the value of 1000 counts/s. The blue dots in shown in Fig. D.9(a) is a fabricated set of data showing the first plateau saturation over an arbitrary intensity range, while the dashed black line depicts the expected linear response of the electric Rayleigh scattering. When this data and linear fit are shown on the same plot window as the higher-order saturation plateaus, it becomes obvious what a dramatic effect the saturation has on the anticipated signal. This is shown in Fig. D.9(b), where the plot window has been extended to show the expected linear curve as well as the actual measured curve. Note: the data points on this plot are made by eye estimates from the measured graphs above. This is purely for demonstrative purposes.

D.4 Limiting the signal to the detector

Since none of the options discussed above were a viable solution to this problem, we implemented a simple technique of limiting the amount of light to the detector. This was done

using a neutral density filter placed in the beam line of the detection optics before the PMT. This alternative simply attenuates the total signal seen by the detector so that the count rate is maintained under the saturation limit of 1000 counts/s. This solution is incredibly simple and straight-forward, but the major downside is that signal is being thrown away; this is why such effort was put into coming up with an alternative solution. Note that the filters used were Newport absorption filters and the optical density was rated at 564 nm. The attenuation at the laser wavelength of 775 nm was measured using a reference beam and a power meter. Measurements were made with and without the filter for a series of input optical powers and the computed ratio yielded the attenuation at the laser wavelength.

APPENDIX E

Details on SMC Rotation Stages

Beyond the experimental methods discussed in the main body of this thesis for zeroing and calibrating the SMC rotation stages, special care had to be taken to ensure their reproducibility and accuracy. Two problems were discovered early in the developmental stages of the scattering experiment which were due to the SMC stages: (1) a large amount of infrared signal was reaching the detector with the laser blocked, and (2) there was an apparent rotation in the angular position of the measured electric dipole maximum. Both of these issues were resolved as explained in the following sections.

E.1 Infrared light leakage

Early on it became obvious there was a source of IR radiation that was making its way to the PMT during our experimental runs. This was discovered when the dark counts that were taken with the Clark-MXR laser blocked were sometimes higher than the actual signal being measured from the scattering source. The source was quickly isolated to inside of the SMC rotation stages, which was confirmed upon removing the outer cover and using the IR viewer to look inside the stage. It was determined there was an IR diode and sensor used for indexing the stage within the stage housing. This light was being refracting into the analyzer as well as leaking out of the edges and causing the count rate to increase dramatically. The solution was to wrap electrical tape around each of the mounts to cover any holes that the light may leak out of.

A simple test was done to measure the amount of IR light reaching the detector from each of the three rotation stages. For this test, the analyzer before the PMT was kept in the vertical orientation and measurements were made as the $\lambda/2$-plate for polarization control was rotated through 180°. This measurement was made for four cases in order to isolate sources of stray radiation that could get to the detector: (1) PMT closed, (2) analyzer only, (3) analyzer and $\lambda/2$-plate (for polarization control), and (4) analyzer and both $\lambda/2$-plates

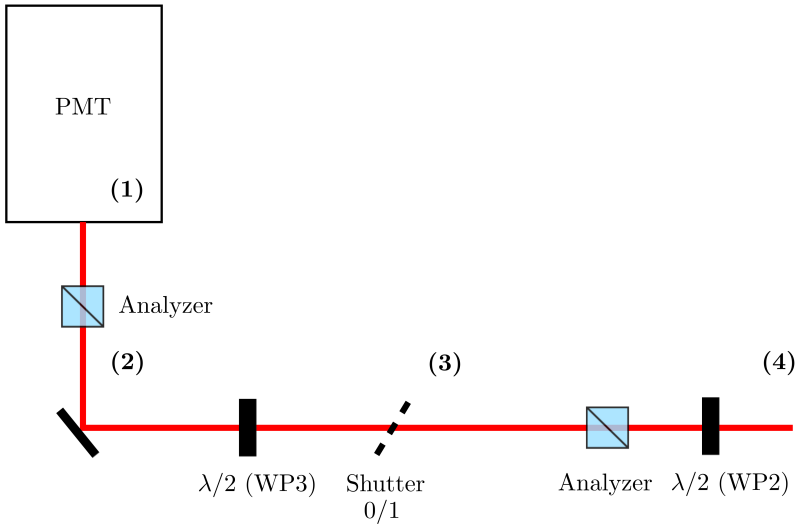

Figure E.1: Sketch showing experimental outline for taking measurements of light leakage. The locations labeled (1)-(4) correspond to regions where a large flat was used to block the beam line.

(as shown in Fig. E.1). For each of these measurements, the beam path was blocked so that light was shielded from each of the potential sources of radiation up the beam line from the PMT. Instead of a sample, a mirror at 45° was used at the interaction point to direct any of the stray light toward the PMT. This mirror was aligned using the Clark-MXR beam while keeping the PMT shutter blocked.

The plots shown in Fig. E.2 show the total counts over a 1 s interval for each of the four measurement cases described above with USB shutter open (Fig. E.2(a)) and USB shutter closed (Fig. E.2(b)). As shown in Fig. E.1, the USB shutter was positioned along the beam line between the two $\lambda/2$-plates and it has a small LED that remains lit while in use. From the data shown in Fig. E.2, it is apparent that when the PMT shutter is open and only the analyzer is unblocked from the beam path the count rate matches that of the device noise (i.e. PMT shutter closed measurement). Then when the two $\lambda/2$ are unblocked, we see a large increase in count rate which is different from when the shutter is open and when it is closed. We can easily infer by looking at the data in Fig. E.2(a) and (b) that both $\lambda/2$-plates (WP3 and WP2) each contribute an additional 10-15 counts/s while the LED from the USB shutter apparently contributes an additional 35-40 counts/s. Although these numbers seem relatively high, they will not be an issue when the experiment is run[1]. The fact that the

[1]This is because the experiment here is using a mirror to take most of the light coming along the beam line and direct it toward the PMT. In the actual scattering experiment, the input laser light is much higher than these small sources of light and so they are very unlikely to induce scattering in the dielectric sample. We are most concerned with confirming that the analyzer which is inside the dark box with the PMT is not adding to the signal.

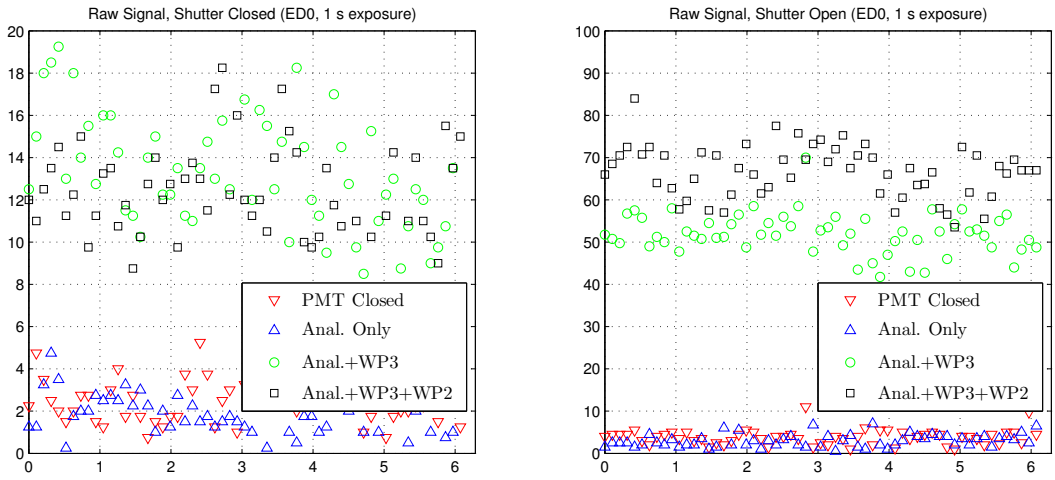

(a) Shutter Closed

(b) Shutter Open

Figure E.2: Experimental check of external sources of radiation in scattering experiment while blocking light at four key places along the beam line. The laser was off during these measurements and (a) shows measurements for shutter closed and (b) for shutter open.

count rate is very low inside of the box is what matters.

We also looked at the total counts as a function of $\lambda/2$-plate angle over a 1 s interval with the laser turned on but attenuated significantly by ND filters. The results of this are shown in Fig. E.3. Here we see a cosine-squared dependence in the measured signals both when the shutter is open and the shutter is closed. As shown in Fig. E.3(a) polarized laser light is apparently leaking through the USB shutter and getting to the PMT, which tells us the shutter does not completely extinguish the light. However, the ratio of light getting through the shutter is about 1:500, which is incredibly low and therefore should not be a contributing factor in experiments when the mirror is replaced with the sample. Furthermore, although the data in Fig. E.3(b) follows a cosine-squared pattern, the PMT must be highly saturated (see Appendix D), so the maximum value of 15×10^4 counts/s is a large under-estimate for the actual amount of signal reaching the detector, meaning the ratio of 1:500 is much larger. The fact the device is being saturated also explains the spikes in amplitude in the valleys of the measured signal in Fig. E.3(b): these are simply due to the nonlinear, highly-saturated PMT response.

What we can conclude from these measurements is the importance of isolating stray sources of IR radiation that could be contributing to our overall signals. By wrapping the SMC rotation stages in black electrical tape, we have been able to reduce the amount of light leakage from the IR diodes that are inside of the devices. Doing so has allowed us to keep the dark noise inside the box equal to that of the noise of the PMT with its shutter

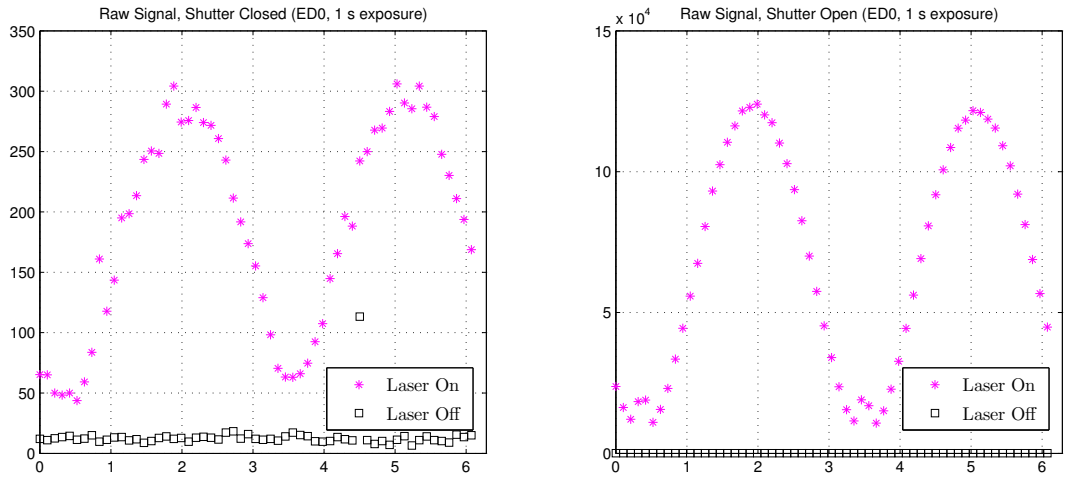

(a) Shutter Closed

(b) Shutter Open

Figure E.3: Experimental measurement of light leakage through USB shutter with laser on for (a) shutter closed and (b) shutter open.

closed. The small contributions from sources outside of the box are not likely to contribute to the measured signal when a sample is being analyzed, and due to their unpolarized nature, can be easily subtracted out if needed. Furthermore, we have shown here that there is some amount of leakage of light through the USB shutter, but we need not be concerned due to its incredibly small signal relative to the beam when the shutter is opened.

E.2 Mechanical backlash

A second major issue we faced with the rotation stages was in the reproducibility of measurements upon multiple rotations of the $\lambda/2$-plate used for the polarization control. This became clear during the calibration stage when measurements of the transmitted optical field through the analyzer for a range of input intensities showed maxima at different values of $\lambda/2$-plate orientation. The data, which should show a series of curves following a cosine-squared dependence with maxima at the same angular position, showed a difference in about 1° for each successive measurement. This problem amounted to an issue of indexing the rotation stage (in other words, mechanical backlash) and was resolved by replacing the Newport SMC stage with a newer stage of the same type that did not show the same problem[2]. An experiment was performed to qualitatively measure the slippage

[2]Because the slippage was only apparent through several uses of the rotation stage, the faulty mount was exchanged with the newer SMC stage used for intensity control. This worked fine since this stage could be calibrated every time an experiment was run and the exact calibration was less important since power

and the aforementioned solution was implemented, the details of both are described below.

First, a simple experiment was conducted to quantify the degree of stage slippage upon successive rotations of the $\lambda/2$-plate. The HeNe alignment laser was used as the light source and the experiment consisted of placing the $\lambda/2$-plate for polarization rotation in the HeNe alignment beam and detecting the signal using the PMT. The beam was attenuated by about OD3.5 using the filter wheel and a piece of frosted tape replaced the sample to act as a light diffuser (this brought the count rate down to about 7,000 counts/s, which was fine for the cw laser being used). The IR filter used in experiments on the front of the PMT was replaced with a narrow-bandpass filter centered on the HeNe wavelength. A series of transmission curves were then recorded as the polarized light was rotated through $360°$ and detected by the PMT. After each curve was recorded, the rotation stage rotated in the backward direction to reset its position before making the next set of movements. This measurement was repeated 12 times and it was determined that the peak shifted upon each successive measurement (see Fig. E.4). The curves were fit according to the function

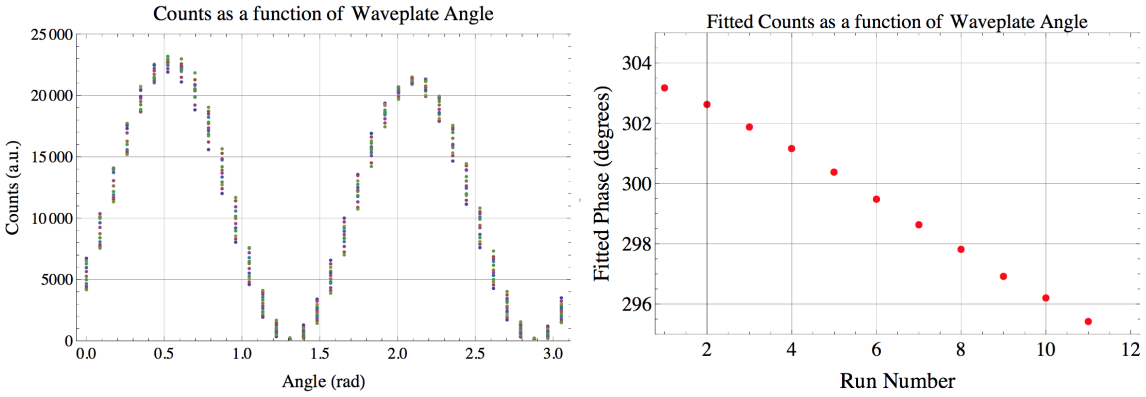

(a) (b)

Figure E.4: (a) The raw counts as a function of angle for 12 successive measurements of light through the analyzer. The asymmetry is likely due to the waveplate being for 780 nm instead of 632 nm. (b) The fitted phase as a function of successive run number. If there were no problem with the stage, this value should be constant.

$$I = A\cos^2(2\theta + \varphi) \ , \tag{E.1}$$

and the fitted amplitude A and phase φ were extracted. Figure E.4(b) shows the fitted phase as a function of run number, and from this plot it is clear that there is a constant slippage of the zero-point on the rotation stage of about $0.8°$ per run.

This issue was resolved when the faulty stage was replaced by a newer model of the

measurements were taken at each intensity point (see Methods chapter for more details).

same stage. An identical measurement was done to check the position of the peaks upon successive measurements of rotated polarized light through the analyzer. The only difference is that this experimental test used the Clark-MXR beam and included transmission through the intensity control system (as outlined in the Methods chapter). The IR interference filter was used and a mirror at $45°$ replaced the sample. The pulsed beam was strongly attenuated and a series of 7 intensity measurements were made as the $\lambda/2$-plate rotated the light through $360°$. Measurements were recorded for the analyzer in four positions: vertical up, vertical down, horizontal left, and horizontal right. The results of this are shown in Fig. E.5, and we can that there is no longer any apparent shift in the position of the maxima. As discussed in the previous section, the data points in the valleys of the transmission curve are due to nonlinear PMT saturation and would not be present at lower count rates. Furthermore, the asymmetry seen in the experiment with the HeNe beam is no longer present since the laser wavelength matches the $\lambda/2$-plate. The set of zeros in the plot of Fig. E.5(b) are present because the laser beam was blocked while the experiment was still running.

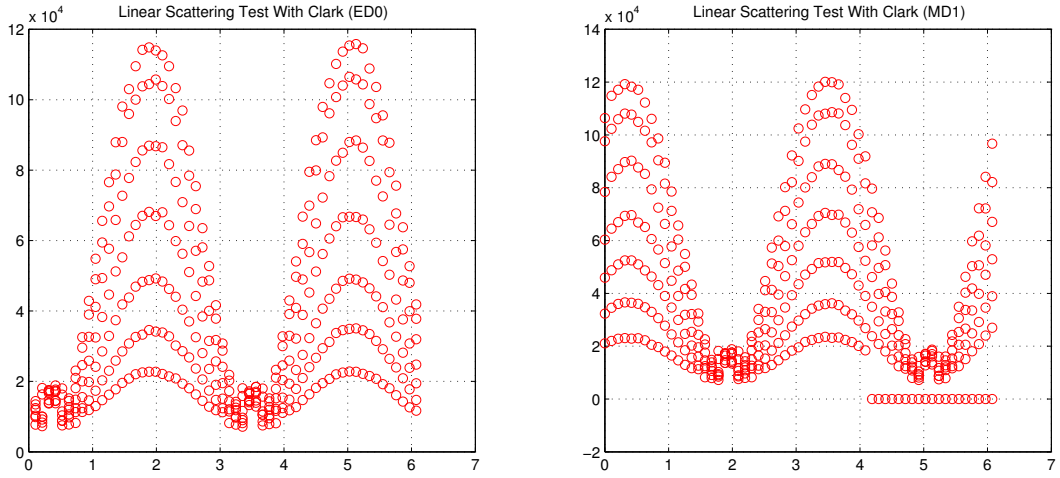

(a) (b)

Figure E.5: Experimental test of transmitted polarized light through the analyzer in vertical (a) and horizontal (b) orientations. There is no longer any apparent slippage of the mechanical stage. In both plots, the horizontal axis is the angle in radians and the vertical axis is the total number of counts. A 3 s count interval was used.

APPENDIX F

Determining the Maximum Intensity from a Gaussian Pulse

We can calculate the peak intensity of a pulse of light if we measure the average power, repetition rate, cross-sectional area, and temporal bandwidth. A convenient back of the envelope method of approximating the max intensity is to simply divide the average power by the rep. rate, beam area, and pulse duration,

$$I_{max} \approx \frac{\text{Average Power}}{(\text{Rep. Rate})\,(\text{Beam Area})\,(\text{Pulse Duration})} \,. \tag{F.1}$$

This expression is an approximation because it assumes that the intensity is essentially evenly-distributed throughout the "volume" created by the product of the cross-sectional area with the pulse duration. In fact, the beam has a Gaussian distribution about each direction within this volume with its maximum value being in the center. Because of this a correction factor must be determined if we wish to derive the true value for I_{max}. This issue is further compounded by the fact that there is not always a consistent measure for what is considered the width of a Gaussian.

All that matters for the sake of this discussion is that the values we measure in the lab can accurately be included in the expression used to calculate I_{max}. Most measuring devices will measure either the full-width at half-max (FWHM), the full-width at $1/e^2$, or some combination of deviations $\pm 2\sigma$, $\pm 4\sigma$, etc. The Thor-Labs beam camera that we use measures the full-width at $1/e^2$, which is the width at about 13.5% of the peak amplitude. The relationship between this width and the FWHM is

$$2w = \frac{\sqrt{2}}{\sqrt{\ln 2}}\text{FWHM} \,, \tag{F.2}$$

where $2w$ is the full-width of the beam at $1/e^2$. The relationship between the deviation σ of a Gaussian and the FWHM,

$$\text{FWHM} = 2\sqrt{2\ln 2}\sigma \ . \tag{F.3}$$

So then the width at $1/e^2$ is simply

$$2w = \frac{\sqrt{2}}{\sqrt{\ln 2}} 2\sqrt{2\ln 2}\sigma = 4\sigma \ , \tag{F.4}$$

and so the actual width at $1/e^2$ is *really* just the width of the beam at $\pm 2\sigma$. Now we know that a single standard deviation is simply the measured width divided by four,

$$\sigma = \frac{2w}{4} \ . \tag{F.5}$$

Take care to note that the value displayed by the camera is the *full* width, which is $2w$, not w.

Now that we have a way to relate the measured beam width from the lab to a some standard deviation, we must determine what value of the width to use in order to correctly identify the *effective radius*. Here "effective radius" refers to the proportion of the measured width we can use so the peak of the Gaussian corresponds to the peak of the top-hat function we are essentially approximating it as. If this logic is unclear, consider two possible cases. In case 1, the radius is taken to be half of the FWHM and in case 2, the radius is taken to be half of the $1/e^2$ width. The beam is identical in both cases, but in case 1 the peak intensity will be higher since the radius is smaller, and in case 2 the peak intensity will be lower. This leads back to the question: what is the appropriate radius so that the value calculated for I_{max} is the true value?

The easiest way to do this is by plotting a normalized Gaussian function (i.e. the area underneath is unity) along with a series of top hat functions with varying dimensions, but which each have area unity. This allows one to see which radius (or width dimension) would give an appropriate amplitude dimension. Here we assume a normalized Gaussian function

$$G(x,\sigma) = \frac{1}{\sigma\sqrt{2\pi}} e^{-x^2/2\sigma^2} \ , \tag{F.6}$$

which is a function of position x and standard deviation σ. Figure F.1 shows the result of plotting several boxes with varying width on the same axes as the normalized Gaussian. The corresponding widths of the boxes are as follows: blue = 2σ, purple = 2.5σ, green = 3σ, and red = 2σ. Clearly the blue box has an amplitude which is about 25% higher than the Gaussian, so we would be over-approximating the actual power in the beam. On the other hand, the red box has an amplitude about 50% lower than the Gaussian, so here we

would be under-approximating the power in the beam. Clearly the best choice is for the purple box, which has a half-width of 1.25σ. It is interesting to note that this is close to the value that most people probably use, which is the FWHM, which has a half-width of $\text{FWHM}/2 = \sqrt{2\ln 2} = 1.18\sigma$.

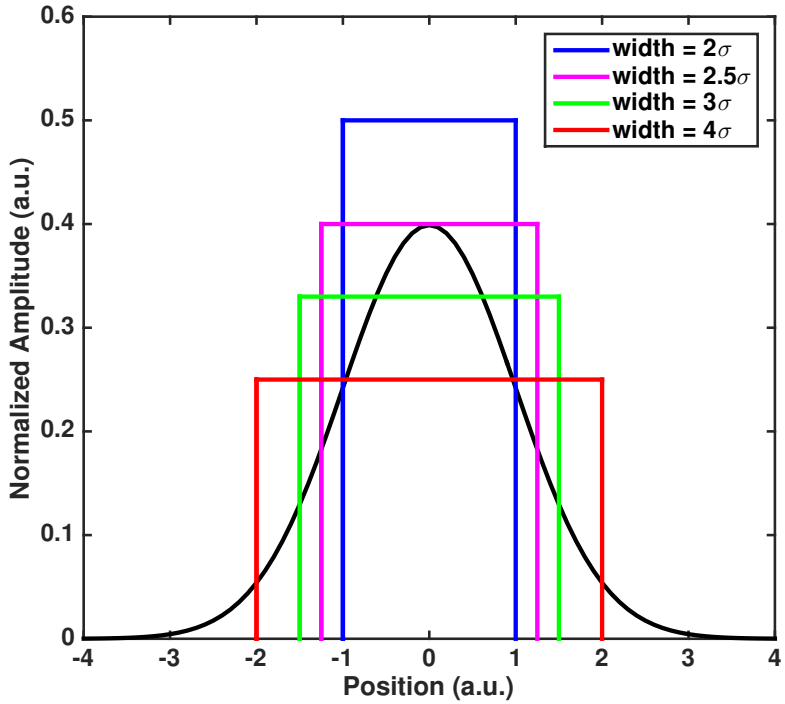

Figure F.1: A normalized Gaussian function with different top hat functions of varying height and width. Here the color codes correspond to widths of: blue $= [-\sigma, \sigma]$, purple $= [-1.25\sigma, 1.25\sigma]$, green $= [-1.5\sigma, 1.5\sigma]$, and red $= [-2\sigma, 2\sigma]$. Here $\sigma = 1$, but the axes simply scale for any other value.

So, basically by inspection, we have found the optimal radius to be 1.25σ when computing the cross-sectional beam area. This idea is easily extended to 2-dimensional Gaussian distributions, which would be fitted according to

$$f(x,y) = \frac{1}{2\pi\sigma_x\sigma_y} e^{-x^2/2\sigma_x^2} e^{-y^2/2\sigma_y^2} \,, \tag{F.7}$$

and the cross-sectional area which best represents the true value of the peak intensity will be

$$\text{Beam Area} = \pi\,(1.25\sigma_x)\,(1.25\sigma_y) = \left(\frac{5}{4}\right)^2 \pi\sigma_x\sigma_y \,. \tag{F.8}$$

This can now be used to help us write down the pulse energy density (or the pulse energy per unit area). The pulse energy is calculated by dividing the average power by the repetition rate of the laser,

$$\mathcal{E} = \text{Pulse Energy} = \frac{\text{Average Power}}{\text{Rep. Rate}} \, . \tag{F.9}$$

Note this quantity has units of J (or can be thought of as J/pulse). The pulse energy density is then just this number divided by the beam area from above,

$$\text{Pulse Energy per Area} = \left(\frac{4}{5}\right)^2 \frac{\mathcal{E}}{\pi \sigma_x \sigma_y} \, . \tag{F.10}$$

Finally, we need to determine the correct way to incorporate the temporal measurement of the pulse. The lab measurement for the pulse duration is provided from the MIIPS system after compression and the measured value is the FWHM. We will assume the intensity of the pulse has a temporal dependence that can be approximated by a Gaussian function,

$$I(t) = I_{max} e^{-t^2/2\sigma_t^2} \, , \tag{F.11}$$

where

$$2\sqrt{2\ln 2}\sigma_t = \text{FWHM}_t \tag{F.12}$$

is the temporal FWHM of the intensity. Integrating $I(t)$ over the entire duration of the pulse gives us the total energy per area of a single pulse, which is precisely what we solved for above in Eq. (F.10). Putting these two equations together, we see

$$\left(\frac{4}{5}\right)^2 \frac{\mathcal{E}}{\pi \sigma_x \sigma_y} = \int_{-\infty}^{\infty} I_{max} e^{-t^2/2\sigma_t^2} dt \, . \tag{F.13}$$

Solving for I_{max} we have

$$I_{max} = \left(\frac{4}{5}\right)^2 \frac{\mathcal{E}}{\pi \sigma_x \sigma_y} \left[\int_{-\infty}^{\infty} e^{-t^2/2\sigma_t^2} dt\right]^{-1} \, . \tag{F.14}$$

The integral in the square brackets evaluates to

$$\int_{-\infty}^{\infty} e^{-t^2/2\sigma_t^2} dt = \sqrt{2\pi}\sigma_t \, . \tag{F.15}$$

Putting these pieces all together, we have

$$I_{max} = \left(\frac{4}{5}\right)^2 \frac{\mathcal{E}}{\pi\sigma_x\sigma_y}\frac{1}{\sqrt{2\pi}\sigma_t} \,, \tag{F.16}$$

which is a general expression for the maximum intensity in terms of σ_x, σ_y, and σ_z.

A final step is to relate this expression to the quantities measured in the lab. First we can rewrite the spatial standard deviations in terms of the measured full-width at $1/e^2$ from the beam camera. Recall from above that the full-width at $1/e^2$ is $2w$ and is equivalent to 2σ from the center (i.e. $2w = 4\sigma$). Because the measurement is the full width, we define a new variable to remove the factor of 2,

$$W_x = 2w_x = 4\sigma_x \,, \tag{F.17}$$

$$W_y = 2w_y = 4\sigma_y \,, \tag{F.18}$$

so then

$$\sigma_x = W_x/4 \,, \tag{F.19}$$

$$\sigma_y = W_y/4 \,. \tag{F.20}$$

We also may replace the temporal deviation σ_t using the relationship between this and the FWHM along t. The intensity then becomes

$$I_{max} = \left(\frac{4}{5}\right)^2 \frac{\mathcal{E}4^2}{\pi W_x W_y}\frac{2\sqrt{2\ln 2}}{\sqrt{2\pi}\text{FWHM}_t} \tag{F.21}$$

$$= \frac{512}{25}\sqrt{\frac{\ln 2}{\pi}}\frac{\mathcal{E}}{(\pi W_x W_y)\,(\text{FWHM}_t)} \,. \tag{F.22}$$

It is essential to realize here that W_x and W_y are the measured values of the beam full-width and the FWHM_t is the measured value from the MIIPS compressor. This equation is written in this way only as a convenience for relating measurements from the lab to the actual intensity.

A final check can be made to see how much this analysis actually changes the value of I_{max} from the back of the envelope approximation established at the beginning of this Appendix. Grouping together the numerical factors (and substituting $2w_{x,y}$ back in for $W_{x,y}$) we see

$$\frac{512}{25}\sqrt{\frac{\ln 2}{\pi}}\frac{1}{4} = 2.4\ . \tag{F.23}$$

This means the calculated values for intensity could be off by as much as a factor of 2.4. Note that this factor comes almost completely from the correct choice of cross-sectional beam radii. The correction to the pulse duration is simply

$$\frac{2}{\sqrt{2\pi}}\sqrt{2\ln 2} = 0.94\ . \tag{F.24}$$

BIBLIOGRAPHY

[1] S. L. Oliveira and S. C. Rand, "Intense nonlinear magnetic dipole radiation at optical frequencies: Molecular scattering in a dielectric liquid," *Phys. Rev. Lett.*, vol. 98, no. 093901, 2007.

[2] S. C. Rand, W. M. Fisher, and S. L. Oliveira, "Optically-induced magnetization in homogeneous, undoped dielectric media," *J. Opt. Soc. Am. B*, vol. 25, no. 1106, 2008.

[3] D. H. Auston, K. P. Cheung, J. A. Valdmanis, and D. A. Kleinman, "Cherenkov radiation from femtosecond optical pulses in electro-optic media," *Phys. Rev. Lett.*, vol. 53, no. 16, pp. 1555–1558, 1984.

[4] W. M. Fisher, *Transverse Optical Magnetism*. PhD thesis, University of Michigan, 2012.

[5] W. M. Fisher and S. C. Rand, "Light-induced dynamics in the lorentz oscillator model with magnetic forces," *Phys. Rev. A*, vol. 82, no. 013802, 2010.

[6] S. C. Rand, "Quantum theory of coherent transverse optical magnetism," *J. Opt. Soc. Am. B*, vol. 26, no. B120, 2009.

[7] P. D. Maker and R. W. Terhune, "Study of optical effects due to an induced polarization third order in the electric field strength," *Phys. Rev.*, vol. 137, no. A801, 1965.

[8] J. C. Ginn, I. Brener, D. W. Peters, J. R. Wendt, J. O. Stevens, P. F. Hines, L. I. Basilio, L. K. Warne, J. F. Ihlefeld, P. G. Clem, and M. B. Sinclair, "Realizing optical magnetism from dielectric metamaterials," *Phys. Rev. Lett.*, vol. 108, no. 097402, 2012.

[9] W. F. Koehl, B. B. Buckley, F. J. Heremans, G. Calusine, and D. D. Awschalom, "Room temperature coherent control of defect spin qubits in silicon carbide," *Nature*, vol. 479, no. 84, 2011.

[10] G. D. Fuchs, G. Burkard, P. V. Klimov, and D. D. Awschalom, "A quantum memory intrinsic to single nitrogen-vacancy centers in diamond," *Nature Physics*, vol. 7, no. 789, 2011.

[11] C. D. Stanciu, F. Hansteen, A. V. Kimel, A. Kirilyuk, A. Tsukamoto, A. Itoh, and T. Rasing, "All-optical magnetic recording with circularly polarized pulses," *Phys. Rev. Lett*, vol. 99, no. 047601, 2007.

[12] L. D. Landau, E. M. Lifshitz, and L. P. Pitaevskii, *Electrodynamics of Continuous Media*. Pergamon Press, 2nd ed., 1984.

[13] G. A. Mourou, Z. Chang, A. Maksimchuk, J. Nees, S. V. Bulanov, V. Y. Bychenkov, T. Z. Esirkepov, N. M. Naumova, F. Pegoraro, and H. Ruhl, "On the design of experiments for the study of relativistic nonlinear optics in the limit of single-cycle pulse duration and single-wavelength spot size," *Plasma Physics Reports*, vol. 28, no. 1, pp. 12–27, 2002.

[14] A. W. Clark, A. K. Sheridan, A. Glidle, D. R. S. Cumming, and J. M. Cooper, "Tunable visible resonances in crescent shaped nano-split-ring resonators," *Appl. Phys. Lett.*, vol. 91, no. 093109, 2007.

[15] W. M. Fisher and S. C. Rand, "Dependence of optical magnetic response on molecular electronic structure," *J. Lumin.*, vol. 129, no. 1407, 2009.

[16] W. M. Fisher and S. C. Rand, "Optically-induced charge separation and terahertz emission in unbiased dielectrics," *J. Appl. Phys.*, vol. 109, no. 064903, 2011.

[17] P. S. Pershan, "Nonlinear optical properties of solids: Energy considerations," *Phys. Rev.*, vol. 130, no. 919, 1963.

[18] W. K. H. Panofsky and M. Phillips, *Classical Electricity and Magnetism*. Addison-Wesley Publishing Company, 1962.

[19] D. S. Wiersma, *Light in strongly scattering and amplifying random media*. PhD thesis, FOM-Institute for Atomic and Molecular Physics, 1995.

[20] J. D. Jackson, *Classical Electrodynamics*. John Wiley and Sons, Inc., 1962.

[21] S. Kielich, "Molecular interactions in optically-induced nonlinearities," *IEEE J. Quant. Elec.*, vol. QE-4, no. 11, 1968.

[22] S. Suresh, A. Ramanand, D. Jayaraman, and P. Mani, "Review on theoretical aspect of nonlinear optics," *Rev. Adv. Mater. Sci.*, pp. 175–183, 2012.

[23] N. Minkovski, G. I. Petrov, and S. M. Saltiel, "Nonlinear polarization rotation and orthogonal polarization generation experienced in a single-beam configuration," *J. Opt. Soc. Am. B*, vol. 21, no. 9, pp. 1659–1664, 2004.

[24] S. Kourtev, N. Minkovski, L. Canova, A. Jullien, and S. M. Saltiel, "Improved nonlinear cross-polarized wave generation in cubic crystals by optimization of crystal orientation," *J. Opt. Soc. Am. B*, vol. 26, no. 7, pp. 1269–1275, 2009.

[25] R. W. Terhune, P. D. Maker, and C. M. Savage, "Measurements of nonlinear light scattering," *Phys. Rev. Lett.*, vol. 14, no. 17, 1965.

[26] S. Sen, V. Galiatsatos, and G. D. Patterson, "Depolarized rayleigh scattering from simple molecular liquids: investigation of transitions in the melt," *J. Chem. Phys.*, vol. 103, no. 892, 1995.

[27] V. N. Lugovoy and A. M. Prokhorov, "On a possible explanation of small-scale trapping filaments," *Zh. Eksperim. i Teor. Fiz. Pis'ma*, vol. 29, 7.

[28] G. Rivoire and J. L. Beaudoin, "Temperature et seuil d'obtention des rais stokes et anti-stokes en effet raman stimule," *J. Phys.*, vol. 29, 1968.

[29] P. D. Maker, "Nonlinear light scattering in methane," *Phys. Q. Elec.*, vol. 14, pp. 681–684, 1965.

[30] Y. R. Shen, "Electrostriction, optical kerr effect and self-focussing of laser beams," *Phys. Lett.*, vol. 20, pp. 378–380, 1966.

[31] S. Kielich, "Optically induced birefringence calculated from light scattering data of liquids," *Phys. Lett.*, vol. 24A, pp. 383–385, 1967.

[32] S. Kielich and A. Piekara, "A statistical-molecular theory of electric, magnetic and optical saturation phenomena in isotropic dielectric and diamagnetic media," *Acta Phys. Polon.*, vol. 18, pp. 439–472, 1958.

[33] H. Broer and M. Levi, "Geometrical aspects of stability theory for hill's equations," *Archive for Rational Mechanics and Analysis*, vol. 131, no. 3, 1995.

[34] C. Cohen-Tannoudji, *Atom-photon Interactions: Basic Processes and Applications*. John Wiley and Sons, Inc., 1992.

[35] S. C. Rand, *Nonlinear and Quantum Optics Using the Density Matrix*. Oxford University Press, 2010.

[36] K. Konishi and G. Paffuti, *Quantum Mechanics: A New Introduction*. Oxford University Press, 2009.

[37] G. Herzberg, *Molecular Spectra and Molecular Structure: I. Diatomic Molecules*. Prentice-Hall, 1939.

[38] C. H. Townes and A. L. Schawlow, *Microwave Spectroscopy*. Dover Publications, Inc., 1975.

[39] J. L. Hopkins, "Dead time," *IAPPP Communications*, no. 46, pp. 9–14, 1992.

[40] V. M. Volynkin, K. V. Gratsianov, A. N. Kolesnikov, Y. I. Kruzhilin, V. V. Lyubimov, S. A. Markosov, P. V. G., A. I. Stephanov, and S. V. Shklyarik, "Reflection by stimulated brilloiun scattering mirrors based on tetrachlorides of group iv elements," *Sov. J. Quantum Electron.*, vol. 15, no. 12, 1985.

[41] M. L. Delwaulle, M. B. Buisset, and M. Delhaye, "The study of chloroiodides of silicon, tin, and germanium using the raman spectra as proof of equilibria," *J. Am. Chem. Soc.*, vol. 74, no. 22, pp. 5768–5770, 1952.

[42] J. H. Hildebrand and R. H. Lamoreaux, "Fluidity: a general theory," *Proc. Nat. Acad. Sci.*, vol. 69, no. 11, pp. 3428–3431, 1972.

[43] B. P. Stoicheff, "High resolution raman spectroscopy of gases," *Canadian Journal of Physics*, vol. 35, no. 6, pp. 730–741, 1957.

[44] G. Varsanyi, *Vibrational Spectra of Benzene Derivatives*. Academic Press, 1969.

[45] D. Mcmorrow, W. T. Lotshaw, and G. A. Kenney-Wallace, "Femtosecond raman-induced kerr effect. temporal evolution of the vibrational normal modes in halogenated methanes," *Chem. Phys. Lett.*, vol. 145, no. 4, pp. 309–314, 1988.

[46] A. A. Fisher, E. F. Cloos, W. M. Fisher, and S. C. Rand, "Dynamic symmetry-breaking in a simple quantum model of magneto-electric rectification, optical magnetization, and harmonic generation," *Opt. Exp.*, vol. 22, no. 3, 2014.

[47] R. R. Sharp, "Field dependence of nuclear magnetic relaxation of 119sn in sncl4, snbr4, and sni4," *J. Chem. Phys.*, vol. 60, no. 1149, 1974.

[48] R. Carley, K. Dobrich, B. Frietsch, C. Gahl, M. Teichmann, O. Schwarzkopf, P. Wernet, and M. Weinelt, "Femtosecond laser excitation drives ferromagnetic gadolinium out of magnetic equilibrium," *Phys. Rev. Lett.*, vol. 109, no. 057401, 2012.

[49] J. B. Pendry, "Negative refraction makes a perfect lens," *Phys. Rev. Lett.*, vol. 85, pp. 3966–3969, 2000.

[50] D. Sievenpiper, L. Zhang, R. F. J. Broas, N. G. Alexopolous, and E. Yablonovitch, "High-impedance, electromagnetic surfaces with a forbidden frequency band," *IEEE Trans. Microwave Theory Tech.*, vol. 47, pp. 2059–2074, 1999.

[51] X. Liu, L. Fu, S. Hong, V. P. Dravid, and C. A. Mirkin, "Arrays of magnetic nanoparticles patterned via "dip-pen" nanolithography," *Advanced Materials*, vol. 14, pp. 231–234, 2002.

[52] J. B. Pendry, D. Schurig, and D. R. Smith, "Controlling electromagnetic fields," *Science*, vol. 312, pp. 1780–1782, 2006.

[53] J. Karch, P. Olbrich, M. Schmalzbauer, C. Zoth, C. Brinsteiner, M. Fehrenbacher, U. Wurstbauer, M. M. Glazov, S. A. Tarasenko, E. L. Ivchenko, D. Weiss, J. Eroms, R. Yakimova, S. Lara-Avila, S. Kubatkin, and S. D. Gainchev, "Dynamic hall effect driven by circularly polarized light in a graphene layer," *Phys. Rev. Lett.*, vol. 105, no. 227402, 2010.

[54] K. Y. Bliokh and F. Nori, "Relativistic hall effect," *Phys. Rev. Lett.*, vol. 108, no. 120403, 2012.

[55] P. A. Obraztsov, T. Kaplas, S. V. Garnov, M. Kuwata-Gonokami, A. N. Obraztsov, and Y. P. Svirko, "All-optical control of ultrafast photocurrents in unbiased graphene," *Scientific Reports*, vol. 4, no. 4007, 2014.

[56] J. Karch, P. Oblrich, M. Schmalzbauer, C. Brinsteiner, U. Wurstbauer, M. M. Glazov, S. A. Tarasenko, E. L. Ivchenko, D. Weiss, J. Eroms, and S. D. Ganichev, "Photon helicity drive electric currents in graphene," *arXiv*, no. 1002.1047v1, 2010.

[57] J. Maysonnave, S. Huppert, F. Wang, S. Maero, C. Berger, W. de Heer, T. B. Norris, L. A. De Vaulchier, S. Dhillon, J. Tignon, R. Ferreira, and J. Mangeney, "Terahertz generation by dynamic photon drag effect in graphene excited by femtosecond optical pulses," *Nano Letters*, vol. 14, pp. 5797–5802, 2014.

[58] K. Sakai, *Terahertz Optoelectronics*. Springer Press, Heidelberg, Germany, 2005.

[59] J. A. Valdmanis, G. A. Mourou, and C. W. Gabel, "Subpicosecond electrical sampling," *IEEE J. Quant. Elec.*, vol. QE-19, no. 4, 1983.

[60] R. P. Smith, D. H. Auston, and M. C. Nuss, "Subpicosecond photoconducting dipole antennas," *IEEE J. Quant. Elec.*, vol. 24, no. 2, 1988.

[61] Y.-S. Lee, T. Meade, V. Perlin, H. Winful, T. B. Norris, and A. Galvanauskas, "Generation of narrow-band terahertz radiation via optical rectification of femtosecond pulses in periodically poled lithium niobate," *Appl. Phys. Lett*, vol. 76, no. 2505, 2000.

[62] P. Liu, X. D., C. Liu, L. D., L. Y., P. Wang, and J. Yao, "p-polarized cherenkov thz wave radiation generated by optical rectification generation for a brewster-cut $linbo_3$ crystal," *J. Opt.*, vol. 13, no. 085202, 2011.

[63] J. Hebling, G. Almási, and I. Z. Kozma, "Velocity matching by pulse front tilting for large-area thz-pulse generation," *Opt. Exp.*, vol. 10, no. 2, pp. 1161–1166, 2002.

[64] C. W. Berry, W. Nang, M. R. Hashemi, and M. Jarrahi, "Significant performance enhancement in photoconductive terahertz optoelectronics by incorporating plasmonic contact electrodes," *Nature Communications*, vol. 4, no. 1622, 2013.

[65] Y. R. Shen, *The Principles of Nonlinear Optics*. John Wiley and Sons, Inc., 1984.

[66] M. W. Klein, C. Enkrich, M. Wegener, and S. Linden, "Second-harmonic generation from magnetic metamaterials," *Science*, vol. 313, no. 5786, pp. 502–504, 2006.

[67] T. Carmon and K. J. Vahala, "Visible continuous emission from a silica microphotonic device by third-harmonic generation," *Nature Physics*, vol. 3, pp. 430–435, 2007.

[68] Q. Lin, T. J. Johnson, R. Perahia, C. P. Michael, and O. J. Painter, "A proposal for highly tunable optical parametric oscillation in silicon micro-resonators," *Opt. Exp.*, vol. 16, pp. 10596–10610, 2008.

[69] J. Chan, T. P. Mayer Alegre, A. H. Safavi-Naeini, J. T. Hill, A. Krause, S. Groblacher, M. Aspelmeyer, and O. Painter, "Laser cooling of a nanomechanical oscillator into its quantum ground state," *Nature*, vol. 478, pp. 89–92, 2011.

[70] C. Zhang, S. Chen, T. Ling, and L. J. Guo, "Review of imprinted polymer microrings as ultrasound detectors: design, fabrication, and characterization," *IEEE Sensor Journal*, vol. 15, no. 3241, 2015.

[71] H. Chandrahalim, Q. Chen, A. A. Said, M. Dugan, and X. Fan, "Monolithic optofluidic ring resonator lasers created by femtosecond laser nanofabrication," *Lab Chip*, vol. 15, no. 2335, 2015.

[72] H. Chandrahalim and X. Fan, "Reconfigurable solid-state dye-doped polymer ring resonator lasers," *Scientific Reports*, 2015.

[73] Z. Mao, S. M. Dorfman, S. R. Shieh, J. F. Lin, V. Prakapenka, Y. Meng, and T. S. Duffy, "Equation of state of a high-pressure phase of $gd_3ga_5o_{12}$," *Phys. Rev. B*, 2010.

[74] Y. Xu and W. Y. Ching, "Electronic structure of yttrium aluminum garnet ($y_3al_5o_{12}$)," *Phys. Rev. B*, vol. 59, no. 16, 1999.

[75] D. J. Jones, S. T. Cundiff, T. M. Fortier, J. L. Hall, and J. Ye, *Few-Cycle Laser Pulse Generation and Its Applications (Carrier-envelope phase stabilization of single and multiple femtosecond lasers)*. Springer Press, Heidelberg, Germany, 2004.

[76] D. J. Jones, S. A. Diddams, J. K. Ranka, A. Stentz, R. S. Windeler, J. L. Hall, and S. T. Cundiff, "Carrier-envelope phase control of femtosecond mode-locked lasers and direct optical frequency synthesis," *Science*, vol. 288, no. 5466, 2000.

[77] E. Gagnon, I. Thomann, A. Paul, A. Lytle, S. Backus, M. Murnane, H. Kapteyn, and A. Sandhu, "Long-term carrier-envelope phase stability from a grating-based, chirped pulse amplifier," *Opt. Lett.*, vol. 31, pp. 1866–1868, 2006.

[78] T. M. Fortier, D. J. Jones, J. Ye, S. T. Cundiff, and R. S. Windeler, "Long-term carrier-envelope phase coherence," *Opt. Lett.*, vol. 27, no. 16, pp. 1436–1438, 2002.

[79] G. F. Knoll, *Radiation Detection and Measurement, 4th Edition*. Hamilton Printing Company, 2010.